SANDIA REPORT

SAND2005-5734
Unlimited Release
Printed September 2005

Bio Micro Fuel Cell Grand Challenge Final Report

Christopher Apblett, Kent Schubert, Bruce Kelley, Andrew Walker, Blake Simmons, Ted Borek, Stephen Meserole, Todd Alam, Brian Cherry, Greg Roberts, Jim Novak, Jim Hudgens, Dave Peterson, Jason Podgorski, Susan Brozik, Jeb Flemming, Stan Kravitz, David Ingersoll, Steve Eisenbies, Randy Shul, Sarah Rich, Carrie Schmidt, Mike Beggans, Jeanne Sergeant, Chris Cornelius, Cy Fujimoto, Micheal Hickner, Swapnil Chabra, Suzanne Ma, Joanne Volponi, Micheal Kelly, Kevin Zavadil, Chad Staiger, Patricia Dolan, Monica Manginell, Jason Harper, Dan Doughty, Steve Casalnuovo

Prepared by Sandia National Laboratories
Albuquerque, New Mexico 87185 and Livermore, California 94550

Sandia is a multiprogram laboratory operated by Sandia Corporation,
a Lockheed Martin Company, for the United States Department of Energy's
National Nuclear Security Administration under Contract DE-AC04-94AL85000.

Issued by Sandia National Laboratories, operated for the United States Department of Energy by Sandia Corporation.

Available to DOE and DOE contractors from
U.S. Department of Energy
Office of Scientific and Technical Information
P.O. Box 62
Oak Ridge, TN 37831

Telephone: (865)576-8401
Facsimile: (865)576-5728
E-Mail: reports@adonis.osti.gov
Online ordering: http://www.osti.gov/bridge

Available to the public from
U.S. Department of Commerce
National Technical Information Service
5285 Port Royal Rd
Springfield, VA 22161

Telephone: (800)553-6847
Facsimile: (703)605-6900
E-Mail: orders@ntis.fedworld.gov
Online order: http://www.ntis.gov/help/ordermethods.asp?loc=7-4-0#online

SAND 2005-5734
Unlimited Release
Printed September 2005

Bio Micro Fuel Cell

Christopher Apblett, Kent Schubert, Bruce Kelley, Andrew Walker, Blake Simmons, Ted Borek, Stephen Meserole, Todd Alam, Brian Cherry, Greg Roberts, Jim Novak, Jim Hudgens, Jason Podgorski, Susan Brozik, Jeb Flemming, Stan Kravitz, David Ingersoll, Steve Eisenbies, Randy Shul, Sarah Rich, Carrie Schmidt, Mike Beggans, Jeanne Sergeant, Chris Cornelius, Cy Fujimoto, Micheal Hickner, Swapnil Chabra, Suzanne Ma, Joanne Volponi, Micheal Kelly, Kevin Zavadil, Chad Staiger, Patricia Dolan, Monica Manginell, Jason Harper, Dan Doughty, Steve Casalnuovo
Sandia National Laboratories
PO Box 5800
Albuquerque, NM 87185-0603

Executive Summary

This LDRD was conceived to develop a power system that could harvest the energy from carbohydrate fuels that are readily available and can be harvested from biological sources. This included the possibilities of generating power from harvested tree sap, sugars, and even mammalian blood. Since the biological host continues to produce and/or replace these fuels as part its normal biological processes, this approach enables a very long lived, power microsystem. Fuel cells were identified as the energy conversion systems most likely to take advantage of the opportunities of a continuous fuel supply, and therefore the project started from an existing foundation in traditional fuel cell operations.

Six basic subtasks were identified for this project; harvesting, membrane separation, catalysis, architecture, enzymology, and power management. Harvesting targeted both harvesting from a tree using a simple spile arrangement, and harvesting through the skin of mammalian hosts using a microneedle patch. Membrane separation provided a physical separator between the anode oxidation of the fuel and the cathodic reduction of oxygen. The catalysis team targeted both the development of new, poison resistant, highly active noble metal catalysts that could readily oxidize the carbohydrate fuel without poisoning the catalysts, and also worked to develop mediator molecules to transport oxidized electrons from enzyme catalysts to anode electrode surfaces. The enzymology team developed protocols for the genetic engineering of enzymes capable of oxidizing the carbohydrates, and also looked into the requirements to immobilize these enzymes against an electrode, together with the catalysis team. The architecture team was tasked with developing a small architecture that could take in these other components and assemble them into working fuel cells running on glucose (a simple carbohydrate) and oxygen. The power management task, added after the initial program was started, focused on handling the variation in the power output from the fuel cells and in turn producing stable, electronic grade power to supply to an external circuit.

At the end of the project, the best power generated from a single, 15mm x 21mm x 1mm fuel cell was about 7 mW/cm^2 running on 1 molar (M) glucose in water and oxygen at room temperature. This was achieved using a noble metal catalyst. The best enzymatic fuel cell using an anode based on glucose oxidase was able to demonstrate

250μW/cm^2 of power from a 50 millimolar glucose solution. In both cases, however, the lifetime was limited to a few minutes . In the noble metal case, oxidation byproducts quickly poison the catalysts. However, a system solution for *in situ* cleaning of the anode with little power penalty eventually extending the lifetime to about 700 hours (nearly one month) while producing about 2 mW/cm^2. In the enzymatic case, the lifetime was limited to minutes of operation by the loss of enzyme and mediator to the flowing fuel. Significant progress was made in stabilizing the enzyme, but mediator lifetime in the flow through cell remains a significant challenge.

Each of the subtasks was able to achieve significant progress in their respective areas and in several cases significant alternative applications for the technology have also been identified and will be pursued in the future. Harvesting was able to demonstrate a series of microneedles, each shorter than a human hair is wide, that were able to dramatically increase the diffusion rate of glucose across pig skin (which is similar to human skin). The microneedle technology developed as part of this project spawned a separate sensor related Laboratory Directed Research and Development (LDRD) project and has also led to significant outside interest for biomedical applications. The membrane task was able to develop a new, novel membrane that was capable of withstanding the transport of glucose and methanol by an order of magnitude over the currently available membrane materials, which improves the performance of the biofuel cell as well as traditional hydrogen and methanol fuel cells. The metal based catalysis program was able to identify several improved catalysts for the oxidation of glucose, and was able to develop a rapid screening protocol to search through thousands of potential catalytic alloys using a parallel electrochemical technique. The enzymatic catalysis effort identified several new mediator molecules for mediating electrons between enzymes and electrodes, which allowed for improved biosensor applications, as well as improved power for biofuel cells. A genetic engineering program was initiated under this grand challenge, and grew to provide Sandia with a strong capability in this area for further genetic engineering work, that appears to be unique among the national laboratories. This new capability enabled us to generate new genetically modified glucose oxidase variants with higher activity than the natural strain toward the oxidation of glucose. The micro fuel cell architecture team was able to assemble and demonstrate record level powers of roughly 700mW/cm^2

for hydrogen and 100mW/cm^2 for methanol, which are good power levels for large scale cells, and unprecedented for fuel cells that are under a cubic centimeter in total volume. Finally, the power management team developed new methods for turning the continually varying power produced by the fuel cells into useable electronic grade power. This is a challenge common to all energy harvesting approaches, and the unique approach developed here is likely to find wider applicability.

Although the wildly ambitious original goal of "100 mW/cm^2 for weeks" was not achieved, impressive progress was made. Our External Advisory Committee stated "*In retrospect this was not a 3 to 4 year project; rather, this was a 10 year project. What has been done from an almost 'zero' starting point, with a limited budget and a relatively short amount of time, has been extraordinary."* Key remaining challenges are understood and viable approaches have been demonstrated that will eventually enable this sort of power system. Furthermore, several new capabilities with wide applicability have been established and strengthened as part of this project. These capabilities will help Sandia to be a significant future contributor at this intersection of microsystems and the biological world.

Table of Contents

1. Introduction to the Bio Micro Fuel Cell Grand Challenge LDRD

1.1 Motivation and Historical Perspective for Fuel Cells

Miniaturization of sensor components have allowed the realization of very compact, reliable systems capable of operating in an unattended mode, with itinerant electronics allowing periodic transmission of the sensed data back to a centralized data handling hub, all in a volume much smaller than a typical watch battery. For field operating sensor systems of this type, however, the volume of the power source quickly becomes the dominant factor in system volume. For systems that are desired to operate for weeks or months in the field without refueling, the volume of the system quickly becomes inconsequential relative to the volume of fuel that must be carried with the system to

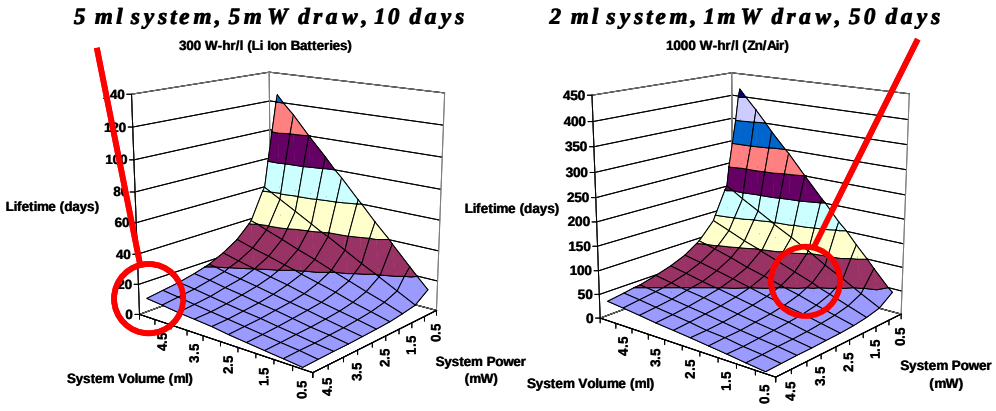

Figure 1.1: Calculated lifetimes of batteries of a given size for a given power draw. With a fixed fuel volume and even modest power requirements, lifetime of operation is severely limited.

provide a needed power for a needed time. Energy density is normally discussed in terms of the number of watts of power delivered from a power source for a given length of time in a given volume, inclusive of the fuel, in Watt-hours per liter of system and fuel. Typical battery storage devices have energy densities on the order of 300-500 W-hr/l, and some of the best battery systems can exceed 1000 W-hr/l. Figure 1.1 shows modeled calculations for two different battery systems in terms of the number of days of operation available for a given system volume and given power output. Even under the most modest considerations of a 1mW power draw in a 5ml total system volume, even the best batteries, supplying 1000W-hr/l, can only operate for 5000 hours, or slightly over 7

months. Clearly, to reach operational lives in the field of months or years, a more dense power solution needs to be developed.

Many chemical fuels have energy densities in the thousands of watt-hours per liter, but require a fuel conversion system to efficiently convert the energy of the chemical bonds into electrical power. Internal combustion engines have traditionally filled this role, and good efficiencies at fuel conversion can be obtained from well designed engines. Long operational lifetimes of 50,000 hours of continuous operation have been demonstrated for large scale combustion engines. These conversion systems, however, do not scale particularly well, due to thermal transfer and tolerance issues associated with the miniaturization of a large scale engine.

Fuel cells are also being considered for small, portable power applications in the industry as a possible complementary technology to batteries. Batteries are energy storage devices, like supercapacitors and inductors, which allow for energy stored within the device to be discharged at a given rate to the ultimate energy stored within the device. In contrast, fuel cells are energy conversion devices, like internal combustion engines, that take a fixed fuel stream and convert the chemical energy of the fuel into electrical energy. To consider fuel cells with batteries, then, requires the setting of a given amount of volume or mass for the fuel, and making a comparison based upon this fixed volume of fuel.

To overcome the volume issue associated with the given fixed volume of fuel would be to harvest the fuel directly from the environment, thus obviating the need to store the fuel onboard the system. Since the fuel is understood to be the majority of the volume of any system, moving to a fuel harvesting converter would allow for dramatic miniaturization of the total system volume, since the fuel volume would no longer be included in the calculation for energy density. This harvested fuel, along with harvested air for the reduction reaction, would be used in a fuel cell system to generate power continuously from the oxidation of the fuel source and the reduction of oxygen in the air. Among the most ubiquitous fuels available in the natural environment are saccharides, or simple sugars. Sucrose, a polysaccharide, and glucose, a monosaccharide, exist in most plant saps in low concentrations, and make an attractive target for oxidation as a fuel, as these fuels are what are used by animals as a fuel source in the natural environment. For

the purposes of developing a fuel cell capable of operating on a saccharide fuel, however, one fuel type was selected for the development of the system, and this was glucose, although some effort at reforming of sucrose into glucose through an enzymatic metabolic pathway was also investigated.

In 1839 Grove discovered the first fuel cell by observing the production of electricity from organic chemicals using precious metal electrodes.[1] [2] These early fuel cells used ionically conductive electrolyte to separate the precious metal anode from the precious metal cathode. These liquid phase separators caused the fuel cells to be large and unwieldy, with constant attention paid to the condition of the electrolyte. The development of solid phase electrolytic materials, however, allowed for the development of thin separators, and it was not until the development of solid polymeric materials that fuel cells began to show their potential as a viable power source.[3] [4] [5] Fuel cells directly convert chemical energy into electrical energy. Typical fuels such as hydrogen, methanol, and ethanol can be directly oxidized and reduced utilizing a platinum or platinum/ruthenium oxide catalyst to generate power.

Unlike batteries, fuel cells can theoretically operate indefinitely by simply supplying more fuel. The efficiency of fuel conversion to power is 40-60% for fuel cells, while current internal combustion engines are only 20-30% efficient.[6] Most systems that are being discussed today discuss fuel efficiency in terms of fuel utilization, or how much energy per unit fuel can be derived. For a harvesting application, however, fuel utilization becomes less important, as the fuel is “free” and essentially can be had in arbitrarily large quantities for a micro-system. The issue, then, comes to designing and building a fuel conversion system that can generate reasonable powers for a given size and fuel flow rate from a readily harvestable source of fuel.

1.2 Organization of the Program

These criteria for harvested fuel systems require the development of several key technologies to be integrated together into a final system. First, the fuel must be harvested from the local environment. The natural environment provides two harvesting opportunities; plants and mammals (including humans). These two fuel sources present very different needs for harvesting, as the fuel types available, rates of extraction, availability during the seasons, and concentrations are very different. Bioharvesting is

the topic for section 2 of this report, and deals with the requirements for harvesting from both of these sources, as well as changing fuels from polysaccharides available in plants into mono-saccharides that can be oxidized on electrocatalysts.

Once the saccharide fuel is harvested from the environment, the fuel must be delivered to the anode catalyst, and generated electrons from the oxidation must be removed to an external circuit. Similarly, the oxidizer, typically oxygen from the environment, must be delivered to the cathode catalyst, and electrons from the external circuit must be delivered to the catalyst reaction sites for the reduction of this oxygen to water. At all times, the two reactants must be kept separate from one another. Any fuel that leaks from the anode to the cathode reacts without separation of the electrons, and becomes a parasitic reaction in the fuel cell, consuming fuel without generating any power. In addition, catalysis of the fuel on the cathode of the cell can cause a drop in the potential of the cathode, which will severely limit the cell potentials that can be developed. To separate fuel from oxygen, seals are needed to keep the flow channels separated, and some sort of separator membrane is required. Design of the architecture of a miniature fuel cell system is discussed in section 3.

Most low temperature fuel cells also require a separator membrane to isolate the oxidation reaction from the reduction reaction in the fuel cell. This separator membrane must play the role of an electrolyte, allowing protons to conduct between the oxidation and reduction catalysts, but forcing electrons into an external circuit. This separator must also provide good diffusion limitation properties for the reactants, so that diffusion based crossover of the oxidizer and the fuel across the membrane is kept to a minimum. For low temperature (<100C) operating fuel cells, a polymer electrolyte membrane (PEM) is used. These polymers conduct protons through a proton hopping mechanism along the polymer backbone of the molecules. This conduction mechanism requires water to be absorbed into the molecular structure of the polymer. This water absorption leads to a swelling of the polymer during hydration, and this dimensional change in the PEM can lead to large stresses built up at the sealing interfaces of the cell. Thus, swelling of the polymer during hydration must also be kept to a minimum. Finally, since the kinetics of the catalysis reaction increases as temperature increases, it is desirable to have a polymer that can absorb and retain water for proton conduction above the normal boiling point of

water. It would be desirable to have a membrane capable of operation at temperatures as high as 130C, which would allow compatibility with fuel streams that may be contaminated with carbon monoxide or other impurities. High temperature operation allows for desorption of these contaminants from the catalysts, which limits the loss of performance of the catalysts by adsorption of these poisons, and thereby allows longer duration operation with a minimum of decay. Development of new polymer exchange membranes are discussed in section 4 of this report.

The catalysis of the harvested fuel itself is quite complex, and a number of different possibilities exist for oxidizing saccharide fuel. The first possibility is to follow a traditional noble metal based approach, and use a non selective catalyst to oxidize one or more electrons from the saccharide. Due to the complexity of the oxidation and the

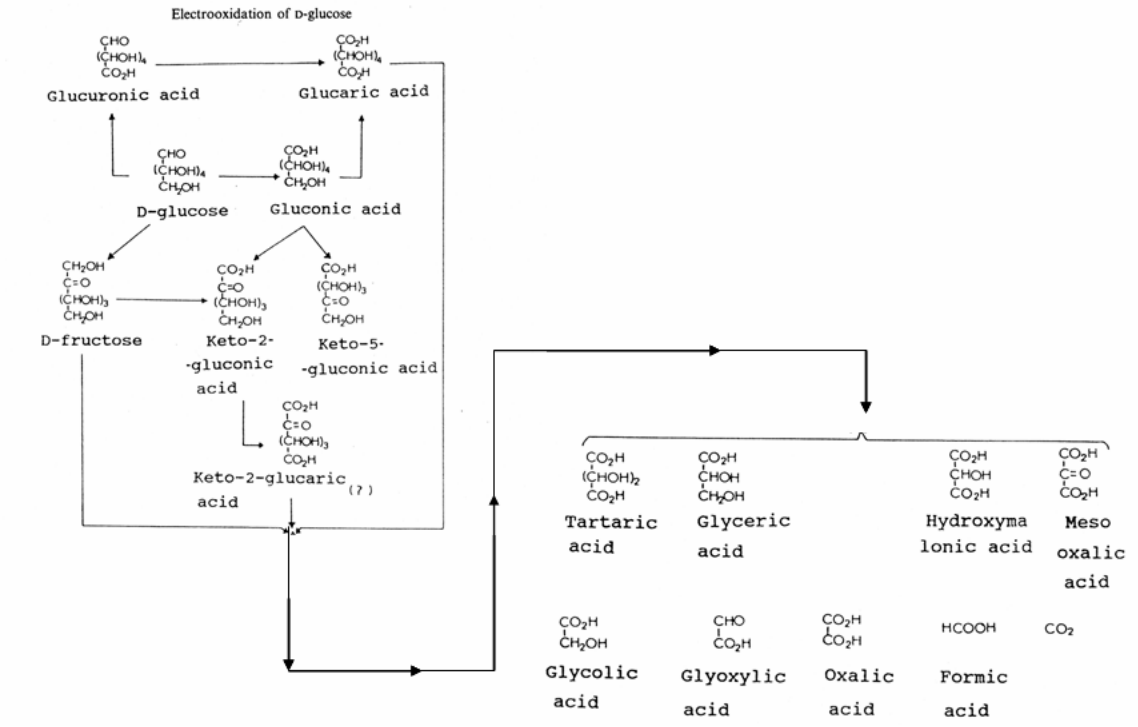

Figure 1.2: Oxidation pathway for glucose to CO2 by electrooxidation. Note all the possible poisoning byproducts.

number of byproducts possible from the oxidation of glucose, however (see Figure 1.2), it was realized early on that platinum catalysts would quickly be poisoned by the byproducts and become useless for catalysis after a relatively short time.[7] Therefore, investigations into platinum alloys through both powder and combinatorial based techniques were investigated, and these results are reported on in Section 5.

The other means of catalytic oxidation of glucose involves using the catalysts that are naturally used by living systems to oxidize saccharides fuels; enzymes. Enzymatic oxidation of sugars to form CO_2 and H_2O is well understood through the Krebs Cycle[8], but the use of these enzymes to catalyze half cell oxidation of glucose is less well understood.

In normal enzymatic oxidation, the electrons from the oxidation reaction are held on the enzyme in the form of an altered oxidation state of a redox atom or atoms until such time as the enzyme is used in the construction of a different molecule, giving up the electrons in the process, and changing the oxidation state back to the starting state of the enzyme. Since their use as a power source requires the enzymes to give up the electrons to a electrode surface and eventually an external circuit, means must be developed to reduce the electrons from the enzyme. This is typically done through a mediator molecule, that has a slightly lower oxidation potential than the enzyme itself, allowing for an electron transfer to this molecule. Once the enzyme has been reduced, it can then proceed to oxidize a new molecule of glucose. The electrons on the mediator molecule must then be removed to an electrode surface, which requires the oxidation of the mediator molecule, with the transfer of electrons to the electrode surface, where free electron conduction then transports the electron to the outside circuit. Similarly, if enzymes are to be used on the cathode, electrons from the cathode electrode must be transferred to the reduction enzyme, with expected losses in potential to overcome the kinetics of the transfer.

It is possible, though difficult, to design systems that do not require a mediator molecule to oxidize or reduce the electrons from the enzyme catalyst. These electrons are instead directly transferred to or from the electrode surface in a process called direct mediation. Direct mediation requires the design of surfaces, potentials, and selection of enzymes so that it is energetically favorable for the electrons to make the transfer in the appropriate direction to or from electrode and enzyme. This has the benefit of no longer requiring an intermediary step with the losses in potential needed to drive the electrons from enzyme to mediator, then mediator to electrode. However, direct mediation typically happens through electron tunneling from electrode to mediator site or in reverse, and such currents are small, and can severely limit the current the electrode/catalyst pair

can produce. The discussion of mediator studies, using a native form of a glucose oxidation enzyme, glucose oxidase, is also covered in section 5.

In addition to work on the mediator molecules, it is possible to modify the function and form of the enzyme itself to better make it able to transfer electrons more rapidly to mediators and electrodes. The techniques of genetic engineering can be applied to enzymes to improve their kinetic rates, their electron transfer rates, their pH and temperature tolerance, and their operational lifetime. Enzymes in nature typically have very short lifetimes, on the order of several days, before the enzymes denature, and are broken down by the host organism and a new enzyme produced to replace it. In a fuel cell application, the enzymes must be made to last for as long as the application is to run, since there is no source of replacement enzymes coming from a host organism. Genetic modification, as well as immobilization of the enzyme onto a substrate, has been shown to increase the lifetime of the enzymes against denaturing[9]. For the case of glucose oxidation, the enzyme of glucose oxidase was chosen as a parental source for mutation. Just choosing this enzyme, however, is insufficient, since there are many strains of organisms that produce the glucose oxidase enzyme, and none of these organisms produce the same exact molecular enzyme. Glucose oxidase from yeasts will be quite different at a molecular level from human glucose oxidase, so it is imperative to understand the source organism for the enzyme of choice, and then make every effort to secure a pure strain form of this enzyme.

Mutations can be introduced into the parental form to increase the tolerance of response of the enzyme to a wide variety of stimuli. Although the rate of oxidation of glucose by glucose oxidase is very rapid in most cases, these measurements are made in solution, where the diffusion of glucose to the enzyme is rapid, and the enzyme can quickly oxidize the glucose. If the enzyme then needs to be reduced to become available to another oxidation reaction, the kinetics of the overall reaction are limited to the rate limiting step, which may be the electron transfer from the enzyme to the mediator or electrode surface. Since the electron transfer rate at a given potential determines the overall current produced by the reaction, and by extension the power generated by a fuel cell, the first target for mutation of the glucose oxidase was the kinetic rate of glucose oxidation itself, or turnover rate. This allowed the genetic engineering work to establish

good protocols and good methods for mutation of the enzymes, as well as replication of the enzymes through growth and secretion by organisms or chemical simulants (a process called expression), and also for methods to determine the quantity and quality of the expressed enzymes (a process called assaying). Discussion of the choice of parental mutant, assay and expression techniques, and the results of genetic manipulation of the glucose oxidase enzyme are discussed in section 6.

1.3 Power Generation and Systemization

Once a suitable catalyst is made in quantities sufficient to be manufactured into a fuel cell, the catalysts must be applied to the separator membrane, and that structure must be put into the fuel cell plates (as discussed in section 3). This is not the end of the assembly, however, as the overall system of the fuel cell also needs to be addressed. Since a single fuel cell produces a potential of typically less than a volt at open circuit, they must be connected in series to attain the potentials needed to be useful in powering an external circuit. A fuel cell that is harvesting fuel from the environment is likely to see large variability in the availability and rate of supply of fuel, and the system must compensate for this input variability through the use of power management electronics to always supply the same voltage necessary to the external circuit. As current is demanded

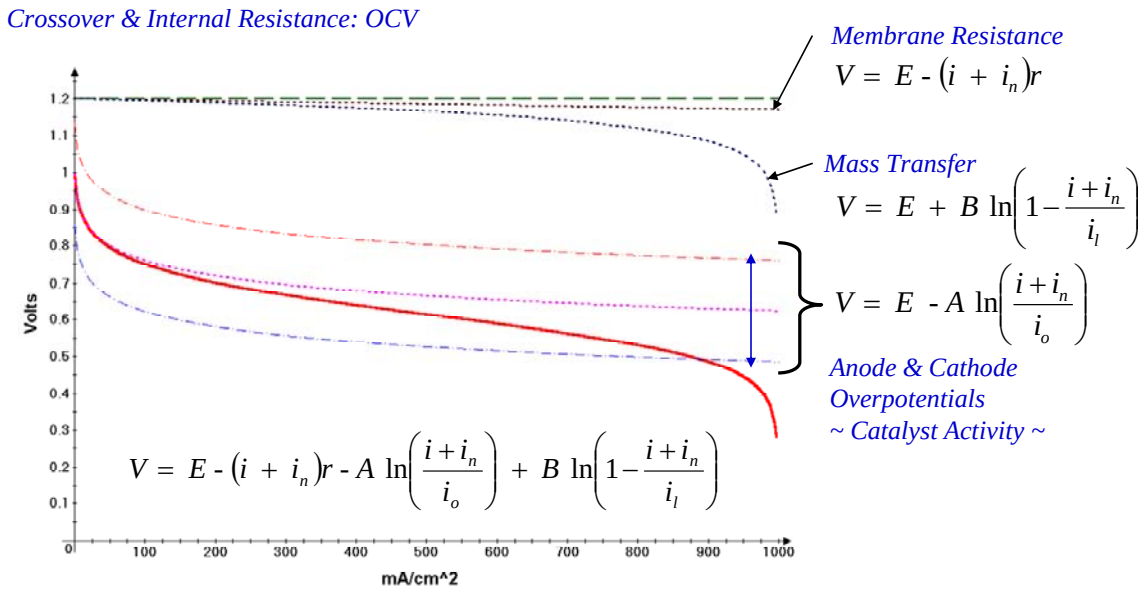

Figure 1.3: Idealized polarization curve for a fuel cell, showing losses due to the various mechanisms involved in mass transport and overpotentials.

by the external application, the voltage supplied from the power source typically drops. The combination of currents delivered at specific cell voltages makes up the polarization curve of a cell.

A typical polarization curve for a fuel cell running on hydrogen and oxygen is shown in Figure 1.3. There are three distinct regions of this curve. The first is in the low current region, where voltages are high. For very small changes in current draw in this region, large changes in voltage occur. This rapid change in voltage, called the overpotential, typically exists due to the kinetics of the reaction at one or both electrodes of the fuel cell. If the kinetics at either electrode is slow relative to the amount of current required, a certain level of voltage polarization is required to provide the necessary driving potential to drive the reaction at that electrode in the correct direction at the needed rate. Once enough overpotential has been applied to overcome the kinetics of the reaction; a second region, characterized by a low linear slope, is dominant. This low slope is the ohmic region, and represents the region of fuel cell operation where the cell's own internal resistances dominate the changes in current and voltage. It is in this region where it is most preferred to operate a fuel cell, and also in this region where the maximum delivered power can be realized. The third region of the polarization curve is also characterized by a large change in voltage for a small change in current, and is found in the high current regime. This region is driven by mass transport issues within the cell, where fuel or oxidizer cannot be delivered to the catalysts fast enough to keep up with current demand. The current is limited by the rate of reactant transport, and independent of the voltage, little additional current can be obtained. Since the current becomes voltage independent in this region, power rapidly drops off once mass transport limitations come to dominate the cell performance.

The systems engineering portion of a harvesting fuel cell requires monitoring of the fuel cell operation, and adjustment of the connection of the stack to keep the supplied voltage at the correct value for operating the external load independent of the load requirements or the variability of the conditions under which the fuel cells operate. This requires the development of a flexible stack of fuel cells, that can be connected in parallel or series as needed to achieve the correct voltage. The individual state of each of the fuel cells needs to also be monitored, to determine the optimal operating conditions for each

of the fuel cells, and to make the overall operating load as close to this condition as possible. Finally, the stack configuration needs to allow for fuel to be supplied to the back of each of the anode plates of the cells, and make a leak free seal to the back of the plates. The design of both the electronics and the mechanical system integration is discussed in Section 7.

Finally, this grand challenge was undertaken with the understanding that not all of the issues regarding the development of this kind of power source were known, and as new issues were discovered during the pursuit of this project, new capabilities that were outside of the scope of the project would need to be developed. To keep the project focused on a form and capability that could eventually be developed into a device capable of operating in the field, a series of discovery presentations and visits were conducted throughout the communities that were regarded as potential early adopters of a harvesting fuel cell technology. In addition to the initial unattended ground sensor application discussed, the possibilities of developing an implantable power supply that would last for a long period of time within or attached to a human host was discussed, as well as the possibility of running a fuel cell off of a mixture of table sugar and water for use as a battery recharger in an operational field environment, since sugar is a logistic fuel that is readily available from most theaters of operations.

2. Harvesting

The main objective of the harvesting task was to obtain carbohydrate fuels (glucose or sucrose) from field-present supplies. This presented a unique challenge: Where is glucose readily available in the field, and throughout the world? It was decided early on that two main sources of glucose supply would be targeted. First, plant life consisting of both shrubs and trees would be targeted for sucrose (a disaccharide consisting of glucose and fructose). This target provided two obstacles: How do you harvest sap from the plant (Section 2.1) and how do you convert the sucrose into glucose for use in the fuel cell(Section 2.2)? Second, mammalian (including human) sources of fuel were studied, principally for glucose contained in subdermal fluids. This presented a truly unique approach, in which the humans who use the fuel cell are themselves the battery. Glucose was to be harvested from humans in a manner that was non-invasive, painless, and not at the detriment to the human subject. Two approaches are presented in this LDRD overview to approach this problem (Section 2.3).

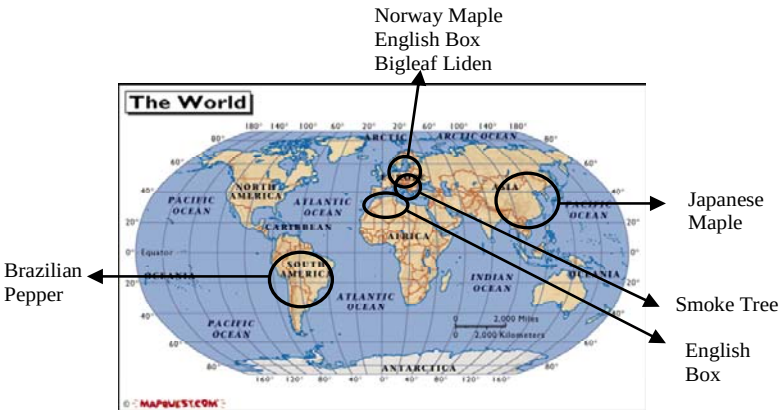

Figure 2.1: Sample distribution of sucrose bearing flora with more than 25% sucrose by weight in the sap.

2.1 Harvesting – Plants

Harvesting carbohydrate fuels from plant life was a logical choice. Plants are abundant in the field, provide reasonable pressure heads and flow rates, and provide a high carbohydrate concentration. One of the major problems associated with plant life is that while they utilize glucose for electron transport in making energy they transport sugars throughout their vascular systems as sucrose (addressed in Section 2.2).

A study of worldwide plant life was conducted to determine what plant life would be a valuable source of sucrose. Plants were chose on location as well as sucrose concentration. Figure 2.1 shows a world map and various plants and their generalized location.

Almost anywhere in the world that humans and civilization can be found, some form of tree can be found. Moreover, although seasonal variations in sap quantity can be dramatic, the sap carbohydrate concentration is relatively unchanged, and represents a reasonably uniform 40-50mM sucrose in the sap of the plants. This sucrose is essentially glucose and fructose bound together to make a higher energy polysaccharide, and can be converted reasonably easily into glucose, the principle fuel for this project.

Figure 2.2: Sap harvesting screw.

To harvest sap from trees, a hollow, threaded screw was machined to act as a spile for the tree (Figure 2.2). The screw is a standard lag bolt with a center bore partially down the length of the bolt. Additionally, there are three radial fluid access ports that allow fluid outside the screw to enter into the center bore and to flow out of the head of the screw to a collection device/fuel cell (Figure 2.3). It is important that the screw be long enough to penetrate the bark of the tree and into the phloem and xylem of the first few tree rings, where sap flow is greatest. Fluid flow in the rings past these first few rings is slower and not necessarily worth accessing. A pilot hole must be drilled prior to application of the harvesting screw. Without a pilot hole, sealing becomes an issue and sap will flow out of the tree external to the screw and not down the shaft.

Figure 2.3: Harvesting screw inserted into a sugar maple. The inset shows a drop of sap dripping from the harvesting end.

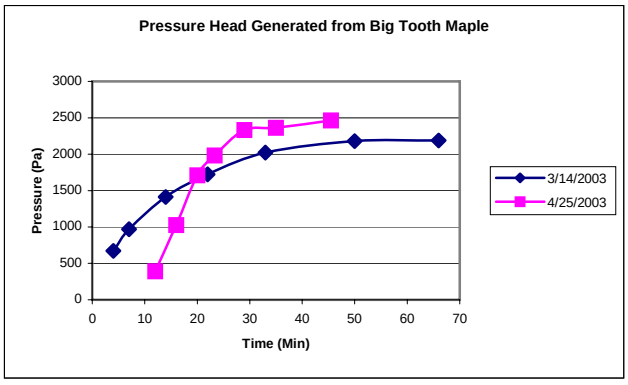

Figure 2.4: Pressure head as a function of time and date for Big Tooth Maple during sapping season. The pressure head developed by the tree is approximately 2500 pascal.

Research in New Mexico focused on Big Tooth Maple, located in 4th of July Canyon in the Manzano Mountain Range. Sap flow from Big Tooth Maple trees first occurs

when daytime temperatures exceed freezing. The greatest flow occurs when the difference between daytime temperature and nighttime temperature is greatest, while at night the temperature returns to below freezing. For 2003, harvesting dates were from the first of February to the first of May. The highest concentration of sucrose occurs earliest in the harvesting season. However, flow rate during this time period is slowest, averaging about 15 mL/hour. As the season progresses sucrose concentration decreases while flow rate increases. The maximum flow rate was recorded on 4/25/2003 at 70 mL/hour. Head pressures generated by the tree during this time were measured using a standard static pressure head sensor affixed to the harvesting spile. These pressures were roughly 2500 Pascal (Figure 2.4).

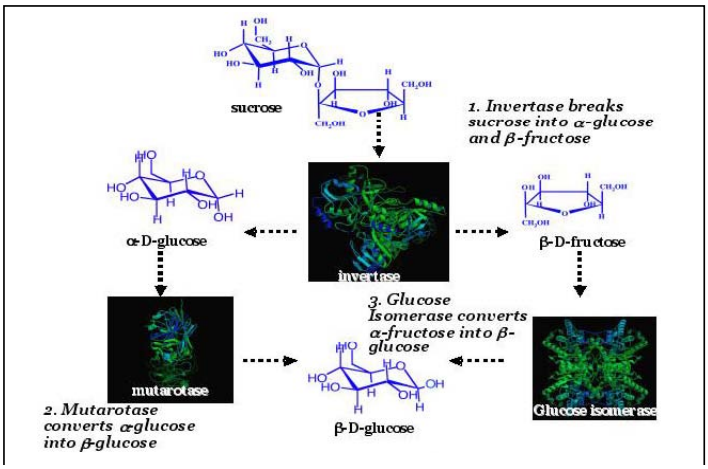

Figure 2.5: The enzymatic cascade utilized in the conversion of sucrose to glucose and the corresponding reaction pathways and products.

2.2 Enzymatic Bioreformation of Fuels

One of the primary limitations of state-of-the-art biologically inspired fuel cells is the quantity and quality of fuel that can be provided to it. In order for maximum performance to be realized, both in terms of power output and power level stability, a fuel supply must be established. In the case of fuel cells that operate on simple sugars, such as glucose, the question is not of finding glucose but converting other simple sugars (sucrose, fructose) to glucose to achieve higher power.

We have developed a method by which complex sugars are converted to simple sugars through an enzymatic cascade. This is realized by establishing a "flow-through" system that contains porous bed into which is immobilized enzymes capable of converting more complex sugars to simpler sugars. The porous bed is permeable to the liquid containing complex sugars dissolved within it. Enzymes are immobilized into the porous bed through established surface chemistry techniques. The input to the system is a feed

consisting of complex sugars, and through a systematic continuum of reactions a simple sugar output stream is realized. A schematic representation a reformation cascade that has been reduced to practice is presented in Figure 2.5.

In order to develop a packed bed that contains immobilized enzymes, an effective methodology must be used to link the enzymes to the beads so that they remain fixed and active throughout the conversion process. We have utilized a general procedure, presented in Figure 2.7, which has proven very robust and effective for all of the enzymes studied. It is based on silanating the native surface of the silica beads with a silane containing an amine functional group. This aminated silica surface is then further functionalized with the addition of glutaraldehyde, an amine group cross-linker. This combination of surface modification allows for the direct tethering of the enzyme to the bead at relatively high loading conditions. The result is an enzyme coated bead that can be easily packed into a flow-through column using standard lab practices.

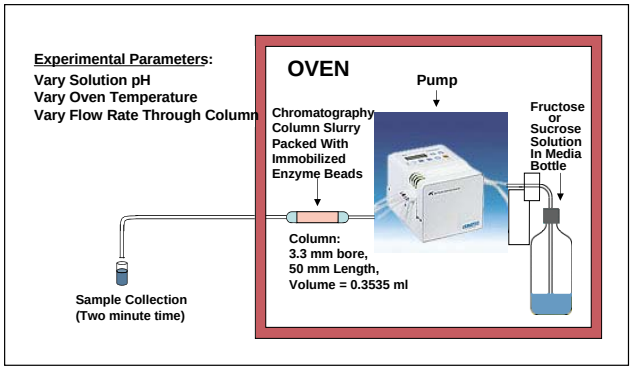

Figure 2.6: Schematic of the apparatus used to pump liquids through the column and collect samples. Each sample is taken as a two-minute fractionation of the column effluent.

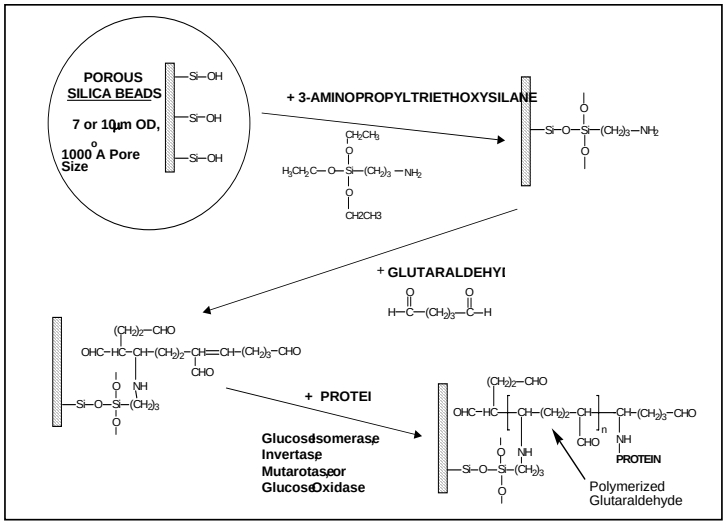

Figure 2.7: General methodology for immobilizing enzymes on silica beads.

Beads are then slurry packed into a cylindrical column through which our reactions will take place. During the column packing, care and monitoring must be undertaken in order to ensure that the enzyme remains immobilized and is still active after the packing process. Typical column packing

involves the use of pressure and time to reach satisfactory conditions, during which the enzyme may be negatively impacted.

As each enzyme has been optimized through evolution so that it operates with its highest activity in only a few conditions, we must tailor the temperature, pH, and buffer conditions for each. An example of the apparatus we have used to evaluate our enzyme columns is presented in Figure 2.6.

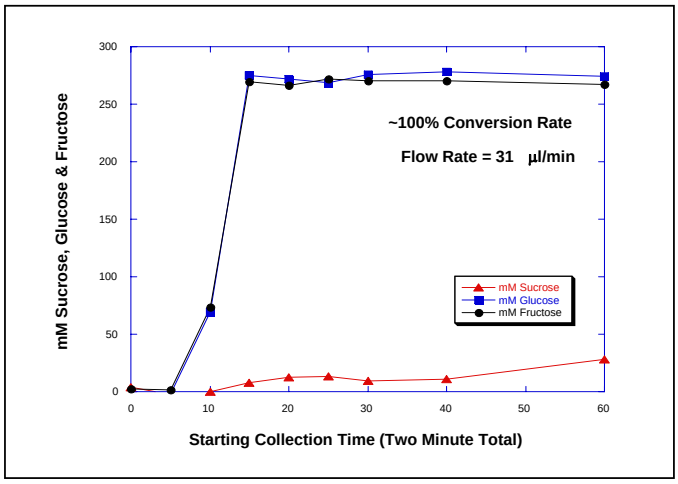

Figure 2.8: Process of sucrose conversion achieved with a column containing the enzyme invertase. A 250 mM solution of sucrose in a pH 4.6 buffer was flowed through the packed column loaded with invertase immobilized porous silica beads at a temperature of 45°C. Glucose, fructose and sucrose were determined in the samples collected at the specific time.

Each enzyme was evaluated separately to establish the optimal conditions for each enzyme and the specific reaction conversion for each step. Figure 2.8 presents the data obtained from a column packed with invertase, which converts sucrose to glucose and fructose. Column conditions were 250 mM sucrose, pH = 4.6 and 45C. The observed conversion is ~ 100% for this process.

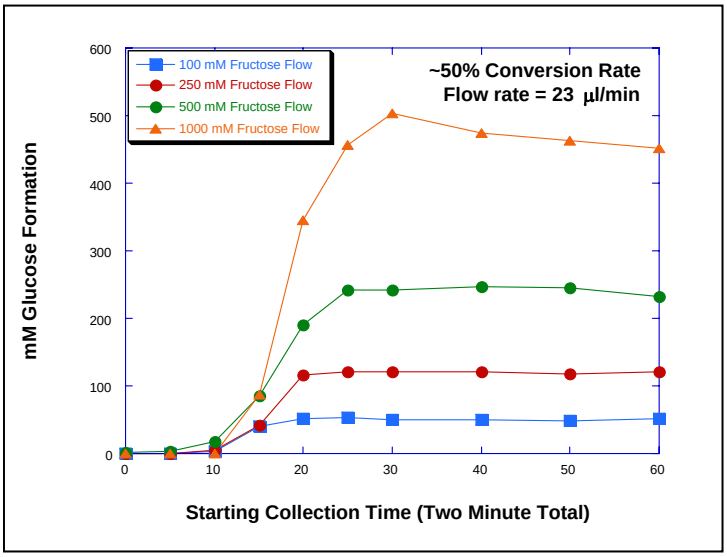

Figure 2.9: Process of fructose conversion achieved with a column containing the enzyme glucose isomerase. Conversion is shown as a function of initial fructose concentration. Fructose solutions in a pH 6.8 buffer were flowed through the packed column loaded with glucose isomerase immobilized porous silica beads at a temperature of 60°C. Glucose was determined in the samples collected at the specific time

The conversion of fructose was achieved with a column containing glucose isomerase. Figure 2.9 presents a

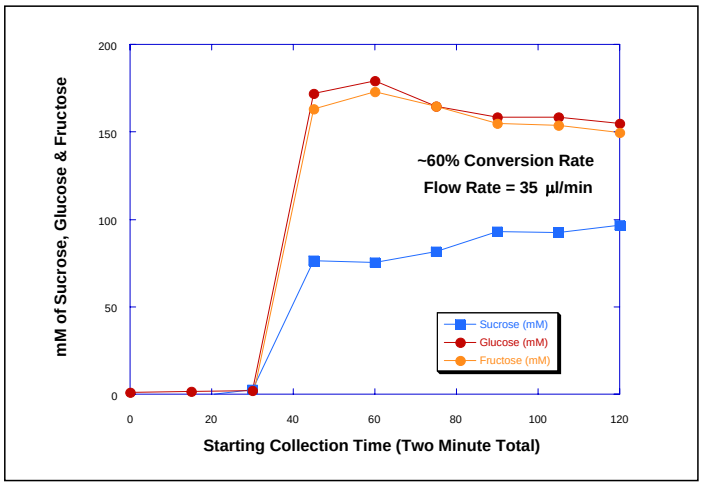

Figure 2.10: Conversion of sucrose to glucose using three columns linked in series, each packed with a specific enzyme. Order of columns is invertase → glucose isomerase → mutarotase. Conditions were determined by averaging all three enzyme optimal operating conditions. A 250 mM solution of sucrose in a pH 5.8 buffer was flowed through the columns at a temperature of 47C.

summary of the data obtained for glucose formation over a wide range of initial fructose concentrations. As depicted in Figure 2.9, the typical conversion values averaged at 50%.

Although each enzyme has its own set of optimal pH and temperature conditions under which it performs, we have obtained a 50% conversion of sucrose to glucose by placing three columns in series and providing a fuel stream with a pH = 5.8 and 47C. This pH and temperature is an average of the ranges that the individual enzymes prefer. The data obtained is presented in Figure 2.9.

We have obtained a 77.4% conversion of sucrose to glucose by placing three columns in series and providing a fuel stream that uses the optimum conditions for the invertase enzyme with a pH = 4.6 and 46C. The data obtained is presented in Figure 2.11.

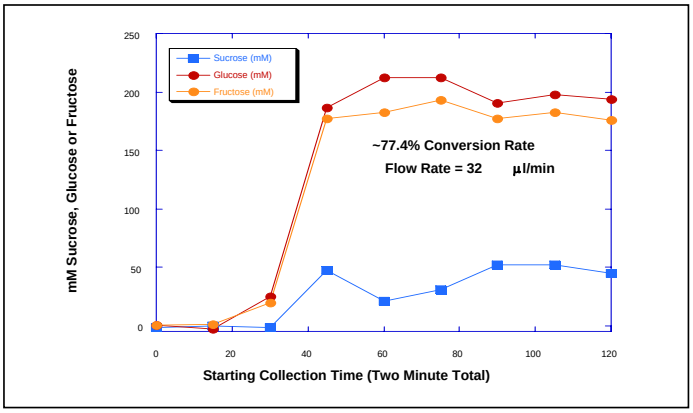

Figure 2.11: Conversion of sucrose to glucose using three columns linked in series, each packed with a specific enzyme. Order of columns is invertase → glucose isomerase → mutarotase. The optimal operating conditions for the invertase enzyme were used. A 250 mM solution of sucrose in a pH 4.6 buffer was flowed through the columns at a temperature of 46C.

We have obtained only a 2.7% conversion of sucrose to glucose by placing three columns in series and providing a fuel stream that uses the optimum conditions for the

glucose isomerase enzyme with a pH = 6.8 and 62C. The data obtained is presented in Figure 2.12.

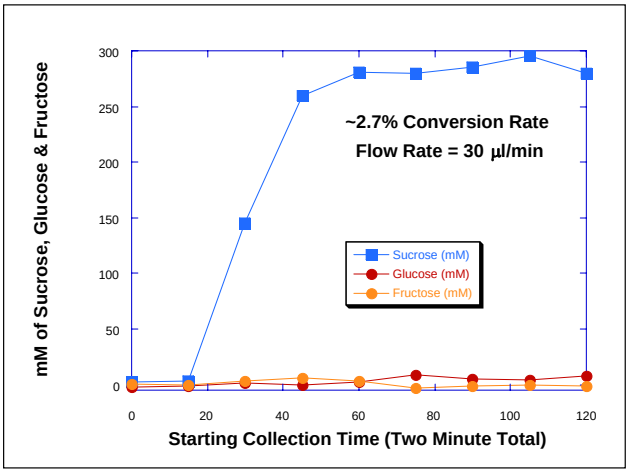

Figure 2.12: Conversion of sucrose to glucose using three columns linked in series, each packed with a specific enzyme. Order of columns is invertase → glucose isomerase → mutarotase. The optimal operating conditions for the glucose isomerase enzyme were used. A 250 mM solution of sucrose in a pH 6.8 buffer with 20 mM $MgCl_2$ was flowed through the columns at a temperature of 62C.

Simply put, there is no currently available technology that allows for the continuous enzymatic based conversion of sucrose to glucose that has been presented in the scientific literature as an operating device. The linking of these enzymes in series has been shown to effectively convert sucrose into glucose. This process of flow-through fuel reformation enables the deployment of a glucose-based fuel cell in environments that possess sucrose in great abundance but minimal glucose (i.e., plants, trees). The concept of an enzymatic cascade is also relevant in the field of alternative fuel production (ethanol) and carbon sequestration, where the use of such a system could prove to be revolutionary in terms of process engineering, cost benefit, and efficiency.

2.3 Harvesting - Mammalian

In order to use mammalian sources of glucose solution (primarily venous blood or interstitial fluids from the near vascular regions of tissue), both the local oxygen concentration and the local fuel concentrations must be considered. Large fuel concentrations (such as from near the intestines) will require large oxygen concentrations to be reduced, in

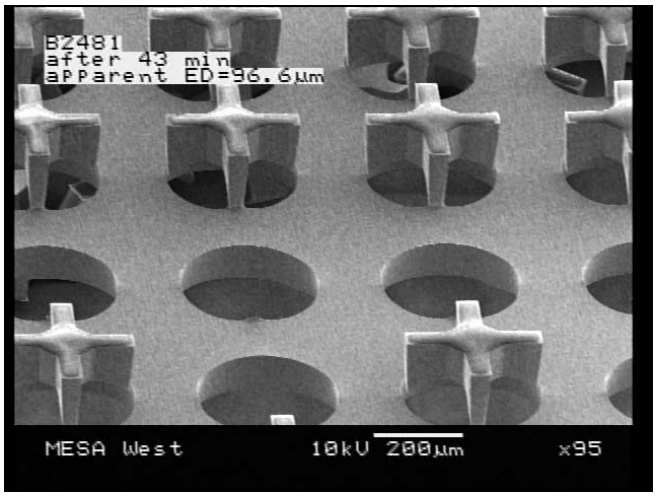

Figure 2.13: Liftoff of microneedles while using the DRIE. Note the loss of some of the needles due to liftoff errors.

order to balance the electrochemical reactions between anode and cathode. Although the nominal blood oxygen content is high, most (up to 97%) of the oxygen is bound to arterial hemoglobin. The solubility of oxygen at arterial partial pressures (12.7 kPa) is only roughly 0.1 mM, whereas the total oxidizable metabolic intermediate concentration is two orders of magnitude higher.[10] The limiting reduction current for this concentration of oxygen would be very small (on the order of μC/cc of fuel), so oxygen must be obtained from the hemoglobin directly, or from the surrounding atmosphere outside the body. Removing oxygen from the hemoglobin is a complex process that was beyond the scope of this work, so it was decided to develop a means to bring the glucose contained in the body fluids to the skin surface where it could be used with a traditional cell configuration using atmospheric oxygen reduction.

For the harvesting of glucose from humans we have focused our efforts on microneedles, tiny micron scale needles. Microneedles are hollow needles with heights that typically range from 300-500 microns tall. They are deep enough to penetrate past the stratum corneum and into the interstitial fluid, just below the skin. However, they are not long enough to reach the sensitive nerve endings deeper in the skin. Access to blood may also be achieved by producing taller microneedles. However, these taller microneedles will also trigger nerve endings and mild pain would be felt. In addition to microneedles, which extract fluid from the subject, we also developed platforms that did not require extraction. These "ElectroNeedles" can be used for in-vivo energy production.

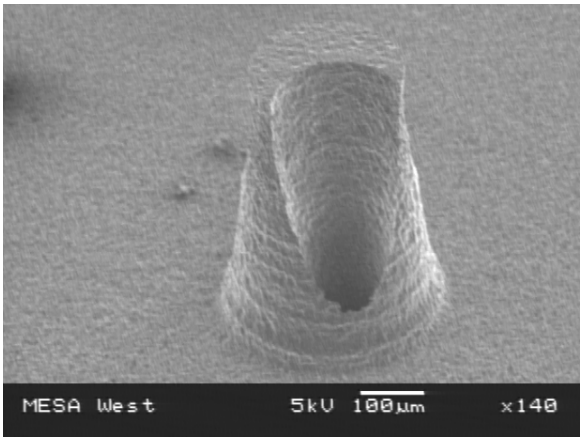

Figure 2.14: A hollow microneedle fabricated in Foturan ®

Our first attempt at producing hollow microneedles focused around the Bosch process discussed by Griss et al.[11] This was a multi-step process using the deep reactive ion etch (DRIE) in Sandia's Compound Semiconductor Research Laboratory (CSRL). After a year of attempting to fabricate hollow microneedles we abandoned the Bosch process because significant issues concerning lift off (Figure 2.13) could not be resolved.

Our next attempt at fabricating hollow microneedles was more successful. Foturan® was chosen as the next substrate for fabrication. Foturan® comprises a lithium-aluminum-silicate glass containing traces of silver and germanium ions. When exposed to UV-light within the absorption band of the metal ion dopants in the glass, the germanium acts as a sensitizer, absorbing a photon and stripping an electron that reduces neighboring silver ions to form colloidal silver atoms. These silver colloids provide nucleation sites for crystallization of the surrounding glass. After a bake step, the exposed region of the glass is transformed into a ceramic that has a much higher wet etch rate in hydrofluoric acid than the surrounding unexposed material. Using Foturan ®, we were able to obtain hollow microneedles, with channels cut through the center of an raised external needle. A micrograph of a single microneedles is shown in Figure 2.14.

The process for fabrication of the hollow microneedles is shown in Table 2.1. During the initial development of this process, the processing of Foturan® was inherently non-uniform and thus difficult to use for direct fabrication. Certain process steps, such as DUV intensity, exposure time, and etch time are highly variable, depending on the particular batch of Foturan® wafers and the pretreatment and aging of the wafers prior to the start of fabrication. Thus, although this process was capable of producing microneedles such as shown in Figure 2.14, small adjustments due to the starting material may need to be made to replicate these results. This problem has subsequently been solved, and the processing stabilized, by changing the wavelength of the exposing light.

Step	Process	Wafers	Description	Comments
1	Label Wafers		Foturan Glass 4" 1mm	Scribe 7/28-A,B,C,D
2	Clean Wafers		Acetone and Alcohol	
3	Deep UV Exposure		4 Hours	Use: Thru Holes
4	Clean Wafers		Acetone and Alcohol	
5	Oven Bake		1Hour 15 min 500C 1Hour 15min 600. Sandwich Foturan wafer between 2 ceramic pieces. Place a couple more on top for added weight.	Ramp bake oven to 500C @ 8.0 degC/min. Hold at 500C for one hour 15min. Ramp to 600C @6.5DegC/min. Hold for 1 hour 15min. Ramp down to 34C @ 8.0 degC/min, end cycle.
6	HMDS			
7	Coat wafers with PR		JSR- 3000 RPM/ 30 Sec	
8	Bake		120C/60sec	
9	Expose		MA6 5.5sec	Use: extraction microneedle

10	Bake	110C/45sec	Hotplate
11	Develop	1:4 55-65sec	Watch wafer develop, once clear wait 3 sec. Rinse
12	DI Rinse		
13	Inspect		Look for correct pattern, resist lifting, unclear spots, scumming, too many defects.
14	Deep UV Exposure	65 Minutes	
15	Strip Wafers		Acetone and Alcohol
16	Oven Bake	1Hour 500C 1Hour 600C Sandwich Foturan wafer between 2 ceramic pieces. Place a couple more on top for added weight.	Ramp bake oven to 500C @ 6.5degC/min. Hold at 500C for one hour. Ramp to 600C @6.5DegC/min. Hold for 1 hour. Ramp down to 29C @ 6.5degC/min, end cycle.
17	Clean Wafers	Piranha	
18	HF Etch	5:1 HF in Ultrasonic Bath	Etch for 20min check ElectroNeedle height. Continue etch if necessary.
19	DI Rinse		
20	Clean Wafers	Piranha	
21	DI Rinse		
22	Metalization	Eg's or Temescal	Place shadow mask over backside of wafer(opposite side of needles)100A Cr/5000A Au Pump machine down to the high or mid 7's. evaporate Cr@ 3A sec. Au @ 10A/sec.
23	Dice		
24	Package		
25	Wirebond if needed		
26	Delivery		

Table 2.1: Process sheet for fabrication of hollow microneedles in Foturan ®.

The Foturan ® microneedles are sufficiently strong to pierce through 125 micron thick aluminum (Figure 2.15). Additionally, no microneedles were broken during repeated punctures of the aluminum foil.

To test whether the microneedle aided in glucose transport across the skin, a Franz diffusion cell, utilizing porcine skin, was used to test for glucose flux. Porcine skin was used because it most closely resembles human skin. On the donor side of the porcine skin (Dermal side), physiological buffer and 10.1 mM glucose was present. On the receiver side deionized water was present. An YSI 2300 glucose analyzer was used for

all glucose measurements. As can be seen in Figure 2.16, greater glucose is transported across the skin using the microneedles. There is a 475-fold increase in glucose flux using the microneedles (the large increase in flux is due to the increase in glucose transport and the difference in open area; the area of the open needles is 3.63×10^{-2} cm^{-2}). To increase glucose flux through the microneedles, various surface treatments were applied to the inside surface of the microneedles. This was done to try to increase the wetting angle to improve the wetting and capillary forces acting within the needle. It was found that chemical processes such as wet and plasma cleans did little to affect the wetting angle, however sputtering gold onto the microneedle internal surface did increase the wetting angle.

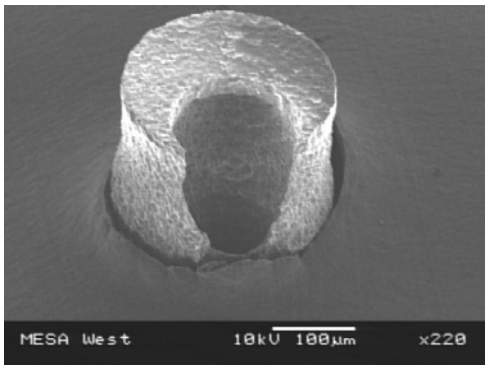

Figure 2.15: Foturan ® microneedle forced through a 125 micron thick aluminum foil, with no damage to the needle itself

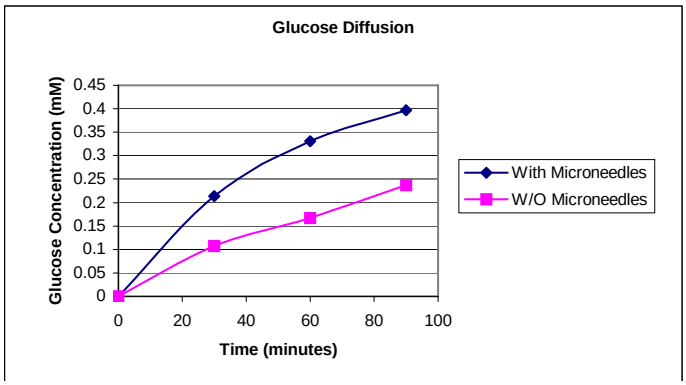

Figure 2.16: Glucose diffusion across porcine skin, with and without microneedles.

Whenever blood or interstitial fluid must be removed from the body for use in an external cell, there will be intrinsic issues regarding biocompatibility, harvesting through the (skin) interface, and long term biorejection or bioresponse to the harvesting system. Still, in order to have the fuel substrate close to the skin surface to take advantage of atmospheric oxygen, such problems will exist and must be overcome.

There is another architectural form, however, that does not require removal of the subdermal fluids, and therefore avoids the concerns associated with pulling fluids out of the body and into a secondary system. These concerns are dehydration of the human subject, issues associated with plumbing fluids from the microneedles to the fuel cell, and the loss of blood volume (albeit small). It was our goal to fabricate a non-invasive

architecture that did not have to extract fluid from the human subject, but rather harvest the glucose in-vivo.

One possible solution was to leave the anode electrodes essentially within the subcutaneous fluids, and transport only the ions to the surface. Fuel would not need to be transported in bulk through the skin, and waste products from the oxidation reactions could be left in the fuel streams. Insertable electrodes that maintained ionic contact with the cathode (air breathing) electrode would allow for greatly simplified fuel side electrodes, at the expense of an increase in complexity for the ionic conductor membrane. Similar to microneedles, the electrode needles are small enough to penetrate the skin, but not tall enough to trigger nerve responses. However, unlike the microneedles these needles do not withdraw fluid. Instead they act as tiny electrodes, implanted into the skin, where the electrochemical reaction is carried out within the human subject. The conductivity of the interstitial fluid is sufficient to allow for the passing of electrons. The system we fabricated was composed of 100 microelectrodes, but adaptable to n electrodes.

The system is designed to stagger the anode and cathode in a checkerboard pattern. This was done to maximize the electrode areas over as much space as possible. For example, in the first version of the hardware (Figure 2.17), the system is designed to have one large cathode, covering half the chip, and one large anode, covering the remaining half, however it was thought that at various times glucose depletion around the electrodes may be a problem. Thus, to avoid this concern the anode and cathode were checkered to be able to access as much area of the skin as possible.

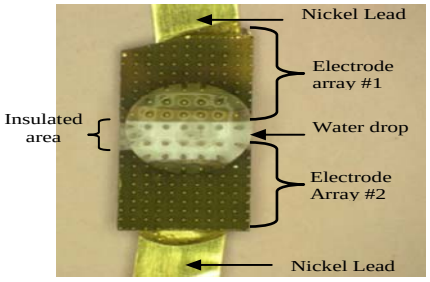

Figure 2.17: Microneedle Electrode array, with the anode and cathode electrodes separated on chip. A drop of water covers the gap between the electrodes. The chip size is 0.5 cm x 1.0 cm.

Table 2.2 details the fabrication of the electroneedles.

Step	Process	Wafers	Description	Comments
1	Label Wafers	5	4" 1.0 mm (5 WAFER START)	
2	Clean Wafers	5	Acetone and Alcohol	
3	Deep UV Exposure	5	4 Hours	Use: SCB 100 Nozzle Mask

4	Clean Wafers	5	Acetone and Alcohol	
5	Oven Bake	5	1Hour 15 min 500C 1Hour 15min 600. Sandwich Foturan wafer between 2 ceramic pieces. Place a couple more on top for added weight.	Ramp bake oven to 500C @ 8.0 degC/min. Hold at 500C for one hour 15min. Ramp to 600C @6.5DegC/min. Hold for 1 hour 15min. Ramp down to 34C @ 8.0 degC/min, end cycle.
6	HMDS	5		
7	Coat wafers with PR	5	JSR- 3000 RPM/ 30 Sec	
8	Bake	5	120C/60sec	Hotplate
9	Expose	5	MA6 5.5sec	Use: SCB 300 Nozzle Mask
10	Bake	5	110C/45sec	Hotplate
11	Develop	5	1:4 55-65sec	Watch wafer develop, once clear wait 3 sec. Rinse
12	DI Rinse	5		
13	Inspect	5		Look for correct pattern, resist lifting, unclear spots, scumming, to many defects.
14	Deep UV Exposure	5	65 Minutes	
15	HF Etch		5:1 HF in Ultrasonic Bath	Etch till holes are open time is not precise.
16	Oven Bake		1Hour 15 min 500C 1Hour 15min 600. Sandwich Foturan wafer between 2 ceramic pieces. Place a couple more on top for added weight.	Ramp bake oven to 500C @ 8.0 degC/min. Hold at 500C for one hour 15min. Ramp to 600C @6.5DegC/min. Hold for 1 hour 15min. Ramp down to 34C @ 8.0 degC/min, end cycle.
17	Piranha			
18	Metal Seed Layer		Eg's or Temescal	100A Cr/5000A Au Pump machine down to the high or mid 7's. evaporate Cr@ 3A sec. Au @ 10A/sec.
19	Electroplate Vias		Gold, Copper or Nickel	Tape seed layer side of wafer with electroplaters tape. Wet wafer with wetting agent. Place into pre- heated electroplating bath. Note parameters in processing notes box.
20	Lap wafer			Mount wafer onto a 4" chuck
21	Polish wafer			
22	Clean Wafers		Acetone and Alcohol	
23	Lap wafer			Flip wafer and mount wafer onto a 4" chuck
24	Polish wafer			

25	Clean Wafers Piranha		Acetone, Alcohol piranha for 20min to clean out the wax and lapping slurry.
26	DI Rinse		
27	HF Etch	5:1 HF in Ultrasonic Bath	Etch for 20min check ElectroNeedle height. Continue etch if necessary.
28	DI Rinse		
29	Metalization	Eg's or Temescal	Place shadow mask over backside of wafer(opposite side of needles)100A Cr/5000A Au Pump machine down to the high or mid 7's. evaporate Cr@ 3A sec. Au @ 10A/sec.
30	Dice		
31	Package		
32	Wirebond		
33	Delivery		

Table 2.2: Fabrication sequence for the microelectrodes.

To demonstrate proof of concept for the ElectroNeedles, a 450 μm thick piece of pigskin was placed in contact with an electrolyte solution containing an electroactive probe molecule, and the other side of the pigskin was exposed to air. The microelectrode needle array was then inserted into the pigskin, and electrochemical measurements were made in an effort to detect the probe molecule present in solution. In the configuration used, the overall needle length is less than the thickness of the pigskin, and as a result will not directly contact the solution on the other side of the pigskin when inserted into the skin. Instead, any species detected by the microneedle electrodes would have to have diffused/migrated into the pigskin to a depth sufficient to contact the needles. A diagrammatic representation of the experimental set-up is shown in Figure 2.18.

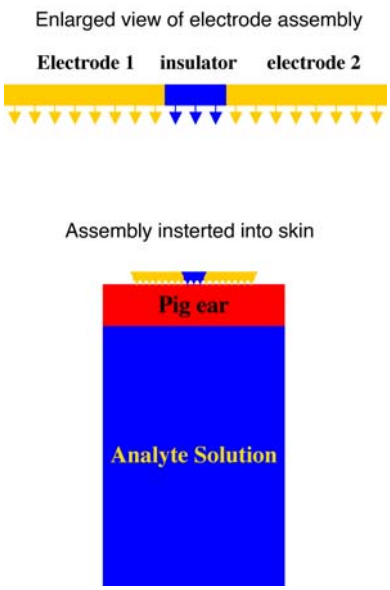

Figure 2.18: Schematic cross section of the microneedle test setup, showing the pig ear and analyte under analysis.

In these initial sets of experiments two different probe molecules were used. These were ferricyanide, a negatively charged one-electron redox couple, and quinone, a neutral

two-electron two-proton couple that resembles the naturally occurring compound, coenzyme Q.

Shown in the Figure 2.19 are the cyclic voltammograms obtained when the microneedle electrode array was inserted into the pigskin in contact with a solution consisting of 1 M K_2SO_4 containing either ferricyanide and/or the quinone probe. As seen, the redox behavior of both probe molecules can be clearly seen, demonstrating the

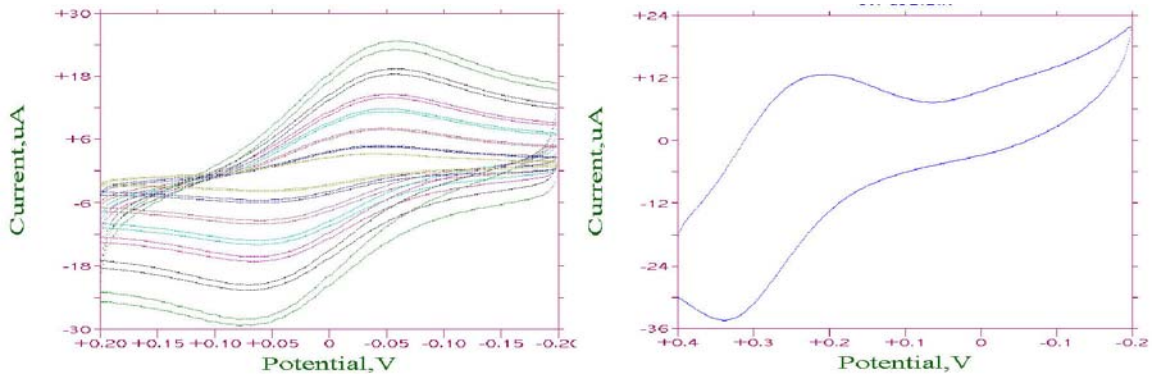

Figure 2.19: Voltammetric response of microneedle electrode array inserted into pig skin containing ferricyanide (left graph) or quinine (right graph). In the case of the graph on the left, the voltammagrams were collected at various scan rates up to 800 mV sec-1, amd two cycles were collected for each. In the case of quinine, the scan rate used was 100mV sec^{-1}.

proof-of-concept for this approach for in-vivo electrochemistry. (Although not shown here, a negative control experiment was performed using a solution that did not contain an electroactive probe, and in this case redox activity was NOT observed.) In the case of the in-vivo experiment using ferricyanide shown on the left below, a series of cyclic voltammograms were collected at a number of different scan rates from 25 mV sec^{-1} to as high as 800 mV sec^{-1} (Two cycles were recorded in each case).

The development of an appropriate harvesting technique will require more effort to develop techniques capable of long term harvesting from both tree and animal sources prior to implementation. However, some of the development work demonstrated here will allow for the harvesting of fuel stocks directly from plant or animal sources, and the conversion of those fuel stocks into directly oxidizable sources for use in a fuel cell. To improve these system components further, additional work on the harvesting of mammalian sources, including flow harvesting rates on biological hosts, needs to be accomplished. Additionally, moving toward a biocompatible material such as plastics, as opposed to the glass needles discussed here will need to be demonstrated in order to

minimize the effects of biorejection. Finally, application of genetic engineering techniques to the enzymes used in the bioconversion of sucrose to glucose will allow for the three enzyme cascade to be optimized to work at a common pH, temperature, and flow rate.

Once the fuel is harvested, it needs to be sent to the fuel cell. In addition, air from the surrounding environment must also be harvested in order to provide a reduction reaction for the couple. Assembling the catalysts, separators, and fluid/gas supply systems into a test architecture is the subject of the next section.

3. Architecture Development

The development of miniature architectures for fuel cell applications has been studied

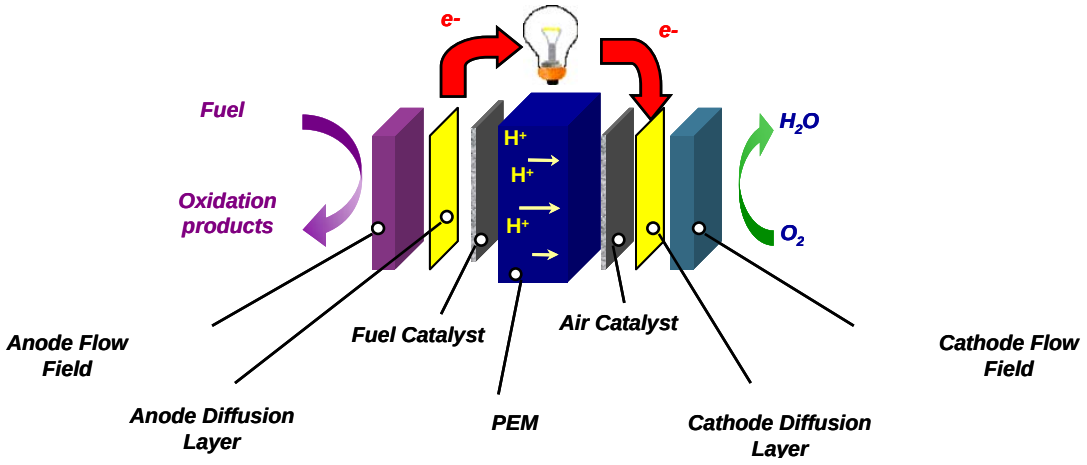

Figure 3.1: Exploded diagram of a typical polymer electrolyte membrane fuel cell.

by various authors.[12] [13] [14] The fuel cell itself is made up of several components (see Figure 3.1). In principle, fuel cells separate an electrochemical oxidation of a fuel source from an electrochemical reduction of an oxidizer. This separation is non conductive, so that electrons cannot bridge the gap between the anode and cathode, and must instead seek a path through an external circuit in order to complete the electrochemical pathway. For low temperature fuel cells, this separator is in the form of a polymeric film that supports ionic conductivity, while being highly resistive to electron transport. This film is called a proton exchange membrane (PEM), and serves as the center section of a fuel cell. On either side of the membrane are the anode and cathode catalysts, which serve to increase the reaction kinetics for the oxidation and reduction of the fuel and oxidizer, respectively. The oxidation reaction for the most common fuel, hydrogen, can be written as

$$2H_2 \rightarrow 4H^+ + 4e^- \qquad \text{Equation 3.1}$$

and for the reduction reaction using oxygen

$$O_2 + 4H^+ + 4e^- \rightarrow 2H_2O \qquad \text{Equation 3.2}$$

Once these half reactions occur on their respective catalyst layers, the electrons need to be conducted away from the reaction site and into an external circuit, while the protons

are conducted through the PEM. The electronic conduction is carried out through two layers, the gas diffusion layer, and the end plate. Both of these components must be electrically conductive and resistant to electrochemical attack in the presence of the fuel or oxidizer. The most common choice is carbon plate, but other materials, such as stainless steel, gold, or silicon, have also been used.[14] [15]

The diffusion layer, in addition to being an electron conductor, also serves as a layer to diffuse out the incoming gas or liquid fuel or oxidizer streams to better cover the catalyst layer with reacting material. The endplates serve to conduct the liquid or gaseous reactants over the diffusion layer, and serve to conduct away any reaction byproducts from the catalyst and diffusion layers.

Although not shown explicitly in Figure 3.1, it is also assumed that there will be airtight seals around the periphery of the fuel cell on each side, to keep the fuel and oxidizer reactants isolated on each side of the membrane. Paths of leakage that allow contact between the reactants will lower the performance of the cell, and (in extreme cases), cause an uncontrolled chemical reaction that could permanently damage and degrade the performance of the cell.

It is the task of the architectures component to design and fabricate the hardware associated with a miniature cell, as well as to test the assembled structures for their performance in both hydrogen and glucose (for the fuels) and in oxygen and air (for the oxidizers).

3.1 Early architectures and performance

Based upon previous work in the literature and the ubiquity of the starting material, Silicon was chosen as a starting material to fabricate the very early fuel cells. In this case, silicon wafers had a silicon nitride support membrane grown upon them, and then that membrane was perforated with a large number of small holes. This perforated membrane served the purpose of the gas diffusion structure. Onto this perforated membrane, a continuous solid film of Pt metal was deposited, which allowed for electronic conduction as well as serving as the catalytic surface. The cell was symmetric, which allowed for two identical plates to be used on either side of the separator membrane. Pt will catalyze both the oxidation of hydrogen, as well as the reduction of

oxygen, and so this catalyst layer was used both on the anode and cathode sides of the cell.

Assembly of completed plates proved problematic, though, as the silicon nitride membranes were too thin (only 2μm thick) and too fragile (consisting of a large number of stress concentrating tiny holes) to withstand direct contact with a solid polymer membrane without rupturing. To circumvent this problem, the polymer electrolyte membrane (in this case, commercially available Nafion®) was dissolved in an alcohol based Scanning Electron Micrograph of a cross section of a silicon nitride membrane fuel cell. Hydrogen was supplied to one flow field, and oxygen to the other. Thin film casting techniques were used to place the polymer membrane onto the silicon nitride membranes. A thin film of Nafion® was placed onto each plate, and then the plates were pressed together in a jig, so that any wedge error in the alignment could be removed. Wedge error would lead to shorting, due to the plates contacting though the liquid membrane at the point of closest approach.

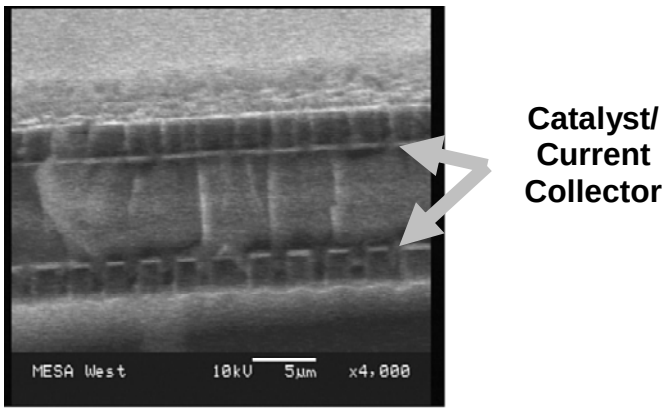

Figure 3.2: Scanning Electron Micrograph of a cross section of a silicon nitride membrane fuel cell. Hydrogen was supplied to one flow field, and oxygen to the other. 0.7 μWatts were produced for 30 minutes from this cell.

This assembly with cast PEM membranes allowed for very thin separator membranes to be produced. Figure 3.2 shows a completed cross section for one such cell, with the separator membrane being only 5μm in thickness. This cell was run under hydrogen and oxygen flow at room temperature with an open circuit potential of 0.5V, and delivered approximately 0.7μWatts of power for roughly 30 minutes, prior to the cell potential decaying away and no power being delivered after that point. The reason for this was that the very thin separator membrane could not significantly retard the diffusion of hydrogen and oxygen across the membrane layer, and competing reactions on the anode and cathode quickly robbed the cell of power. Still, this was the thinnest, smallest cell in

the literature at the time of its fabrication, and provided a good learning tool for the next set of hardware assemblies.

3.2 Foturan Flow Plates

Foturan™ is a photodefinable glass, which reacts on exposure to UV light to become extremely soluable in dilute hydrofluoric acid. This glass can be exposed, but not etched, and subsequent processing can then occur on top of the glass, prior to etching in HF. This is the same material that the microneedles from Section 2.3 were fabricated from. This feature of the material was exploited to develop a second early architecture for the fuel cells, where the glass was used as the flow field, and a gold grid was patterned on top of the exposed glass flow field. On top of the gold grid, a catalytic slurry of Nafion® and platinum particles was cast to provide a catalytic layer. Two of these flow field/catalyst layer structures could then be released in HF, and then pressed against a PEM to complete the fuel cell structure. A SEM image of the released flow field with the gold grid in place over it is shown in Figure 3.3. Although a significantly larger area of catalyst was present with this design than with the original thin membrane design, only a total of 2.0μWatts was generated from this cell. The open circuit potential for this (in hydrogen/oxygen at room temperature) was also very, very low, at 80mV, indicating that there were significant problems in leakage of the reactants, either through the glass, or around the catalyst layers, that prevented the cell from performing at an appropriate level.

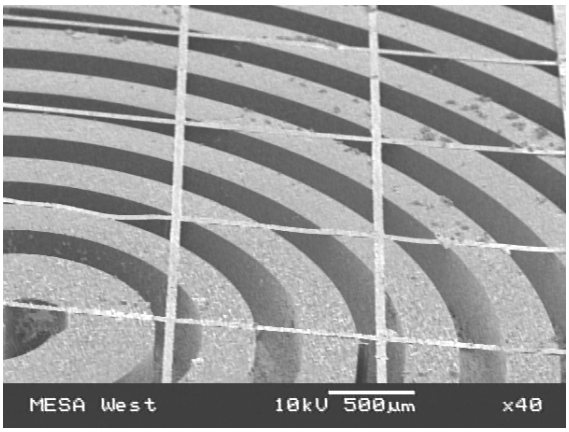

Figure 3.3: Foturan™ flow field covered by a gold current collector grid. These layers would then be coated by a catalyst, and pressed against a PEM. The power output from a cell comprised of these structures delivered 2.0μW, with an open circuit potential of 80mV.

3.3 Membrane-Electrode Assembly (MEA) and Final Assembly

To improve the power output from individual cells, a standard large cell fabrication of the membranes and electrodes was pursued to insure a level of performance commensurate with larger scale cells. For this technique, fabrication of the electrode structure employed a mixture of platinum (for the cathode structure) or platinum-

ruthenium (for the anode structure), Nafion® dissolved in a solution of alcohols, and a Teflon® binding agent. These three components were mixed together and mechanically treated to drive off the solvent structure, leaving behind a porous, claylike material. This material was then pressed to the final use thickness (in this case, 50μm), and pressed against the gas diffusion layer. The gas diffusion layer was commercially available Toray ™ paper, which is a graphite paper with ~50μm wide fibers pressed together into 175μm thick sheets. Once the catalyst layer was pressed to the diffusion layer, the combined electrode/gas diffusion layer structure was cut to a 1cm x 1cm area for the active electrodes.

A piece of 175μm thick fully hydrated Nafion® was used as the separator membrane. The previously fabricated electrode/gas diffusion layers (GDL) were placed on either side of the hydrated membrane, and this assembly stack, consisting of the Toray® paper for the anode gas diffusion layer, the Pt-Ru electrode, the Nafion® separator, the Pt cathode electrode, and the cathode Toray® paper gas diffusion electrode, was then placed into a hot press, and compressed at 80C to diffuse the electrode structures into the Nafion®, and decrease the electrical and ionic impedance at this interface. For all the electrodes listed in the following sections, the cathode was never varied from being a pure Pt black electrode structure, and the various metals used as anode catalysts for glucose were fabricated in the same fashion, except where the fabrication technique has been noted.

Seals were prepared from a thin commercially available acetate (2mil thick VHB™ acetate tape from 3M), punched into a pattern that allowed for seals to be created around the edge of the plates and the manifolds, while leaving the channels and the connections to the manifold uncovered. A total thickness of 150μm of acetate tape was used to create the seals on both the anode and cathode side by first applying the acetate seal to the end plate. The MEA assembly was placed against the acetate seal ring so that the seal ring was in contact with the edges of the Nafion® membrane, and lightly compressed to allow the tackiness of the acetate tape to hold the MEA in place. The anode end plate was then assembled with an acetate seal ring and pressed against the anode gas diffusion layer and lightly compressed to seat the acetate seal ring against the membrane. Once complete, this assembly is then compressed in a conventional press. The daylight gap is reduced until a force is detected on the load cell of the chucks, which indicated that the cell was

now clamped by the chucks. An additional ~75μm of displacement was then placed on the chucks to compress the cell. This displacement typically results in a load force of around 600psi on the end plates. Most of the displacement is taken up in the difference between the height of the acetate seal gaskets from the membrane (150μm nominal) and the height of the Toray™ gas diffusion layer and electrode (225μm nominal).

Once the main cell assembly is complete and compressed, the cell is placed into a stainless steel test rig. This rig has a 250μm recess in the center of each plate that is the same size as the end plates of the cell. A 125μm thick graphite foil gasket is placed into this recess to provide sealing to the back of the end plate of the cell, as well as electrical conductivity between the test plate and the end plate of the cell. Holes for the inlet and outlet manifolds are punched into the graphite foil with a die punch prior to inserting the gasket into the recess. The test rig plates channel the inlet and outlet from the end plate to a standard ¼" Swagelok® fitting on either end of the test plate for connection to the gas/liquid supply. The plate also has connections for electrical, temperature monitoring, and bolt compression. Four ¼"-32 bolts hold the test plates together, with the assembled cell sandwiched in between. A final torque compression of 8 inch-lbs is used on the bolts to set the graphite foil seals to the back of the end plates.

Assembled cells were broken in prior to testing by holding the cells at 80C for 24 hours with 20sccm of hydrogen and 20sccm of oxygen, with a fixed potential of 0.5V across the cell. This potential would typically result in a current of roughly 400-500mA across the cell.

3.4 Carbon Flow Plates

Non-porous graphite carbon plates are used in large scale fuel cells due to their good electrical conductivity and relative electrochemical inertness to most chemical attacks. These plates are relatively thick, however, and comprise up to 95% of the volume of larger fuel cells. In order to miniaturize these plates to the volumes necessary for a miniature fuel cell, thinned plates of nonporous graphite (POCO™) were obtained. The first attempts at smaller carbon flow plates were a straight scaling from larger scale flow plates. These plates had a relatively large inlet and outlet header (1mm wide), which were connected by parallel 250μm wide channels separated by 250μm wide ribs. These

ribs were recessed into the plate by 100μm, to allow for space for a traditional 175μm thick gas diffusion layer.

Machining of the flow field into these plates was accomplished by ultrasonic milling at an offsite facility (Bullen Ultrasonics, OH). To fabricate these plates, a negative master mold of the pattern to be machined into the plates is made through plunge wire electric discharge milling. This negative master is then mounted to an ultrasonic horn, and a slurry of 0.3μm alumina slurry is passed over the graphite work piece, and the negative master is pushed, under ultrasonic vibration, against the work piece. The vibration causes the alumina slurry to grind away the work piece, resulting in a positive pattern being etched into the work piece by the ultrasonic grinding action. This process was relatively inexpensive (~$30 per plate), and could be used to mass produce large numbers of plates from a single master. The smallest resolution achievable with this technique, however, was 250μm, as the ultrasonic vibration amplitude resulted in a 50μm tolerance for the parts.

Testing of the carbon plates using hydrogen and oxygen revealed a problem involving the straight miniaturization of large scale plates. Since the channels of the plates were also shrunk in dimension, the capillary forces within these channels was much stronger than for the larger scale equivalent structures for an end plate flow field. For a hydrogen-oxygen fuel cell, this increased capillary action resulted in a higher propensity for water droplets to condense in the cathode flow field, which would choke off further oxygen flow to the cathode electrode, and result in a loss of power. In Figure 3.4, cell polarization curves are presented for flow fields with a 250μm wide channel, 250μm

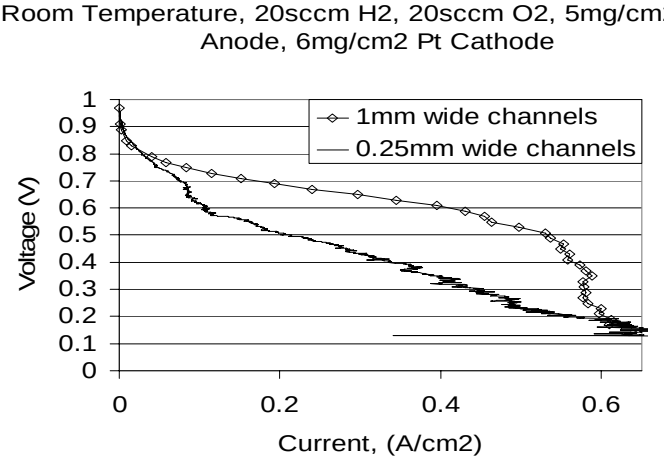

Figure 3.4: Polarization curves for miniature fuel cells with 1mm wic 0.25mm wide channels. All other conditions (compression, catalyst l temperature, fuel flow rates) are equivalent. The "noise" in the curr for the small channels is indicative of water droplets forming and bei forced out of the cathode flow fields.

deep, and a 1000μm wide channel, 250μm deep (the maximum depth of channel allowed by the 500μm thick graphite plate with a gas diffusion layer recess). For the 1mm wide channels (similar in width to a large scale fuel cell), the polarization curve is well behaved, and exhibits the expected regions of polarization overpotential, ohmic behavior, and finally, mass transport limited polarization. For the 250μm wide channels, the current measurements are characterized by a large noise signal over the high current region of the performance curve, as well has dramatically reduced performance when compared to the large channel cell performance.

The reasons for this change in the cell performance can be attributed to the cathode performance at high currents. As the reduction reaction proceeds at a higher rate (higher current density), water is generated in greater volumes on the cathode. Smaller channels on the cathode side of the cell will provide stronger capillary action to wick water together into droplets, and smaller droplets will be able to effectively seal off the smaller channels of the flow field. When the flow channels are blocked by water, the oxygen is forced into moving down the unobstructed channels. This maldistribution in the oxygen flow leads to lower power outputs, which explains the general shape of the curve producing lower currents at equivalent polarizations.

The noise signal on top of this general shape is also generated by the water droplets being formed in the cathode flow channels. As water is build up in the channels, it constricts the oxygen flow to a fewer number of channels. Eventually, back pressure in the flow field from water blocked channels will overcome the capillary action that is acting to keep the water droplets in place, and they will break free and be forced from the channel, opening up the flow field to fresh oxygen flow. This will result in an instantaneous rise in current, as the mass transport limited regime in which the flow field was operating with the water blockages intact is no longer limiting the reaction rate at the cathode, and current increases. With a higher current, however, a higher water generation rate is maintained, and this acts to quickly block other channels, or re-block the same channel, resulting in a drop in current output, as the flow field drops back into a mass transport limited regime again.

To alleviate some of the water management issues from the cathode plate of the fuel cell, 1mm wide channels with 1mm wide separator ribs were developed. In addition, in

order to use as much of the plate depth as possible, the center recess for the Toray® paper was also removed from the design. This change required a thickening of the sealing gaskets, to allow for the identical structure of the MEA to be used on these end plates without the gas diffusion layer recess. Even with this change, however, the channel depths were only 400μm, and some amount of capillary force was still present due to the small depth dimension of these plates.

The hydrophobicity of the carbon plates also exacerbated the water management issues on the cathode, since any water droplets that would condense within the cathode flow field would tend to coalesce into larger droplets, rather than spread out into a film across the flow channels, due to the highly hydrophobic nature of the carbon surface. To decrease the hydrophobicity of the flow channels, a thin (~1-2μm) layer of evaporated gold was deposited over the flow field. This was done without any form of adhesion layer, since the adhesion layers available for gold are all electrochemically active at the potentials of interest for the cell, and a corrosion couple could be established on the adhesion layer, leading to higher resistances for the cell. Instead, gold was evaporated directly onto a carbon surface. Prior to deposition, the carbon was cleaned in an ultrasonic bath using an isopropanol/deionized water mixture to remove any surface contamination on the carbon. After this cleaning, gold layers were evaporated at 10A/sec. In the early part of the studies with these plates, 2 microns of gold was used, but as work progressed, this layer was switched to 1 micron with no loss in the performance of the devices. A comparison between a fuel cell assembled with the gold coated flow fields versus one without gold coating is shown in Figure 3.5. The slope of the ohmic region of

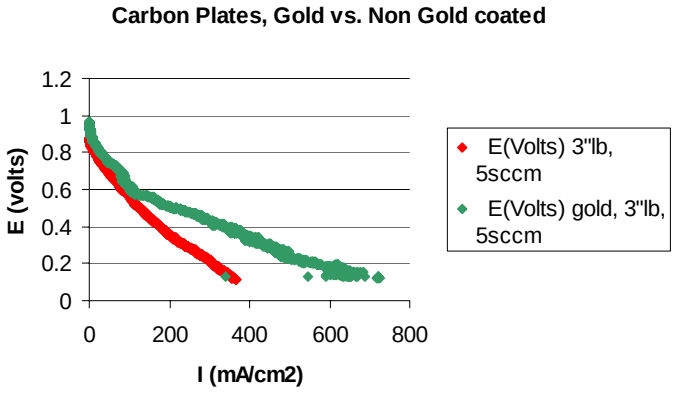

Figure 3.5: Comparision of identical flow fields with (green line) and without (red line) gold coating over the flow fields. Gold coating helps both the series resistance of the cell, as well as the water management issues on the cathode flow plate.

the curve is dramatically better for the gold coated cells, and higher currents are sustainable without water problems in the case of the gold coated electrodes.

3.5 Cell Assemblies

There are two basic configurations for fuel cell stacks to be assembled in. The first type has the cathode flow plate from one cell being connected to the anode flow plate of the next cell. Typically, both of these flow fields are etched into a common plate, and no electrical connection is needed, provided the plate is electrically floating relative to the stack terminals. This configuration is called a bipolar stack, and is a series configuration for the cells. While this configuration simplifies the electrical connections between the cells, it complicates the flow channel connections between the various plates, and makes some form of common manifolding on the fuel and oxidizer plates a requirement. In order to achieve manifolding for both the fuel and the oxidizer, the flow fields must be at right angles to one another, with the manifolds for the fuel and the oxidizer also being at right angles on the plate. A total of four manifolds are then needed in each plate to allow for the fuel inlet and outlet, and the oxidizer inlet and outlet, to each side of the flow plate. When such plates are stacked up with appropriate seals, fuel can be input on one side of the stack, and the oxidizer introduced on the opposing plate of the stack, and the voltage between the two end plates of the stack will be the summation of the voltages of the individual cells within the stack. Manifolding must also be applied through the membrane separator, as gases must be allowed past the membrane in the manifold to reach the next cell in the stack. A six cell bipolar stack, using acetate gaskets and cross channel manifolding for fuel and oxygen, is shown in Figure 3.6. This stack measures roughly 16mm in each

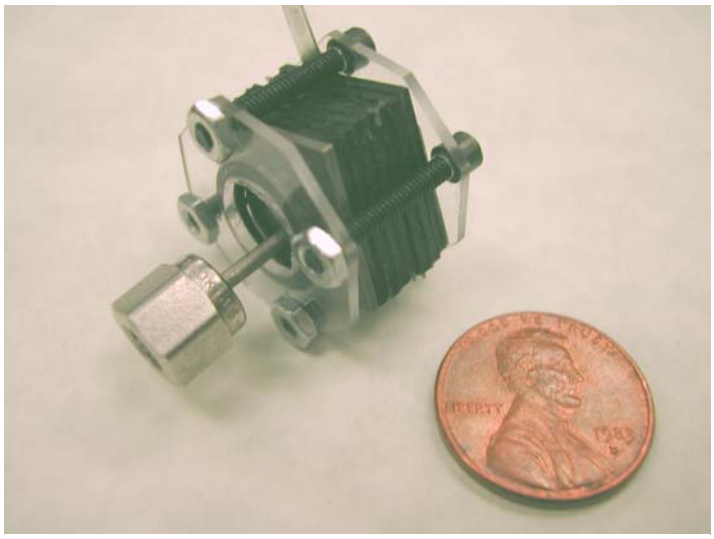

Figure 3.6: Bipolar Stack forced hydrogen/forced oxygen fuel cell. This cell produced 0.8W of power at 20sccm of hydrogen/20sccm of oxygen at room temperature.

dimension, and was capable of producing 800mW of power at 3V using hydrogen and oxygen at room temperature.

One of the problems in a bipolar stack configuration, however, is that the oxygen must be delivered to the cell under pressure to be forced through the oxidizer manifolds. Passive air operation, where ambient air diffuses to the cathode to provide the oxygen for the reduction reaction, was more desired from a system standpoint, as harvesting fuel would be rendered useless if compressed oxygen had to be delivered to the cell. Once forced convection of the oxygen is removed, however, the cathode reactions quickly become mass transport limited in a bipolar stack configuration, as the diffusion lengths through the manifold become too large to provide a high volume of oxygen to the cathodes in the stack. For the case of passive air cells, a monopolar configuration is more commonly used.

Monopolar cell stack configurations are the opposing design from bipolar stacks, in that all the fuel manifold inputs come from the same side of the cell, and so manifolding of the fuel becomes a relatively easy task. However, the electrical connection between the cells to connect the cells in series now becomes more difficult. For the final design of the monopolar array (detailed in Section 0), each cell was connected directly to the fuel manifold, but the individual anode and cathode connections were left separate, so that the cell could be converted from a series wiring configuration to a parallel wiring configuration "on the fly", to better handle changes in load conditions for the cell. In a monopolar array, all the anodes face in one direction, toward a common manifold, and all the cathodes face in the same direction, typically toward the outside air. A prototype monopolar array configuration is shown in Figure 3.7. In this case, the cathodes are facing up, with a

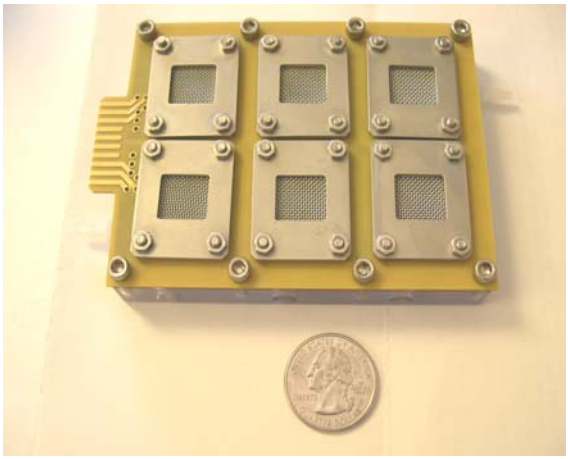

Figure 3.7: Monopolar cell array. The cathodes are all face up in this picture, with a stainless steel mesh over each cathode gas diffusion layer to take the place of the cathode flow field. The anode flow fields of each cell are facing down, and are in contact with a common manifold. The anode and cathode electrical connections are brought out on the tab at the left edge of the cell.

stainless steel mesh covering the gas diffusion layer on the cathode side of each cell. No flow field is necessary on the cathode in this configuration, as there is only diffusional transport of oxygen to the cathode from the surrounding air. The manifold for the fuel is the bottom part of the cell, and supplies each anode flow plate from the common manifold.

3.6 Testing in Hydrogen

Cell testing in hydrogen was done at various temperatures using fully humidified hydrogen gas. During cell operation at high currents, water is dragged from the anode to the cathode along with the protons through the membrane. This effect, known as osmotic drag, has the effect of dehydrating the anode, and superhydrating the cathode. As mentioned previously, cathode overhydration can lead to water formation in the flow channels, and a subsequent blocking of oxygen from moving through the flow channels. Anode dehydration has the effect of locally raising the interfacial impedance of the electrode structure to the membrane structure, as the lower water content makes it more difficult for the protons to move from the electrodes into the membrane. To combat this effect, saturated hydrogen gas was used on the anode.

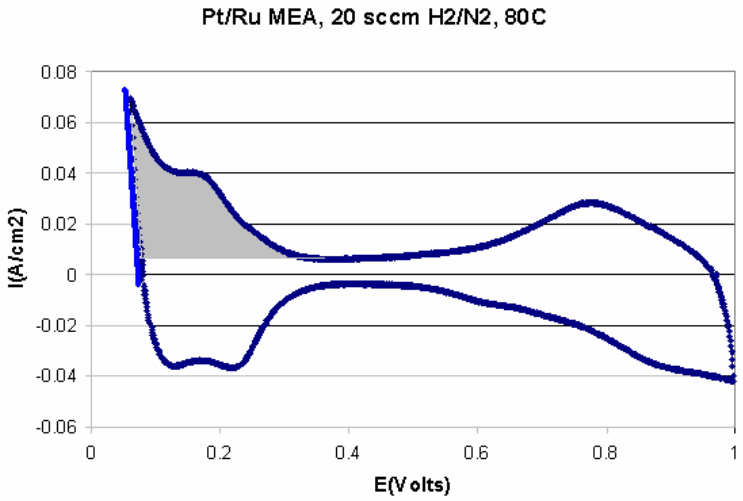

Figure 3.8: Cyclic voltammagram of the cathode of a typical fuel cell. The gray region (0.05-0.4V vs. NHE) is the area used to calculate the electrochemically accessible surface area. The inverse of the slope of the blue line gives the total resistance of the assembly, inclusive of the electrical leads.

The first test sequences for any new cell assembly was to characterize the anode and cathode in terms of electrochemical activity and area. Cyclic voltammetry was used for this measurement, and a typical cyclic voltammagram for a Pt electrode is shown in Figure 3.8. Following the methodologies in the literature[16], the electrode being measured (the working electrode) was kept in saturated humidified nitrogen, and

the counterelectrode was held in saturated hydrogen. This hydrogen electrode also served as a psueudoreference potential, as the hydrogen-platinum couple that this electrode has could be used to define the potentials of the working electrode.

Two useful measurements can be gained from this data. The first is a measure of the electrochemically accessible area of the electrodes. Since these electrode structures are constructed of a network of small precious metal catalysts, the hydrogen absorption/ desorption region of the voltammagram gives a measure of how much of this electrode is being accessed by the hydrogen gas, and by comparison, how much surface area exists within each nominal square centimeter of electrode area. The area under the oxidation peaks, with the background of the double layer capacitance subtracted, gives such a measure of the electrode area (See Figure 3.8). For a well assembled electrode structure with good interfacial impedance to both the Toray® gas diffusion layer as well as the membrane, an electrochemical surface area would be in the range of 350-400 cm^2 per cm^2 of actual electrode area.

The second measurement is that of the slope of the reduction curve coming from the hydrogen evolution region of the voltammagram (0.06V, increasing). The inverse of this slope gives a measure of the total resistance of the test assembly, including all the resistances from the electrical leads, the cell impedances, and the membrane. If the cell was incorrectly compressed during assembly, a high resistance for the cell would be observable using this technique. Normal values for a well compressed, well assembled cell would be in the range of 0.65-0.8 Ω.

The next measurement technique would be to run a standard polarization curve on the cell assembly. This was done at 80C, and saturated hydrogen and oxygen. The data collection was done potentiostatically, by controlling the voltage of the cell, and measuring the current produced at a given potential. Data points were taken after stabilization for 20 seconds at each potential. In addition to the voltage and current at each potential, a “current interrupt” technique was employed to ascertain the resistance of the membrane. In this technique, the current at a given potential setting is momentarily interrupted, and the potential is allowed to rise in response to the current being halted. By measuring the time response of the voltage rise, a measure of the instantaneous (electronic) and time dependent (ionic) resistance within the cell can be gained. The

electronic resistance within the cell is due predominantly to interfacial impedance losses between the catalyst electrodes and the membrane, and between the catalyst electrodes and the gas diffusion layers, with the former being a majority of this signal. For good interfacial impedances between the electrodes and the membrane, this measure of high frequency resistance (HFR) should be in the 0.18-0.25 Ω/cm^2. A polarization curve of a typical carbon plate forced hydrogen-forced oxygen cell operating at 80C is shown in Figure 3.9, along with a measure of the HFR as a function of current density.

The polarization curve demonstrates the three well characterized regions of a fuel cell polarization curve. The first region is the overpotential polarization region, where large changes in voltage are needed to generate small increases in current. This is due to the overpotential needed to start to drive an appreciable reaction rate of hydrogen oxidation on the platinum. The second region is characterized by a linear region with a slight negative slope. This linear region is the ohmic region, and is characteristic of the internal impedance of the cell itself. The slope of this line should be equivalent to the resistance of the cell measured through current interrupt techniques. The third region, in which large changes in voltages again occur with little change in current at high current densities, is characteristic of the mass transport limited regime of cell operation. In this region, the current generated by the cell is limited by the ability of the cell to diffuse more of the fuel and oxidizer to the catalyst sites. This region can be adjusted by pressurizing the cell, and raising the partial pressure of reactants. This region also sets the limiting current for the cell, based upon a given set of operating conditions (pressure, temperature, flow rate).

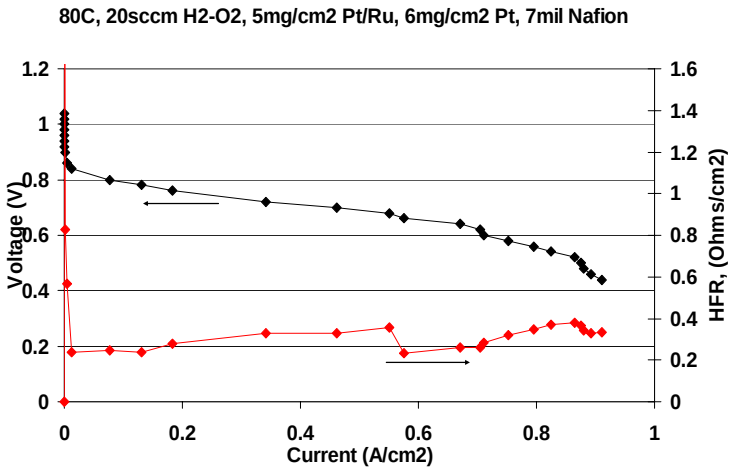

Figure 3.9: Polarization curve and cell impedance for a typical carbon plate cell running on hydrogen and oxygen. The cell impedance is higher than is typically reported, due to the miniaturization of the cell disallowing higher compressions. The start of mass transport limitation is also earlier in onset than is normal, due to the shallow channels used in the miniature cell.

3.7 Testing in Methanol

Although not the focus of this project, some testing using methanol fuels was done to provide some reference point against the literature for liquid fuels prior to testing in glucose. Methanol will wet the surfaces of the electrode materials well, and so issues surrounding hydrophobicity are somewhat mitigated in the use of this fuel. For these tests, a one molar concentration of methanol in deionized water was used, and was supplied to the anode of the cell at 100µl/min. The cathode side remained unchanged from the hydrogen cell, with a 20 sccm of hydrated oxygen being supplied to the cathode. The performance curve for methanol at 80C is shown in Figure 3.10. Open circuit voltages of 0.75V are similar to what has been reported in the literature[17] for this fuel, but performance is well below the expected values of performance for a large scale cell operating under these conditions. For a 1M methanol fuel solution, running on forced oxygen at 80C, an expected current of 100-120mA/cm2 at 0.5V is typical, whereas this cell was showing only 50mA of current at the same conditions. Part of the explanation for the lower than expected performance may lie in the high degree of overpotential polarization observed in this cell. Almost 120mV of polarization is needed to start to draw significant current from the cell, where normal overpotentials for methanol based cells are more in the 40-50mV range. This is likely due to the effects of the cathode structure in limiting the initial reaction rates of the reduction reaction. By changing the cathode structure, this high overpotential could be eliminated.

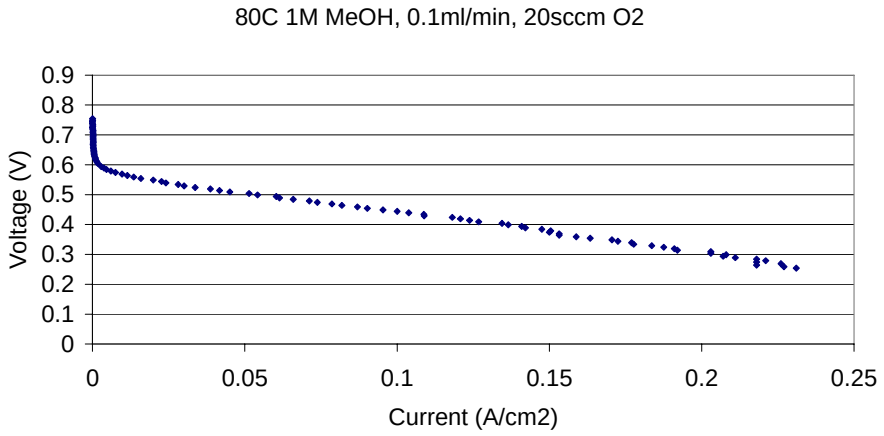

Figure 3.10: Methanol polarization curve for a single cell operating at 80C, using forced air and 1M methanol. Performance is below expected values from large scale methanol cells, which may in part be due to higher than expected overpotential polarizations and small channel effects within the cell.

3.8 Testing in Glucose

Glucose fuel testing was conducted in a manner similar to that used for methanol testing, with a fixed 1M solution of glucose in deionized water being used as the fuel stock, and a feed rate of 0.1ml/min into the cell. Glucose concentrations this high are slightly viscous when compared to straight water, and the hydrophobicity is increased somewhat over what would be expected for a pure water solution when glucose is added. These factors influence the capability of the glucose fuel stock to appropriately wet all the surfaces in the flow field, the diffusion layers, and the catalyst layers of the fuel cell. In order to insure maximum wetting of the fuel cell layers prior to the introduction of glucose, a methanol fuel solution was delivered to the anode of the cell for a minimum of one hour to insure that all the surfaces were completely wetted. The feedstock solution was then converted from methanol to glucose over a period of four hours, after which time the fuel was completely converted to 1M glucose solution. This was found to be critical to proper testing in glucose. In cases where incomplete or improper wetting of the anode was observed, very low open circuit voltages would be observed, and extremely low currents would be able to be drawn from the cell.

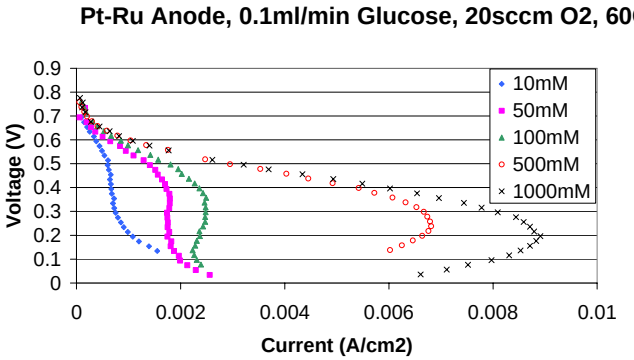

Figure 3.11: Polarizations of fuel cells at various concentrations of fuels at elevated temperatures.

With proper wetting, the cell could then be run on glucose. The glucose oxidation process on the anode is a two electron oxidation which generates two electrons and two protons, and leaves behind an adsorbed byproduct, gluconolactone, which acts as a poison for the catalyst and prevents further oxidation of additional fuel. This poisoning effect is manifested in the polarization curve, shown in Figure 3.11 for various concentrations of fuel. As can be seen, the open circuit potentials are between 0.7 and 0.8V. Increasing the concentration of the fuel increases the current density, as expected, and the current at 0.35V, plotted against concentration, is reasonably linear. The

manifestation of poisoning at higher concentrations, however, can be seen as a "hook" in the polarization curve. This hook comes about due to the increasing rate of poisoning at higher current densities overwhelming the fuel oxidation rate. Once the surface has started to poison, the availability of catalytic sites will start to drop off, and the availability of catalytic sites will begin to predominate in determining the current of the cell, rather than the reaction rate at the anode, and this availability will decrease continuously, forcing the current back down, even in the presence of a lower potential.

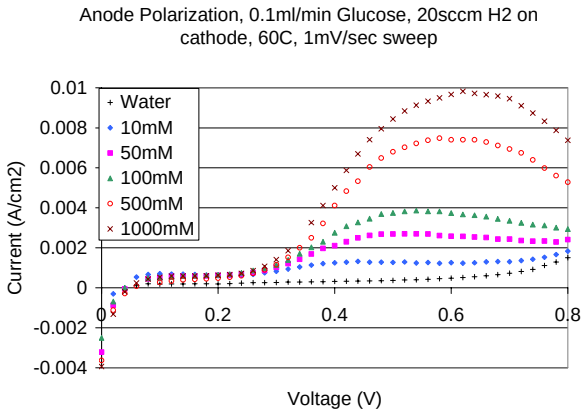

Figure 3.12: Anode polarization curves for a Pt-Glucose anode at various concentrations. Three regions of PtO2 reduction, slow 1 electron oxidation, and fast 2 electron oxidation of glucose are evident. Higher concentrations and higher currents lead to a poisoning effect that causes currents to drop at higher voltages.

The amount of poisoning can also be seen through the use of an anode polarization curve. In this case, the cathode is held under hydrogen gas to provide a pseudoreference potential of the normal hydrogen electrode(NHE). The anode is kept in a flowing field of glucose solution, as in the normal operation of the cell, and the cell is polarized by sequentially higher potentials. Since the cathode is at 0V vs. NHE, and is very active relative to the glucose on the anode, it will remain unpolarized at 0V independent of the current of the cell. Thus, any polarization will result in a movement of the anode potential. A series of anode polarization curves for various concentrations is shown in Figure 3.12. Several regions of interest are observable in this data. The first is the region very close to 0V vs. NHE. The current under this bias is cathodic, and most likely represents a reduction of PtO_2 to platinum metal on the anode. Once the catalyst metal is reduced, there is a slight positive current which is observable between 50mV to 300mV vs. NHE in all cases where there is glucose in the solution, but not in the case of pure deionized water. This current is also insensitive to concentration. This current is most likely due to a constant slow one electron oxidation of glucose to adsorbed glucose, as outlined by Lamy and

coworkers[18] [19]. This reaction is extremely slow, and would be insensitive to concentration, since diffusion would not be rate limiting in this case. The final region, starting at around 350mV vs. NHE and continuing up to the highest polarization measured, constitutes the region where glucose and adsorbed glucose are being oxidized to gluconolactone. A large, concentration dependent current is seen, followed by a drop in current at high potentials. This drop at very high potentials (which would be equivalent to low cell potentials where the anode voltage is very close to the cathode potential) can only be due to anode poisoning, since all other factors surrounding cell performance have been removed in this experiment. This agrees well with the full cell polarization data, and strengthens the argument that poisoning at high currents is what is causing the hook phenomenon.

3.9 Lifetime Operations with Glucose

Poisoning in the higher current regime can occur quite rapidly, with a large drop in current noticeable within minutes after starting to draw high current. Figure 3.13 shows a trace of the current vs. time for a fixed potential load of 0.35V on the cell. An initial current of almost 40mA is drawn on the cell, but this decreases to only 10mA after only two minutes of operation. This is one of the fundamental limiters for long time operation of a noble metal catalyzed fuel cell running on glucose, and this anode poisoning must be overcome if the cell is to function for any longer than a few minutes. Typical schemes for cleaning electrodes involve biasing the electrodes up to strongly oxidizing potentials, and allowing the poisons to be oxidized off of the surface of the anode. This process usually implies reversing the cell, so that current must be supplied to the cell in order for the cleaning process to take place.

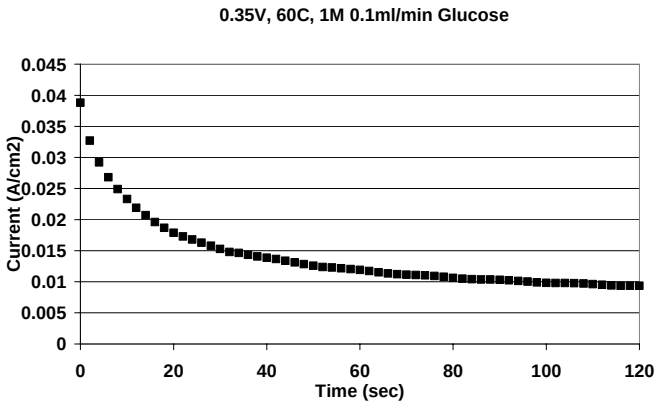

Figure 3.13: Decay over time of the cell performance on exposure to glucose. 0.35V potentiostatic load, 60C, 20sccm humidified O2 on the cathode.

The nature of a small, glucose based fuel cell allows for another possibility for cleaning of the anode that does not require cell reversing in order to clean the poisons from the cell. First, the use of a traditional cathode, which is normally the polarizing electrode, becomes a pseudo fixed electrode in the glucose cell, due to the much higher activity for oxygen on platinum than glucose on platinum. Thus, in any polarization of the cell, the voltage of the anode will move relative to the voltage of the cathode, with the cathode only polarizing as much as would normally be expected with a low current load. For our measurements of hydrogen/oxygen polarization of the cell, at ~5mA of current, the cathode is only polarized by ~80mV vs. NHE.

Since the cathode is now relatively fixed by its high activity and low current of the cell, if the cell is shorted, the anode polarizes up to the cathode potential. This has the effect of causing the anode to become strongly oxidizing, like in the case of the cell reversal, only in this case, the cell continues to be operated in the forward direction, with large currents being delivered from the cell during the shorting. This large (but decreasing) current is likely caused by the stripping of poisons from the anode. Once the cell is brought back under load, the anode is again capable of further oxidation of the glucose fuel, until poisoning once again contaminates the anode surface.

This concept has been used with this cell architecture to deliver power from a glucose/water stream for up to 400 hours, with no significant decrease in power delivered. A cell cycle, starting with a shorting pulse, then a load pulse, and finally ending with an open circuit rest to recover open circuit potentials, is shown in Figure 3.14. As can be seen, a significant initial stripping current is observed when the cell is first shorted, and this current decreases with time. After 30 seconds, the cell is put back under a 0.4V load, and the cell exhibits an initial

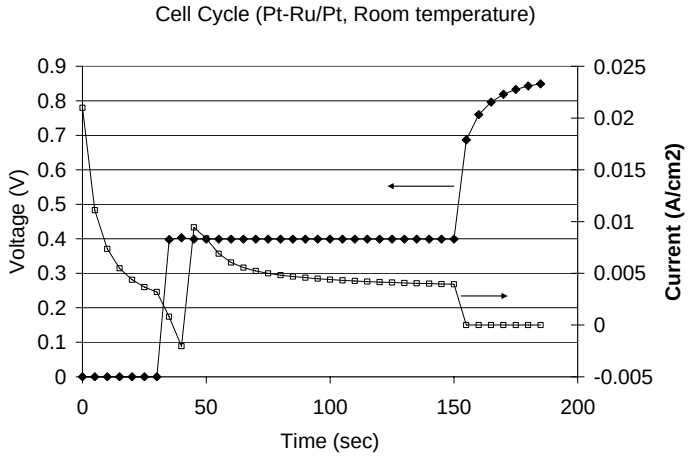

Figure 3.14: Cycle for recovery of anode activity. 30 second short, 120 second load (0.4V), 30 second open.

drop in current. This reducing current is likely akin to the reducing current observed in the anode polarization curve, which was attributed to the reduction of platinum oxide. After this initial reduction, the current raises back up as glucose is oxidized to glucanolactone, and the current exhibits decay similar to that demonstrated in Figure 3.13. This decay is most likely due to the poisoning of the anode over time. After 2 minutes of load, the cell is brought to open, and the open circuit potential is allowed to recover in a rest cycle for 30 seconds before the next short circuit cycle is applied.

This cycle can be repeated continually, and data can be drawn out of each cycle to establish a lifetime chart such as that shown in Figure 3.15. In this case, the current at the end of the load cycle is used to calculate a minimum power delivered during the load cycle at 0.4V. The curve exhibits two regions, a low time region (0<t<50 hours) and a stable longer duration region (t>50 hours). The first region is characterized by an unstable cell, with large cycle to cycle changes in the current delivered at the end of the load cycle. Although it is not clear what causes this, and many factors may contribute to this behavior, one such possible explanation is that, by cycling the cell in this manner, more and more of the electrochemically active surface area of the anode made accessible by improvements in the wetting and the structure of the anode itself. Unlike a methanol cell, no gaseous byproducts are observed from the anode outlet, so that catalyst surface, once wet, is likely to remain wetted. However, poisoning may be contributing to some degree, as the smaller pore catalysts may not be able to flush away the byproducts from the oxidation site before the next load cycle is applied and the poisons may become redeposited on the surface of the catalyst. The second region is characterized by

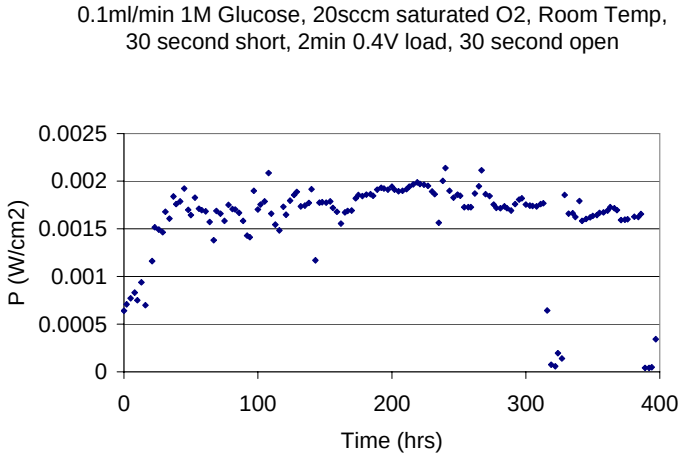

Figure 3.15: Lifetime of a Pt/Ru cell operating on Glucose/ Oxygen at room temperature, using the cycle outlined in the text.

reasonably stable performance, and it is from this region that the cycle shown in Figure 3.14 is taken.

This testing with commercially available electrode and membrane materials establishes a baseline for performance against which improvements in these components can be judged. Principally, one would like to develop a better anode catalyst that more efficiently oxidizes the incoming fuel, and a membrane that is better able to resist cross over contamination to the cathode material, so that we can continue to use a platinum based cathode and gain optimal performance from the cathode half reaction. In the next section, we will discuss the efforts to develop advanced membranes that have better crossover characteristics vs. glucose, and also allow for better temperature and structural stability, while maintaining the ionic conductivity found in Nafion®.

4. Membranes

One of the basic needs for the membrane material is to be ionically conductive at normal temperatures, which would include a range from room temperature to 80C or above. Nafion® suffers from decomposition at relatively low temperatures, and is extremely dimensionally unstable, swelling by more than 30% with the uptake of water. Nafion® uses a Teflon™ backbone, but other backbone materials that will resist swelling, have high decomposition or softening temperatures, and are still amenable to modification to improve ionic conductivity exist. Adding sulfonic acid groups to these backbones is a first step in synthesizing a better membrane material.

A series of poly(phenylene) based polyelectrolytes were synthesized from 1,4-bis(2,4,5-triphenylcyclopentadienone) benzene and 1,4-diethynylbenzene by Diels-Alder polymerization. Post sulfonation of this high molecular weight and thermochemically stable poly(phenylene) with chlorosulfonic acid resulted in homogenous polyelectrolytes with controllable ion content (IEC = 0.98 – 2.2 meq/g). Fuel cell relevant properties such as high proton conductivity (123 mS/cm), good thermal stability, and sulfonated films that are tough and flexible suggest that this polyelectrolyte material shows promise as a potential candidate for utilization in a polymer electrolyte membrane fuel cell (PEMFC). These materials have lower glucose crossover properties than Nafion®. Physical properties of this material, such as water uptake, thermal stability, and proton conductivity are reported with respect to ion exchange capacity (IEC).

Currently, the state of the art PEM material used in fuel cells is Nafion® (DuPont, United States). Nafion® is a polytetrafluoroethylene (PTFE) polymer that is polymerized in the presence of sulfonic acid containing fluorinated α-olefin.[20 21] This type of chemistry leads to a random structure of Nafion®, which is schematically illustrated in Figure 4.1 revealing its PTFE backbone, and pendant sulfonic acid group. Nafion® has been demonstrated as

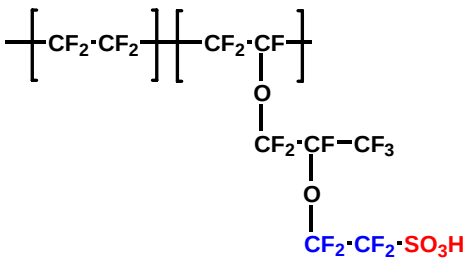

Figure 4.1: Schematic representation of Nafion® containing a PTFE backbone with a fluorinated pendant side group containing a sulfonic acid moiety.

an excellent PEM material, its high material cost is a barrier for consideration in many practical proton-exchange membrane fuel cell (PEMFC) applications as well as its extremely high methanol permeability.[22 23 24 25] Although these issue exists, Nafion® is almost exclusively used in Direct Hydrogen and Direct Methanol Fuel Cells (DHFC and DMFC) because of its excellent proton conductivity and chemical inertness.

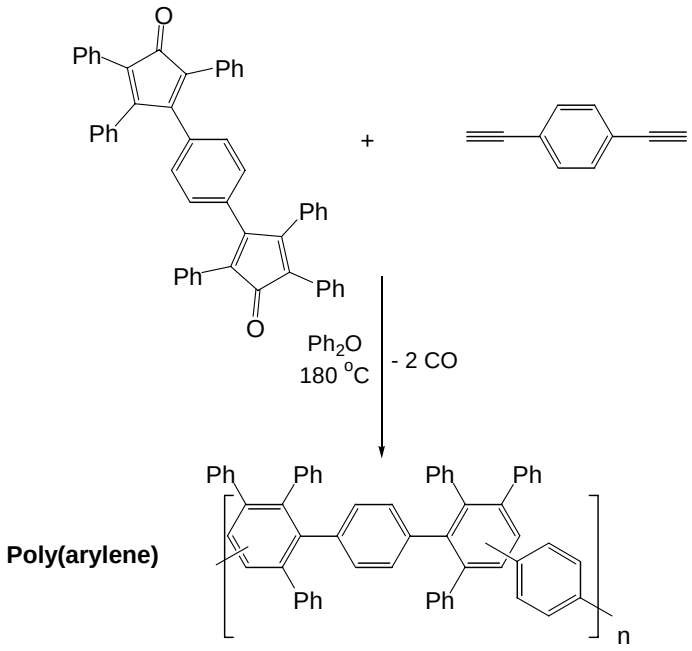

Figure 4.2: Diels Alder Polymerization of 1,4-bis(2,4,5–triphenylcyclopentadienone) benzene and di(ethynyl)benzene.

The cost and performance limitations of current perfluorinated polymer electrolyte membranes (PEM) such as Nafion™ have hindered large-scale commercialization and market penetration of polymer electrolyte membrane fuel cells (PEMFC) in mobile and stationary systems. This has sparked a worldwide research effort to design alternative polymer electrolyte membrane (PEM) materials with high ionic conductivity, thermal stability to allow operation over 100 °C, chemical stability to a strong acid proton conductor and oxidation, good processability, and excellent barrier properties to fuels (e.g. methanol, oxygen, etc.)[26 27]. One common approach has been to sulfonate existing thermoplastics such as polystyrene, polyetherketones, and polyethersulfones.[28 29 30 31 32 33] This has generated mostly PEM's with lower costs and improved thermal stability, but generally lower ionic conductivities at comparable ion exchange capacities than Nafion.[34] However, many of these thermoplastics based PEMs are more susceptible to oxidative or acid catalyzed degradation than Nafion.[35]

Utilizing a purely aromatic polymer, such as poly(phenylene)s, provides a route to potentially improve the thermochemical stability of PEMs due to their inherent thermochemical stability. High molecular weights are necessary for these aromatic

polymers to ensure polymer chain entanglements that are responsible for producing physically robust PEM films that can be processed into membrane electrode assemblies that survive within a PEMFC. An example of a sulfonated substituted poly(phenylene) is poly(4-phenoxybenzoyl-1,4-phenylene) that has shown relatively high proton conductivities (10^{-2} S/cm) and good PEM characteristics.[36] However, achieving high molecular weights based upon this class of polymer is dependent on the pendent group of the aryl halide monomer, which limits sulfonation and broad functionalization.[37]

The subject of this research is the design, synthesis, and physical properties of a sulfonated, highly phenylated poly(phenylene) that provides a very promising solution to achieving PEMs with high molecular weights and overcomes the limitations of sulfonation and broad functionalization (Figure 4.2). This research developed a fully aromatic polymer electrolyte that was designed to be processible, thermally and chemically robust, with ionic conductivities rivaling those of Nafion. The backbone polymer, prepared by the Diels-Alder polymerization of 1,4-bis(2,4,5-triphenylcyclo-

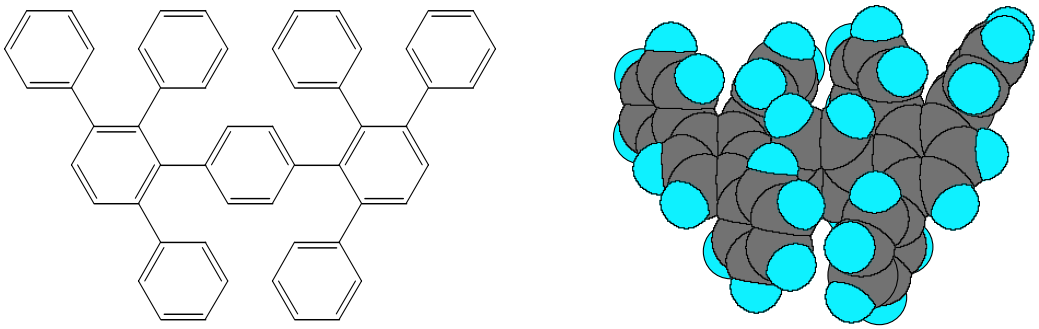

Figure 4.3: Minimum energy molecular model of repeat unit

pentadienone) benzene with diethynylbenzene, (Figure 4.2), can be prepared with a wide range of functionalities and configurations that provide a number of opportunities to optimize the chemical and physical properties desirable for PEM's.[38] A minimum energy molecular model (Figure 4.3) of the polymer repeat unit shows a non coplanar phenylene backbone and indicates a rigid rod structure. By themselves, the polymers are insulating and thermally stable to 500C, a fact that has made them one of the more important spin-on dielectric materials.[39] Six pendant phenyl groups per repeat unit and the mix of meta and para configurations imparted by the regiochemistry of the Diels-Alder polymerization make these materials readily soluble in organic solvents and easy

processed into thin films. The large number of pendant phenyl groups provides for the facile introduction of up to six sulfonic acid groups per repeat unit, a fact that we use to study the influence of the degree of sulfonation on ionic conductivity, water uptake, and thermal stability.

4.1 Synthesis

The efforts of this research were directed at designing an alternative Nafion® polymer electrolyte membrane having conductivities equal or better than Nafion® will having lower glucose cross-over characteristics. These technical challenges were addressed by utilizing the polyphenylene polymer developed in this LDRD and the properties for this material will be discussed in the following sections.

Preparation of Diels Alder poly(phenylene)s has been described elsewhere and briefly described above.[40 41] Within this report, we use a naming convention based upon the degree of sulfonation of the poly(phenylene) backbone polymer, ranging from SDAPP0 (no sulfonation) to SDAPP4 (maximum sulfonation). Sulfonation of SDAPP0 has not been reported, but substituted 1,4-poly(phenylene) has been sulfonated with concentrated sulfuric acid with levels of sulfonation controlled by varying the reaction time. Our approach to sulfonating SDAPP0 was the creation of a 6 wt% polymer solution of SDAPP0 and methylene chloride that was subsequently homogeneously sulfonated in situ with chlorosulfonic acid.

The repeat unit of SDAPP0 with its six pendent phenyl groups (Figure 4.4), provides a number of possible sites for sulfonation. However, sulfonation is thought to occur predominantly at the para-positions of the pendant phenyl groups due to their positioning

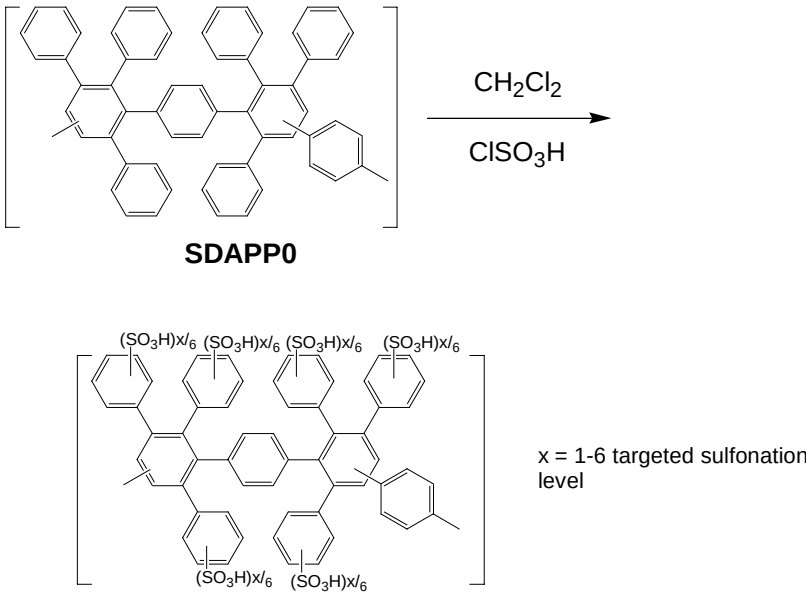

Figure 4.4: Sulfonation of Diels Alder poly(phenylene)

about the sterically congested, con-coplanar, rigid rod backbone.[42] Therefore, the limits of sulfonation are projected to be between 0 and 6 sulfonic acid groups per repeat unit. By varying the ratio of moles of chlorosulfonic acid to moles of polymer repeat unit charged to the sulfonation reaction, 0.8 to 2.1 sulfonic acid groups per repeat unit were achieved as measured by titration (see below).

Sample	IEC	Methylene chloride	DMAC	NMP	Water
SDAPP0	0	+	-	-	-
SDAPP1	0.98	-	+	+	-
SDAPP2	1.4	-	+	+	-
SDAPP3	1.8	-	+	+	-
SDAPP4	2.2	-	+	+	-
SDAPP5.5		-	- +	- +	Hydrogel

Table 4.1: Solubility of Sulfonated Diels Alder poly(phenylene) samples (SDAPP) in the sodium salt form

Introduction of increasing numbers of sulfonic acid groups onto polymers improves their ionic conductivity, but also makes the polymers more hydrophilic. In order to have a suitable membrane for PEMFC's, there must be sufficient sulfonic acid groups (meq/g) to provide suitable proton conduction, but few enough to insure that the polymeric film does not lose its mechanical integrity. Table 4.1 displays the solubility characteristics of the sulfonated samples in a variety of common solvents with respect to the sample's IEC. At every level of sulfonation, the polymer was insoluble in methylene chloride, in contrast to unsulfonated parent polymer. Between IECs of 0.98 and 2.2 meq/g, the samples were soluble in polar aprotic solvents, while remaining insoluble in water. This IEC range is very similar to IEC values studied in other sulfonated aromatic polymers such as sulfonated poly(ether ether ketone) (SPEEK). However, when the IEC was increased over 2.2 meq/g. the polymer formed a hydrogel in water eliminating the feasibility of forming a film from these highly sulfonated samples.

Sample	Sulfonation Stoichiometry*	IEC Experimental	Actual Sulfonation**	Sulfonation Efficiency***
SDAPP1	1	0.98	0.8	80
SDAPP2	2	1.4	1.2	60
SDAPP3	3	1.8	1.6	53
SDAPP4	4	2.2	2.1	52

Table 4.2: Targeted Sulfonation (Sulfonation Stoichiometry) and Experimentally Determined Ion exchange capacity of SDAPP,
**** moles of chlorosulfonic acid added per moles of polymer repeat unit in reaction***
***** calculated average number of sulfonic acid groups per repeat unit from IEC***
******{[Actual Sulfonation] ¸ [Sulfonation stoichiometry]} x 100***

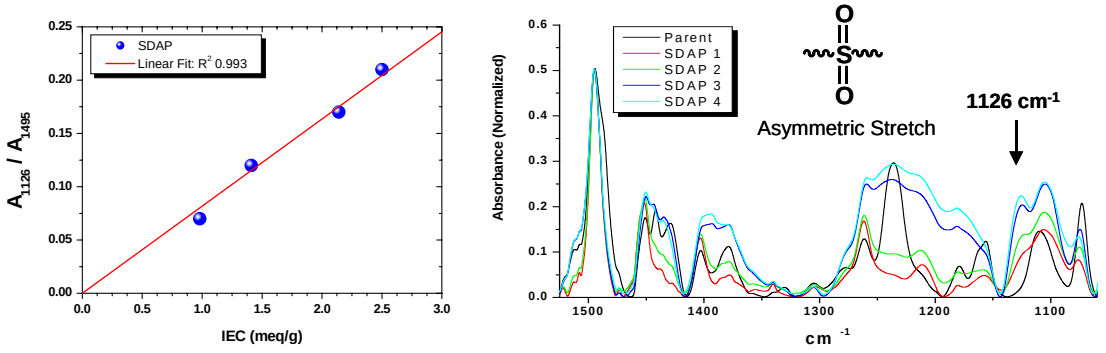

Figure 4.5: Targetted vs. actual degree of sulfonation (left figure). Right figure shows an IR spectra of SDAPP0 through SDAPP4, showing the increase in asymmetric and symmetric stretching frequencies at 1126cm^{-1} and 1036cm^{-1}, respectively.

Table 4.2 summarizes the ratio of moles of sulfonating agent to polymer repeat unit charged in the reaction (sulfonation stoichiometry), experimentally determined IEC, actual sulfonic acid per repeat unit (actual sulfonation), and the ratio of actual sulfonation to sulfonation stoichiometry (sulfonation efficiency). A plot of targeted versus actual sulfonation is shown in Figure 4.5. As expected, the actual sulfonation steadily increased with increasing stoichiometry of chlorosulfonic acid. At low sulfonation levels the sulfonation efficiency was relatively high (80 %), but decreased to 60 – 66 % with increasing concentration of chlorosulfonic acid.

Spectroscopic evidence of sulfonation of the base polymer was provided with the presence of infrared absorptions characteristic of aryl sulfonic acids. In Figure 4.5, the IR spectra of SDAPP0 through SDAPP4 are plotted. The infrared spectra of p-

poly(phenylenes) contain two single bands, 770-730 cm^{-1} and 710-690 cm^{-1}, which correspond to the out-of-plane vibrations of the five adjacent aromatic hydrogen-carbon bonds of the pendant phenyl groups.[37] In the unsulfonated polymer, these strong absorptions occur at 758 and 696 cm^{-1} respectively. The intensities of these peaks in SDAPP are diminished, which suggests that sulfonation is occurring predominately on the pendent phenyl groups due to the conversion of mono-substituted phenyl rings to di-substituted. The asymmetric and symmetric sulfonate stretching frequencies adsorptions, 1126 and 1036 cm^{-1} respectively, increased in intensity with sulfonation level. The aromatic in-plane skeletal deformation at 1494 cm^{-1}, present in both unsulfonated and sulfonated polyphenylene was used as an internal standard to quantify the amount of sulfonic acid groups in each sample.[43] The ratio of the intensity of the absorption peaks at 1126 and 1494 cm^{-1} was plotted versus IEC and resulted in a near linear correlation, Figure 4.5, providing additional evidence for incorporation of sulfonic acid units on the backbone of the polymer in addition to IEC.

1,4-Bis(2,4,5-triphenylcyclopentadienone) benzene, or bis-tetracyclone, was prepared as described elsewhere. 1,4-Diethynylbenzene was purchased from GFS and sublimed at room temperature before use. Diphenyl ether, chlorosulfonic acid, dimethylacetamide (DMAc) and anhydrous methylene chloride was used as received from Aldrich.

Polymerizations were performed using a slight modification of the method described in the literature. To bis-tetracyclone (50.0 g; 72.4 mmol) and 1,4-diethynylbenzene (9.13 g; 72.4 mmol) in a 500 mL Schlenk flask, diphenyl ether (250 mL) was added and the resulting mixture was frozen in an ice bath. The mixture was freeze-thaw degassed (3X) before heating under argon (1 atm) at 180C for 24 h. Periodically, carbon monoxide was vented to avoid over-pressurization of the reaction flask. Subsequently, additional diethynylbenzene (0.10 g; 0.8 mmol) was added to the viscous slurry and the mixture was stirred for an additional 12 h at 180C. The reaction vessel was then cooled to room temperature and its contents were diluted with toluene (300 mL). The polymer was precipitated by dropwise addition of the solution to 1000 mL of acetone. This dilution in toluene and precipitation in acetone was repeated and the resultant white solid was dried in a vacuum oven for 12 h at 80C, 48 h at 230C, and 24 h at room temperature. A 96 % yield (52g collected) of a tough, yellow solid was obtained.

In a typical sulfonation, SDAPP0 (7.02 g) was added to a flame dried, 500 mL three-neck, round-bottom flask under argon and dissolved in methylene chloride (6 % solution by weight). The solution was cooled to – 50C (dry ice/acetonitrile) and chlorosulfonic acid (4.30 g, 36.9 mmol) diluted in chloroform (20 mL) was added dropwise though an addition funnel over 15 minutes while being vigorously stirred with a mechanical stirrer under an argon atmosphere. This amount of chlorosulfonic acid gave a 4:1 ratio of acid to polymer repeat unit. Other ratios of sulfonating agent to polymer repeat unit were prepared to attain polymers with various ion exchange capacities, as discussed in Section 4.7. The mixture darkened from bright yellow to black during chlorosulfonic acid addition. After 30 minutes the reaction was warmed to room temperature at which point a dark solid precipitated. The organic solvent was decanted and to the remaining solid was added 300 mL of a 0.5 M solution of NaOH that was allowed to react at room temperature for 12 h. The slurry was then heated for 4 h at 80C to ensure sulfonyl chloride conversion. The off-white solid was Soxhlet extracted with de-ionized water for 48 h and dried in a vacuum oven at 100C for 48 h to obtain light yellow solid (9.52 g). 1H NMR (d-DMSO): δ (ppm) = broad signal 6.35 – 7.22 (peaks at 7.19, 7.09, 6.95, 6.88, 6.64, 6.54). 13C NMR (DMSO-d6): δ (ppm) = broad signal 138 - 141 (peak at 139) broad signal 131 – 126 (peaks at 126.9, 128.7, 129.5, 131.0).

The sodium salt of the sulfonated polymer was dissolved in DMAc (10 % weight solution) and filtered though a 2 μm syringe filter (glass microfiber filter). The solution was cast onto a clean glass plate in an oven at 90C under N2. After 20 h, the film was removed from the glass plate and immersed in de-ionized water (1 L, 18 MΩ) for one hour at 100C to extract any residual DMAc. The resultant film was then converted into the acid (proton) form by immersion in 2.0 M H2SO4 at 100C for one hour. The film was then rinsed thoroughly with de-ionized water and then soaked in de-ionized water (18 MΩ) at 100C for another hour to remove any residual acid. The film was stored in de-ionized water until used.

4.2 Characterization

FTIR spectra of polymer powders/KBr pellets were collected using a Perkin-Elmer System 2000 spectrometer. Thermogravimetric analysis (TGA) under nitrogen was carried out on a Perkin Elmer TGA-7 at a heating rate of 10C/min. All samples were

heated in the TGA furnace at 110C under dry nitrogen for 30 min to remove water before the full scan from 50C to 950C was performed. Differential scanning calorimetery (DSC) was performed on a TA Instrument 2010 with a heating rate of 10C/min.

The ion exchange capacity (IEC) of the samples was determined by titration of acidified films. Films (approximately 5cm x 2cm) were soaked in 50 mL of 1.0 M Na_2SO_4 for 24 h. The solutions were then titrated to an endpoint of pH 7 with 0.01 M NaOH. The IEC of the film was computed by

$$IEC = \frac{v_{base} * [NaOH]}{m_{dry} * 0.001} \qquad \text{Equation 4.1}$$

where v_{base} is the volume of base required to reach the endpoint, [NaOH] is the concentration of the base, and m_{dry} is the mass of the dry polymer. All IEC values reported in this work are the average of three titrations.

Films after conversion to the acid form were stored in deionized water for at least 24 h. The films were removed from the water, blotted dry to remove surface water, and quickly weighed to determine the wet mass of the film (W_{wet}). The films were then dried under P_2O_5 and full vacuum at room temperature for 24 h and weighed again to determine the dry mass of the film (W_{dry}). Water uptake was calculated by the following equation

$$Uptake = \left[\frac{W_{wet} - W_{dry}}{W_{dry}} \right] * 100\% \qquad \text{Equation 4.2}$$

The proton conductivity of films samples was measured by four probe electrochemical impedance spectroscopy (EIS) using a Solartron 1260 frequency response analyzer and a Solartron 1287 potentiostat. A schematic diagram of the membrane conductivity cell is shown in Figure 4.6. The outer electrodes are connected to the

1. Securing screws
2. Teflon blocks
3. Stainless steel electrodes
4. Equilibration windows
5. Membrane sample

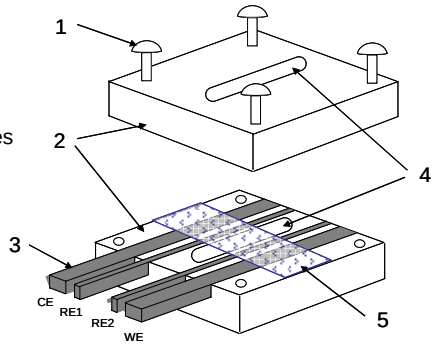

Figure 4.6: Schematic of 4-Point Membrane Proton Conductivity Cell

working and counter electrodes on the 1287 potentiostat, and the two inner electrodes are connected to the reference electrodes.

EIS was performed by imposing a small sinusoidal (AC signal) voltage, 10 mV, across the membrane sample at frequencies between 100 kHz and 100 Hz (scanning from high to low frequencies), and measuring the resultant current response. From the amplitude and phase lag of the current response, a complex number was computed which is called the impedance composed of a real component, Z', and an imaginary component, Z". An example of the raw data is shown in Figure 4.7. To compute the membrane proton conductivity from the complex impedance response, the low frequency impedance line is extrapolated to the x-axis. The extrapolated value of the real impedance where the imaginary response is zero (Z' at Z" = 0) is then taken as the resistance of the membrane and Equation 4.3 is used to compute the membrane proton conductivity,

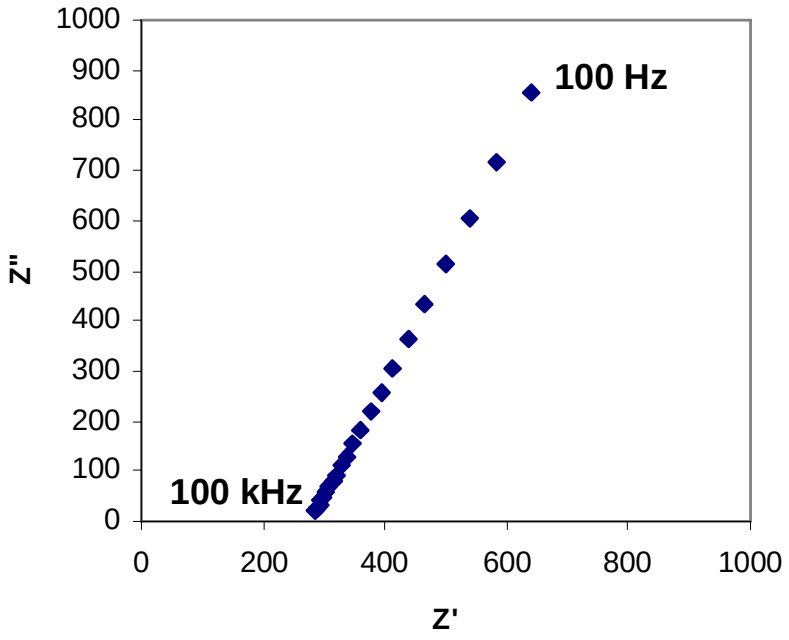

Figure 4.7: Impedance response of a typical proton conducting membrane between 100kHz and 100 Hz

$$\kappa = \frac{L}{Z'A} \qquad \text{Equation 4.3}$$

where L is the length between the sense electrodes, Z' is the real part of the impedance response (extrapolated to Z" = 0), and A is the area available for proton conduction (width x thickness). All proton conductivities reported here were measured with the film immersed in liquid water at 30C during the measurement time.

Density measurement data were based on Archimedes Principle utilizing a Mettler AJ100 analytical balance fitted with a Mettler ME-33360 density determination kit. The Archimedes principle is based on the fact that when a solid body is immersed in a liquid it displaces an equivalent mass of liquid. This displaced liquid mass is determined indirectly utilizing this kit, and allows one to calculate the density of the unknown sample based on the difference in its mass when measured in air and a liquid. Equation 4.4 gives the relationship between predicted density, sample mass, and liquid density. In this equation, the predicted density of the polymer film is represented by ρfilm, the masses of the films measured in air and liquid are m_{air} and m_{liquid}, and the density of the liquid is ρ_{liquid}. Octane was employed as the liquid medium and was chosen for these measurements because the polymers were not soluble in it, the solvent has a low surface energy that aided in wetting film samples, and the liquid has a low vapor pressure and negligible toxicity. Prior to making density measurements, films were dried for 24 hours at 120C in a vacuum. The reproducibility in measuring density based on this technique was found to be 0.5% or 0.004 g/ml.

$$\rho_{film} = \frac{m_{air}}{m_{air} - m_{liquid}} * \rho_{liquid} \qquad \text{Equation 4.4}$$

The densities of the SDAPP series were examined utilizing Archimedes Principle to study the role of density and increasing IEC. A linear relationship between increasing sulfonation level and density was observed for the SDAPP series, which is shown in shown in Figure 4.8.

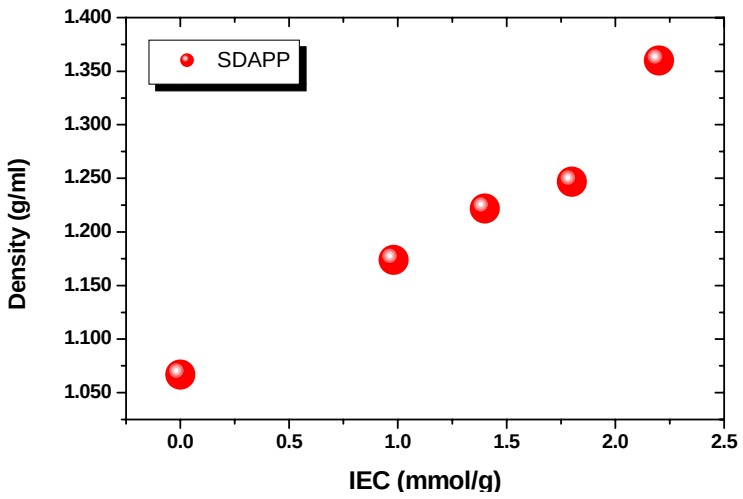

Figure 4.8: Density of SDAPP series as a function of increasing sulfonation level.

This linear increase in mass per unit volume or density with increasing sulfonic acid concentration or IEC was anticipated and could be used to assist

in the characterization of the IEC of these materials along with IR. Interestingly, the linear relationship between increasing acid concentration and conductivity that is observed for many acids is also observed for these SDAPP materials and additional work with other ionomers displaying this relationship may be useful in understanding the role of proton conductivity and IEC.

4.3 Hydrogen Fuel Cell

The hydrogen fuel cell performance of the SDAPP series of materials was investigated to evaluate its potential as a fuel cell membrane. In order to evaluate the potential of the SDAPP materials it was necessary to form a membrane electrode assembly (MEA). MEA's were formed based on standard ink hand painting techniques developed at Los Alamos National Laboratory. This process involves creating a colloidal suspension of Pt/Pt-Alloy catalyst in water, isopropanol, and Nafion 1100 solution. The final target composition was 10 wt% ionomer in the cathode and 15 wt% ionomer in the anode with the remaining component being the Pt/Pt-Alloy catalyst (HISPEC Pt/Ru black anode, HISPEC 1000 Pt black cathode). Electrodes were applied to the PEM by painting multiple layers of the catalyst ink suspension with a paintbrush to achieve the target catalyst loading. The final MEA is then assembled into a Fuel Cell technologies 5cm2 test cell and tested using ETEK LT-1400W 18 mil thick gas diffusion layers at the anode and cathodes. A 120A Fuel Cell technologies Test unit equipped with high frequency impedance was used to evaluate all samples. This test unit has the capability to measure the bulk proton conductivity of the PEM, follow changes in high frequency resistance (HFR) due to membrane dry out, electrode failure, and assess the role interfacial resistance due to pore adherence between the PEM and electrode composite. Future research efforts will be aimed at elucidating the role of the interface between the electrode and the PEM as it relates to performance and interfacial stability.

Figure 4.9 and Figure 4.10 examine the performance of the SDAPP series as a function of conductivity, at typical hydrogen fuel cell conditions, and finally at an elevated temperature and low relative humidity. Fuel cell operating conditions were 100C at 100% relative humidity with pure hydrogen and oxygen flowing at 500 SCCM with a backpressure of 20 psig on the cathode and anode.

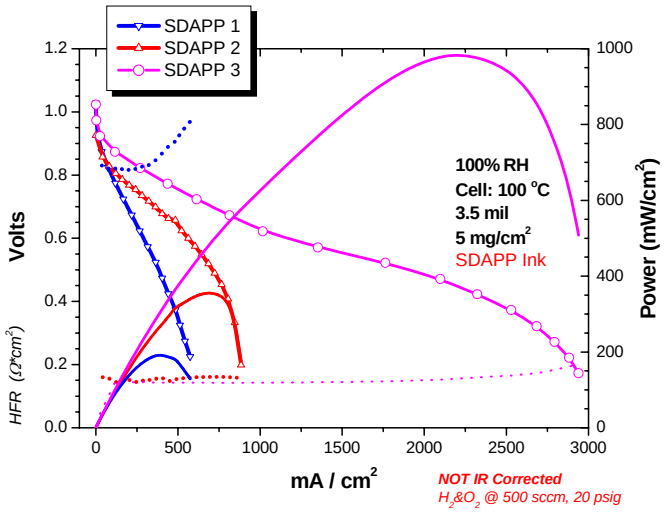

Figure 4.9: Increasing fuel cell performances with increasing SDAPP proton conductivity. Fuel cell conditions were 100 °C, 100 %RH, and 5mg/cm^2 of catalyst on each side of the PEM. Electrode ionomer ink was based upon SDAPP4.

Figure 4.9 shows the relationship of increasing conductivity of the SDAPP materials as it relates single cell fuel cell performance. As shown in this figure a large HFR (0.82 Ω*cm^2) is observed for SDAPP1 that quickly increases with increasing current density. This behavior is attributed to membrane dehydration due to electro-osmotic drag that also results in a loss in proton conductivity. Overall, this sample has an inadequate concentration of sulfonic acid groups necessary for good proton conductivity and fuel cell performance. Increasing the concentration of sulfonic acid groups from an IEC of 0.98 to 1.4 results in a dramatic increase in fuel cell

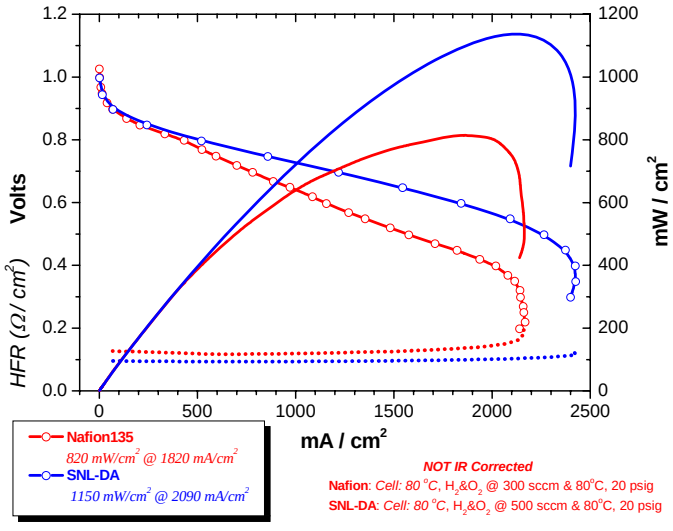

Figure 4.10: Fuel cell performance of SDAPP3 versus Nafion1135. Fuel cell conditions were 80 °C, 100 %RH, and 10mg/cm^2 of catalyst on each side of the PEM. Electrode ionomer ink was based upon Nafion1100 for both samples.

performance as demonstrated with SDAPP2 (350 mW/cm^2) versus SDAPP1 (175mW/cm^2). This increase in IEC also results in a significantly low HFR (0.15 Ω*cm^2) that is constant throughout the fuel cell test. This performance improvement is attributed to the increase in proton conductive carriers (sulfonic acid groups) and better electrode adherence to the PEM. Maximum fuel cell performance was observed for SDAPP4 that also had a low HFR throughout the test (0.15 Ω*cm^2). The power density of this sample reached 980 mW/cm^2 at 2900 mA/cm^2, which is 2.8 times greater than SDAPP2 and 5.6 times greater than SDAPP1. This dramatic improvement in fuel cell performance resulting from increasing the IEC from 0.98 to 1.8 appears to suggest a percolation effect with regard to performance. In fact the transition appears to be centered between an IEC of 1.4 and 1.8. While SDAPP4 was not tested, it is expected to result in further fuel cell power density improvements over SDAPP3. However, SDAPP4 increased fuel cell performance may not be attractive due to the tradeoff in increased swelling and future studies will evaluate this transition region as it relates to membrane mechanical integrity and fuel cell performance.

Figure 4.10 is a comparison of the SDAPP3 versus Nafion® 1135 of equivalent thickness (3.5mil) and identical catalyst loading (10mg/cm2), application technique, and Nafion® 1100 in the electrode. Fuel cell operating conditions were 80 C at 100% relative humidity with pure hydrogen and oxygen flowing at 300 SCCM for the Nafion sample and 500 SCCM the SDAPP3 sample with a backpressure of 20 psig on the cathode and anode for both samples. SDAPP3 was observed to be capable of achieving a higher current density than Nafion® 1135 (2100 mA/cm^2 versus 2400 mA/cm^2). Also observed for the SDAPP3 sample was a relatively low and constant HFR (0.10 Ω*cm^2) with increasing current density while in contrast to this behavior Nafion® 1135 had an increasing HFR with increasing current density. This decrease in proton conductivity with increasing current density for Nafion® 1135 is why its peak power is only 800mW/cm^2 versus 1100 mW/cm^2 observed for SDAPP3. Preliminary experiments measuring the electro-osmotic drag of SDAPP3 revealed that this sample has a lower electro-osmotic drag than Nafion® (1.5 versus 3.0), but further studies need to be carried out in this area. However, a lower electro-osmotic drag would explain the observations

made in this polarization curve regarding the different responses in HFR response of both samples.

The high temperature performance of SDAPP3 was evaluated versus Nafion® 112 to test is potential as a high temperature fuel cell membrane. The film thickness of SDAPP3 and Nafion® 112 were 3 mil and 2 mil respectively as measured in the dry state for both samples. A catalyst loading of 0.4 mg/cm2 was applied to both the anode and cathode by hand painting as previously described utilizing DeNora 20 wt% Pt on XC-72 for both the anode and cathode electrodes. Fuel cell operating conditions were 120C at 50% relative humidity with pure hydrogen flowing at 250 SCCM and air flowing at 500 SCCM throughout the test. The SDAPP MEA had an ether version of SDAPP in the electrode while Nafion1100 was used with the Nafion112 MEA. The results of this study are shown in Figure 4.11 and show that the performance of SDAPP3 is promising when compared to Nafion®, which is also thinner than the SDAPP3 MEA sample. Even though the Nafion® sample is 50% thinner than the SDAPP3 MEA, which should result in better performance at higher currents, the thicker SDAPP3 sample still out performed the Nafion® 112 MEA. While this result shows promise for the SDAPP materials, significant work needs to be completed to optimize the electrode structure and evaluate the role of thickness on the fuel cell performance at these very challenging fuel cell conditions. Based upon these results further work is warranted examining the potential of these materials as a replacement for Nafion.

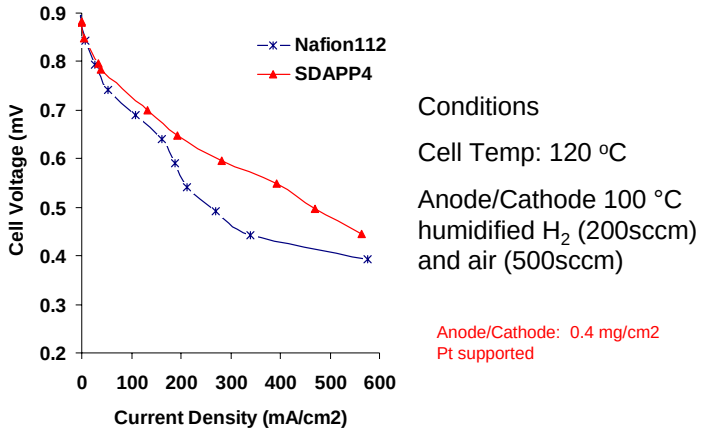

Figure 4.11: Fuel cell performance of SDAPP3 versus Nafion112. Fuel cell conditions were 120 °C, 50 %RH, and 0.4mg/cm^2 of catalyst on each side of the PEM.

4.4 Methanol Fuel Cell

One goal of this research program was to minimize fuel crossover, which causes a mixed potential at the cathode and an overall reduction in achievable fuel cell performance. In order to evaluate the potential of the SDAPP for reducing fuel crossover, the methanol fuel cell performance of the SDAPP series was tested. MEAs were formed based on standard ink hand painting techniques as previously described. The final target composition was 10 wt% ionomer in the cathode and 15 wt% ionomer in the anode with the remaining component being the Pt/Pt-Alloy catalyst (HISPEC Pt/Ru black anode, HISPEC 1000 Pt black cathode, and Nafion® 1100 electrodes). The final MEA is then assembled into a Fuel Cell technology's 5cm^2 test cell and tested using ETEK LT-1400W 18 mil thick gas diffusion layers at the anode and cathode, and tested with a 120A Fuel Cell technologies Test unit. Fuel cell operating conditions were 80C at 100% relative humidity with 0.5M methanol flowing at 2.0 mL/min at the anode and air flowing at 100 SCCM with no backpressure for all samples tested.

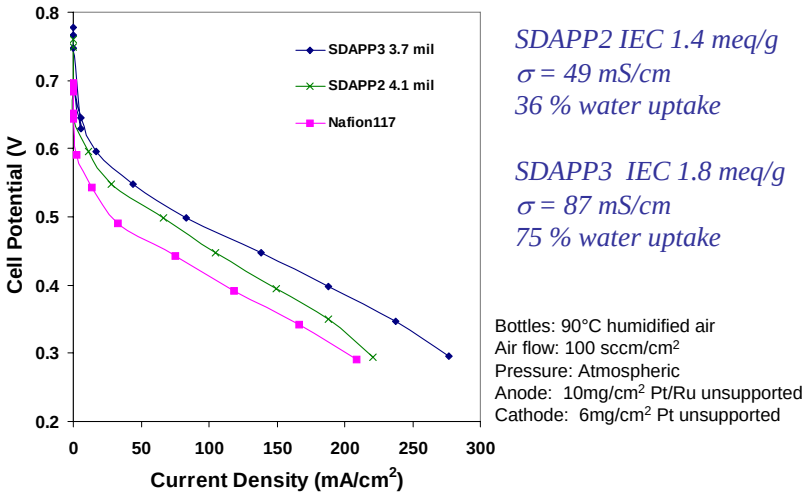

Figure 4.12: Performance of MEAs based upon SDAPP2 and SDAPP3 with thickness of 4.1 mil and 3.7 mil compared to Nafion117 (7 mil thickness).

Figure 4.12 shows the performance of MEAs based upon SDAPP2 and SDAPP3 with thickness of 4.1 mil and 3.7 mil compared to Nafion117 (7 mil thickness). While the SDAPP series are 70% thinner than Nafion® 117, they still had better performance due to lower methanol crossover. This low crossover characteristic of the SDAPP materials would translate to lower glucose crossover and the benefits of a lower glucose crossover resistant membrane would need to be evaluated versus Nafion® . Further work is necessary on electrode tailoring for direct methanol fuel cells (DMFC) in order to

optimize the electrode structure with the new material. If the SDAPP materials were used in glucose fuel cells an electrode optimization would also need to be performed to minimize mass transport losses and increase fuel cell performance.

4.5 1000 Hour DMFC Life Test with SDAPP Membrane

A life test was conducted on an SDAPP2 (IEC = 1.4 meq/g, κ = 0.05 S/cm, $DH_{glucose}$ = $1.3*10^{-8}$ cm^2/s, DH_{CH3OH} = $7.1*10^{-7}$ cm^2/s) membrane for 1000 hours under standard direct methanol fuel cell (DMFC) conditions. The test was performed to evaluate the longevity of the SDAPP membrane in a fuel cell application. Periodically, the potentiostatic life test was stopped to run diagnostic measurements to assess the performance of membrane and the electrodes. A 5 cm^2 membrane electrode assembly (MEA) was fabricated with a 3.7 mil (1 mil = 0.001 inches) thick (when wet) SDAPP2 membrane.

The composition of the MEA was: SDAPP2, 3.7 mil wet thickness, HISPEC Pt/Ru black anode, HISPEC 1000 Pt black cathode, ETEK LT-1400W 18 mil thick gas diffusion layer on anode and cathode. The electrodes where handpainted onto the MEA at 60C with standard compositions;14 weight % Nafion® in the anode and 10 weight % Nafion® in the cathode.

The MEA was placed in a standard Fuel Cell Technologies 5cm^2 set of single-cell hardware with the ETEK gas diffusion layers and 8.5 mil Furon (Fiberglass reinforced Teflon) gaskets. The cell was torqued to 75 in-lb on all 8 bolts. The conditions for the life test were as follows:

potentiostatic at 0.5V

80C cell temperature

2 mL/min. 0.5M CH_3OH feed at ambient pressure – not preheated

500 standard cc/min. (sccm) air humidified to a dewpoint of 80C at ambient pressure

At each time interval the tests performed were:

polarization curve with CH_3OH

crossover current to gauge membrane health and resistance to methanol crossover

anode polarization to asses the anode's activity towards methanol

hydrogen air polarization curve to measure the cathode activity

The current density measured over the 1000 hour time period is shown in Figure 4.13.

From the figure, the cell began the test producing approximately 55 mA/cm^2 and decayed to around 10 mA/cm^2 at just less than 1000 hours. The current density does increase after the diagnostic tests are performed which is indicated by the periodic jumps in Figure 4.13. The stretch of 90 hours at 40 mA/cm^2 beginning at roughly time = 600 hours was due to a slight backpressure in the cathode compartment which artificially increased the current density. When this problem was corrected, the current density immediately dropped.

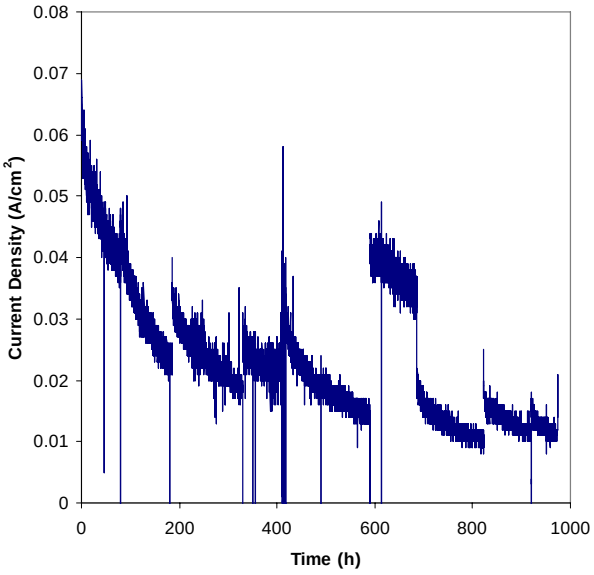

Figure 4.13: Current density as a function of time for CH_3OH 1000 hour life test.

Two modes of DMFC electrode degradation have been proposed, a short-term degradation that is thought to be related to the catalyst surface (oxidation) and a long-

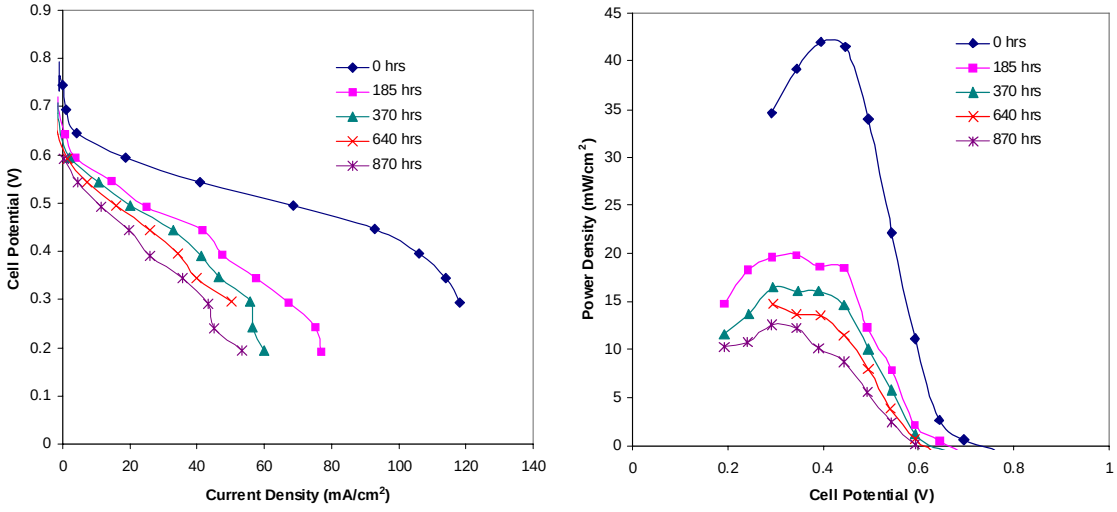

Figure 4.14: DMFC performance at various times throughout the life test. shows the methanol polarization curves and cell power at various times throughout the life test.

term degradation that is related to ruthenium loss from the anode and slow erosion of the ionomer (recast Nafion) in the electrode. The short-term degradation is recoverable and engineering design of the system with voltage pulsing or air break can mitigate this loss. Long-term degradation is a poorly understood phenomenon, but in future work we propose to use a methanol resistant polymer (SDAPP) in the electrode to lessen this erosion. While electrodes were not a deliverable on the membrane task for this project, we will continue to explore this problem.

Figure 4.14 shows the methanol polarization and cell power density curves at various times throughout the life test. The degradation of performance was quite pronounced during the initial 185 hours of the test, and slowed as time progressed. The other diagnostic information is presented in Table 4.3.

Time (h)	HFR (Ω-cm^2)	I_x (mA/cm^2)	I @ 0.8V H_2/Air	I_{AP} @ 0.35V
0	0.04	44	89	127
185	0.04	48	n/a	85
370	0.04	46	n/a	73
640	0.04	50	44	21
870	0.04	48	44	18
980	0.04	57	38	15

Table 4.3: information at various times throughout the life test.

HFR = high requency resistance measured at 5 kHz by electrochemical impedance
I_x = methanol crossover current at open circuit
I @ 0.8V H_2/Air = current produced by cell at 0.8V under hydrogen air conditions – indicates activity of cathode
I_{AP} @ 0.35V = anode polarization current at 0.35V – measure of the anode's ability to consume methanol

The high frequency resistance and methanol crossover current stayed relatively constant over the course of the test. The experimental error on the methanol crossover is estimated to be +/- 3 mA/cm^2. The data shows that there was a slight increase in the methanol crossover, especially between 870 and 980 hours, and this could be an indication of membrane weakening or thinning, but the crossover increase is not substantial enough to cause additional performance losses. The large performance losses occurred due to the electrodes. The activity of the cathode dropped from 89 mA/cm^2 to 38 mA/cm^2 under hydrogen/air conditions and the activity of the anode was reduced by almost a factor of 10. Both engineering controls and redesign of the electrodes with methanol resistant ion conducting polymer binders can help to decrease these losses.

The SDAPP polymers will need to be optimized for use in hydrogen/air fuel cells and will require a 1000 hour test with the optimized MEA. It is anticipated that the hydrogen/air test will be performed with an SDAPP membrane and SDAPP-based electrodes. The current DMFC test also demonstrates the need for new electrodes for DMFCs. Electrode performance degradation is a key concern for commercial deployment of these types of fuel cells.

4.6 Thermal Stability

Thermal gravimetric analysis of SDAPP0 under nitrogen revealed a 5 % weight loss occurring at 660C. SDAPP in the acid form displayed a three-stage weight loss pattern (Figure 4.15). Although the sulfonated polymers were dried at 110C for 30 min. immediately prior to the analyses, the samples showed an initial weight loss between 0.5 – 1.0 % due to the loss of water. As the sulfonation level increased from 0.98 to 2.2meq/g, the second decomposition temperature (at 5% weight loss) decreased from 442 to 363C. SDAPP2 lost 13.6 % of its mass (after absorbed water loss), which is close to the theoretical value of 11.2 % after SO_3 cleavage. These results suggest the second weight loss (after water loss) in SDAPP is attributed to the loss of sulfonic acid groups, which typically range from 285 - 426C in highly phenylated arylene-sulfonic polymers, while the third transition was associated with backbone degradation.[39] Overall, the high thermal stability of these sulfonated poly(phenylene)s is an attractive PEM trait.

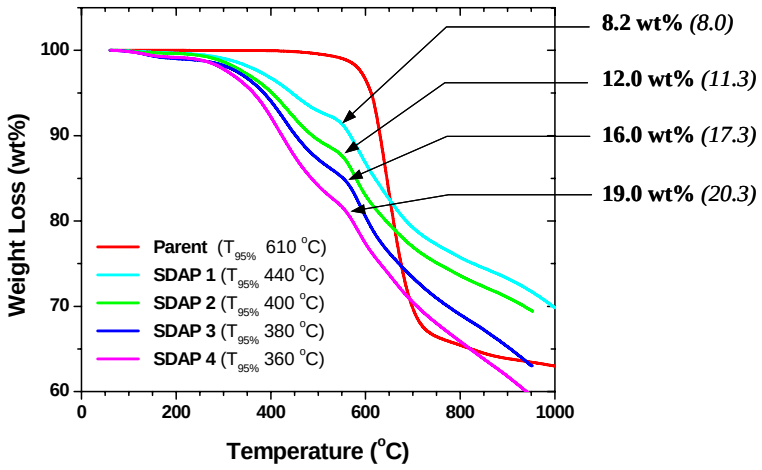

Figure 4.15: Thermogravimetric evaluation of SDAPP series including theoretical and experimental observations of complete loss of sulfonic acid groups.

Differential scanning calorimetry was used to determine the glass transitions temperature (T_g) of SDAPP0 and the sulfonated SDAPP samples. High T_g PEM

materials are desirable in high temperature fuel cell applications since maintaining good mechanical properties requires the glass transitional temperature to be higher than the operating temperature. In addition, hydrated ionomeric membranes have reduced T_g since water acts as a plasticizer, further reducing the operational fuel cell temperature range of the membrane.[40] The unsulfonated polymer SDAPP0 had a high T_g occurring at 388C, indicating a very stiff backbone due to the large pendent groups (aryl) and rigid rod backbone. Although the high T_g of the material was desirable, the structure-property relationship between high degree of chain stiffness as it relates to proton conductivity and water uptake was of interest.

Since sulfonic acid groups increase the steric congestion of a polymer backbone and can interact via hydrogen bonding, the T_g of sulfonated polymers are greater than their non-sulfonated analogs.[39] Unfortunately the thermal decomposition of the sulfonic acid group occurred below the T_g of all sulfonated SDAPP0 polyelectrolytes, which prohibited the measurement of the T_g of these samples by by DSC or dynamic mechanical analysis (DMA).

Dynamic Mechanical Thermal Analysis (DMTA) spectroscopy was used to characterize the T_g and molecular transitions in the polyimides with a Rheometric Scientific Mark IV DMTA. Experimental runs were completed on film samples having a length of 15mm, a width of 4mm, and a nominal thickness of 0.07mm. The run conditions were conducted with a strain of 0.01%, a constant static force of 0.015N, and a heating rate of 2C per minute in air. The low strain and force were chosen in order to ensure a linear viscoelastic response (stress proportional to strain) during an experimental run. Furthermore, the sample dimensions

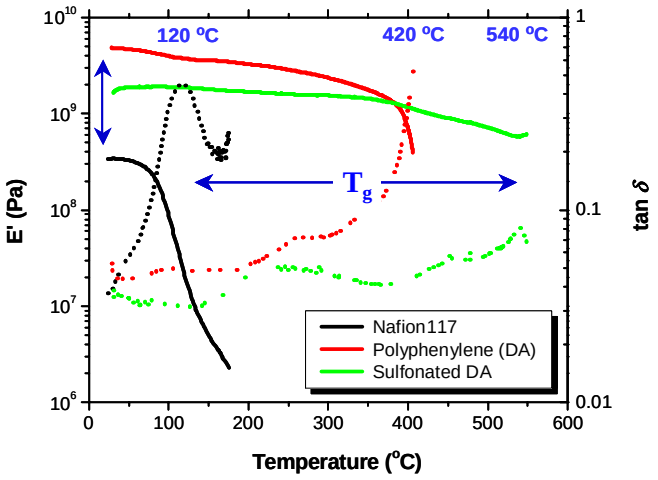

Figure 4.16: Dynamic mechanical thermal analysis for SDAPP0 (Polyphenylene), SDAPP3 (Sulfonated DA), and Nafion 117 showing changes in E' and tanδ.

were set to exceed a length to width ratio of three to minimize sample edge effects during a DMTA test. Because all the samples elongated various degrees during a test, the data reported from this instrument was only from the first heating run. The reproducibility in measuring the T_g was found to be 0.2% or 0.5C for the results discussed in the following section.

The T_g and storage modulus (E') for SDAPP0, SDAPP3 and Nafion® 117 are summarized in Figure 4.16. A T_g of 420C was observed for SDAPP0 and a T_g of 520C was observed for SDAPP3, but no further measurements were made because of the changing nature of the sulfonated series with increasing temperature precluded them from being able to have their T_g measured by this technique and in the protonated state. Furthermore, completely dry Nafion has been reported by others to have a T_g near 150C as determined by differential scanning calorimetry (DSC). The lower T_g is attributed to water plastization that will reduce the T_g of Nafion to c.a. 100C when it is completely hydrated. Further work needs to be completed in the area of hydrogen bonding and plastization of these SDAPP materials to determine the amount of water remaining in its structure and its impact on conductivity.

4.7 Water Uptake and Proton Conductivity

Electrochemical Impedance Spectroscopy (EIS) was used to collect proton conductivity data for these materials. The instrument and settings used to collect the data were a PAR 273A potentiostat and Schlumberger 1255 High Frequency Analyzer with Z-plot software measuring over a frequency range of 100 kHz to 0.1 Hz at 0V versus an open circuit and 10mV amplitude. A series of Nyquist plots were generated based upon this experimental setup represented by real (Z') and imaginary resistance (Z") in Ohms. The intercept of the x-axis of the imaginary Z" with the real Z' in conjunction with the film thickness and electrode area is used to determine the proton conductivity of PEM materials. Measurements were preformed on PEM samples that were allowed to swell and equilibrate in deionized water at 25C. Proton conductivity was determined from these samples by quickly removing the swollen films from the water and measuring their resistance. The following proton conductivity results are based upon this experimental approach, and thin films having a nominal thickness of 2.5mil or 63.5μm.

Recently, it has been suggested that the temperature (either room temperature or 100 C) used in acid pre-treating films influences the ionic domain microstructure of sulfonated polymers.[41] Sulfonated poly(arylene ether sulfone) copolymer membranes acidified at elevated temperatures were found to imbibe more water and have higher proton conductivities than membranes acidified at room temperature. Since fuel cells typically operate above room temperature all films in this work were pretreated at 100C.

Sample	IEC (meq/g)	Water uptake (weight %)	λ (H_2O/SO_3H)	Conductivity (mS/cm)
SDAPP1	0.98	21	12	13
SDAPP2	1.4	36	14	49
SDAPP3	1.6	75	19	87
SDAPP4	2.2	137	30	123

Table 4.4: Influence of ion exchange capacity for SDAPP samples on water uptake and proton conductivity

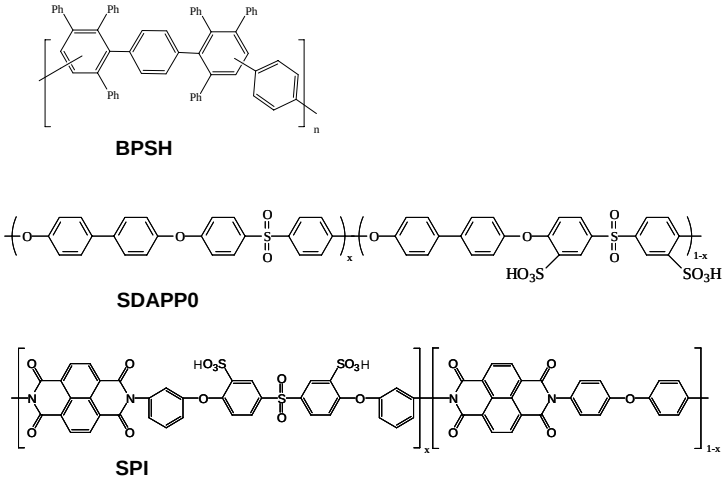

Figure 4.17: Chemical structures of SDAPP, BPSH and SPI

Table 4.4 shows the water uptake and proton conductivity of the SDAPP samples. In order to ascertain structure-property relationships, the SDAPP polymers were compared to other aromatic sulfonated polymers such as BPSH and sulfonated polyimide (SPI), whose structures are presented in Figure 4.17. A plot comparing water uptake versus IEC of SDAPP, BPSH, and SPI.24 is displayed Figure 4.18.[42 43 44] BPSH was used as a reference experimental proton exchange membrane because it has been widely studied, while SPI represented an example of a rigid rod type backbone, similar to SDAPP. The SDAPP water uptake increased linearly from 21% to 75% as the IEC increased from 0.98 to 1.8 meq/g, respectively. As the IEC was further increased to 2.2 meq/g, water uptake

increased markedly to 136 %, indicating that the sulfonic acid domains may have begun to form a co-continuous morphology between IECs of 1.8 to 2.2 meq/g. Wang et al., using tapping mode AFM, provided evidence of this co-continuous morphology of the sulfonic acid containing domains in the BPSH series of polymers.[27] We believe that this same phenomenon may be occurring in the SDAPP series of polymers and attempts are underway to image the domain structure of these polymers.

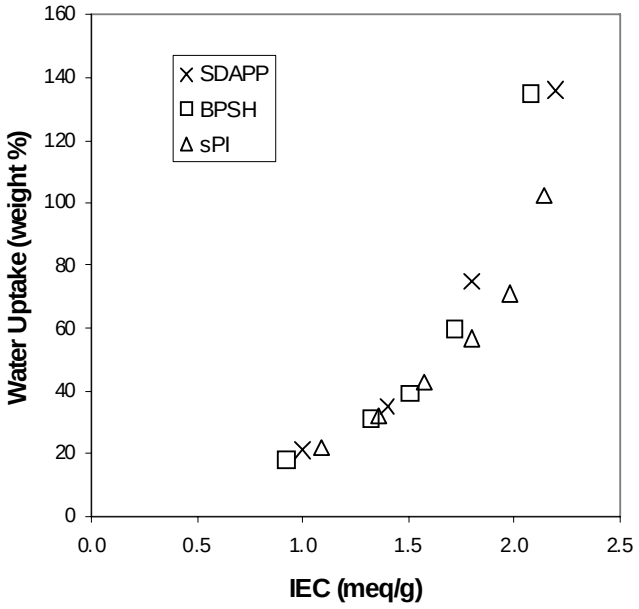

Figure 4.18: Water Uptake versus IEC for SDAPP, BSPH and SPI

In Figure 4.19, proton conductivity of SDAPP when fully immersed in liquid water at 30C increased with IEC from 13 mS/cm (1 meq/g) to 123 mS/cm (2.2 meq/g). The proton conductivity of BPSH and the sulfonated polyimide polymer increased in a linear fashion with IEC. At similar IEC, the BPSH and SPI polymer showed slightly higher proton conductivities than the SDAPP. This may be due to the nature of the polymer backbone, the concentration density of ionic groups within the polymer, and how the water is bound within its

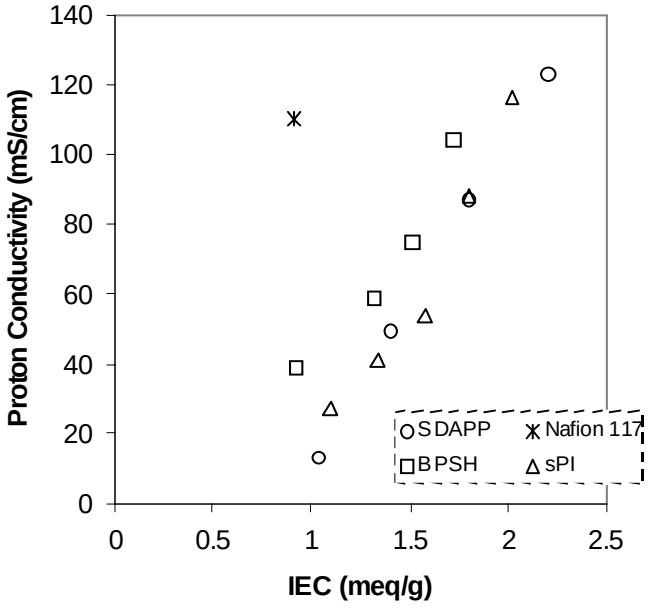

Figure 4.19: Proton Conductivity versus IEC for SDAPP, BSPH and SPI

microstructure.

Hickner proposed that polymers with stiffer backbones will have lower conductivities due to the inability for the ionic groups to fully phase separate and form concentrated ionic domains thus causing the absorbed water to be more bound in the polymer microstructure.[44] The similar responses of changing proton conductivity and water uptake with IEC for these series polymers appear to conform to the hypothesis of a stiff

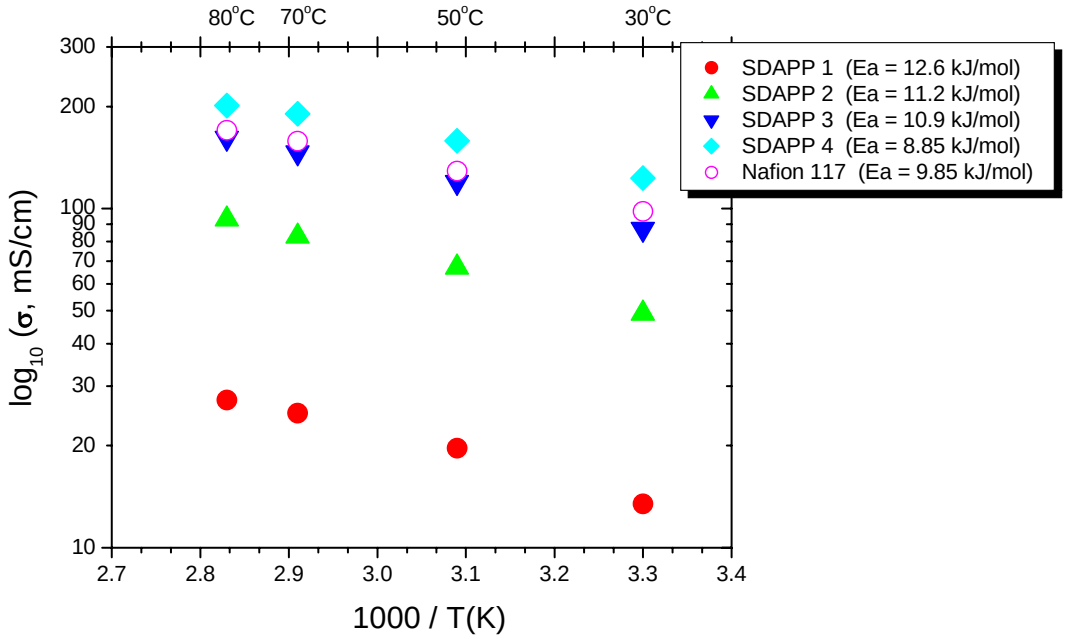

Figure 4.20: Relationship between proton conductivity, temperature, and activation energy of SDAPP series versus Nafion117 in deionized water from 30°C to 80°C.

polymer backbone. The overall proton conductivity of the SDAPP series is plotted in Figure 4.20 versus Nafion® 117 as a function of temperature. The results from this study show that it is possible to lower both the activation energy for proton conduction compared to Nafion® , but it is also possible to exceed the proton conductivity of Nafion as demonstrated with SDAPP4.

Interestingly, even though the SDAPP polymers have very stiff backbone which result in high T_g materials, the membrane properties of this class of polymer is comparable to the water uptake and proton conductivity of other types of sulfonated aromatic polymers such as BPSH. BPSH reaches its percolation limit at a lower IEC and has higher proton conductivity than SDAPP at comparable IECs. This could be attributed to the

concentration density of ionic groups within the polymer and the stiffness of the backbone. Other factors for these differences may stem from a variety of reasons such as sulfonation (post vs. monomer), position of sulfonic acid (pendent group vs. backbone), and repeat group (phenylene vs. either-sulfone).[45] This class of polymer affords attractive proton conductivities with relatively low water uptakes.

In order to increase our understanding of the performance of the SDAPP materials as it relates to fuel cell performance wide angle x-ray scattering (WAXS), small angle x-ray scattering (SAXS) and small angle neutron scattering (SANS) were completed in collaboration with Clemson University. Because of the repeat unit of the SDAPP polymer it is expected to display rigid rod behavior due to the backbone of the polymer (no flexible linkages). Understanding some of the structural aspects of this polymer is

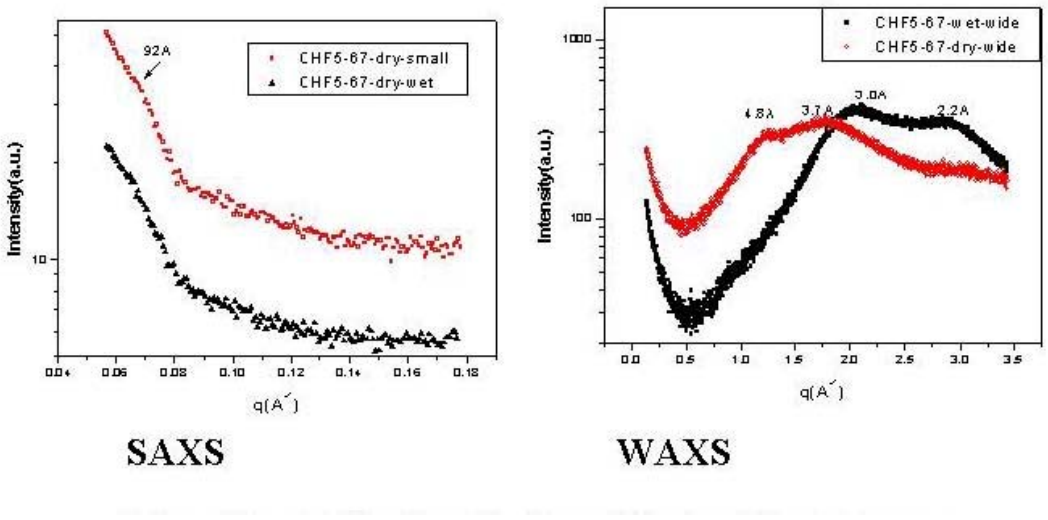

Figure 4.21: Small and wide-angle X-ray scattering of SDAPP1. Measurements have been carried out at room temperature on a Sintag Θ−Θ geometry.

important to realizing its potential and also understanding its limitations.

Studies were carried out on SDAPP with IEC capacity ranging from 1 to 2.4, which corresponds to sulfonation levels from 10% to 55%. Neutron and x-ray scattering have investigated the structure of the SDAPP membranes with different sulfonation levels. Combination of both techniques allows probing of multi length scales from angstroms to nanometers. Further information has been obtained from atomic force microscopy. Shown in Figure 4.21 are representative x-ray patterns of dry and water-swollen membranes. The dry film appears to be amorphous, which is consistent with literature

and our measurements of the parent SDAPP0 with DSC and DMTA. Three broad lines are resolved at average distances of 3.0Å. and 2.2Å. A weak shoulder is observed at 5.0Å. The 3.0 Å. and 2.2Å lines are consistent with intra molecular dimensions. As the membrane swells with D_2O, three lines at 4.8, 3.7 Å appear. The line at 2.2 Å becomes less visible as hydration takes place. Adding water allows stacking of some of the aromatic parts. A 3.8 Å line often corresponds to π–π distance of hinderance for aromatic rings. No clear periodicities have been detected at the SAX regime.

On a very large length scale: the use of Guinier Approximation in this system

$$I(q) \propto \exp(-q^2 R_g^2 / 3)$$

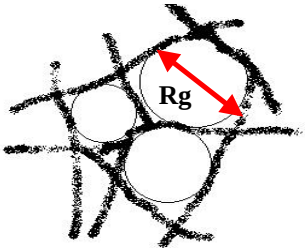

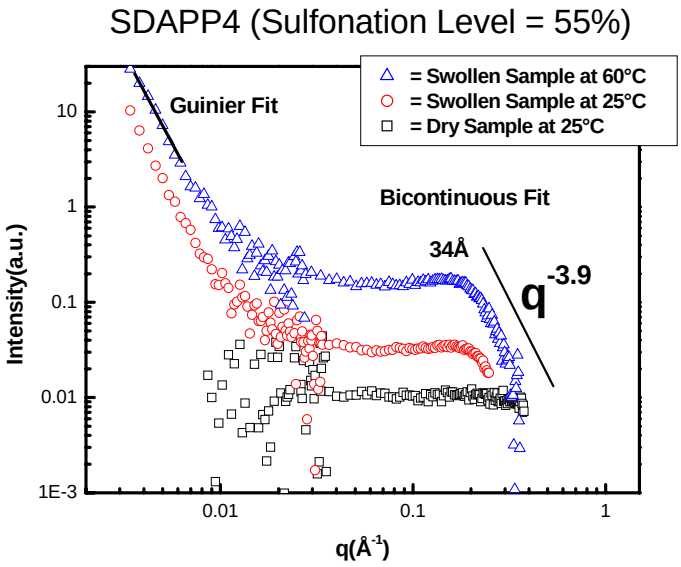

Figure 4.22: Small angle neutron patterns of a 55 % sulfonated PP membrane dry and swollen at the indicated temperatures, shown on right. The solid line at low q corresponds to a Guinier fit and the line at high q to a bicontinuous model. Outline of Guinier approximation, shown on left.

Probing the nanometer dimension by SANS data covers dimensions of 2-250 nm directly and extrapolation can be made to larger dimensions. These are the dimensions that correspond to the ionic peak and the matrix signature in Nafion®. Figure 4.22 is the SANS data for SDAPP4 (55% sulfonated) both in the dry state and water-swollen states at room temperature and elevated temperatures. In contrast to Nafion®, the dry film does not exhibit any signal at the measured range of 53Å as observed in Nafion®. The lack of signal is indicative of a different structure in the dry membrane of SDAPP polymers as compared to Nafion®. Since the backbone of this polymer is much stiffer than the backbone on a perfluorinated hydrocarbon, the chains cannot fold to allow the formation

of ionic clusters or well defined hydrophilic and hydrophobic parts in the dry state, which accounts for the inability to observe an ionic peak in the dry state.

However, when the samples are allowed to soak in D^2O at 25C for an hour, a signal develops at low q. In parallel, a peak develops at ~34 Å. The signal at low q is attributed to a sparse network. A Guinier approximation introduced in Figure 4.22 has been used to analyze this regime. The network is described by a series of balls that define the mesh size. The peak at 34 Å has been fit to a bicontinuous model listed below.

$$S(q) = \frac{kT}{a_2 + c_1 q^2 + c_2 q^4}$$

$$d = 2\pi\left[\frac{1}{2}\left(\frac{a_2}{c_2}\right)^{\frac{1}{2}} - \frac{c_1}{4c_2}\right]^{-\frac{1}{2}} \qquad \zeta = \left[\frac{1}{2}\left(\frac{a_2}{c_2}\right)^{\frac{1}{2}} - \frac{c_1}{4c_2}\right]^{-\frac{1}{2}}$$

Equation 4.5

The specific structure within this network is still under study. Water swollen Nafion exhibits a bicontinuous network of hydrophilic and hydrophobic domains. In the present system, the chemical structure results in a much more rigid framework.

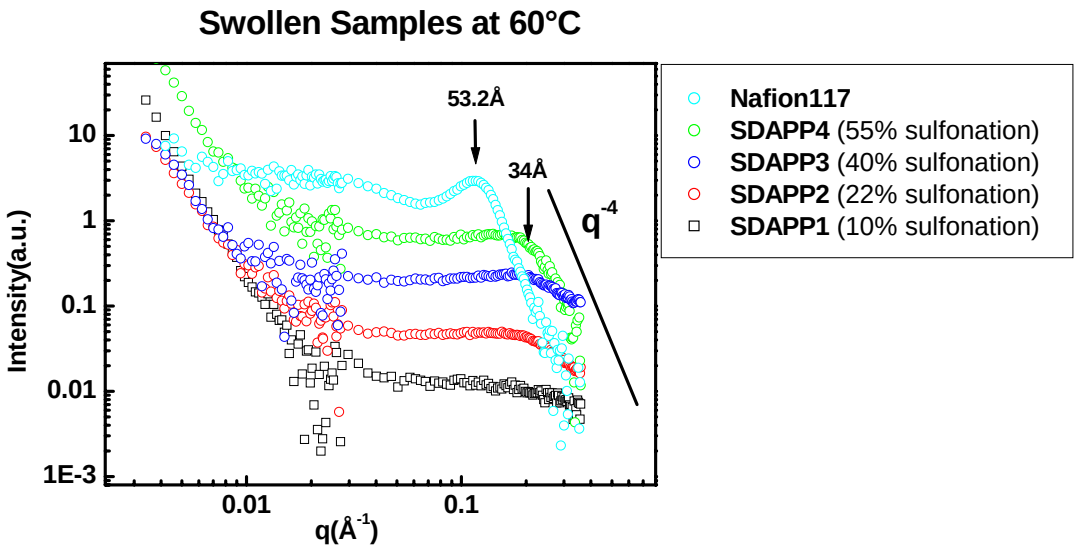

Figure 4.23: SANS data for water swollen SDAPP membrane at 60 oC at the indicated sulfonation levels. SANS pattern of Nafion under the same conditions are shown for comparison.

While the signal at low angle is only slightly dependent on ionic strength, the peak at 34Å becomes more pronounced as the ionic strength of the polymer increases, as shown in Figure 4.23. Also, with increasing ionic strength, the slope of the I(q) at high q

approaches more the q^{-4}. This is an indication that with increasing ionic strength the interface between the solvent and the polymer becomes more defined and the slope of –4 suggests that the SDAPP becomes bicontinuous systems at higher sulfonation levels. In contrast to the large ionic cluster of 53Å observed for Nafion, the smaller 34Å ionic cluster associated with the SDAPP series may account for the lower crossover characteristics as compared to Nafion. Further studies need to be completed to understand the role of decreasing ionic domain size as it relates to transport phenomena and fuel cell performance.

4.8 Glucose and Methanol Transport and Fuel Cell Performance

The challenge of the membrane task was to create an alternative PEM material that had the same conductivity as Nafion, but lower glucose crossover. The problem of glucose crossover is summarized in Figure 4.24. This is an idealized case of glucose crossover where the membrane is challenged with a fuel compartment containing 1 M glucose at ambient conditions. It is apparent from this problem that a significant amount of glucose accumulates at the cathode side of the fuel cell and the rate of accumulation will increase with increasing temperature. However, it should be noted that the MEA electrode can be altered to minimize this effect and work previously reported has led to the development of a novel method for consuming glucose at the cathode by shorting the fuel cell (see section 3.9). Fundamentally, the catalyst can consume fuel that permeates from the anode to the cathode when the fuel cell is shorted because oxygen and fuel (glucose) are both present at the cathode. This technique is possible due to the slow permeation rate of glucose through Nafion®, and it should be noted that this was not known at the beginning of this research program. Because methanol has a very high permeability rate through

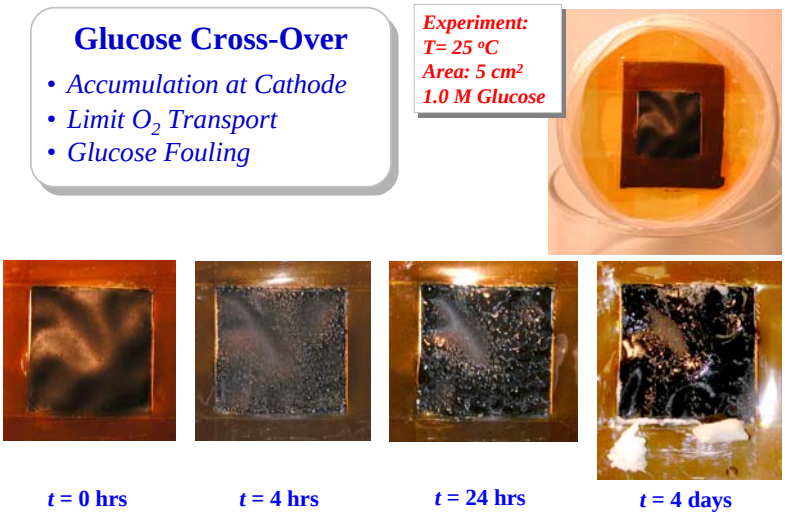

Figure 4.24: Glucose crossover in Nafion117 as a function of time at ambient conditions with 1 *M* glucose.

Nafion®, applying this technique is probably not practical. If glucose crossover exceeds the rate of the cathode being able to consume it or glucose decomposition products at the cathode become significant, then there exists the potential of cathode fouling, which would limit oxygen diffusion to the catalyst site and may even foul flow channels if the decomposition products become significant. This potential problem is a major research motivation for developing membrane materials that can minimize or eliminate glucose crossover.

In order to further understand the impact of fuel crossover in fuel cells both glucose and methanol were used to challenge SDAPP3 and Nafion117 at a concentration of 1 M glucose and methanol at 25C and 60C. The results from this study are summarized in

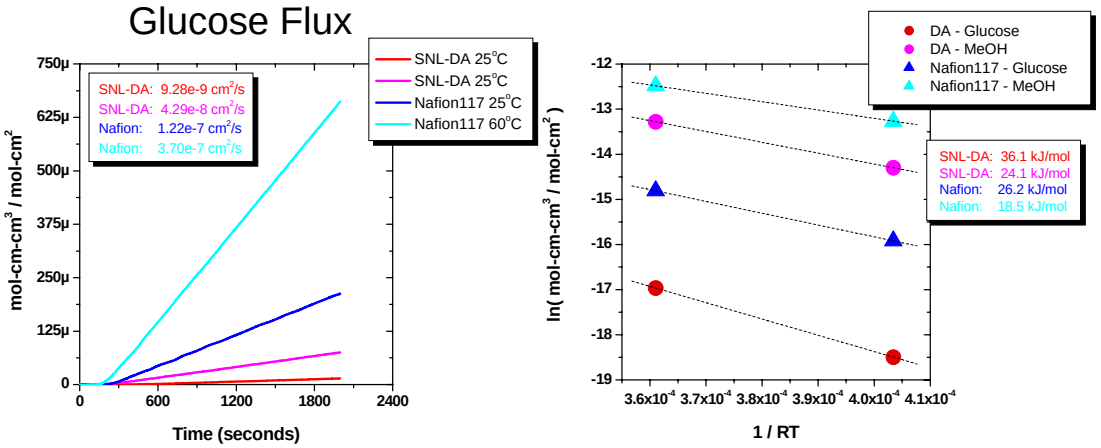

Figure 4.25: Glucose crossover in Nafion117 as a function of time at ambient conditions with 1 *M* glucose. Red symbols and lines correspond to SDAPP3 and glucose, magenta lines and symbols correspond to SDAPP3 and methanol, blue lines and symbols correspond to Nafion117 and glucose, and cyan lines and symbols correspond to Nafion117 and methanol.

Figure 4.25 which shows that methanol is much more permeable than glucose and Nafion® has significantly higher permeation rates for both methanol and glucose. It was observed during these studies that Nafion® increased in both methanol and glucose flux much more significantly than SDAPP3. Nafion117 had much higher activation energy and permeability for glucose and methanol than SDAPP3. The activation energy and permeability for Nafion 117 for 1.0 M glucose was 26.2 kJ/mol and $3.70e^{-7}$ cm^2/s at 60C while SDAPP3 was 36.1 kJ/mol and $4.29e^{-8}$ cm^2/s at 60C. Examining these same values for the much more challenging 1.0 M methanol resulted in an activation energy and permeability for Nafion 117 of 18.5 kJ/mol and $1.80e^{-7}$ cm^2/s at 60C while SDAPP3 was

24.2 kJ/mol and 1.30e^{-8} cm^2/s at 60C. Overall, the results of this initial study show that the SDAPP materials is capable of reducing methanol and glucose crossover as well as being less temperature sensitive to the kinetically activated process. The implication of the lower crossover resistant SDAPP membrane is that a much thinner film can be utilized while not suffering from significant increases in fuel crossover that will occur with thinner films.

Figure 4.26 shows the fuel cell performance of SDAPP3 versus Nafion117. While the results show that the SDAPP material has better fuel cell performance these results must be tempered with the fact that the electrodes are not identical and the impact on the observed fuel cell performance cannot be completely explained by the utilization of the SDAPP material. Future work should be done in this area to understand the performance increases, if any, that are obtained by utilizing a much higher fuel crossover resistant membrane.

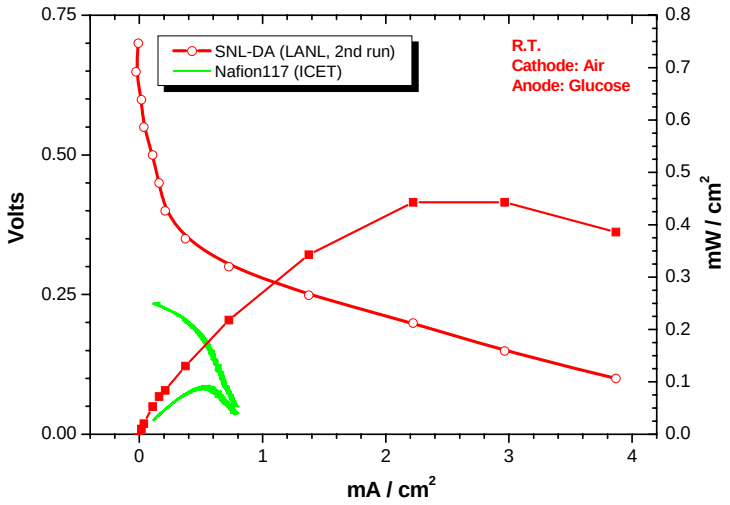

Figure 4.26: Glucose crossover in Nafion117 as a function of time at ambient conditions with 1 *M* glucose.

In conclusion, the poly(phenylene)s synthesized via Diels-Alder condensation resulted in polyelectrolytes that could be post sulfonated in a controllable manner with chrolosulfonic acid. The aryl backbone resulted in a tough rigid-rod material, indicated by its high T_g and inherently high thermochemical stability. This type of high glass transitional temperature material possesses physical properties that are attractive in high temperature fuel cell applications. In addition, the backbone stiffness does not negatively affect membrane properties such as water uptake (21 to 137%) and proton conductivity (13 to 123 mS/cm) with IEC that are typically employed with sulfonated aromatic

polymers (0.98 to 2.2 meq/g). The resultant polymers could be solution cast into robust, creaseable films and displayed properties that suggested this class of sulfonated polymer is a potential candidate for hydrogen and methanol fuel cell applications. Strategies to enhance their conductivity especially under partially dry conditions are being explored.

While the development of a new membrane to reduce crossover and increase proton conductivity improves the lifetime of the cell by limiting the reactions which rob the fuel cell of power, it is the catalyst layers themselves that are predominant in generating power in the first place. It was shown in Section 3 that severe limitations on the power and lifetime of a glucose cell comes from poisoning of the anode catalyst layers. Improvements in these catalyst layers thus become of primary importance for allowing higher powers and longer life. There are two methods to improve on the catalyst layers. In Section 5 improvements on metal catalysts that are more resistant to poisoning are discussed. In section 5.4, another concept is introduced; that of using enzymes themselves as catalysts for glucose oxidation. This method requires mediation of the electrons, and discussions in this section as well as in section 6 discuss the issues surrounding using an enzyme as a catalyst for oxidation of glucose.

5. Electrocatalyst Development

Key aspects of the fuel cell are the electrocatalysts and membrane electrode assemblies (MEAs) prepared from them. Because of their critical nature for the development of a direct glucose fuel cell, two parallel approaches to catalyst development were proposed at the outset of the program. They are categorized based on two general classes of materials under consideration, and these are: 1) metal-based catalysts (the more traditional approach); and 2) enzyme-based catalysts (an advanced development approach). Within each category several parallel approaches were pursued as outlined below.

Metal-based electrocatalysts for oxygen reduction have been available for many years, and the most effective catalysts in this regard are Pt-black materials, both supported and unsupported. Furthermore, processes and procedures for the preparation of MEAs using this catalyst are also well developed, so it was merely a question of adopting this well established technology to the architectural configurations being developed in this program.

In the case of the oxidation of carbohydrates, specifically glucose and/or sucrose, good catalysts are not available. In these cases the oxidation is incomplete, the rate of the reaction is low, and the species formed often poison the catalyst. (From a fuel cell standpoint, these issues speak directly to power and lifetime, parameters that we are attempting to maximize.) All of these issues are very similar to those challenges presented for the direct oxidation of methanol, and in fact it is because of these and other similarities to methanol that we identified a bimetallic for use as the baseline catalyst for glucose oxidation, specifically the 1:1 PtRu-black that is used for the direct oxidation of methanol. This also served as the starting point for the pragmatic approach to catalyst development that also included a review of the literature in order to identify any and all catalytically active electrode materials. In the third and final year of the program additional resources were made available, and three other approaches to catalyst discovery were added. First and foremost among these was the inclusion of a combinatorial development approach that supplements the pragmatic approach. Proof of

concept level of efforts for bioinspired catalyst discovery and the use of nano-materials as catalysts were also added.

In the case of enzymes, glucose oxidase catalyzes the two-electron, two-proton oxidation of glucose to gluconate, and this enzyme was selected for use as the catalyst in our system. Our initial work focused solely on adapting procedures described in the literature by both Heller[46] [47] [48]and Katz and Willner[49] [50] to our system. However, in reproducing this work it became apparent that the adaptation to our system was not so straightforward, and that there were several shortcomings of the systems that were not identified in the references, such as the limited lifetime. In the third year of the program when additional resources became available we expanded our activity to address these shortcomings, with the major emphasis being mediators.

In the third year of the program we also expanded our work with enzymes to focus on the oxygen electrode, and we identified two enzymes that could be used for the four-electron four-proton reduction of oxygen to water. These enzymes are laccase and bilirubin oxidase, with the predominance of our work focusing on laccase. In this program we evaluated several potential laccase sources, and identified the preferred material. We also developed an immobilization procedure compatible with our prismatic architecture.

5.1 Baseline Electrocatalysts

The efficacy of bimetallic systems for the oxidation of glucose has been demonstrated by various investigators, and interestingly enough a challenge similar to that found for direct methanol oxidation has been hypothesized for the case of direct glucose oxidation. Namely, an intermediate reaction product is formed that acts as a poison, and its presence accounts for the dramatic lowering of the oxidation rate for some of these sugars. Bi-functional catalysts have been identified and utilized to mediate the slow oxidation rate. Because of the similarities with direct methanol oxidation, the baseline catalyst system was selected to be the well-known platinum-ruthenium bi-metallic catalyst that has been shown to achieve high direct methanol oxidation rates presumably due to the bi-functionality of the catalyst.

We have completed an investigation of the direct electrochemical oxidation of glucose in both half-cell and full-cell operating contexts, and shown in Figure 5.1 is some of the data that was acquired under these conditions. The results of this initial investigation suggest that the carbohydrate fuels, specifically glucose and sucrose, are very interesting

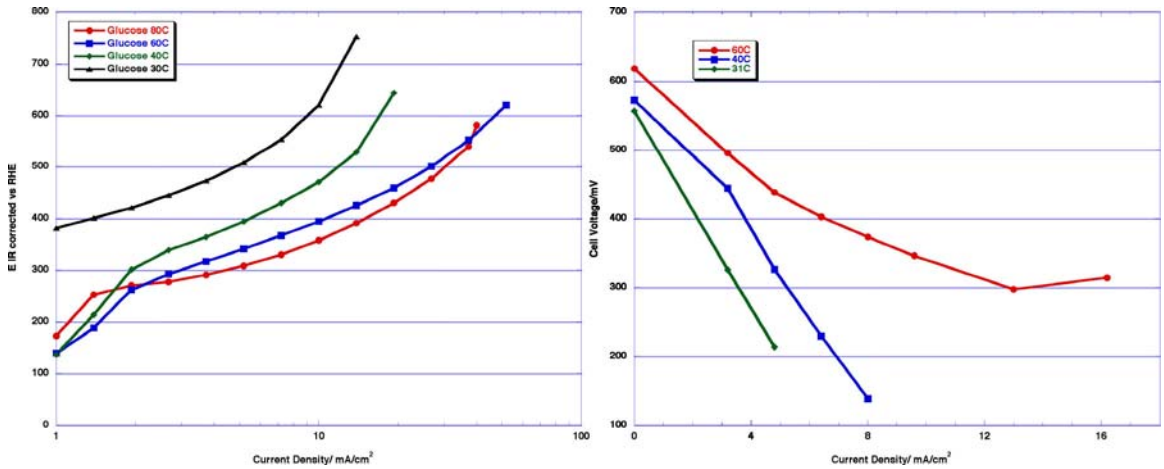

Figure 5.1: Half-Cell polarization data for glucose oxidation at Pt-Ru electrode as a function of temperature and fuel cell data as a function of temperature for a glucose-air fuel cell. (Half cell: 1M sulfuric acid electrolyte, SCE reference, graphite counter electrode, working electrode area: 0.95cm^2. Anode contains ~15 w% Nafion™ based on catalyst loading. Fuel cell: Aqueous 1M glucose solution was circulated in the anode compartment at a rate of 1 ml/minute. Air flow : high (~7X stoich). Electrode area: 5 cm^2)

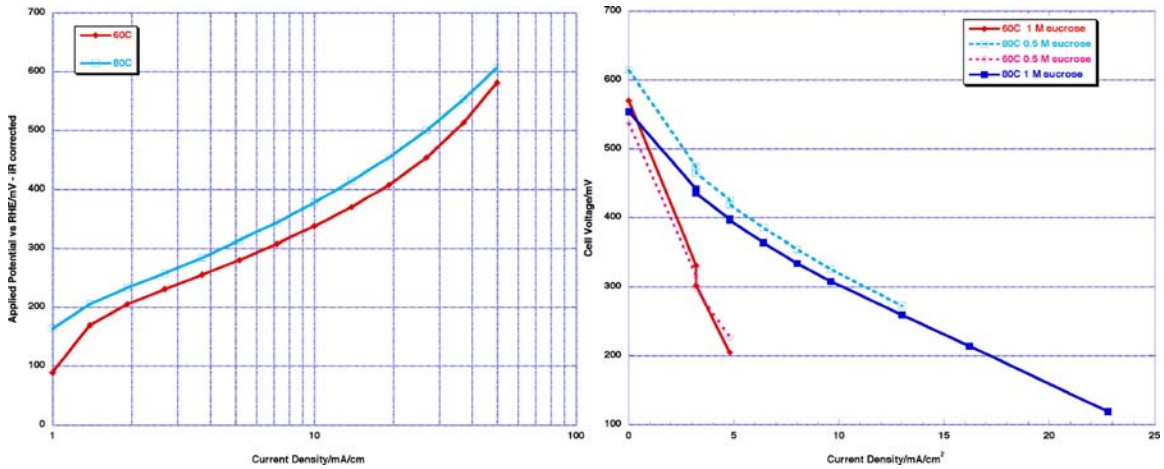

Figure 5.2: Half-Cell polarization data for sucrose oxidation at Pt-Ru electrode as a function of temperature and fuel cell data as a function of temperature for a glucose-air fuel cell. (Half cell: 1M sulfuric acid electrolyte, SCE reference, graphite counter electrode, working electrode area: 0.95cm^2. Anode contains ~15 w% Nafion™ based on catalyst loading. Fuel cell: Aqueous 1M glucose solution was circulated in the anode compartment at a rate of 1 ml/minute. Air flow : high (~7X stoich). Electrode area: 5 cm^2)

candidate fuels for special application fuel cells. The oxidation rates however are sluggish until the temperature is raised.

Since the fuel oxidation electrodes utilized for these studies were those developed and optimized for direct methanol oxidation fuel cells, it is not unreasonable to expect that improved oxidation performance could be achieved, even at relatively low temperatures, by a systematic investigation of catalysts and electrode structural parameters. For example, we have determined that Nafion®, when processed in the normal fashion that includes heat treatment to promote crosslinking, presents a significant impediment to mass transfer of glucose (see section 4.8). While this behavior will minimize and/or eliminate cross-over, its presence in the anode structure of the MEA can serve to only reduce electrode performance. This was investigated further by eliminating all of the Nafion® in the anode catalyst layer of some electrodes, and we did observe an improvement in oxidation performance. Both the individual polarizations at a given current density and the apparent limiting currents were better for the "no-Nafion®" electrode. Although Nafion® is typically added to an electrode to enlarge the available catalyst area for a given electrochemical reaction, in this case there appears to be a mass transfer limitation imposed.

The other carbohydrate identified early in this program as a possible fuel source was sucrose, a disaccharide composed of glucose and fructose and also the primary carbohydrate from plant sources. As a part of this preliminary investigation of the activity of the bimetallic PtRu catalyst, we also completed half-cell and full-cell studies for sucrose oxidation, and these data are shown in Figure 5.2. As seen by this data, the behavior for sucrose is similar to that seen for glucose, where the kinetics of the oxidation reaction are relatively low until higher temperatures are used.

Since the fuel oxidation electrodes utilized for these studies were those developed and optimized for direct methanol oxidation fuel cells, it is not unreasonable to expect that improved oxidation performance could be achieved, even at relatively low temperatures, by a systematic investigation of catalysts and electrode structural parameters. Other studies on glucose oxidation have identified alternate catalysts that apparently oxidize glucose at a rate superior to the platinum-ruthenium catalyst that was used in this study, and we initiated studies aimed at identifying and developing improved catalysts. This

work forms the basis for a pragmatic approach to metal catalyst development described next.

5.2 Metal Catalyst Discovery

5.2.1 Pragmatic Approach to Catalyst Discovery for the Oxidation of Glucose

The typical approach to electrocatalyst discovery is highly pragmatic in nature, and is generally founded on an iterative build and test strategy. And in those instances where little of no electrochemical information is available, the task of electrocatalyst discovery can be truly daunting. However, because of its importance in a number of areas such as the food industry or in a clinical setting, a significant body of literature exists on the electrochemical behavior of both glucose and sucrose, and this served as a starting point for our work.

The catalysts under consideration for direct glucose fuel cell anodes include metals (e.g., Pt, Pt-black, Au), noble metal bimetallic alloys (e.g., Pt-Ru), and other Pt-based compositions (e.g., Pt-Co, Pt-Sn). An initial evaluation of the electrochemical behavior of glucose at these electrodes was performed using cyclic voltammetry and quasistationary rotating disk electrode (RDE) voltammetry in a conventional three-electrode electrochemical cell. A saturated calomel electrode (SCE) or silver/silver chloride (Ag/AgCl) electrode was used as the reference. In some instances the cell potentials are reported relative to the reversible hydrogen electrode (RHE). A platinum wire was used as the counter electrode. Experiments were performed in a variety of supporting electrolytes. Acidic electrolytes were conducted in 0.5 M H_2SO_4 or 0.5 M CF_3SO_3H, neutral pH electrolytes was a 0.1 M potassium phosphate buffer solution, and the alkaline electrolyte was 0.1 M KOH. All glucose solutions were prepared fresh daily, and this was done by dissolving anhydrous d-glucose (Fisher Scientific) in the aqueous supporting electrolyte solution sufficiently in advance of the voltammetry experiment to allow the mutarotation between α- and β-forms to reach equilibrium. This occurs very rapidly under alkaline conditions, but takes approximately 3 hours at neutral pH. Prior to the voltammetry experiment, the catalyst was electrochemically conditioned in the cell by briefly (~ 5-10 seconds) polarizing the working electrode to potentials where hydrogen adsorption and evolution occur. After this step, the surface was cleared of hydrogen gas bubbles prior to commencing the voltammetry experiment.

Metal catalyst samples were obtained from De Nora North America, Inc. (ETEK Division). In the results summarized in this report, we examined platinum-metal binary catalysts ("Pt-M") supported on a high surface area carbon (Vulcan XC-72, 30 nm particle size, 254 m2/g surface area). The metal content of the carbon-supported catalyst was 20% in all cases, and the metal particles are reported by the manufacturer to be 2-4 nm in diameter. The catalysts were deposited from aqueous slurries onto surfaces of highly-polished glassy carbon working electrodes. After allowing the water to evaporate, a thin film (~ 0.6 μm) of Nafion® 1100 was deposited onto the working electrode (from a dilute methanol solution) to aid in adhesion of the catalyst powder to the electrode. (Note – the Nafion in this case was not thermally cured subsequent to deposition, and as such does not present a barrier to mass transfer of glucose.)

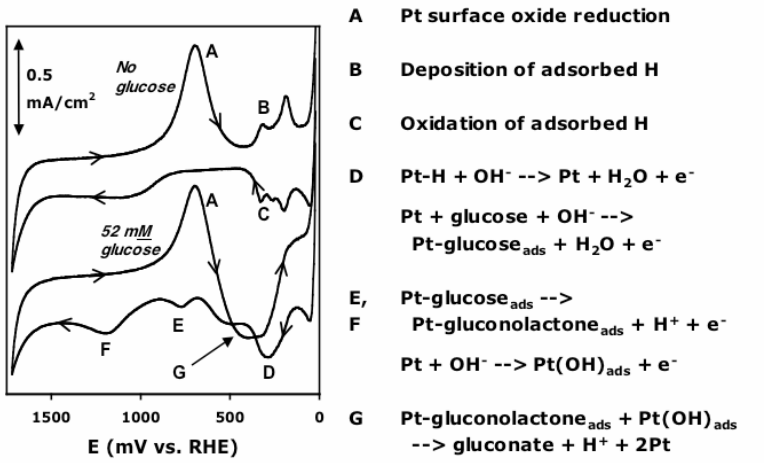

Figure 5.3: Cyclic voltammograms at a stationary Pt disk electrode. Potential sweep rate: 100 mV/s. Supporting electrolyte: 0.1 M phosphate buffer (pH 7). Top curve: no glucose. Bottom curve: 52 mM glucose. Temperature: 20°C. The electrochemical reactions associated with key peaks in the voltammograms (labeled A – G) are detailed in the legend.

Shown in Figure 5.3 is the cyclic voltammetry (CV) for glucose at a highly polished polycrystalline Pt disk electrode in a pH 7 phosphate buffer. The background voltammogram (top curve) contains the well-known features for Pt electrochemistry: oxidation of the Pt surface at anodic potentials (> ~ +900 mV vs. RHE), reduction of the surface oxide (peak A), and hydrogen adsorption and desorption (peak sets B and C, respectively). When glucose is added to the supporting electrolyte (bottom curve), several oxidation peaks are observed. During the forward (anodic) scan, oxidation peaks are attributed to chemisorption and oxidative dehydrogenation of glucose (peak D), oxidation of the chemisorbed species to form a weakly-adsorbed gluconate (peak E), and

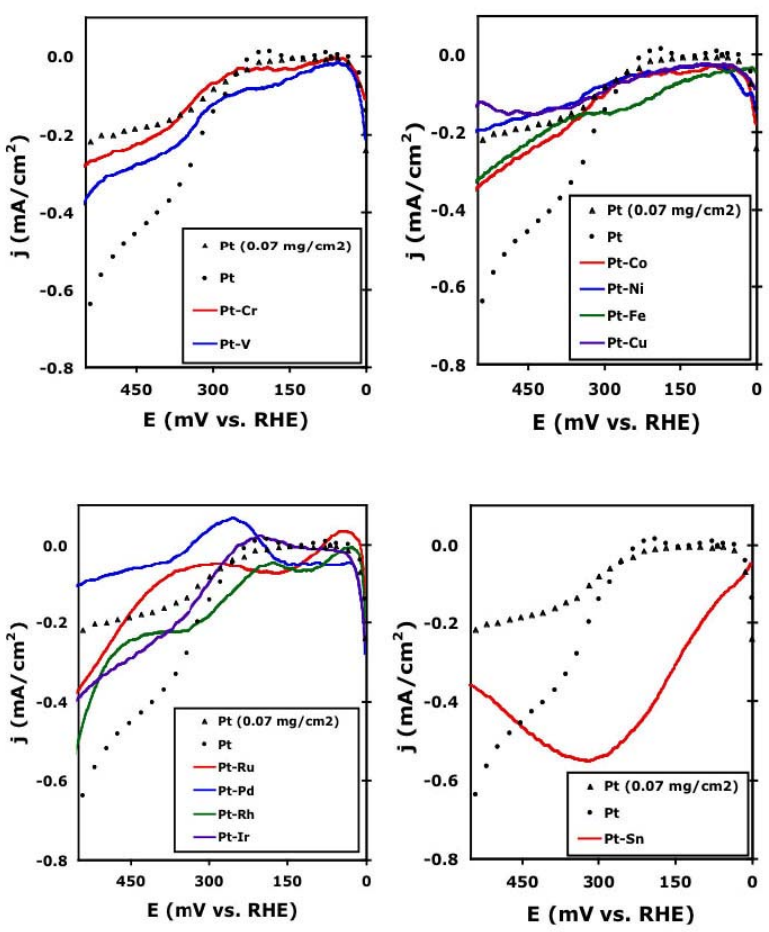

Figure 5.4: Background-corrected linear sweep voltammograms at catalyst-modified glassy carbon electrodes. Catalysts are 20% metal (or metal alloy) on Vulcan XC-72 carbon support. Catalyst metal (or metal alloy) loading on electrode is 0.14 mg/cm^2 (except where noted). Supporting electrolyte: 0.1 M phosphate buffer (pH 7). Glucose concentration: 52 mM. Potential sweep rate: 2 mV/s. Electrode rotation rate: 2500 rpm. Temperature: 20°C.

oxidation of the chemisorbed species to form a strongly-adsorbed gluconolactone (peak F). During the reverse (cathodic) scan, gluconolactone products continue to accumulate on the surface until enough reactive oxygen is produced to oxidize gluconolactone to the weakly-adsorbed gluconate species, resulting in a large oxidation current (peak G). Presumably included in this oxidation peak is a contribution from chemisorption and oxidative dehydrogenation of glucose since the potential is sufficiently anodic to also drive this reaction at an appreciable rate.

There are several hypothesized and demonstrated mechanisms for improved performance of Pt alloys (compared to that of pure Pt) for oxidation of small, oxygenated organic molecules such as glucose. Two such mechanisms are the bifunctional mechanism and the ligand effect. In the bifunctional mechanism, the alloy metal dissociatively adsorbs and oxidizes water to form Pt-M$(OH)_{ads}$. If this happens at lower overpotentials than for the case of pure Pt (where Pt-$(OH)_{ads}$ is formed), then the reactive

forms of oxygen that can dramatically facilitate glucose and gluconolactone oxidation are available at lower overpotentials. This can lead to increased power generation in fuel cell applications using these catalysts. The ligand effect results from changes in the electronic structure of Pt. This is the result of the presence of the alloying metal, which in certain cases can result in a weakening of the Pt-gluconolactone bond. This facilitates oxidative removal of the gluconolactone (the "depoisoning" reaction), a beneficial performance attribute for anode catalysts. We have characterized the behavior of 11 Pt-M binary catalysts including: Pt-Ru, Pt-Rh, Pt-Pd, Pt-Ir, Pt-V, Pt-Cr, Pt-Fe, Pt-Co, Pt-Ni, Pt-Cu, and Pt-Sn, at various values of pH.

In Figure 5.4 a series of rotating disk voltammograms are shown for carbon-supported Pt and for the 11 carbon-supported Pt-M binary alloy catalyst materials. In the four sets of voltammograms depicted, the results for the binary alloys are compared to that of pure Pt in the potential region between 0 and +550 mV vs. RHE. In each voltammogram the binary alloy loading on the electrode was 0.14 mg/cm^2, while two different loadings (0.07 and 0.14 mg/cm^2) are shown for Pt. The catalysts can be ranked on the basis of the onset potential for threshold values of oxidation current density. (For optimum fuel cell power performance, it is desirable to obtain high oxidation currents at low overpotentials with respect to RHE.) The onset potentials for 0.1, 0.2, and 0.5 mA/cm^2 are shown in

Table 5.1. Based on this evaluation method, 20% Pt-Sn on Vulcan XC-72 is superior

Catalyst	**Alloy (a/o)**	**Onset Potential (mV *vs.* RHE)**		
		0.1 mA/cm^2	**0.2 mA/cm^2**	**0.5 mA/cm^2**
(0.14 mg/cm^2 metal loading, except as noted)		***(Relative ranking of top 3 in parentheses)***		
20% Pt-Sn on Vulcan XC-72	1:1	30 (1)	100 (1)	250 (1)
20% Pt-Fe on Vulcan XC-72	1:1	190 (2)	420	> 650
20% Pt-Rh on Vulcan XC-72	4:1	240 (3)	300 (2)	550 (3)
20% Pt-V on Vulcan XC-72	1:1	260	350	590
20% Pt on Vulcan XC-72	-	280	320 (3)	490 (2)
20% Pt-Ir on Vulcan XC-72	4:1	300	360	620
20% Pt-Co on Vulcan XC-72	1:1	300	380	650
20% Pt-Cu on Vulcan XC-72	1:1	300	640	> 650
20% Pt on Vulcan XC-72 *(0.07 mg/cm^2)*	-	310	490	> 650
20% Pt-Cr on Vulcan XC-72	3:1	330	400	> 650
20% Pt-Ni on Vulcan XC-72	1:1	330	550	> 650
20% Pt-Ru on Vulcan XC-72	1:1	400	460	> 650
20% Pt-Pd on Vulcan XC-72	1:1	540	630	> 650

to the other 10 binary catalysts for glucose oxidation at pH 7 at 20C. Other researchers have

Table 5.1: Onset potentials for glucose oxidation current densities of 0.1, 0.2, and 0.5 mA/cm^2. See Figure 5.4 caption for experimental conditions.

Catalyst	Alloy (a/o)	Onset Potential (mV *vs.* RHE)		
		0.1 mA/cm^2	0.2 mA/cm^2	0.5 mA/cm^2
(0.14 mg/cm^2 metal loading, except as noted)		*(Relative ranking of top 3 in parentheses)*		
20% Pt-Sn on Vulcan XC-72	1:1	30 (1)	100 (1)	250 (1)
20% Pt-Fe on Vulcan XC-72	1:1	190 (2)	420	> 650
20% Pt-Rh on Vulcan XC-72	4:1	240 (3)	300 (2)	550 (3)
20% Pt-V on Vulcan XC-72	1:1	260	350	590
20% Pt on Vulcan XC-72	-	280	320 (3)	490 (2)
20% Pt-Ir on Vulcan XC-72	4:1	300	360	620
20% Pt-Co on Vulcan XC-72	1:1	300	380	650
20% Pt-Cu on Vulcan XC-72	1:1	300	640	> 650
20% Pt on Vulcan XC-72 *(0.07 mg/cm^2)*	-	310	490	> 650
20% Pt-Cr on Vulcan XC-72	3:1	330	400	> 650
20% Pt-Ni on Vulcan XC-72	1:1	330	550	> 650
20% Pt-Ru on Vulcan XC-72	1:1	400	460	> 650
20% Pt-Pd on Vulcan XC-72	1:1	540	630	> 650

also noted the excellent properties of Pt-Sn catalysts with respect to electrooxidation kinetics of methanol.[51]

Based on the promising half-cell results for glucose oxidation at Pt-Sn catalysts, we fabricated MEAs consisting of a 20% Pt-Sn on Vulcan XC-72 anode, a Pt black cathode, and a 7-mil thick Nafion®117 polymer electrolyte membrane. Evaluations of these MEAs in fuel cell tests using hydrogen, methanol, and glucose as fuels, and using oxygen and air as oxidizers, are currently underway. These performance results will be compared to those previously obtained with MEAs fabricated using a variety of anode catalysts (Pt black, Pt-Ru black, and Pt-Pd black, among others).

5.2.2 Combinatorial Catalyst Discovery

As should be apparent from the small amount of data shown and discussion of the preceding section, identification of a suitable electrocatalyst for any application is a significant undertaking considering the wide range of candidate systems that must be

evaluated. Critical variables that will determine overall catalyst functionality include the catalyst composition, catalyst structure, chemical environment and electrical duty cycles (which translate into electrochemical cycling). Combinatorial techniques may lesson the experimental burden posed by such a large phase space by enabling simultaneous fabrication or evaluation of many candidate catalysts.

Recently, a number of researchers have developed and applied combinatorial or rapid sequential techniques to improve efficiency in screening catalytic behavior. Many of the approaches developed to date rely on fabricating an array of electrodes with varying composition and then employing a screening technique that can be simultaneously applied to the entire population of electrodes or rapidly scanned across the array. Examples of screening technologies include: fluorescence, $H_{2(g)}$ detection, mass spectrometry and direct electrochemical measurements. In addition to measuring catalytic behavior, any combinatorial approach to catalyst development must include a methodology for fabricating the catalyst structures. Many of the cited approaches rely on manual sequential methodologies for generating electrodes although some have used automated sequential methodologies for rapidly building libraries of catalysts.

In the present work we sought to develop a combinatorial approach with the following attributes: (1) multiple electrodes are fabricated simultaneously, (2) each electrode is electrically isolated from the remainder of the array, enabling parallel characterization using a multipotentiostat, (3) combinations of environment and catalyst composition can be evaluated with increased efficiency over serial approaches, (4) electrochemical measurements are used that enable comparisons of current density and provide differentiation of catalyst lifetimes.

Our goal was to develop a screening technique that is ideally suited to the goal of assessing combinations of catalyst composition and operating environment; in essence to be able to assess X compositions in Y environments while minimizing the number of fabrication and experimental steps. The approach was to build a 10X10 array of platinum electrodes that could be used as a substrate for electrodeposition of candidate catalyst compositions. A test cell was constructed that enabled isolating an individual row or column of 10 electrodes. Electroplating was performed on rows of electrodes with the plating conditions altered for each row, resulting in 10 duplicates of 10 different catalyst

compositions. Electrochemical evaluation was performed on columns of electrodes with a different environment (e.g., pH) for each column. In each experiment 10 different electrode compositions were simultaneously tested in a given environment using a multipotentiostat. After 10 experiments comprised of 10 electrode compositions evaluated in 10 environments, a total of 100 unique combinations will have been evaluated. This approach results in a factor of ten increase in the efficiency over serial electrodeposition and electrochemical evaluation steps as seen by the summary provided in Table 5.2.

Approach	Number of electrodeposition steps	Number of electrochemical experiments	total number of steps required for evaluation
Serial	100	100	200
Combinatorial	10	10	20

Table 5.2: Comparison of processing steps and efficiencies of serial and combinatorial screening approaches.

To assess the feasibility of using this approach for identifying combinations of materials and environment for glucose oxidation, the binary Pt-Ru system was evaluated in glucose solutions of varying pH. Results previously described using traditional electrode evaluation techniques identified Pt-Ru as a viable candidate for glucose oxidation. Additionally, techniques for Pt and Pt-Ru alloy electrodeposition have been reported in the literature and provided a foundation upon which to develop the electrodeposition techniques used in this study.

The 10X10 electrode array designed and fabricated using an acrylic electrode template that accommodates 100 electrodes on 0.76 cm spaced centers in a 10X10 pattern. One mm diameter Pt wires were fitted with pin-type connectors and inserted into the acrylic base. The electrode array was then potted and the surface polished to a 1 μm finish using an alumina slurry, cleaned with laboratory cleanser and rinsed copiously in flowing deionized water. A ten-pin connector was fabricated that enables either a multipotentiostat to address ten electrodes individually (for evaluation) or a single-channel potentiostat to address ten electrodes simultaneously (for electrodeposition processes).

A test cell fabricated from acrylic enables isolation of individual rows or columns of the array. A base plate was constructed that holds the array and test cell in alignment.

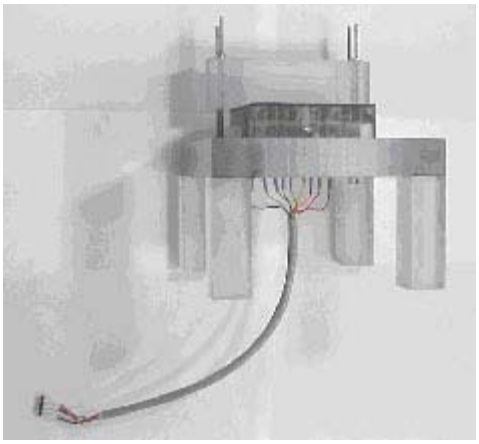

Figure 5.5: Electrode array, base plate and test cell used for electroplating and evaluating catalyst materials.

Threaded steel rods hold the test cell in place and allow the cell to be tightened against the array. A gasket between the array and the test cell prevents leaks at this interface. Once assembled, the test cell accommodates a Pt wire counter electrode, an electrode well housing a saturated calomel reference electrode (SCE) and approximately 25 ml of test solution. Optical photographs of the various cell parts are shown in Figure 5.5.

Prior to electroplating, the Pt surfaces were cleaned by repetitive cycling in 1 M H_2SO_4. Electroplating baths were made by mixing stock solutions of 10 mM $PtCl_6$ and $RuCl_3$. Each stock solution contained 50 mM K_2SO_4 as a supporting electrolyte. A study was performed to identify ranges of bath chemistry that produced electrodeposits ranging from Pt-rich to Ru-rich compositions as well as to develop an understanding of the relationships between the electrochemical deposition parameters and the resulting metal composition that we determined using Auger electron spectroscopy subsequent to deposition. As an example of this work, shown in Figure 5.6 is the functional relationship between the bath and deposit compositions that was developed.

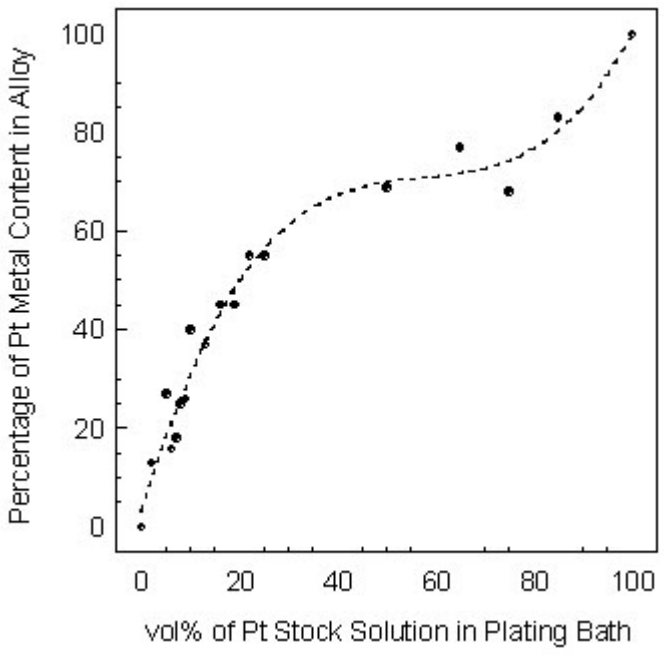

Figure 5.6: Relationship between the volume of Pt stock solution used in the plating bath and the metal content of the resulting electrodeposit. ● measured values, --- third order polynomial fit to data.

Catalyst performance was initially screened using cyclic voltammetry (CV). The electrodes were exposed to solution then polarized to -1.5 V (vs SCE) for 15 s in order to reduce the electrode surfaces. The potential was then returned to open circuit (E_{oc}) for approximately 30 s while a syringe was used to displace any $H_{2(g)}$ bubbles that had formed on the electrodes. The potential was swept from E_{oc} in the active direction, followed by a forward sweep to more noble potentials and finally back to the initial E_{oc}. In all experiments the sweep rate was 20 $mV \cdot s^{-1}$. Limits on the sweep potentials were set as to minimize water reduction and oxidation and were determined empirically for each pH investigated. Typically the sequence of preconditioning, bubble displacement and CV was performed three times in succession for each column of electrodes tested in a given environment.

Catalyst performance was also evaluated using a potentiostatic hold with glucose addition. This experiment was developed to ascertain the instantaneous (peak) oxidation currents as well as to differentiate the catalysts in terms of time-to-poisoning and total integrated charge prior to poisoning. In these experiments the electrodes were exposed to a buffer solution of desired pH and pretreated as described above. After $H_{2(g)}$ bubbles were displaced, the applied potential was set to a target value. After allowing the background current to stabilize (typically hundreds of seconds), an aliquot of glucose concentrate (1 M) was added to the buffer to bring the glucose concentration to 0.3 M. The current for each electrode was monitored until it returned to the baseline level achieved prior to glucose addition. The primary metric of catalyst performance used in this experiment was the integrated charge following glucose addition. Background currents were subtracted prior to the charge calculation.

The 100-element array was plated with 10 different Pt-Ru catalysts ranging from pure Pt to pure Ru. Each catalysts composition was evaluated in glucose containing and glucose-free environments ranging in pH from 5 to 10. At pH 5 no activity of the catalysts was observed and pH 10 was considered an upper limit to operating parameters for a fuel cell; therefore, the majority of the testing was bounded by these pH values. Making quantitative comparisons of catalyst behavior based on interpretation of the CV data was not possible due to the inability to identify a parameter that could be tracked from one data set to the next; pH and alloy composition caused shifts in peak shapes,

peak heights and background current levels. No method of data normalization was successfully applied to all data sets. However, the CV data can be used to illustrate the basic electrochemical behavior of the catalysts and to show gross differences due to alloy composition.

Figure 5.7 shows examples of voltammetric behavior obtained using the array, and in this case the data was collected at pH 7 for 100% Pt, 100% Ru and a 55:45 Pt-Ru binary alloy. As seen, these materials do act as active electrodes for the oxidation of glucose. It is possible to draw general conclusions from a qualitative examination of the CV data, and in this case it is seen that 100% Ru material is ineffective at catalyzing glucose oxidation (the current is suppressed in the presence of glucose). Both the 100% Pt and

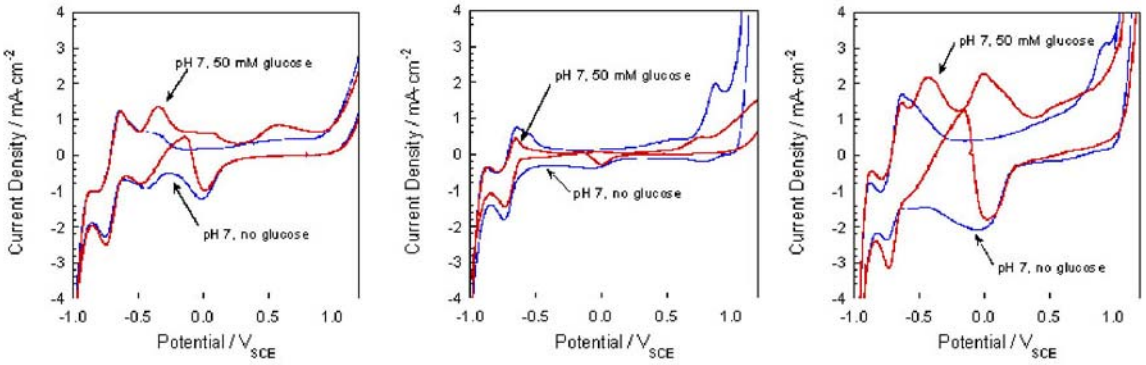

Figure 5.7: CV data for electrodeposited Pt (on left), Ru (in center), and Pt-Ru ~55:45 (on right) in pH 7 electrolyte showing an increase in oxidation current in the absences and presence of 50 mM glucose.

55:45 Pt-Ru alloy electrodes are effective at glucose oxidation, with the Pt-Ru alloy showing higher current densities. (It should be noted that the electrochemical surface area has not been determined for these electrodes and differences in oxidation current are assumed to be due to the catalyst compositions.) It was also found that other alloys of various Pt-Ru compositions were also found to be effective catalysts; however, quantitative differentiation was not made from the CV data.

In order to generate data sets that could be readily reduced to yield quantifiable parameters related to catalyst performance, experiments were undertaken in which current decay was monitored following glucose addition at constant applied potential. An example of a raw data set is shown graphically in Figure 5.8. Three parameters can be extracted that relate to catalyst performance: the maximum current density achieved

upon glucose addition, the integrated charge related to glucose oxidation and the time until the catalyst poisons and the current returns to the baseline level. Although time-to-poisoning can be a critical parameter for catalyst use in a fuel cell application, the value assigned to this parameter will vary depending on what endpoint is selected for a cut-off current density, thus complicating using time-to-poisoning as a readily assessed metric. Likewise the maximum current density may not provide an accurate representation of the useful power available from a catalyst as the value does not contain information on the decay rate. The integrated charge was found to be the most useful parameter for screening catalysts as it scales with both the power density and the catalyst lifetime. Moreover, it is not significantly influenced by the choice of an endpoint for integration, simplifying analysis. Testing of Pt-Ru catalysts in 0.3 M glucose solution indicated a maximum in integrated charge for an alloy composition of approximately 55:45 Pt:Ru.

Compositions of Pt-Ru ranging from pure Pt to pure Ru were evaluated using the potentiostatic technique in solutions ranging in pH from 5 to 9. The results of this testing are summarized in Figure 5.9 and suggest that the 55:45 Pt:Ru composition at pH 8 provides the overall best catalytic performance for the phase space investigated. A bias exists in this data set however, as the same applied potential (0 VSCE) was used for all pH's tested. At lower pH the glucose oxidation occurs at more positive potentials and testing at 0 VSCE could lead to non-optimum conditions for oxidation. A better comparison of the effect of pH would require additional experimentation to also include determination of the optimum potential for each pH. Nevertheless, the data of Figure 5.9 do show that the 55:45 Pt:Ru composition gave the best performance for all

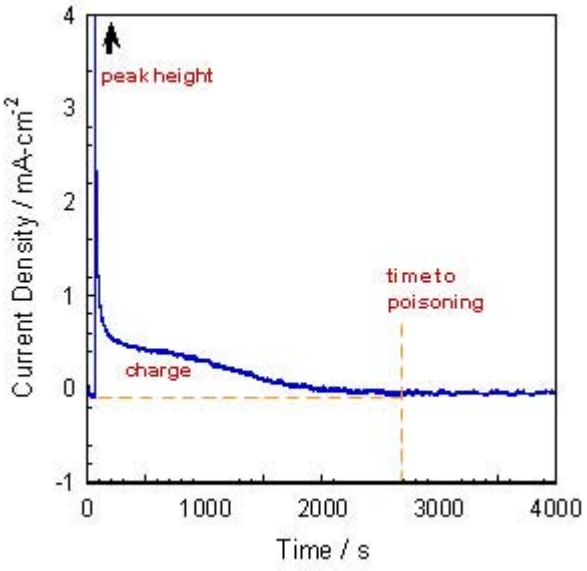

Figure 5.8: Current decay data for a 69:31 Pt-Ru catalyst in pH 8 electrolyte. Upon addition of the glucose concentrate, the glucose concentration in solution was 0.3 M. Integrated charge provides a good metric for comparing catalyst behavior as it reflects both power density and lifetime without sensitivity to the choice of endpoint for integration.

pH's investigated, lending credence to the conclusion that this is the optimal binary composition. Furthermore, CV testing at pH 5 and 6 qualitatively showed worse performance than at higher pH. Taken together, the CV and potentiostatic data identify 55:45 Pt:Ru at pH 8 to be the optimal combination of composition and pH for glucose oxidation.

The effect of applied potential on catalytic activity for a subset of the Pt:Ru binary catalysts was evaluated at pH 8, and these data show that an applied potential of 0 VSCE results in the highest integrated charge values for all catalyst compositions investigated. Similar (but slightly lower) integrated charge was observed down to -0.1 VSCE and a significant decrease was observed when the potential was reduced to -0.2 VSCE. Similarly, increasing the potential to 0.1 VSCE results in a significant decrease in charge. Thus, the highest efficiency for catalyst performance is obtained at pH 8, 0 VSCE with an approximate catalyst composition of 55:45 Pt:Ru.

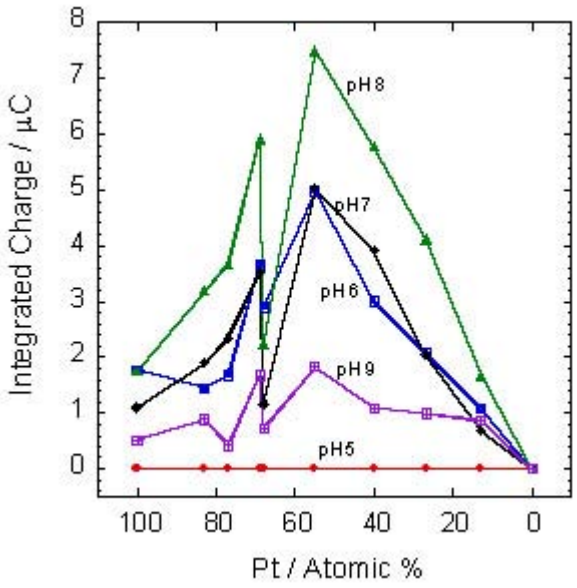

Figure 5.9: Effect of solution pH and alloy composition on integrated charge measured during a potentiostatic hold. The applied potential was 0 V_{SCE} and the glucose concentration was 0.3 M in all experiments.

The next phase of the combinatorial catalyst development activity is to broaden the phase space investigated to include ternary catalysts. Based on literature data, alloy additions such as Pb or Sn can increase the lifetime of Pt based catalysts before poisoning of the glucose oxidation reaction occurs. The present study will be addressing the effect of Pb additions to the Pt-Ru system. As an initial screening, and to determine plating conditions for ternary materials, several Pt-Ru-Pb catalysts were generated and tested using glucose addition fixed potential. Preliminary results indicate that a composition of 54:36:10 Pt:Ru:Pb yields a significant improvement over the binary 55:45 Pt:Ru alloy. Furthermore, significant improvements in current density and time-to-poisoning have

been observed as shown in Figure 5.10. Current efforts are targeting refinements in ternary electrodeposition and higher throughput electrochemical testing.

The approach of using a microelectrode array in combination with catalyst electrodeposition and electrochemical evaluation provides a significant improvement (10X) in the efficiency of screening combinations of catalyst composition and environmental variables compared to sequential methods. CV testing provides a good qualitative comparison of catalyst performance; however, a consistent metric for making quantitative comparisons from the CV data was not identified. Difficulties ensued from the dependence of oxidation peak positions and background currents on alloy composition and environmental parameters. A potentiostatic glucose addition experiment provided a means to quickly quantify catalyst performance in terms of total integrated charge. Power density values and poisoning times can also be extracted from these data. For the phase space investigated, the optimum combination of environment and composition identified for glucose oxidation was pH 8, 0 VSCE and 55:45 Pt:Ru. This conclusion is based primarily on comparisons of integrated charge values. No evaluation of the effect of glucose concentration on performance was made. Initial data from Pt:Ru:Pb ternary catalysts indicates significant improvement in both current density and time-to-poisoning due to the Pb additions.

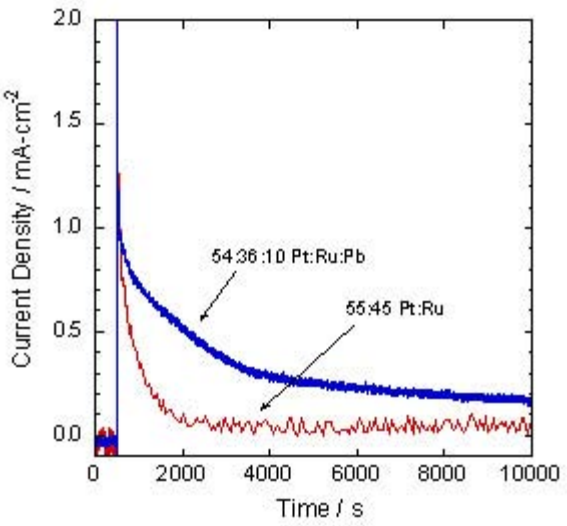

Figure 5.10: Comparison of current decay at 0 V_{SCE} in 0.33M glucose, pH 8 electrolyte for 54:36:10 Pt:Ru:Pb and 55:45 Pt:Ru. The addition of Pb appears to be beneficial both in terms of increased current density and increased time-to-poisoning.

5.3 Bioinspired Catalyst Development

An alternative to the pragmatic build and test approach to catalyst design and development is one based on computational modeling. In the ideal case one can envision writing the equation for the reaction of interest and the conditions under which the reaction is run, and from this developing a composition and structure of the ideal catalyst.

Alternatively, one might think of using an existing catalyst as a model, an enzyme for instance, and from this develop a fully functional computationally derived synthetic analog. With this composition and structure in hand, one could then prepare the compound and introduce it into the industrial system. However, not only has the computational design of catalysts never been demonstrated, it is also not clear if this is even a computationally tractable problem at this period in time.

Our objective in this activity was to begin to explore the feasibility of using enzymes as models for computationally based catalyst development. Our focus for this work was the reaction occurring at the cathode in the fuel cell, namely the oxygen reduction reaction that typically proceeds in either a two-electron or four-electron process as seen below.

Two-electron process

$$O_2 + 2e^- + 2H^+ \rightarrow H_2O_2$$ Equation 5.1

Four-electron reaction

$$O_2 + 4e^- + 4H^+ \rightarrow 2H_2O$$ Equation 5.2

There are a number of enzymes that catalyze these reactions, and in fact different variants of the same enzymes (e.g. the laccase or the cytochrome C oxidase families) will catalyze either the two- or the four-electron processes which is very useful for development of structure activity relationships. However, computational modeling of enzymes is beyond the scope of work in this program, we identified much smaller synthetic analogs of heme containing enzymes that are know to catalyze the reduction of oxygen. This initial work focused on the face-to-face (FTF) porphyrins developed by Anson and Coleman that exhibit both two- and four-electron reductions of oxygen.

In this work we have used density functional theory with the B3LYP functional, as implemented in the Jaguar program suite, to describe the energetics of the reactive species in this work. We use an implicit solvent model to represent the water solvent when appropriate.

The FTF porphyrins were initially studied because of the similarity in structure and in the chemistry they catalyze to the cytochrome C oxidases. The basic structure of the FTF

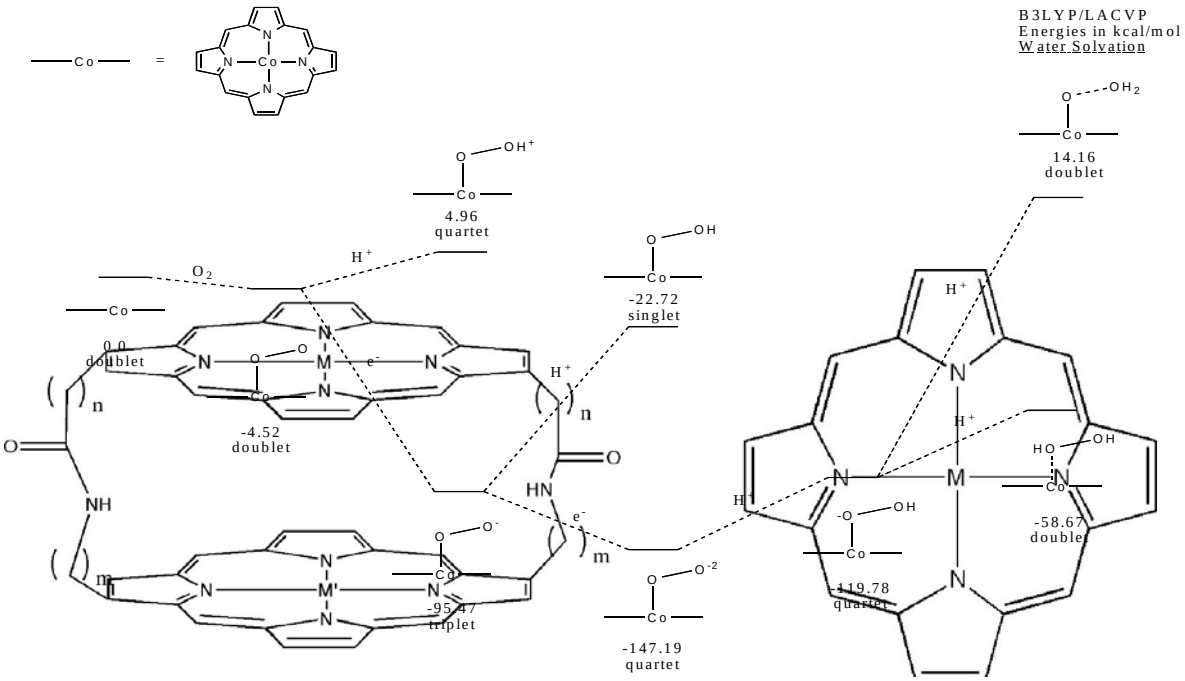

Figure 5.12: Co monoporphyrin oxygen reduction reactions in water (on the right)

family is shown in Figure 5.11. Anson and Coleman's study found that one particular member, named Co_2FTF_4 (with M=M'=Co, and n=m=1) showed particular activity toward the four-electron reductions, whereas all other members, including very similar species such as $CoPdFTF_4$ and $CoFTF_3$, showed only the two-electron reductions. Additionally, the monoporphyrin structures (Figure 5.11 on the right with, for example, M=Co) showed high activity for the two-electron reduction, but with a much shorter lifetime than the FTF porphyrins.

Since the Co monoporphyrin and the Co_2FTF_4 species differ only in the presence of the second porphyrin ring and the scaffolding that holds it in place, we have sought to understand the difference between the activities toward oxygen reduction of these two compounds.

Figure 5.12 shows the oxygen reduction reactions of the Co monoporphyrin species in water. Several things are notable about this mechanism. First, it correctly predicts that the two-electron reduction to hydrogen peroxide is favored over the four-electron

reduction to water. Additionally, this mechanism predicts that both electrons add before either of the protons add, which is different from the analogous mechanism in the gas phase (not shown here), where the electrons and protons alternate as they add. Finally, there are several stable intermediates containing either superoxide (O_2^-), peroxy radical (HOO), or peroxy anion (HOO^-); it is likely that dissociating these species is energetically favorable, which could likely explain the short lifetime that these species exhibit under oxygen reduction.

Figure 5.12 shows the first steps in computing the analogous mechansism using the Co_2FTF_4 moiety. Our hypothesis is that the particular way in which the oxygen binds to the cobalt atoms dictates the chemistry that is performed. Figure 5.12 shows that the peroxy bonding, which we anticipate will lead to the four-electron chemistry, is dominant in the Co_2FTF_4 compound. We anticipate that FTF compounds with smaller spacing between the two porphyrin rings (FTF_3) will favor the "outside" bonding, since there will not be enough room between the two rings to accommodate oxygen. We anticipate that this configuration will demonstrate chemistry identical to the Co monoporphyrin reductions in Figure 5.13 and will thus lead to the two-electron reductions of oxygen. Additionally, we anticipate that the FTF compounds with larger spacing between the two porphyrin rings (FTF_5, FTF_6) will favor the either the "T" style bonding, as there will be too much distance between the two porphyrins to allow "peroxy" style bonding, or the "outside" bonding, and will also demonstrate the two-electron oxygen reductions. Our belief is that the "peroxy" style bonding is unique to the FTF_4 compounds, and helps dictate the four electron reductions. Calculations of the remainder of the reduction pathway using the "peroxy" bonding motif are currently underway.

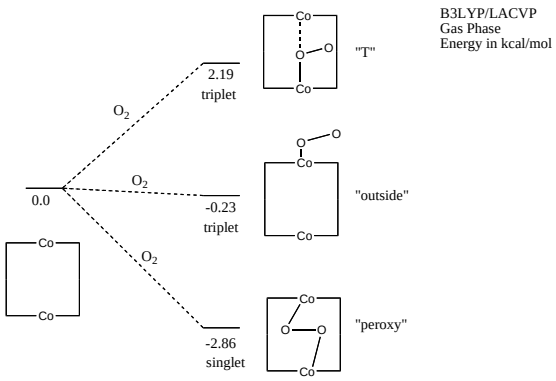

Figure 5.13: Oxygen binding to the Co_2FTF4 compound in the gas phase. The rectangular species is meant to represent the Co_2FTF4 moiety.

Should this structure-dictates-chemistry hypothesis hold, it will have significant ramifications for bio-inspired catalysts, as we will be able to identify a specific style of

bonding (oxygen being coordinated to two metals) as being responsible for the four-electron reductions of oxygen. This correlation will provide a rapid screening process for enzymes that will analyze their metal-metal distances for likely oxygen binding sites to pre-select candidates that are likely to yield good four-electron reductions. It also suggests which portions of the active site must be preserved when isolating a part of an enzyme on an electrode: our belief is that the essential part is to coordinate the Co atoms at the appropriate distances, and that the particular electrostatic characteristics of the active site do not play as large a role as the nature of the oxygen binding between the metal atoms.

5.4 Enzyme-based Electrocatalysts

The other approach pursued for catalyst development is based on the use of enzymes as catalysts. Enzymes that catalyze the reduction of oxygen to either water or peroxide, as well as for the oxidation of glucose are available, and the principal activity in this task is focused on development of methods for fabricating enzyme-based electrodes for both oxygen reduction and glucose oxidation electrodes that are compatible with the existing architecture. Furthermore, these electrodes must be able to meet the technical objectives for both power and stability. The work using glucose oxidase for glucose oxidation and laccase for reduction of oxygen is presented in the following sections, and it should be noted that like the case for the expanded program on metal-based catalysts, this aspect of the program did not begin until the third and final year of the program.

Glucose oxidase from *aspergillus niger* has been identified as the baseline enzyme for use as the electrocatlayst for the two-electron two-proton oxidation of glucose to gluconate. This enzyme is a large glycoprotein with the active site buried deep within the enzyme structure, and in fact is so far removed from the surface of the enzyme that direct electron transfer between the active site of the enzyme and the electrode does not occur. Two approaches have been identified for accomplishing the electron transfer reaction, and these are deglycosylation of the enzyme and the use of mediated electron transfer

5.4.1 Deglycosylation as a means for improving electron transfer.

In this approach the carbohydrate coating of the glycoprotein is removed, either in whole or in part, through a series of chemical reactions. In this way the distance of closest approach between the electrode and the reaction center may be reduced to the

point where a direct electron transfer process can occur. While finding a mediator that operates at a suitable potential is critical, the operating potential can also be improved by modifying the enzyme. By partially deglycosolating glucose oxidase, the oxidation potential is also seen to shift to more negative potentials, and this is seen in the voltammograms on the left of Figure 5.14. In this case either native or deglycosylated glucose oxidase has been immobilized on a glassy carbon electrode using a mediator (FTMAB - described in the next section), and as seen the peak oxidation potential was 40 mV lower in the case of the deglycosylated enzyme.

Also seen in the voltammograms of this figure is a comparison of the electrochemical behavior of both native and deglycosylated glucose oxidase at a polished glassy carbon electrode with no mediator present. As seen, in this case it is possible to achieve the direct electron transfer between the enzyme and electrode surface with deglycosylation, whereas in the case of the native enzyme direct electron transfer is not possible. However, the currents observed are still too low for making this a practical approach.

5.4.2 Mediated Electron Transfer

Electron transfer mediators are typically electroactive species that can approach both the electrode as well as the active site of the enzyme to a distance sufficient to allow for direct electron transfer, and by shuttling back and forth between these two sites allow for

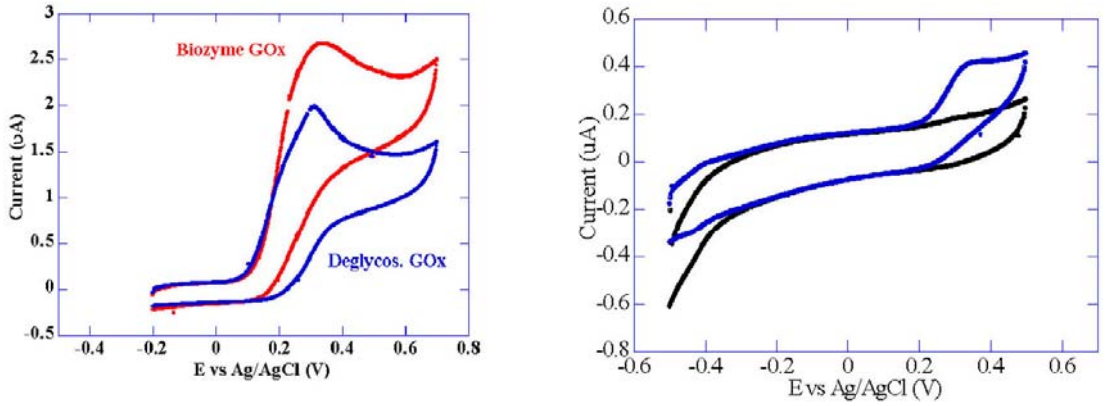

Figure 5.14: Comparison of native and deglycosylated enzyme in 50 mM glucose in the presence (on left, pH 7) and absence (on right, pH 5) of mediator.

transfer of electrons between the electrode and enzyme. In the case of glucose oxidase, the mediator acts as a replacement for molecular oxygen by accepting electrons from the

enzyme. For our situation the enzyme/mediator combination needs to provide high power, that is both good thermodynamic and kinetic characteristics for the reactions in question, and demonstrate long-term stability.

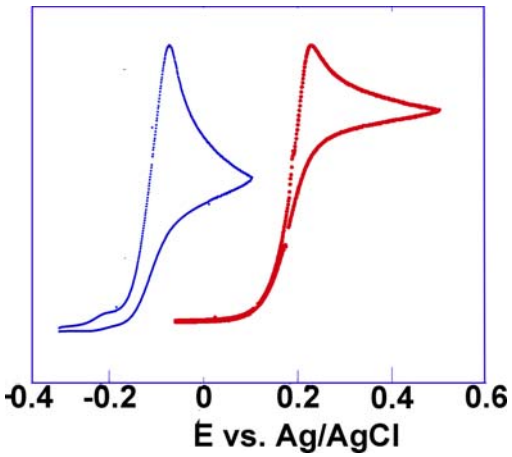

Figure 5.15: Normalized current as a function of potential for the mediated oxidation of 50 mM glucose solution using FTMAB (in red on the right) and PMS (in blue on the left).

We have evaluated a number of mediators in this work, and the results obtained with two of these, 11-ferrocenylundecyl trimethylammonium bromide (FTMAB) and phenazine methosulfate (PMS), are discussed here. Both have been reported to successfully mediate electron transfer with glucose oxidase, and the structures of both compounds are shown in Figure 5.16.

Shown in Figure 5.15 is the cyclic voltammetric response from each of these mediators in the presence of both glucose oxidase and 50 mM glucose in deoxygenated solution. As seen, both compounds exhibit the classic voltammetric behavior for a mediated electron transfer process. In the case of FTMAB, the peak oxidation current for the mediated electron transfer occurs at approximately 340 mV vs. Ag/AgCl, approximately 100 mV more positive that E_p of the parent in the absences of both glucose oxidase and glucose. In the case of PMS, the E_p of the catalytic oxidation wave is seen at approximately -70 mV, significantly more negative than in the case of FTMAB. This large difference in redox potentials between these two mediators highlights an important characteristic for mediators for fuel cell applications in that higher operating voltages will be observed in a fuel cell that utilizes a mediator having the most negative oxidation wave, in this case PMS. In fact, all other things being equal, the open circuit voltage of a

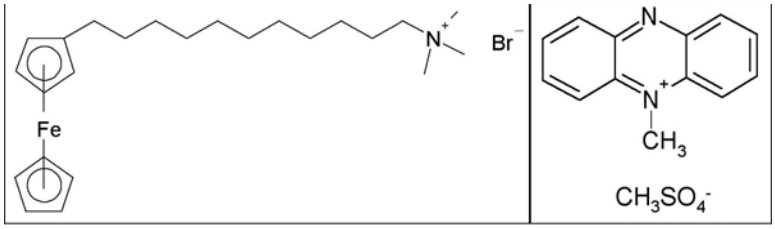

Figure 5.16: Structure of FTMAB (on left) and PMS (shown on the right)

direct glucose fuel cell using PMS as a mediator for the glucose oxidase will be approximately 410 mV higher than a fuel cell operating with FTMAB as the mediator.

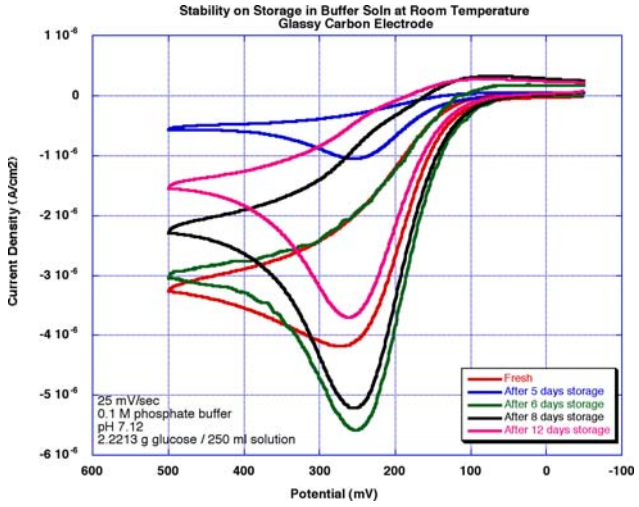

Figure 5.17: Mediated oxidation of glucose using FTMAB as a mediator after storage of electrode in solution at periodic intervals. Prior to collection of this data, the electrode was allowed to soak in a FTMAB solution for 30 minutes prior to running.

In addition to its mediating properties, FTMAB can also be used as a means for immobilization of glucose oxidase on the electrode surface. The immobilization is accomplished merely by placing a clean electrode into a buffered solution containing both glucose oxidase and FTMAB. The pH of the immobilization solution is below the isoelectric point of the glucose oxidase, and as such the enzyme is negatively charged. In the presence of FTMAB, a large positively charged surfactant molecule, an interaction that is presumably based on ion exchange and solubility characteristics occurs, resulting in formation of a complex that chemisorbs to the electrode surface. On storage at room temperature in an aqueous solution, this immobilized species is relatively stable, and even after 17 days the activity of the electrode is maintained, as seen by the data of Figure 5.17. One of the shortcomings of this system is that the FTMAB is lost from the electrode, either through decomposition or loss to solution, and the electrode must be reexoposed to a fresh solution of FTMAB in order to restore full activity.

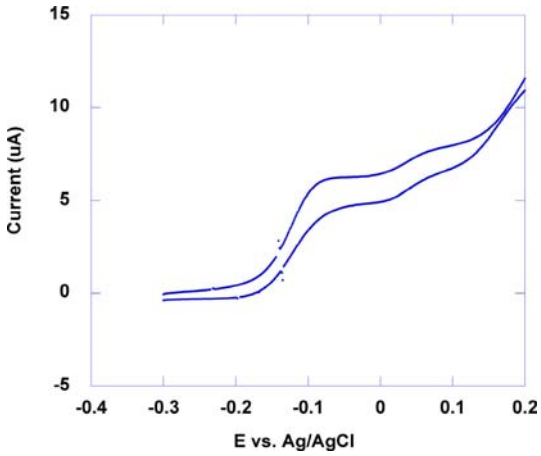

Figure 5.18: Cyclic volatmmagram of immobilized glucose oxidase using PMS and FTMAB on a carbon electrode with 50 mM glucose in solution and after two days storage in solution.

We have determined that this route to immobilization, that is the combination of glucose oxidase with a large cation at a pH below the isoelectric point of the enzyme, can

be accomplished using any large positively charged species and not just FTMAB. We used this approach to fabricate an immobilized glucose oxidase and a combination of mediators, specifically PMS and FTMAB. In this case the electrode was prepared by preparing a 10 mg/ml PMS and 10 mg/mL glucose oxidase solution in 0.1 M phosphate buffer at pH 7 and adding a small amount of the sparingly soluble FTMAB. A few drops of this solution was placed on a glassy carbon electrode and allowed to dry. As seen by the voltammogram of Figure 5.18, the modified electrode does show the mediated oxidation of glucose, and in fact the contribution due to both the PMS (seen at about -130 mV) and FTMAB (seen at about 50 mV) are clearly identified.

This approach allows for immobilization of glucose oxidase with a PMS mediator, as well as increases the stability of the PMS. A solution of PMS does not appear to be particularly stable, as evidenced by a gradual change in color of a PMS solution from yellow to dark green over a period of a few hours. The immobilization procedure appears to significantly increase PMS stability, and in fact the voltammogram shown in Figure 5.18 was recorded two days after electrode preparation and storage in a phosphate buffer solution while the electrode was not in use.

We have also started to look at the general applicability of these immobilization procedures for use in fabricating electrodes that are compatible with the existing architecture and that provide the requisite current, especially considering the fact that the oxidation of glucose by the enzyme is strictly a two-electron process. We have determined that using the FTMAB immobilization procedure with Toray paper or

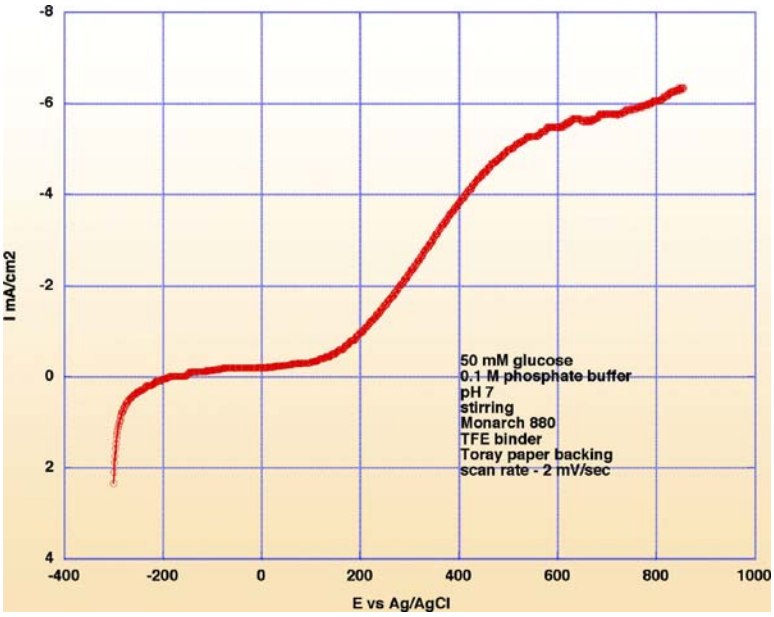

Figure 5.19: Limiting current at FTMAB-glucose oxidase immobilized electrode. The electrode is Monarch 880 on Toray paper.

carbon deposited onto Toray paper, electrodes that are compatible with the existing architectural design, it is possible to achieve higher current densities. Shown in Figure 5.19 is a linear sweep voltammogram collected in a 50 mM solution of glucose at pH 7. In this case the solution was stirred to avoid a mass transfer limited response. As seen, currents on the order of 6 mA cm^{-2} were easily attained, and it is expected that significantly higher currents can be achieved once the immobilization procedure is better defined and optimized for this electrode configuration.

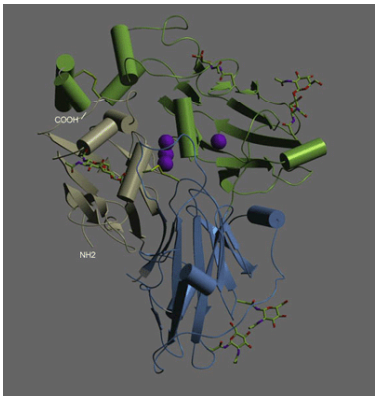

Figure 5.20: Structure of laccase from T. *versicolor* showing positions of copper atoms (purple spheres) in the structure.

5.4.3 Oxygen Reduction

Several enzymes capable of reducing oxygen to water are available, and we identified the class of blue copper enzymes for use in this work, beginning first with the laccase and then with bilirubin oxidase. The active site of the laccases used in this work is a three-metal copper containing site. There is another copper metal center in the protein located approximately 12.5 Å away from the three-metal center and between these centers and the perimeter of the molecule, as seen in the Figure 5.20. Because of the general placement of the copper metal centers with respect to outer perimeter of the molecule, it is possible to achieve direct electron transfer between the electrode surface and the active site of the enzyme.

At least compared to glucose oxidase, the immobilization procedure of the laccase is relatively straightforward. In this case the enzyme is dissolved in water, placed onto the electrode surface, and then allowed to dry. The enzyme is adsorbed/chemisorbed to the electrode surface, and is fully active. We have looked at laccase from different sources, and the best behavior is seen from the fungal laccase, C hirsutus. For this enzyme the redox potential is seen at only 59 mV below the reversible redox potential for oxygen reduction, and this enzyme does show complete four-electron reduction to water. We have also evaluated different carbons for use for fabrication of the electrode, and have determined that the best behavior is observed when using hydrophilic carbons, in this

case Monarch 880. Finally, we have demonstrated 500 hours of continuous operation at 5 mA cm^{-2}.

Although the development of mediated electron transfer for the anode represents a significant move forward in using enzymes to catalyze sugars for power generation in a fuel cell, it would be far more beneficial to remove both the thermodynamic as well as (possibly) kinetic limitations that this molecule would place on the performance of the anode. Deglycosilation of the enzyme, a relatively simple enzymatic modification, was shown earlier to allow for direct electron transfer, but at currents that were too low to be practically useful for the development of a direct electron transfer high current anode.

The other possibility involves the genetic manipulation of the enzyme itself. The enzymes will need to be compatible with the cell environment, which may include temperatures different than the optimal for enzyme normal operation, as well as changes in pH and other constituents in the harvested fuel. By genetically modifying the enzyme to be more tolerant to these changes, as well as modifying the enzyme to promote direct electron transfer, as well as covalent bonding to an electrode and higher electrochemical activity, significant improvements in current and voltage can be achieved. The third year of the project, then, began a large scale effort at developing genetic engineering techniques with the target of improving the catalytic activity of the enzymes toward glucose as a first step toward a designer enzyme that would provide high powers and stable, long life. The next section of this report details some of this work toward developing the techniques necessary to bioengineer the enzymes used in the fuel cell.

6. Bioengineering of Enzyme Catalysts

One of the major goals for this project was to develop a fuel cell that can produce power through the oxidation of glucose using enzymes as the catalysts instead of precious metals. There are several major advantages to using enzymes instead of precious metals as these catalysts, including (1) increased selectivity of the enzymes to a specific fuel source, (2) increased stability as enzymes have been shown to last for months when properly stabilized,[52] and (3) the opportunity to significantly ease the engineering and assembly of a complete fuel cell in terms of a alternative architectures.[53] Our initial focus in the first two years of this project was to develop an enzyme-based fuel cell that used naturally occurring (a.k.a. wild type) enzymes on both the anode and the cathode. The anode would utilize glucose oxidase, an enzyme that oxidizes glucose into gluconolactone (a.k.a. gluconate) through the mechanism shown in Figure 6.1. Glucose oxidase is produced primarily by filmanetous fungi such as Aspergillus niger and Pencillium amagasakiense. It is a holoenzyme consisting of two identical 80 kDa subunits and requires a cofactor (flavin adenine dinucleotide, or FAD) for activity, as shown in Figure 6.2. The cathode would use either laccase or bilirubin oxidase enzymes to complete the reaction cycle necessary to produce power (Figure 6.1). The results we obtained from the wild type enzyme utilized in such a fuel cell is presented in the electrochemistry section of this report. It was determined early on that the use of the wild type enzyme of glucose oxidase had several drawbacks that must be overcome in order to produce a robust fuel cell capable of meeting our programmatic and technical milestones.

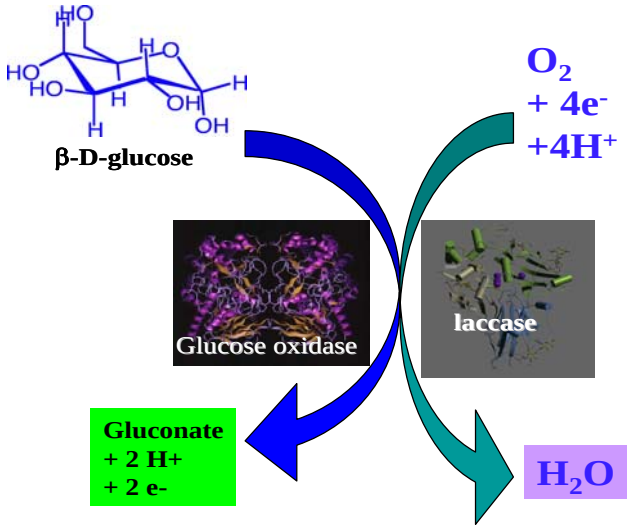

Figure 6.1: Schematic of the enzyme-based fuel cell process, with the glucose oxidase enzyme serving as the anode and the laccase enzyme serving as the cathode.

To achieve these goals, we embarked upon a course to modify the genetic structure of the enzyme to make it a better functional catalyst. Generating better enzymes for fuel cell applications involves evolutionary design approaches. Specifically, we developed a process to improve the activity of the enzyme, glucose oxidase, in the oxidation of glucose using a combination of rational redesign and directed evolution (random iterative mutagenesis, development of mutant libraries, screening and selection of mutants for desired performance) by using standard genetic engineering and recombinant protein techniques. Although much work has been done in the field of directed enzyme evolution,[54] there are significantly fewer reports on the genetic manipulation of glucose

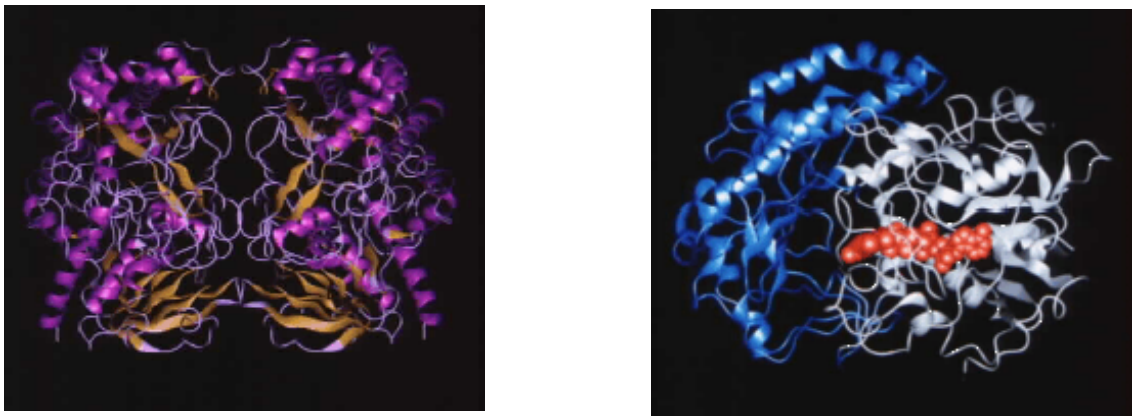

a) **b)**

Figure 6.2: Model representations of (a) holoenzyme of glucose oxidase, showing the two symmetric 80 kDa subunits, and (b) cut-section view of the enzyme showing the location of the FAD cofactor (red) in one of the subunits.

oxidase[55] and the recombinant expression of this enzyme.[56]

We have already demonstrated direct wiring of glucose oxidase to electrodes and have produced electricity from a glucose-powered fuel cell (electrochemistry section above). Our ultimate goal is to operate an enzymatic fuel cell at high power levels (100mW/cm^2). To do this the specific enzyme activity, longevity, and the electron transfer rate from the redox center to the electrode on which the enzymes are immobilized must be improved. Currently, the electron transfer from the redox active site to an electrode is accomplished through a mediator (typically a metallocene derivative). The addition of a mediator to an enzyme immobilization scheme is problematic and creates several lifetime and stability issues. If glucose oxidase could be engineered to eliminate the need for mediators it

would be very beneficial in terms of system fabrication and ease of manufacturing. Additionally, engineering new enzymes with improved properties will allow us to transition this effort into a fuel cell architecture designed around the specific operational requirements of the enzymes, selective membranes, and electrode configuration.

6.1 Methodology

Since the crystal structure of glucose oxidase from Aspergillus niger and Pencillium amagasakiense has been determined,[57] we can use a combination of both rational redesign through site-directed mutagenesis and an independent process pathway, known as directed evolution, to tailor the catalytic activity and electron transfer of glucose oxidase. Using site-directed mutagenesis, specific changes are made to the amino acid sequence based on prior knowledge of protein structure and function. Directed evolution, on the other hand, does not require the understanding of the relationship between sequence and structure as well as that between structure and function. This technique mimics some of the key processes of Darwinian evolution based on iterative random mutagenesis and recombination coupled with a selection process. In this study we will perform iterative random mutations of segments of genes to construct a diverse library of glucose oxidase mutants. We will then develop a screening strategy for glucose oxidase activity to identify those enzymes that perform the desired function (i.e., exhibit an increase in activity and/or increased electron transfer to an electrode). The information gained from the first round of mutagenesis and selection will then be used to either minimize the number of gene sequences involved in the next round of mutagenesis or will be used to identify specific amino acid residues for site-directed mutagenesis.

6.1.1 Site-Directed Mutagenesis

In order to be implemented effectively, a careful study of the amino acid sequence and protein structure must be completed before work begins. An analysis of sequence-structure-function relationship in homologous oxidase enzymes from different organisms is typically conducted to identify a) organisms that may already process glucose oxidase exhibiting higher specific activity through natural evolution b) sequence differences within conserved regions across organisms that may be targeted for initial mutagenesis. This entire design stage can be performed using a variety of available Search Engines and Protein Databases. In addition, theoretical investigations based on free-energy effects of

amino acid sequences will be used to design strategies for rational redesign and directed evolution. Figure 6.3 represents some of the information that can be acquired through these databases. Figure 6.3 illustrates conserved domains present in the glucose

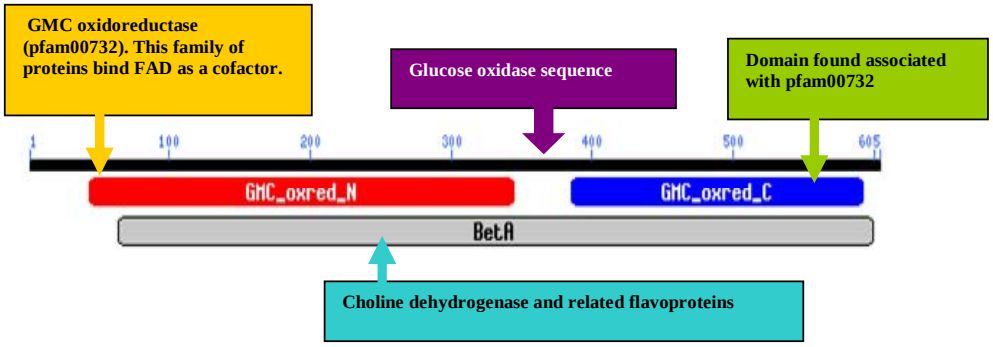

Figure 6.3: Examples of the conserved domains found between homologous enzymes.

oxidase (1.1.3.4) sequence. When this genetic sequence analysis was completed between the organisms that produce glucose oxidase, the following observations were found:

- Penicillium amagasakiense: six-fold higher affinity constant for β-D-glucose and ten-fold higher specificity constant than the enzyme from A. niger
- Aspergillus niger: more stable than P. amagasakiense
- High degree of conserved sequences in the FAD- and substrate-binding domains

We then developed the following plan for the site-directed mutagenesis activity:

- Target specific, dissimilar amino acids in the conserved FAD- and substrate-binding sites of A. niger for site-directed mutagenesis to mirror the comparable residues from Penicillium
- Specifically, those residues that exhibit consistent or recurring shifts in either the size, shape, charge, hydrogen-bonding capacity or chemical reactivity of their side-chains
- Target specific amino acids in the active sites of A. niger for saturation mutagenesis, i.e., the introduction of all possible amino acid substitutions at key residues
- Conduct mutations, use a recombinant protein expression system for enzyme production, screen for activity

An original identification of 17 mutation sites (see Figure 6.4) that are involved in the binding of the GOx to the glucose fuel were used as the starting point for the site-directed mutagenesis activity. Once these variants have been produced using targeted mutagenesis kits and expressed, a time based evaluation of the colorimetric response is used to determine the effectiveness of the variant.

6.1.2 Directed Evolution

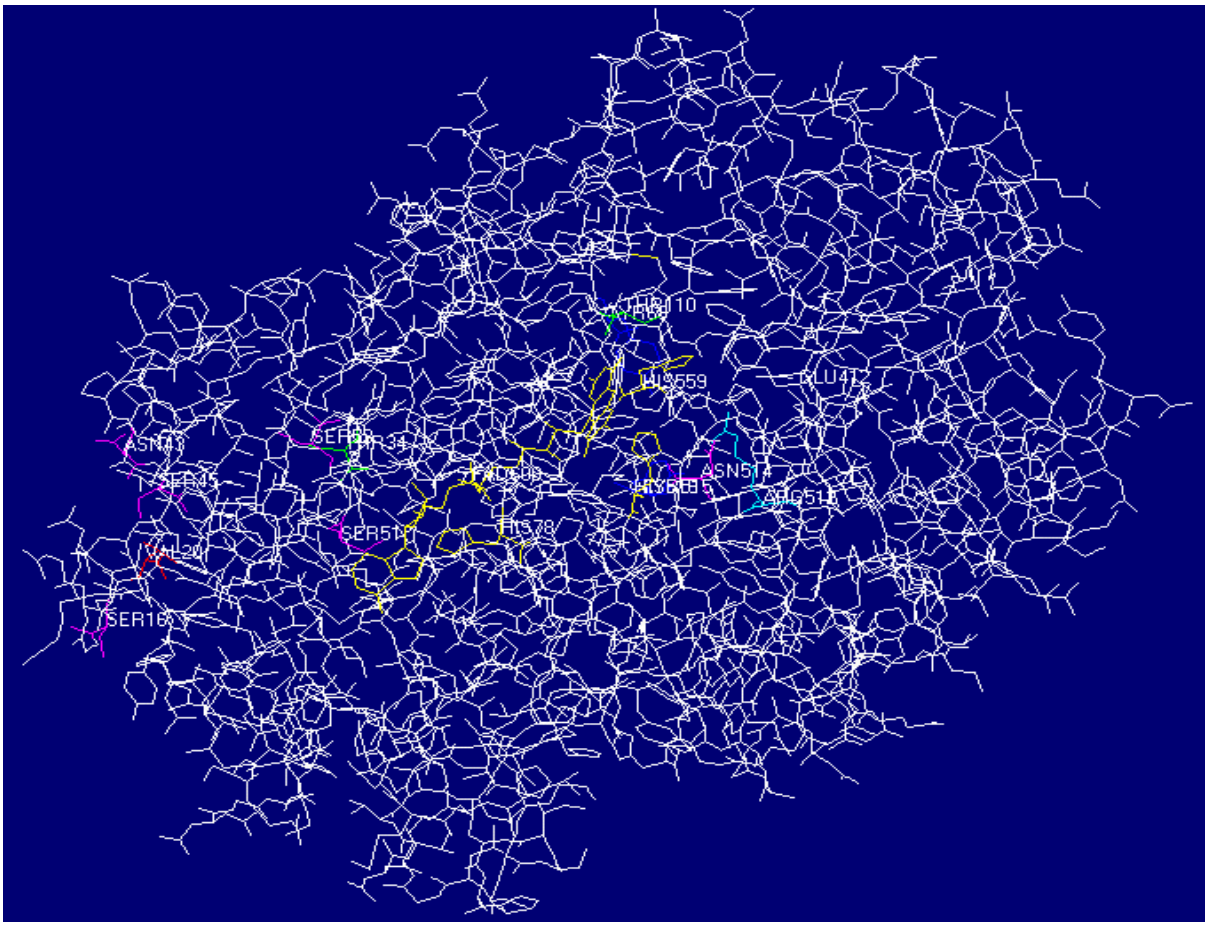

Figure 6.4: Molecular model of glucose oxidase, with the 17 initial binding amino acids identified for genetic modification. The yellow section in the center is the FAD binding site, a critical portion of the enzyme.

Directed evolution is a powerful technique by which the native functionality of the enzyme can be improved upon in terms of specific activity, pH tolerance, and thermostability (Figure 6.5).[58] Our efforts in directed evolution have centered on the introduction of random mutations in the genetic sequence through a process known as error-prone polymerase chain reaction (PCR). The process of error-prone PCR is just that

– the introduction of random mutations in the genetic sequence followed by the screening and isolation of the desired enzymes. To apply this technique effectively, however, a host organism and/or expression system that is capable of taking up the modified genetic

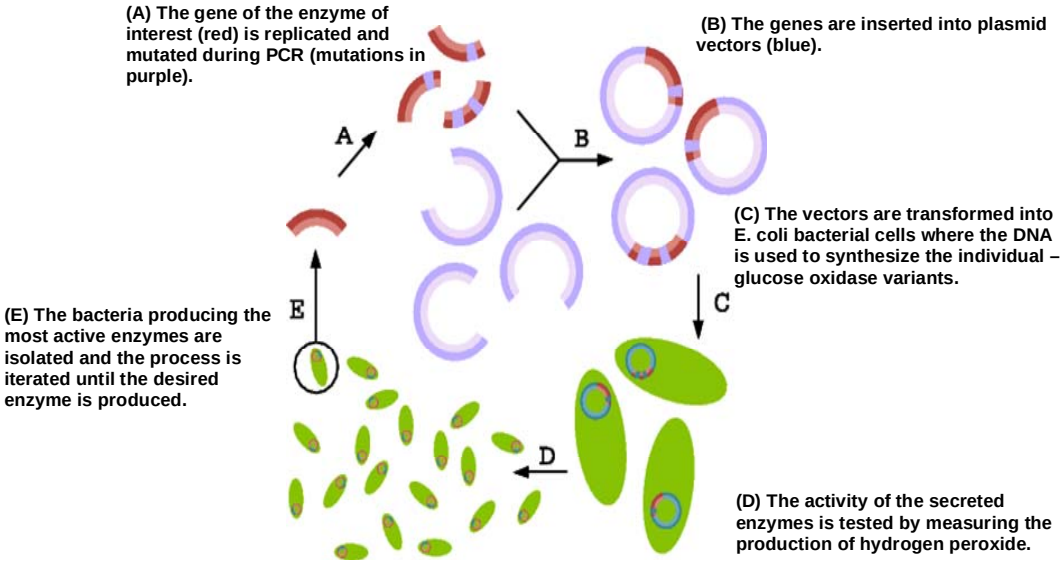

Figure 6.5: Process schematic for the directed evolution of enzymes. Adapted from *67H*http://www.curj.caltech.edu/archives/vol1/1002032/

sequence into its own DNA must be identified. Once this organism takes up the genetic variant, the cellular structure must then be capable of generating the variant glucose oxidase. Once the variant genes have been transformed into the appropriate expression system, the final step is to induce the expression of the enzyme and analyze its activity. An increase in enzyme performance indicates that the genetic modification is generating an enzyme with better properties than the parent enzyme. This step is known as assaying, and a different assay must be established for every performance characteristic, e.g., activity, pH tolerance, or temperature tolerance.

Enzyme	Method	Results	Expression Organism	Citation
subtilisin E	Error prone PCR	500x increase in activity	*B. subtilis*	You & Arnold (1996)
β-galactosidase	DNA shuffling	66x increase in activity	*E. coli*	Zhang *et.al.* (1997)

myoglobin	**Error prone PCR**	**25x increase in peroxidase activity**	***E. coli***	**Wan *et. al.* (1998)**
phospholipase A1	**Error prone PCR**	**11 oC increase in thermostability**	***E. coli***	**Song & Rhee (2000)**

Table 6.1: Examples of modified enzymes produced by directed evolution.

After screening has identified the genetic variants possessing the desired characteristics, the mutated DNA is recovered, Table 6.1 lists several examples obtained from the scientific literature demonstrating the effectiveness of this technique to significantly alter the operating characteristics of several enzymes. Directed evolution is an iterative technique, often requiring several rounds of mutations before the desired results are achieved. This technique generates thousands of mutants per iteration, and therefore a high-throughput process must be implemented to deal with the tens of thousands of mutants produced over the entire project length. This pipeline has been created and utilized at Sandia National Laboratories in less than 9 months of activity.

6.1.3 Gene Optimization and Recombinant Protein Expression

The correct source selection of the DNA used for the genetic engineering of enzymes is critical for mission success. We have ordered chemically synthesized genes encoding glucose oxidases derived from reported sequences of the enzymes found naturally in A. niger and P. amagasakiense. This DNA was obtained from a commercial vendor, DNA 2.0 (Menlo Park, CA). These synthesized sequences offer several advantages over the lengthy and complex isolation of the native genes in that they can be tailored a priori for the desired system of use. The developed sequences have been optimized in terms of rare codon usage for expression in multiple host organisms, undesirable restriction sites for ease of cloning, as well as modified N-terminal sequences for successful intra-cellular expression. In addition to full-length sequences two variants of each have been obtained. The variant sequence encodes for a truncated protein lacking the N-terminal signal peptide and a few more residues to aid in the expression of the recombinant protein in a variety of expression systems. The synthesized gene encoding the glucose oxidase is

inserted in a suitable GATEWAY© (Invitrogen, Inc.) entry vector which when shuttled into a suitable expression vector allows for expression in a number of in vivo hosts as well as in vitro systems. An example of the optimized genetic sequence obtained is presented in Figure 6.6.

In order to produce the enzyme in sufficient quantities to be analyzed and ultimately

GGCTCCGCGGCCGCCTTGTTTAACTTTAAGAAGGAGCCCTTCATAATGCAGACTCTGCTGGTGAG
CTCCCTGGTTGTGTCTCTGGCTGCAGCACTGCCACATTACATCCGTTCTAATGGTATCGAAGCAT
CTCTGCTGACTGATCCAAAAGACGTTTCTGGCCGTACCGTGGATTACATTATCGCAGGTGGTGGT
CTGACTGGTCTGACTACGGCAGCACGTCTGACTGAAAACCCGAACATTAGCGTGCTGGTAATCG
AAAGCGGTTCTTATGAAAGCGATCGTGGCCCAATCATTGAGGATCTGAACGCTTACGGTGATATT
TTCGGCTCCTCCGTTGATCATGCTTATGAGACTGTCGAGCTGGCGACTAACAACCAGACGGCCCT
GATCCGTTCTGGTAATGGTCTGGGTGGTTCCACGCTGGTTAATGGTGGTACTTGGACTCGTCCAC
ATAAAGCACAGGTGGACAGCTGGGAAACGGTTTTCGGCAACGAAGGCTGGAACTGGGATAATGT
CGCTGCGTATTCCCTGCAGGCAGAACGTGCACGTGCTCCAAACGCAAAACAGATCGCAGCAGGT
CACTATTTCAACGCTAGCTGTCACGGTGTTAACGGTACCGTACACGCTGGTCCACGTGATACTGG
TGATGATTACTCCCCTATTGTAAAGGCACTGATGAGCGCTGTTGAAGATCGTGGCGTTCCGACCA
AGAAAGACTTTGGTTGTGGTGATCCACATGGTGTTTCTATGTTCCCGAACACTCTGCACGAAGAC
CAGGTACGTAGCGATGCTGCACGTGAATGGCTGCTGCCAAACTATCAGCGTCCGAACCTGCAAG
TTCTGACCGGTCAATACGTGGGTAAAGTTCTGCTGTCTCAGAATGGTACCACTCCTCGTGCAGTA
GGCGTGGAATTTGGTACTCACAAAGGTAACACGCATAATGTGTACGCAAAACACGAAGTGCTGCT
GGCTGCTGGTTCTGCTGTCAGCCCAACTATCCTGGAGTATTCCGGTATCGGTATGAAGTCTATTC
TGGAACCTCTGGGCATCGACACTGTTGTTGACCTGCCAGTAGGCCTGAACCTGCAGGATCAAAC
TACTGCTACTGTTCGTAGCCGTATCACCTCTGCAGGTGCAGGCCAAGGTCAAGCAGCTTGGTTC
GCTACCTTCAACGAAACCTTCGGTGACTACTCCGAGAAAGCTCACGAACTGCTGAACACCAAACT
GGAACAGTGGGCGGAGGAAGCAGTTGCACGTGGCGGTTTCCATAACACTACTGCTCTGCTGATC
CAATACGAAAACTACCGTGATTGGATCGTCAATCACAATGTAGCATACAGCGAACTGTTTCTGGAT
ACCGCAGGCGTTGCATCTTTTGATGTTTGGGACCTGCTGCCGTTCACTCGTGGTTATGTTCATAT
CCTGGACAAGGACCCATATCTGCACCACTTCGCGTATGACCCACAATATTTCCTGAACGAACTGG
ACCTGCTGGGTCAAGCAGCAGCTACCCAACTGGCACGTAATATCAGCAATAGCGGTGCTATGCA
GACGTACTTCGCAGGTGAGACCATTCCTGGTGATAACCTGGCCTACGACGCAGATCTGAGCGCT
TGGACTGAATACATTCCATACCACTTCCGTCCGAACTACCACGGCGTTGGTACCTGTTCTATGAT
GCCGAAAGAGATGGGTGGTGTGGTTGACAATGCGGCTCGTGTATATGGTGTACAGGGTCTGCGT
GTCATCGACGGTTCCATCCCTCCAACTCAGATGTCTTCTCATGTGATGACTGTTTTCTACGCGATG
GCACTGAAGATCAGCGACGCTATTCTGGAAGATTACGCGAGCATGCAGTGAAAGGGTGGGCGCG
CCGAC

Figure 6.6: genetic sequence produced by DNA 2.0 based on the sequence of the enzyme produced in *Aspergillus niger*.

used in a fuel cell, the genetic sequence is placed in an appropriate expression system. These expression systems can be either cellular or cell-free in their mechanism of protein expression. We have identified three possible expression systems for use in our research effort:

1. Escherichia coli – Overall the simplest and fastest strategy. Mutated DNA will be cloned into specific expression vectors with appropriate promoters and active sites. These vectors will then be transformed into E. coli BL21 GOLD® (Stratagene, Inc) cells for simultaneous cloning and protein expression. The transformed cells will be plated

and individual colonies picked into 96-well plates. We will then induce expression and lyse (break-up) cells, followed by the appropriate screening protocols.

2. Saccharomyces cerevisiae– A technique that has been proven in the scientific literature as suitable for glucose oxidase expression, but hampered by low transformation efficiencies of yeast competent cells – an important factor for generating large mutant-gene libraries. Mutated DNA will be cloned into specific expression vectors with appropriate promoters and active sites. These vectors will then be transformed into INVSC1 yeast cells for protein expression. The transformed cells are then plated and individual colonies picked into 96-well plates. We will then induce expression and lyse cells, followed by the appropriate screening protocols.

3. Escherichia coli cell extract (Expressway™ Plus system from Invitrogen) – A new, commercially available system that allows for recombinant protein expression without involving the cellular machinery that may hinder that expression. It is a very convenient and rapid method to express and screen desired proteins in a 96-well plate format.

6.2 Enzyme Assay Development

Glucose oxidase (GOx) catalyzes the oxidation of β-D-glucose to D-glucono-1,5-lactone and hydrogen peroxide, using molecular oxygen as the electron acceptor as shown in the following reaction scheme:

$$\beta\text{-D-glucose} + GOx\text{–}FAD + H_2O \leftrightarrow GOx\text{–}FADH_2 + \text{gluconolactone} + 2H^+ + 2e^-$$

$$GOx - FADH_2 + O_2 + 2H^+ + 2e^- \rightarrow GOx - FAD + H_2O_2$$

The production of hydrogen peroxide can be monitored with several different techniques that lend themselves to their utilization as an assay. We have developed protocols for two different assays for use in the screening of genetic variants that key off the production of hydrogen peroxide – colorimetric and electrochemical. The assays are absolutely essential in the screening and identification of desired mutants, and must be normalized to some standard in order to be evaluated correctly.

6.2.1 Colorimetric Assay

The glucose oxidase colorimetric assay we selected for use is the Amplex Red Glucose Oxidase Assay (Molecular Probes, Eugene, OR). This assay was chosen because it is a fairly simple assay and is readily commercially available. The Amplex Red Glucose Oxidase Assay Kit provides a sensitive one-step method for detecting

glucose oxidase. The Amplex Red reagent (10-acetyl-3,7-dihydroxyphenoxazine) is colorless, stable and an extremely versatile peroxidase substrate. Since peroxidase and glucose oxidase mediated reactions can be coupled, it is possible to measure glucose oxidase activity in either a continuous or discontinuous assay. For the Amplex Red Glucose Oxidase Assay a standard curve with glucose oxidase concentrations ranging from 0-10mU/ml was constructed. The reaction solution consisted of 50µL of protein sample combined with 50µL of working solution. Three repetitions were performed and measured for each concentration for statistical analysis purposes (Figure 6.7). This experiment demonstrates that the Amplex Red assay is effective in determining the presence of glucose oxidase activity and amenable to high-throughput application. This assay is, therefore, the dominant mode of colorimetric analysis utilized over our course of research.

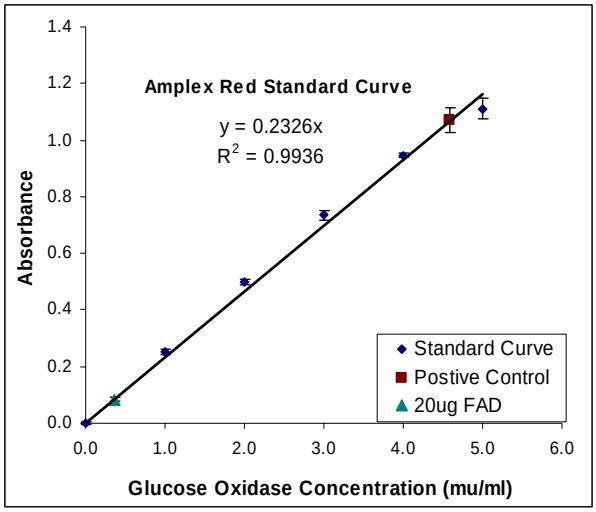

Figure 6.7: Amplex Red standard curve demonstrating the relationship between glucose oxidase concentration and measured activity.

6.2.2 Electrochemical Assay

The electrochemical measurement of the production of hydrogen peroxide provides a very useful, sensitive method for studying the kinetics of electron transfer between glucose oxidase and oxygen. Enzyme kinetic data, i.e., v (initial velocity/reaction rate), V_{max}, K_m, K_{cat} (turnover number), can be calculated from these measurements.

Initial reaction (or catalysis) rate (v) is the number of moles of product formed per second.

V_{max} is the maximum velocity of the reaction.

K_m is the concentration of substrate at which the velocity of the reaction is half Vmax, and is referred to as the Michaelis-Menten constant.

K_{cat} (turnover number) reflects the molecular activity of the enzyme, specifically, the number of moles of substrate transformed into product per minute per mole of enzyme when the enzyme is fully saturated with substrate.

In addition to elucidating kinetic information, electrochemical analysis can also provide information about the stability of the enzyme as a function of temperature, pH and ionic strength. This data is shown schematically in Figure 6.8.

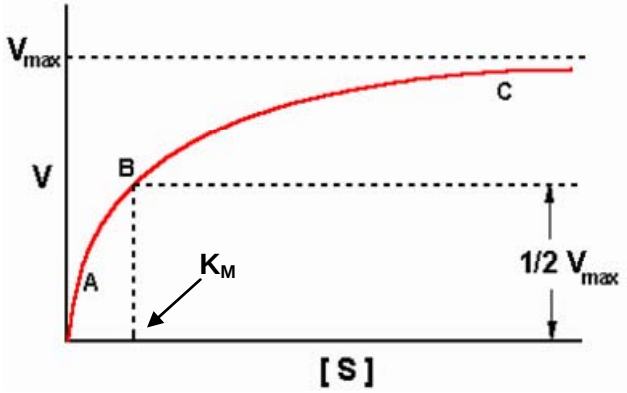

Figure 6.8: Graphical analysis of reaction rate (V) versus substrate concentration [S] produces a hyperbolic rate plot

To determine the validity and accuracy of using an electrochemical assay to measure glucose oxidase activity, a three-macroelectrode system (i.e., platinum working, Ag/AgCl reference and platinum auxiliary microelectrodes; 6 ml total volume of sample using phosphate buffer, pH 7.0) was used to measure the current flow between the electrodes, when polarized with a potential of +660 mV (vs. Ag/AgCl). This current is directly proportional to the H_2O_2 in the sample (Figure 6.9). From these measurements initial reaction rates were calculated for different concentrations of commercial glucose oxidase (Biozyme, CA). Initial reaction rate/velocity (v) is directly proportional to [E] at all substrate concentrations. As [GOx] increased, velocity increased.

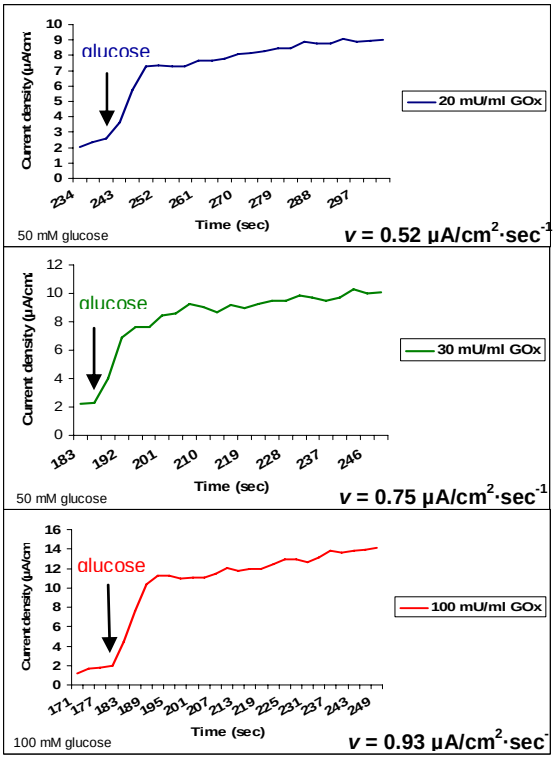

Figure 6.9: Electrochemical response to varying levels of glucose oxidase

New hardware is being designed to support an automated microelectrode assay station that can do multiple assays in a 96-well microplate. Future studies will validate the use of an electrochemical assay to obtain kinetic data in a multiplexed micro-system amenable to use in a high-throughput regimen.

To properly select mutants with improved enzymatic activity for further iterations of mutagenesis and use as catalyst in a fuel cell, a quantitative and reproducible activity assay is required. Typically, colorimetric assays are used to measure enzymatic activity. However, colorimetric activity assay can be unreliable. These assays generally rely on secondary enzymes, chemical reagents, or dyes to report activity. The environment and chemical sensitivity of these reagents, in addition to batch to batch regent variation may lead to inconsistent results. Inconsistent agreement between different colorimetric assays is also possible and was observed in this work. Finally, accurate kinetic rate data is often unattainable using colorimetric assays.

To overcome these challenges an electrochemical activity assay was developed. The mechanism of this activity assay entails the electrochemical oxidation of hydrogen peroxide produced by glucose oxidase during the enzymaticly catalyzed reaction (equation 6.1):

$$\text{glucose} + O_2 \rightarrow \text{gluconic acid} + H_2O_2 \qquad \text{Equation 6.1}$$

At a positively charged platinum electrode, hydrogen peroxide is oxidized and releases 2 electrons (equation 6.2):

$$H_2O_2 \rightarrow 2H^+ + O_2 + 2e^- \qquad \text{Equation 6.2}$$

The current measured as a result of hydrogen peroxide oxidation are directly related to peroxide concentration. This real-time measurement of product formation of the enzymatic reaction serves as a direct measurement of the enzymatic activity. Advantages of this electrochemical assay include that it is: 1) well characterized and reproducible, 2) does not depend on secondary enzymes or reporters, and 3) accurate kinetic rate data is obtainable as the measurement is direct and real-time.

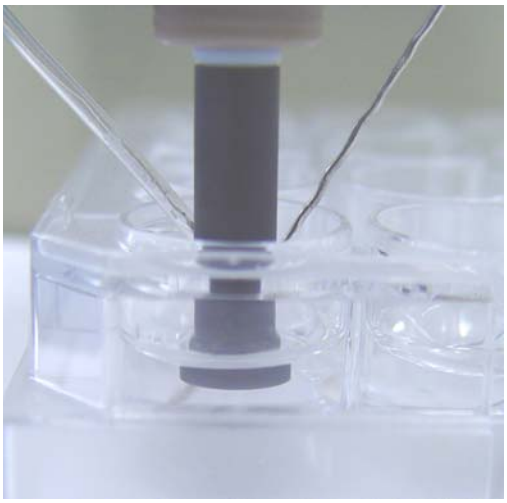

Figure 6.10: Electrochemical assay experimental setup. Pt rotating disk working electrode, Ag/AgCl (3M KCl) reference electrode, Pt wire counter electrode, in a 24 microwell plate with 1.8 mL working volume.

The electrochemical assay experimental setup (see Figure 6.10) and

protocol consisted of a 3 mm diameter rotating disk working electrode (Bioanalytical Systems; West Lafayette, IN) which was polarized at +700 mV vs. the Ag/AgCl (3M KCl) reference electrode (Microelectrodes, Inc.; Bedford, NH). A platinum wire was used as the counter electrode. The working electrode was rotated at 6000 rpm in a 24 microwell plate with 100 mM sodium potassium phosphate buffer, pH 6.8, as electrolyte solution. The ionic strength and pH of the electrolyte solution were optimized to generate the greatest current response during peroxide oxidation.[59] A Voltalab PGZ 402 potentiostat (Radiometer Analytical; Lyon, France) was used to control the potential and monitor the current response.

A peroxide calibration curve was obtained by measuring the current response for eleven different concentrations of peroxide. Runs were randomized and 3 replicates were performed. A highly reproducible linear current response was observed for concentrations of 1 μM through 1 mM peroxide (see Figure 6.11**)**. The assay sensitivity of 84.3 nA/μmolar H_2O_2 was similar to that reported by Heller and Kissinger of 84.5 nA/μmolar H_2O_2.[60] The detection limit of 1.7 mUnit GOx/mL was adequate for testing

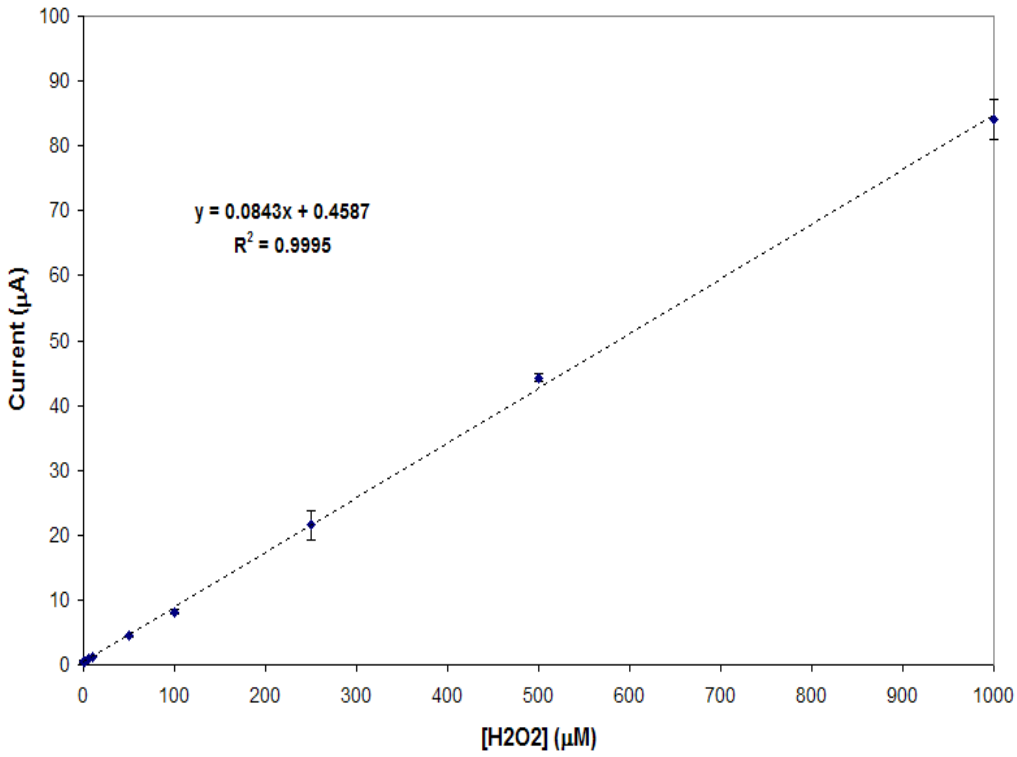

Figure 6.11 Hydrogen peroxide current response for electrochemical assay. Error bars are one standard deviation generated from 3 or 4 data points. Experimental runs were randomized. Inset is a close up of results from concentrations of 1 μM – 10 μM peroxide.

GOx expressed in *S. cerevisiae* culture without sample pretreatment. Controls for glucose oxidase activity assay were preformed using commercially available glucose oxidase (Biozyme; South Wales, UK). The specific activity and kinetic rate parameters provide by Biozyme were compared to those obtained using the electrochemical assay. Experimental conditions for glucose oxidase activity assay were identical to those described above for the peroxide current response with the exception that glucose at various concentrations was added to the electrolyte solution for polarizing the electrode. A μL volume of glucose oxidase was injected into the microwell after a steady state current response had been obtained at +700 mV vs. the reference electrode). The maximum slope of the initial 3-10 seconds after injection of enzyme was used to determine the initial rate velocity, v ($[H_2O_2]$/min). Initial rate velocities obtained at several different glucose concentrations were used to calculate the enzymatic activity kinetic parameters. The kinetic parameters obtained experimentally for Biozyme glucose oxidase agreed closely (< ±10%) with those provided by the manufacturer. Activity assay positive controls of Biozyme glucose oxidase were preformed before assays of SNL produced glucose oxidase.

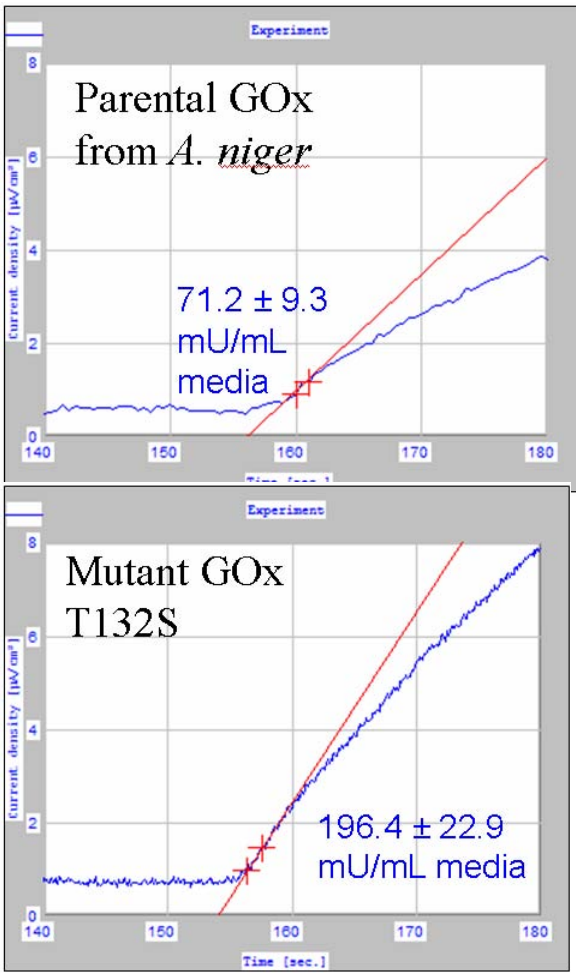

Figure 6.12: Initial rate current response vs. time for SNL produced parental glucose oxidase (above) and SNL produced mutant T132S glucose oxidase (below). Injection consisted of concentrated media supernatant.

Activity assays performed on induced *S. cerevisiae* cultures produced at SNL verified that parental and mutant glucose oxidase was expressed and active. Uninduced *S. cerevisiae* cultures (negative controls) showed no peroxide formation via the electrochemical assay.

This also demonstrated that the electrochemical assay is highly specific among proteins that yeast naturally produces and secretes into the culture media. Initial rate measurements were used to compare the specific activity of the parental glucose oxidase strain to SNL produced mutant T132S glucose oxidase. Results of the electrochemical assays with 2 replicates were a specific activity of 71.2 ± 9.3 mU/mL culture media for the parental stain, and 196.4 ± 22.9 mU/mL culture media for mutant T132S (see Figure 6.12). This is a nearly 3 fold improvement in specific activity of mutant T132S over the wild type parental glucose oxidase.

6.3 Recombinant Protein Expression

We attempted to express the glucose oxidase in three separate systems and identify which one was most suitable for our genetic engineering activity. Our results (Figure 6.13) indicated that two out of the three systems are successful in the expression of recombinant glucose oxidase.

The system that involves the use of *E. coli* as an expression system did not show any glucose oxidase activity after induction, and based on other reports in the scientific

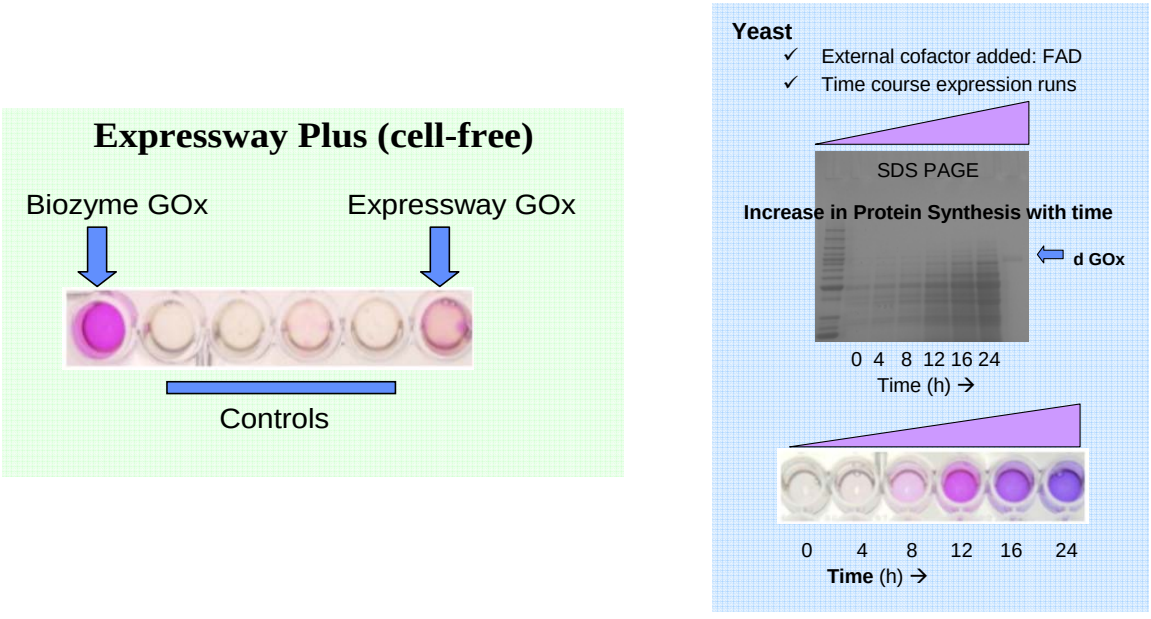

Figure 6.13: Results obtained from the expression of glucose oxidase in (l) Expressway Plus system available from Invitrogen, and (r) the yeast *S. cerevisiae* that also demonstrates the expected time dependence on the level of protein expression. Both sets of data were obtained using the Amplex Red assay.

literature, [61] we determined that the protein does not properly fold in *E. coli* to maintain enzymatic activity. The yeast system produced active protein, as did the cell-free system.

Based on these results, it was decided that the cell-free system would be used in the site-directed mutagenesis activity based on ease of use, whereas the directed evolution effort would utilize the yeast recombinant protein expression system based on cost and scalability.

6.3.1 Site-Directed Mutagenesis

The original identification of 17 mutation sites was targeted for mutation using site-directed mutagenesis protocols. Once the mutants had been generated, the resultant proteins were expressed using the Expressway Plus system. This round of mutations yielded approximately 1200 mutants. Due to cost and time considerations, targeted mutants were selected for screening and analysis. We have analyzed approximately 30 of the mutants produced by this method. Of particular interest were the mutations targeted at changing the cofactor and substrate binding regions of the enzyme. Once the variants have been developed and expressed, a time based evaluation of the colorimetric response was used to determine the effectiveness of the variant. Some of the mutants showed considerable differences when compared to the parental gene type as shown in Figure 6.14.

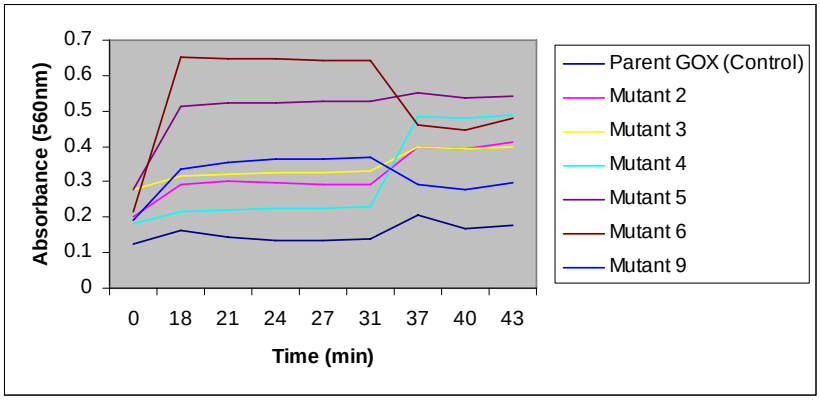

Figure 6.14: Plot showing the comparative activities of 6 mutants produced through site-directed mutagenesis as compared to the protein expressed from the parental gene. All measurements were conducted using the Amplex Red colorimetric assay.

As can be seen, there are differences not only in the maximum activity of the enzyme, but also changes in the times at which these maxima occur. This indicates that we are also affecting the enzyme kinetics through genetic modifications. Further examination of the variants and their time response characteristics compared to the native enzyme is shown in Table 6.2.

	Parental *A. niger* GOX (Control)	Mutant 2	Mutant 3	Mutant 4	Mutant 5	Mutant 6	Mutant 9
	Peak Time: 0:56 - 1:09	Peak Time: 1:50 - 2:02	Peak Time: 1:33 - 1:46	Peak Time: 1:22 - 1:36	Peak Time: 0:37 - 0:50	Peak Time: 0:18 - 0:31	Peak Time: 1:33 - 1:46
	0.327	0.449	0.446	0.577	0.55	0.652	0.624
	0.255	0.422	0.434	0.582	0.537	0.645	0.626
	0.254	0.43	0.429	0.583	0.544	0.645	0.638
	0.261	0.429	0.427	0.574	0.545	0.642	0.643
	0.257	0.425	0.432	0.56	0.542	0.642	0.648
Mean	**0.271**	**0.431**	**0.434**	**0.575**	**0.544**	**0.645**	**0.636**
Std Dev	**0.032**	**0.011**	**0.007**	**0.009**	**0.004**	**0.004**	**0.01**
t-test (*P*)		**7.83E-05**	**1.28E-04**	**2.97E-05**	**2.62E-05**	**7.35E-06**	**2.98E-05**

Table 6.2: Tabulated results of activity as a function of peak time for parental enzyme and selected mutants

One variant in particular stands out, designated as mutant 6 in Table 6.2. This variant reaches its peak activity in one-third the time of the parent, and also reaches a peak absorbance/activity that is two to three times higher than the parent enzyme. This mutant was sequenced to determine the exact genetic mutation that had taken place. Sequencing revealed that a single point mutation had occurred that replaced a threonine amino acid with a serine amino acid. This mutation occurred at a flavin adenine dinucleotide (FAD) binding site (the shorthand for this mutation is T132S). From these results, it is clear that variants can be developed through site-directed mutagenesis that are significantly more active with glucose than the parental glucose oxidase.

6.3.2 Directed Evolution

The work involving the introductions was conducted for two generations of mutants numbering 3000 colonies in each. We transformed, grew, induced and screened for increased glucose oxidase activity when compared to parental gene type. The yeast cells were then lysed and the protein released and analyzed for activity. The comparison of the ABTS and Amplex Red assays in one 96-well screen of mutants produced and screened for activity is presented in Figure 6.15.

There is good general agreement between the two assays in terms of enzymes that are active after mutation. A clearer comparison between the parental and mutant enzyme is presented in Figure 6.16, which compares the relative normalized activity levels from a

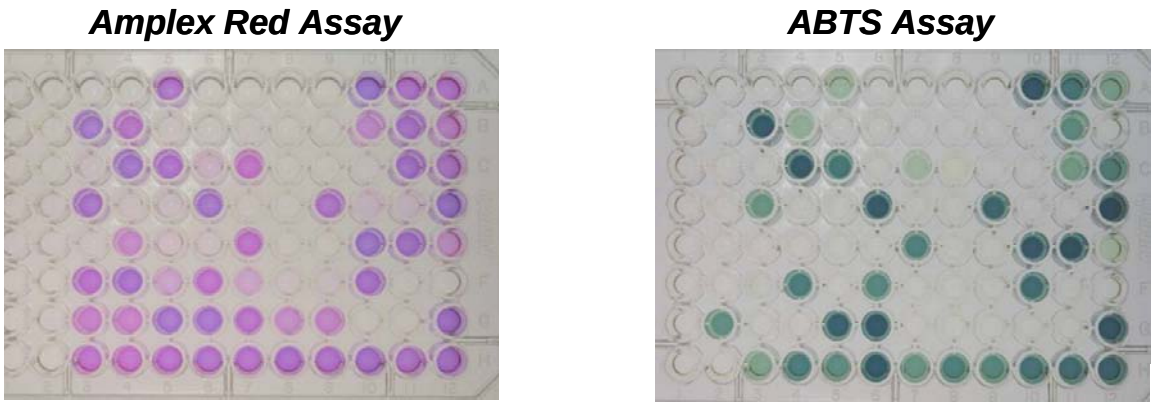

Figure 6.15: Comparison of results obtained from colorimetric assays (Amplex Red and ABTS) of glucose oxidase mutant enzymes expressed in yeast, recovered, and after glucose addition.

selection of mutants and the wild type enzyme. It can be seen that several of the mutant enzymes generated by this approach indicate higher activity than the wild type enzyme. These mutants would then be selected as the starting point for further mutations in subsequent rounds of mutagenesis and screening until an ideal mutant enzyme capable of enhanced direct electron transfer is produced and isolated.

We have demonstrated the feasibility of genetic engineering to produce improved enzymes for use in a fuel cell designed to run on glucose. We have utilized random mutagenesis approaches to insert mutations into the genes responsible for the expression of glucose oxidase. We have found two recombinant protein expression systems that can produce these mutant enzymes in sufficient quantities to be detected through both electrochemical and colorimetric assays.

We have identified a specific mutant through the site-directed work that appears to possess a higher activity when compared to the wild type. The random mutagenesis work has

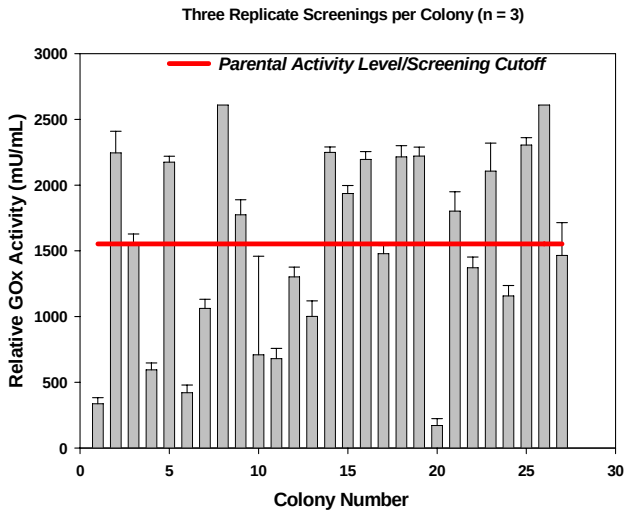

Figure 6.16: Bar chart of enzyme activity of mutants compared to baseline activity of wild type.

identified several candidate mutants that can be used as a starting point for further mutations and screening using this technique. We have also established a high-throughput pipeline for protein expression and screening that is capable of handling thousands of mutations per generation. These results are the first important steps towards the realization of an enzyme capable of producing significant amounts of power for extended periods of time in a microsystem format.

6.3.3 Protein Purification

Purification of recombinant glucose oxidase was achieved by using a tetradentate nickel chelate (Ni-NTA) purification system from Invitrogen Corporation (Carlsbad, CA). The system is designed for purification of recombinant fusion proteins that are tagged with six tandem histidine residues by affinity to Ni^{2+} ions.

After 24-hour growth in 50mls of YP-Gal induction media the soluble his-tagged glucose oxidase was harvested by centrifugation at 1400xg. The media was subsequently dialyzed with 50mM NaH_2PO_4 buffer pH 8.0 to remove residual amino acids and concentrated down to several milliliters. Purification was carried out under native conditions essentially as described in Invitrogen's Ni-NTA Purification Instruction

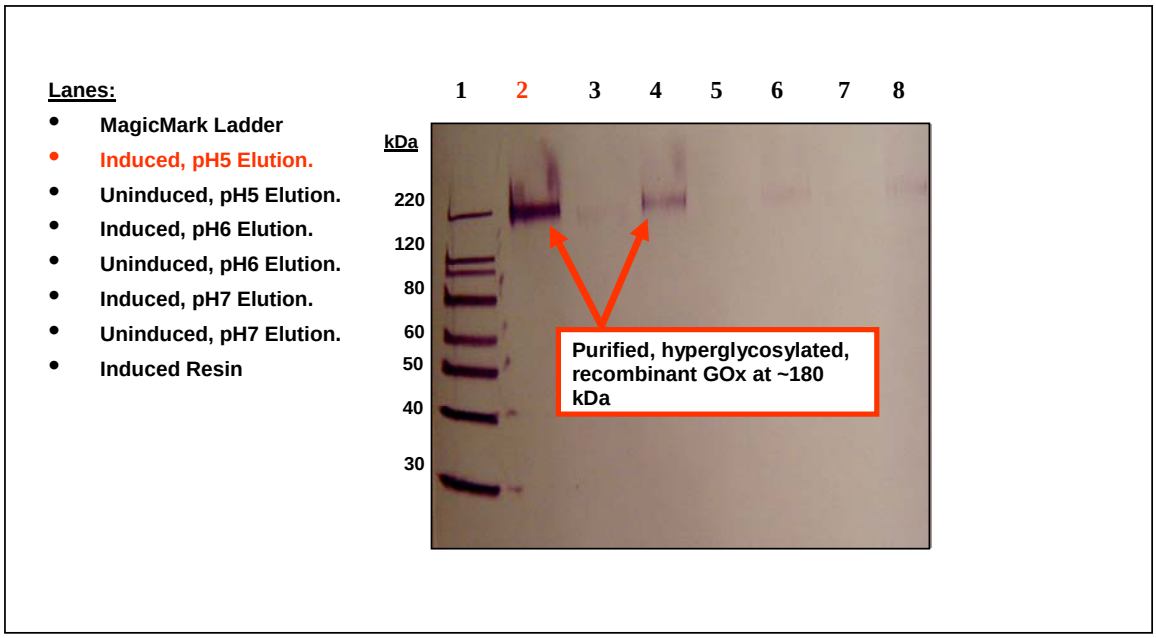

Figure 6.17: Gel Chromatograph of purified protein, showning induced and uninduced modified protein after successive elutions to remove the protein from the purification column.

Manual with slight modifications. Briefly, 1ml of Ni-NTA resin was added to polypropylene columns, washed and then equilibrated with 50mM NaH_2PO_4 buffer containing 20mM imidazole (native binding buffer). Concentrated glucose oxidase samples were brought to 3ml volumes using sddH_20 and then 3mls of native binding buffer was added. Samples were incubated for 1hour, 25°C with mixing on a Nutator. After washes the purified glucose oxidase was eluted off the resin using 1.5 mls of an elution buffer consisting of 50mM NaH_2PO_4, 250 mm imidazole pH 5.0. The resin was incubated in the elution buffer for 15 minutes with mixing.

The presence of the 6X histidine and V5 epitope tags allowed for the use of affinity chromatography and immunodetection as tools to evaluate the presence of recombinant glucose oxidase in the purified sample. Post purification concentration was done and an aliquot was then removed for SDS-PAGE. Samples were run on 10-20% Tris-Glycine gels for 1 hour. The proteins were then transferred and immobilized onto a nitrocellulose membrane via standard Western blot procedure followed by immunodetection using an anti-V5 (C-term)-AP antibody and Invitrogen's WesternBreeze® Chromogenic Immunodetection Kit: After blocking, the membrane was incubated with 15ml of a 1:2000 dilution of anti-V5 (C-term)-AP primary antibody. A secondary alakalike phosphatase conjugated anti-IgG antibody (supplied) was used to visualize the Magic Mark Protein standard ladder. After washing the membrane was incubated 10ml of BCIP/NBT chromogenic substrate for alkaline phosphatase. Purple bands representing epitope tagged proteins appeared after approximately 10 minutes, as shown in Figure 6.17. Hyperglycosylated recombinant glucose oxidase was positively identified at ~180kDa.

7. System Engineering

As the circuitry contained in electronic products becomes increasingly smaller and more powerful, the power source is rapidly becoming the limiting factor in reducing overall product size and weight. This has led to a substantial worldwide effort to develop alternative sources of electrical power called fuel cells. These derive energy from organic compounds, typically using catalysts at the anode and cathode to produce electrons and water from alcohols or carbohydrate (sugar) solutions.

While alcohol-based fuel cells are now becoming available commercially, their use is limited by the availability of sources of high-purity liquid fuel. Unfortunately, in some applications, the weight and logistical requirements for producing, transporting, & packaging a specially produced liquid fuel becomes problematic. In these situations, carbohydrate-based fuels cells are very attractive, as fuel can be derived from the environment, e.g., tree sap, or obtained from local food supplies, e.g., Coke®, or brought in as lightweight powder to be mixed with locally-available water, e.g., Kool-Aid®.

7.1 The Electronic Problem

Batteries and power supplies used to provide power to electronic devices have well-characterized voltage vs. current relationships (I/V characteristics), and exhibit relatively low impedances (milliohm) at high frequencies. Carbohydrate-based fuel cells, in contrast, are expected to exhibit significant variability in their electrochemical performance based on a number of uncontrollable environmental variables, making the fuel cell unsuitable for directly driving electronic circuitry. In field applications, for example, the fuel source is likely to be variable in concentration, especially where it is environmentally derived or reconstituted with water. The catalytic reactions are sensitive to variations in pH and are highly temperature-dependent. In addition, the catalysis of carbohydrates is generally not complete, producing complex byproducts that can reduce fuel cell performance over time, in a process known as poisoning.

This electrochemical variability manifests itself as variations in electrical power output, the output voltage, and the apparent electrical impedance of the fuel cell. Furthermore, the maximum fuel cell open-circuit voltage is limited by electrochemistry to around 0.7V and drops quickly as current is drawn to a peak power point of ~0.33V. Because electronic circuits require more than a forward-biased diode drop (~0.6V for proper operation and generally require 1.8-2.0V minimum, the fuel cell output power must be converted to a higher operating voltage using a highly efficient voltage step-up converter.

7.2 Commercial Off-the-Shelf DC-DC Converters

The performance of COTS DC-DC converters was analyzed to determine whether their design was appropriate for use with the fuel cell. Of the products available in December 2003, the Maxim's MAX1675 offered the highest efficiency with the lower

quiescent power consumption. The datasheet claimed operation down to 0.7V with a 94% efficiency at 200mA. Closer examination of the performance curves revealed that the efficiency was a strong function of power output. As the expected operating voltage and power levels were far below the IC's design points, the converter was analyzed in the laboratory.

The MAX 1675 was tested using a 2V input, assuming that a series configuration of six fuel cells could provide a minimum of 0.33V each. As discussed later, while a series

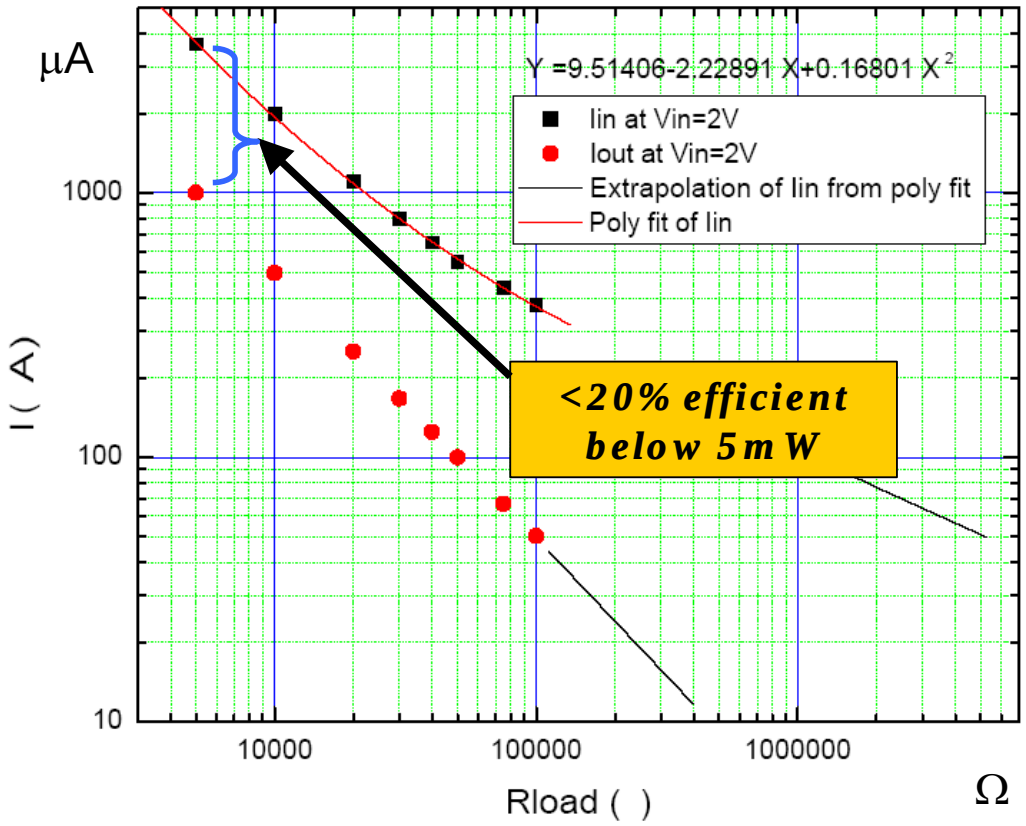

Figure 7.1: Performance of MAX1675 Under BMFC Conditions.

configuration is not appropriate for steady state operation due to electrolysis effects, this assumption provided a best-case starting point. The output power was measured using different load resistors and the results plotted in Figure 7.1. Because the output voltage remained constant at 2V, the power output is greatest at the left side of the figure, where the resistances were the lowest. The bracket overlay indicates that for a 5mW power output, the converter is less than 20% efficient. If the plots were extrapolated to the left

(higher powers), the two lines get closer—indicating efficiencies approaching the 94% given in the specification sheet. However, the BMFC operating region lies at the 5mW and lower power points (to the right), where efficiencies start off at below 20%. Furthermore, in actual applications the input voltage must be provided from an array of fuel cells connected in parallel, i.e., closer to the 0.33V peak power output of the fuel cell. Other tests indicated the minimum operating voltage at the 5mW level was 0.8 volts. Therefore, it was concluded that the best-available COTS DC-DC converter was unsuitable as both the BMFC output voltages and converter efficiencies are too low.

7.3 PowerManager: Power Conditioning Matched to BMFCs

The PowerManager described next is simply an electronic circuit that provides the power conditioning and impedance matching necessary to convert the variable output of the fuel cell to a stable, low-impedance voltage source necessary for powering application electronic circuitry. The voltage step-up principles are similar to the capacitor switching methods used in commercial devices, but the circuit is controlled using a microcontroller using Microchip's nanoWatt technology. This allows customized state control and operation management using very low quiescent power consumption.

The PowerManager employs switches that connect an array of fuel cells in series to allow startup and then switches to a parallel configuration to reduce losses. It uses frequency and duty-cycle variations in charge-pumping switches to raise the voltage to a desired set point and regulate it under variable application loads. Control of long-term performance in the presence of poisoning is achieved by allowing individual cells to be disconnected from the circuit, allowing it to rise to open-circuit potential ("rest state") while the remaining cells provide application power. A disconnected cell may also be shorted or connected in reverse for a brief time to the output capacitor stack to allow electrochemical "cleaning." All duty cycles and timing are controllable in software.

7.3.1 Startup

The startup phase of the PowerManager relies on the complementary properties of JFETs and MOSFETs to provide the appropriate series or parallel connection. The electrical schematic of the Power Manager is provided separately as an Adobe Acrobat file. The fuel cells are shown as boxes on the left side, with anode and cathode connections at the top and bottom, respectively.

In the unpowered state, the main capacitor bank (Q12-Q28) that is connected across the output voltage V+ has been discharged and V+ is 0 V. The gates of MOSFETs Q11, Q12-Q17, Q20-Q25, and Q27-Q32, and Qload are connected to the outputs of the microcontroller. Since the microcontroller supply, V+ is 0 V, the gate voltages are zero and the MOSFETs are not conducting. The gate voltages of JFETs Q2-Q8 are equal to the source voltage (0 V), turning them on with a series resistance of approximately 18 ohms. The conducting JFETs connect the six fuel cells in series and to V+ (Q2) and signal ground (Q8).

This circuitry therefore configures the fuel cells at startup in a series configuration connected across the main capacitor bank. When J3 is inserted (the "on" switch is closed), the series fuel cell array will begin to charge the capacitor bank with a time constant determined by the series resistance of the JFETs, the total bank capacitance, and the current available from the fuel cell when loaded by 126 ohms (18 ohms/JFET x 7 JFETs) of the fuel cells. By isolating V+ from the application circuit through Qload, the rate of capacitor charging is maximized.

As the capacitor bank charges, V+ will increase, pulling the JFET gate voltages up through R5 to keep them conducting to maintain the series connection. In this circuit, the capacitor bank has a total capacitance of about 100 uF (C29 in parallel with series C13-C24). Charging it to 2 V will require (Q=CV) 200 uCoulombs. Assuming an average fuel cell current of 0.01 mA (across a range of voltages from zero to ~0.33 V ((2 V – 126 ohms x 0.01 mA)/6), the fuel cells will charge the bank in 20 seconds.

When V+ reaches 2 V, the microcontroller (Microchip 16F737) will start operating. It is configured in RC_Run mode which consumes 7 uA @2V, requiring ~14 uW of power. At this current level, the seven JFETs will consume 6 nW (7 uA through 126 ohms).

7.3.2 Series to Parallel Reconfiguration

Once the series-connected fuel cells charge the capacitor stack, the PowerManager changes the fuel cell array to a parallel configuration. This reconfiguration is necessary to prevent electrolysis between fuel cells in the water-based fuel. Because the fuel is water-based and is delivered to fuel cells from a common supply, electrolysis occurs wherever a there is a voltage difference of greater than 1.23 V. In a six-cell series stack at 2 V total output, for example, the anodes of the top fuel cell and the bottom fuel cell

will a differential of ~1.67 V—well above the electrolysis threshold. Because achieving the 2 V requirement to start-up the microcontroller requires a series configuration, the PowerManager tolerates electrolysis for a brief period during which it initially charges the capacitor bank. Once the cells are connected in parallel, the voltage is no longer large enough to maintain the capacitor bank voltage V+ at 2 V required by both the microcontroller and the application load, although the total current available is increased six-fold. The PowerManager uses capacitor switching to individually charge series-connected capacitors to boost voltage.

Once the microcontroller starts running, it configures a timer to output a four-bit counter output on pins DIO-A0-A4. For each count, the analog multiplexers U7-8, and U9-10, connect their common terminal to the positive/negative end of the electrolytic capacitor. Charging the 16 capacitors (C13-C28) individually and then drawing power from the end of the series bank accomplishes a 16x increase in voltage. Note that the ground reference for the series bank is four capacitors above the lowest potential (between C24 & C25). In steady-state operation assuming a 0.33 V fuel cell output, the total differential voltage across the stack rises to 5.28 V (16 x 0.33 V), but is distributed as a +3.96 V and –1.32 V voltage due to the ground reference.

The common terminals of the multiplexers are connected to fuel cell anodes/cathodes when the EN_GFCx lines for the associated MOSFETs are high. If multiple EN_GFCx lines are high, the associated fuel cells are effectively connected in parallel, and their current output is delivered to the capacitor selected by the DIO lines. Conversely, a specific cell is disconnected from the parallel configuration by keeping EN_GFCx low.

The ability to disconnect individual fuel cells in steady state can be used to increase lifetime, but is also critical to making the transition from series to parallel configuration. When the capacitor bank is fully charged in the series configuration, the JFETs are all conducting, as their gates are pulled higher than any of their source voltages by R5. This connects the low fuel cell cathode to ground, producing a single-ended source through Q8(on).

However, the switching network will only function if the common multiplexer inputs are floating. Initially, all fuel cells are disconnected from the multiplexers (EN_GFCx=0). After the microcontroller starts the switching operation, it connects the

JFET gate voltages to the V- supply by setting ~EN_SERIES low (Q11). Since the series configuration only charges the positive side of the capacitor bank (C13-24), V- is at zero volts (assuming C30 was discharged through R16). Now, because the JFET sources are at different voltages (in the series stack), they will turn off according to their source-gate voltage differential. Assuming 0.33 V per fuel cell, the source voltages for fuel cells from top to bottom will be 2.0, 1.67, 1.33, 1.0, 0.67, 0.33 V, respectively. The resulting Vgs will turn off the JFETs to varying degrees as they are pinched off (-1.67, -1.33, -1.0, -0.67, -0.33, -0 V, respectively for V- = 0V). The JFETs near the topmost fuel cell, i.e., Q2, Q3, will be effectively turned off, disconnecting this fuel cell from the series array. The microcontroller can enable the topmost fuel cell, connecting it to the common anode/cathode multiplexer inputs. The switching process thus enabled can begin developing the negative supply voltage, reducing V- from 0 V to more negative values. As V- decreases, Vgs for other JFETs increase, increasing the isolation from the series configuration. At steady state with a V- = -1.32 V, all the JFETs will be turned off (assuming Vgs(off) specification for the JFET <- 1.32 V), isolating all the fuel cells, and allowing them all to be enabled to contribute current to the switching upconverter.

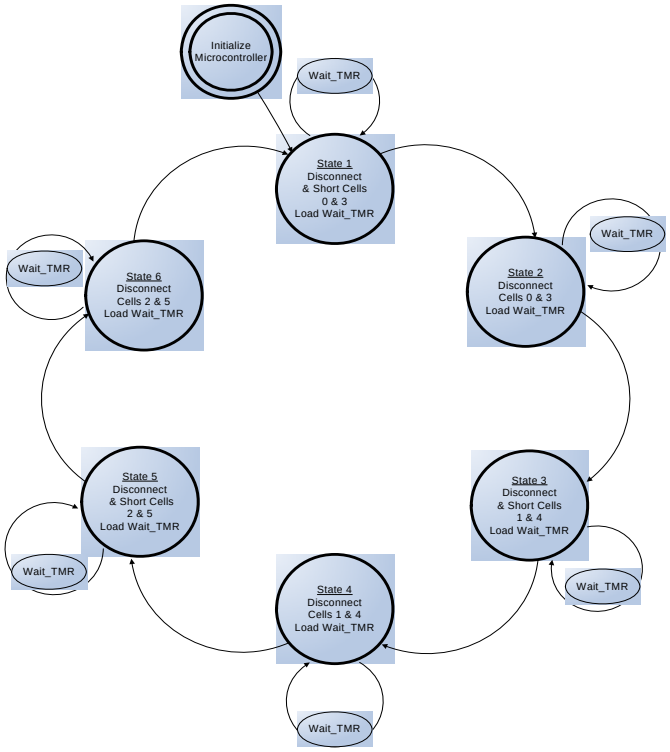

Figure 7.2: State Diagram of Logic for Conditioning Fuel Cells in an Array.

7.3.3 Software for Steady State Operation and Lifetime Control

Once operating in steady state by switching the parallel-connected fuel cells, application power would be enabled through a MOSFET, e.g., Qload (not shown). The output voltage, V+, is continuously compared with a

preset threshold (R2, R3) using the microcontroller comparator (pins RA0/AN0 and RA2/AN2) and the voltage reference U1 (1.0 V). As the application load varies, the threshold crossing would be detected by the microcontroller, which could adjust the frequency and/or duty cycle of switching, or could enable/disable individual fuel cells (to prolong lifetime when power requirements are low).

In addition to disconnecting individual cells during steady state operation, lifetime can also be enhanced by periodic conditioning of individual cells in the array. Conditioning consists of a specific sequence and timing of operating a cell under load, without a load, under short-circuit conditions, or by applying reverse voltage pulses. To accomplish the continuous conditioning of individual cells (or groups of cells) in the array, an internal state machine is built into the microcontroller, running the cells through a preset sequence of conditioning configurations.

The firmware developed for the Power Manager actively controls the life cycle for each fuel cell. During the cycle two cells will be changed simultaneously. The life cycle of the cells go through three distinct phases. Phase one is a shorting phase in which the cells are electrically disconnected from the parallel stack and shorted for a duration of thirty seconds. Phase two is a disconnect phase that electrically disconnects the cells 270 seconds. Phase three reconnects the cells to the parallel stack providing power to the Power Manager circuitry and lasts for 600 seconds. Total cycle time for all three phases to complete is 900 seconds.

The 6-state diagram is given in Figure 7.2 and a time-sequence diagram given in Figure 7.3. In each state, two of the 6 cells in the array is being conditioned, either with an open- or short-circuit. The system remains in each state for a preset amount of time,

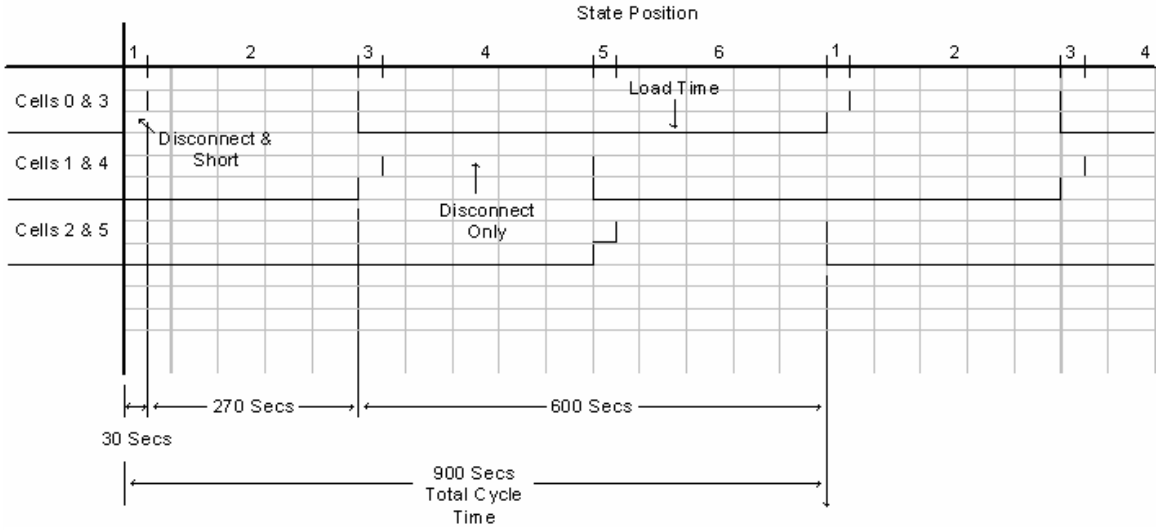

Figure 7.3: Time-Sequence Diagram for State Machine.

progressing to the next state upon expiration of a timer. The sequence repeats indefinitely.

7.3.4 Detailed Program Flow

The line numbers in the following description refer to the program listing in the Appendix.

Lines 10 through 87 define the microcontroller configuration, variables, timers, and port pin names. The configuration word at line 18 set the microcontroller to run off an internal oscillator and disables several other functions such as brown out detect, watch dog timer and power up timer. Disabling these functions decreases power consumed by the microcontroller. Lines 50 to 87 list the different variables used. There are timer-preset variables, interrupt masks, and data registers. The timer-preset variables can be adjusted to maintain precise timing of each phase of the fuel cell cycle. Interrupt masks disable or enable different interrupts depending on what state the program is in. Data registers are used as counters or data storage.

Lines 90 to 98 direct program flow. The vector 0x00 at line 92 jumps to CONFIG at line 102. The vector 0x04 at line 95 jumps to the interrupt routine, which will be detailed later. Starting at line 102, the microcontroller configures I/O ports, internal oscillator

settings, and interrupts. Line 111 switches from bank 0 to bank1, which allows special function registers (SFRs) to be configured. The first SFR to be configured is the Option Register at line 114. The Option Register is loaded with value 0xC0, which disables PORTB pull-up resistors and selects interrupts to occur on the rising edge of the RB0 pin. TRIS C is loaded with value 0xC0 at line 115. This directs PORTC pins as either digital input or output. At line 118, the next SFR configured is the oscillator, which is loaded with the variable SYS_CLK. Current settings set the oscillator to run in low power mode with a 32 kHz internal oscillator. Line 122 clears TRISB, which makes PORTB pins all digital output. Line 125 configures ADCON1 (AD control register 1), which configures PORTA pins to be either digital I/O or analog inputs. The current setting configures PORTA pins 0 and 1 as analog inputs and all other pins as digital I/O. The next SFR set up is the TRISA register on line 128. TRISA sets all other PORTA pins to digital outputs. The next two SFRs configured are the peripheral interrupt enable (PIEX) registers that define which interrupts are enabled or disabled. Both PIE1 and PIE2, starting at line 131, are loaded by variables PIE1_MSK and PIE2_MSK respectively. The PIE1_MSK enables only the Timer 1 interrupt overflow bit. This flag bit sets when Timer 1 rolls over from a count of 0xFFFF to 0x0000. At this point the program will jump to vector 0x04, as discussed above, directing the program to an interrupt routine. The PIE2_MSK doesn't enable any interrupts in the current configuration. At line 136, the program switches back to bank 0 and final SFR setups are completed.

Starting at line 138, SFRs such as PORTA, PORTB, and PORTC are loaded with values and SFRs such as INTCON and TMR1 are set up for operation. PORTA, PORTB, and PORTC configure the cells for the different phases in the cycle. PORTA will short a pair of cells. PORTB will electrically disconnect the same pair of cells from the stack, and PORTC will cycle through the capacitor-switching network. Line 138 clears all digital outputs for PORTA, meaning no cell is shorted. Line 141 loads variable register Wait_TMR with variable Wait. The variable register Wait_TMR is a counter that counts to either thirty seconds or 270 seconds, depending on current state, before allowing the state machine to increment to the next state. The variable Wait has to be adjusted depending on the oscillator configurations, currently set for 32 kHz operation. Line 144 loads PORTC with 0xC0, which resets the capacitive switch counter to 0x00. Line 147

loads SFR INTCON (interrupt control register) with the variable T0_OFF_MSK. T0_OFF_MSK (Timer 0 OFF) disables Timer 0 interrupts and enables all unmasked interrupts, including peripheral interrupts such as Timer 1. Timer 1 is a 16-bit timer/counter and requires two 8-bit registers to preload the count. TMR1H (Timer 1 High byte) and TMR1L (Timer 1 Low byte) are loaded from lines 151 to 155 with the variables HI_BYTE and LO_BYTE respectively. These variables are adjusted when changes to the oscillator occurs. Currently, Timer 1 interrupt will time out at 3.75 seconds. Line 158 starts Timer 1, which increments once every instruction cycle.

Lines 159 to 165 set the state machine to state 0. Line 160 preloads variable Wait_CNT with the value 0x08. The counter Wait_CNT controls the duration of time the cells are disconnected from the stack. Wait_CNT will only be incremented in certain states and only after Wait_TMR has expired. Line 162 increments STATE_CNT register, which is a simple counter that determines the next state of the state machine. At Line 164, PORTB is loaded with 0xDB, which electrically disconnects Cell 2 and Cell 5 from the stack. PORTA clears to 0x00 at line 165. This ends the set up portion of the program and the program steps into the main loop.

In the main loop, starting at Line 167, the capacitive switch count is incremented, cycling through the up conversion process. Lines 168 to 173 test the value on PORTC to determine if the switch count has reached its maximum count, if not, increment PORTC and jump back to line 168 and repeat. If the count has reached the maximum value, then jump to line 175 to clear only the pins in PORTC that control the switching. Lines 175 through 178 clear appropriate pins by masking the upper bits and clearing the lower bits of PORTC.

Lines 181 to 188 maps the location of the Disable look up table. This table is used to determine which cells to disconnect from the stack for each state. Lines 190 to 197 maps the location of the Short look up table. This table determines which cells, if any, to short for each state.

Line 200 has the label ISR (Interrupt Service Routine) and this is where the program jumps to after Timer 1 has overflowed from 0xFFFF to 0x0000. Lines 201 to 203 save the working register and STATUS register to temporary data registers. This stored data will be returned to these registers at the end of the ISR maintaining smooth program flow

when the program jumps back to the main portion of the program. Line 205 clears the Timer1 interrupt flag. Lines 207 to 211 reload Timer 1 to maintain consistent timing as was done at lines 151 to 155. Lines 213 to 241 determine which state is the next state and jumps to that state.

Line 245 is the start of STATE_0. State 0 waits for Wait_TMR to time out, disconnects Cells 2 and 5, loads Wait_TMR, increments the STATE_CNT register, and clears Wait_CNT register. STATE_1 begins at line 265. Here after Wait_TMR has rolled over from 0xFF to 0x00, which takes thirty seconds, Wait_CNT is incremented. After Wait_CNT increments to the value 0x09, State 1 disconnects Cell 0 and Cell 3, shorts both cells, reloads the Wait_TMR, clears Wait_CNT, and increments the STATE_CNT. STATE_2 begins at line 295 and waits for Wait_TMR to expire. After which state 2 disconnects Cells 0 and 3, no cells shorted, reloads Wait_TMR, clears Wait_CNT, and increments STATE_CNT. At line 314, STATE_3 begins to wait for Wait_CNT to reach value 0x09, and then it disconnects Cells 1 and 4, shorts both cells, reloads Wait_TMR, clears Wait_CNT, and increments STATE_CNT. Line 345 starts STATE_4 waiting for Wait_TMR to expire, then disconnects Cells 1 and 4, no cells shorted, reloads Wait_TMR, clears Wait_CNT, and increments STATE_CNT. STATE_5 begins on line 365, waits for Wait_CNT to count up to 0x09, then disconnects Cells 2 and 5, shorts both cells, reloads Wait_TMR, clears Wait_CNT, and resets STATE_CNT to 0x00.

After each state increments the STATE_CNT, the program jumps to END_ISR at line 395. Here the temporary data registers containing the working register data and the STATUS register data are dumped into their respective registers preparing them for the main program. Then the program jumps back to the point where the interrupt occurred, anywhere between lines 167 and 178. This program continuously repeats as long as the cells produce enough power for the stack switching to do the up conversion.

7.4 Experimental Results

Two PowerManager PCBs were fabricated and tested using fuel cells simulated using AA cells powering forward-biased 1N4001 diodes as shown in Figure 7.4. The forward-biased diode provides an open circuit voltage of about 0.7V and R2 simulates the V/I ratio at the projected optimum power level for a fuel cell. Six circuits were used to simulate an array.

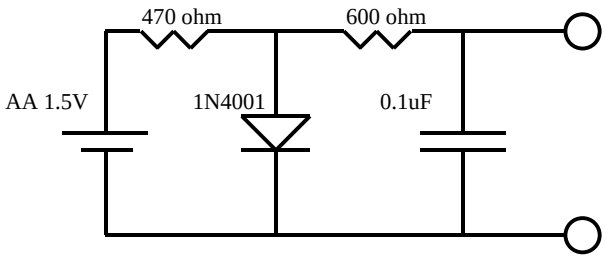

Figure 7.4: Fuel Cell Simulator Circuit.

The power input during PowerManager operation was calculated using the voltage drop across a 10 ohm resistor placed in series with each simulated fuel cell. Figure 7.5 shows the results indicating an input to

Power Measurements of Power Manager

Board 1

Power In

Fuel Cell	V_{out} (V)	I_{out} (A)	P_{FC}
0	0.715	0.004843	0.003462
1	0.744	0.001476	0.001098
2	0.760	0.001527	0.001161
3	0.756	0.000657	0.000497
4	0.752	0.001132	0.000851
5	0.689	0.001465	0.001009
		Total Power In (W)	0.008078

Power Consumed

Microcontroller		
V_{IN} (V)	I_{IN} (A)	Power Consumed (W)
3.901	0.00001210	0.00004720
3.901	0.00002010	0.00007841

Mux Switches			
Switch	V_{IN} (V)	I_{IN} (A)	Power Consumed (W)
0	4.160	0.00000015	0.00000062
1	4.160	0.00000015	0.00000062
2	4.160	0.00000015	0.00000062
3	4.160	0.00000015	0.00000062
		$P_{SWITCHES}$	0.00000250
		Total Power Consumed	0.00004970
		Worst-Case	0.00008091

Board 2

Power In

Fuel Cell	V_{out} (V)	I_{out} (A)	P_{FC}
0	0.715	0.004843	0.003463
1	0.744	0.001476	0.001098
2	0.760	0.001527	0.001161
3	0.756	0.000657	0.000497
4	0.752	0.001132	0.000851
5	0.689	0.001465	0.001009
		Total Power In (W)	0.008079

Power Consumed

Microcontroller		
V_{IN} (V)	I_{IN} (A)	Power Consumed (W)
4.266	0.00001280	0.00005460
4.266	0.00001360	0.00005802

Mux Switches			
Switch	V_{IN} (V)	I_{IN} (A)	Power Consumed (W)
0	4.002	0.00000017	0.00000068
1	4.002	0.00000017	0.00000068
2	4.002	0.00000017	0.00000068
3	4.002	0.00000017	0.00000068
		$P_{SWITCHES}$	0.00000272
		Total Power Consumed	0.00005733
		Worst-Case	0.00006074

Figure 7.5: Quiescent Power Consumption.

the PowerManager of between 497 – 3463uW for each cell, depending on the state of the battery. Total power input from the array was approximately 8mW.

Power consumed by the microcontroller was measured using a 1k current sampling resistor, while power consumption of the analog switch ICs was calculated using specification sheets. Using the low-power clock on the microcontroller, the total power consumed by the control circuitry for the PowerManager was between 60-80uW, or about 1% of the total power consumed. The final efficiency of the PowerManager will depend on the application load characteristics, including the apparent application power port input impedance. In further tests, we anticipate the switching losses will dominate power consumption and will require the addition of inductances to "tune" the PowerManager/application combination to mitigate transients. Provision for such inductors is built into the current printed wiring board, but is not used.

7.4.1 Summary and Recommendations for Future Work

The PowerManager system provides the electronic circuitry necessary to convert energy from water-based fuel cells to a form usable by conventional electronics. It manages operation by allowing voltage bootstrapping using a series array configuration for startup, then converting to a parallel configuration during operation to reduce electrical losses and limit electrolysis. It accomplishes these tasks while consuming a minimal amount of power.

The PowerManager was developed as for lab instrumentation purposes. Two main categories of additional capabilities and performance enhancements would be desirable in future revisions. First, it would be useful to perform more sophisticated monitoring of the state of health of the individual fuel cells in the array. As fuel cell characteristics becomes more repeatable, performance curves could be incorporated into the PowerManager to track expected output based on temperature, fuel pH and concentration, humidity. These could be used with the characteristic curves to predict remaining lifetime and adjust lifetime conditioning timing sequences. The output from each fuel cell at DC and its impedance at a known frequency, e.g., 1kHz, could be measured using current sampling and AC signal injection techniques. This information could be used to modify the upconversion switching frequency and duty cycle. A feedback controller could be added to provide a more stable output voltage and reduce ripple.

Allowing individual cells automatic health monitoring should also improve the efficiency and life expectancy of the cells by permitting dynamic adjustment of

conditioning sequences. Monitoring the cells individually and allowing a cell to go into a shorting phase when needed rather than being time based should increase the cell's life. The limitation would be no more than two cells can be disconnected at a time. Priority levels can be set that would allow a cell to be reconnected to the stack prematurely if the microcontroller senses a different cell showing substantially lower output that would endanger system operation. Achieving this type of control will require a larger microcontroller, but not necessarily more power consumed by the new microcontroller. A recommendation would be a member of Microchip's PIC 18FXXXX Nanowatt technology device.

An application scheduler module will be necessary to adjust fuel cell operating conditions to accommodate application requirements. This module could possibly be implemented with an additional PIC16F737. This module would monitor the state of charge of an energy reservoir, such as a supercapacitor, that would serve as the interface between the PowerManager and load. This information would be used by both the PowerManager and the application hardware to schedule appropriate charging and discharging events. For example, it is theorized that fuel cell longevity is maximized by reducing the drain, thus preventing buildup of byproducts. Disconnecting the fuel cells during periods when the energy reservoir is charged adequately to meet application requirements would maximize longevity. Also, if the application detected a depleted energy reservoir, it could adapt, possibly informing a host of the low power status and consequently reduced communication interval.

7.5 Air Breathing System Hardware

The electronics for switching and control must be integrated into the same hardware that will contain the flow channels and the fuel cells themselves, as well as the wiring interconnections for the individual cells. The design of this system required as much free access to air from the surrounding atmosphere as possible (to allow maximum flow of oxygen to the cathode). The system was intended to harvest from a single harvesting point (see Section 2), and distribute the harvested fuel from the harvesting point to the inlets of each of the cells.

Design of the manifolding for this distribution required that the channel length for each of the distribution channels be the same, in order to develop the same pressure drop

to each of the fuel cells. If the pressure drop was unequal, flow maldistribution would quickly be set up, causing more fuel to be distributed to the cells with lower pressure drops, and less fuel to be distributed to the cells with higher pressure drops. Low fuel flow in a fuel cell that is under load can lead to the cell "reversing", or becoming a negative potential between the anode and cathode. At this point, the reversed cell becomes a current draw, and electrolysis occurs at the anode can cathode of the reversed cell. Generation of hydrogen within the cell causes a number of problems, from gas generation causing the flow channels to block, to supplying an ambient gas that may be reactive with the saps. Although some of the electronics described above are designed to detect a cell that has gone into reversal and remove the load from it, there is no system for actively controlling the flow distribution from the manifold, and so this must be balanced with care from the initial run.

To balance the flow field, 6 individual control flow valves were incorporated into the flow distribution system. For symmetry, 3 of the valves were located on the inlet side of the fuel cell, and 3 of the valves were located on the outlet side of the fuel cells. The layout for the flow field is shown in Figure 7.6. There are 12 posts that accept a 4-40 screw, and these posts are lifted above the level of the flow field to accommodate the electronics described in the previous section.

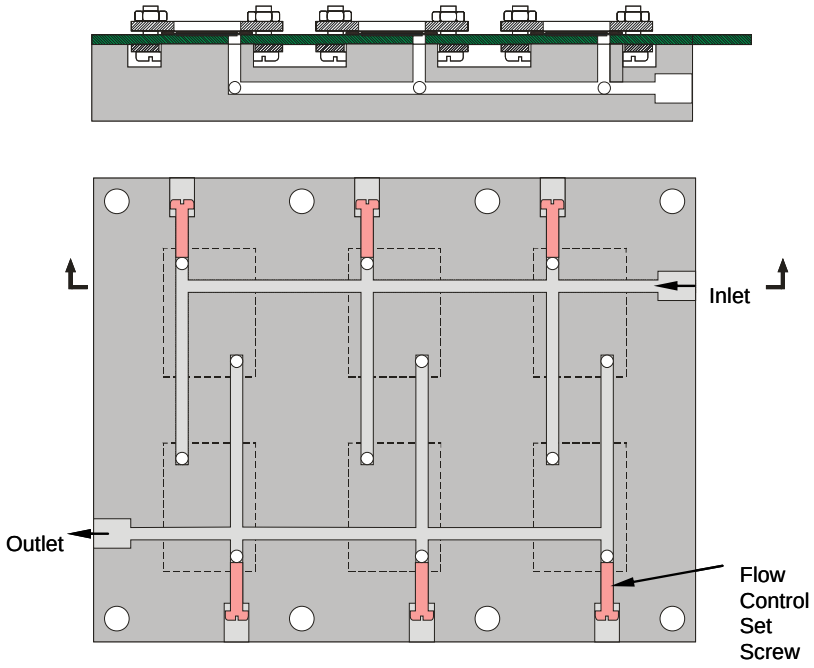

Figure 7.6: Schematic layout of the 6 cell monopolar cell flow field. The set screws allow for individual control of the flow into each cell, allowing for flow balancing of the system.

To allow for the electrical interconnections of the fuel cells, a printed circuit board

that accommodates all the electronics, as well as the wiring connections for both series and parallel configurations was fabricated. This circuit board contained the circuitry described above, as well as the contacting points for the anodes and cathodes of each cell. A parallel connected was also fabricated on the edge of the board that allowed independent access to the cell anodes and cathodes to allow for testing of individual cells without the control circuitry.

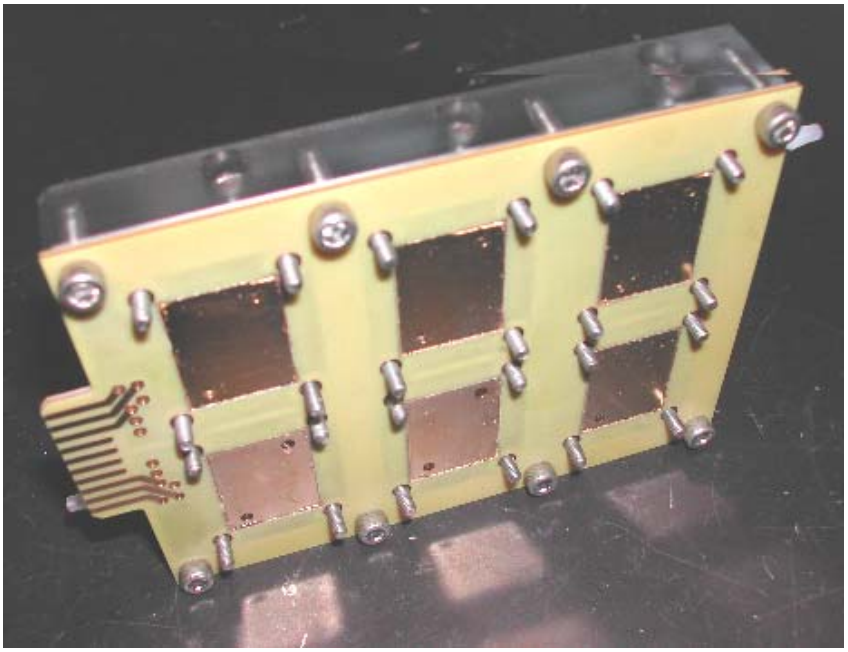

Figure 7.7: A fully integrated 6 cell monopolar stack. The fuel cells have been removed to show the circuit board. The electronics are mounted facing away from the viewer, toward the plastic fuel manifold. The inlet is on the right hand side.

To balance the cell flow field, each individual cell was isolated from the flow field so that it was the only cell receiving fuel, thus insuring that the cell would wet fully, and not provide any additional back pressure due to wetting of the anode surfaces. Each cell in turn was isolated and flow was forced into each anode independently to insure good wetting. Each cell was then put under a constant load, and the flow adjusted using the valves until the same current and voltage was gotten for each cell. With the cell fully wetted and balanced, experiments on the full system configuration could begin. A picture of the fully integrated system with the circuit board in place, but minus the fuel cells, is shown in Figure 7.7.

8. Project Development and Project Status/Summary

Development on several aspects of this project was halted after 3 years, and a very limited set of subtasks were continued into the fourth year. At the end of the third year, it was clear that the limiter for power generation from a carbohydrate fuel lay in the

development of better, longer lasting catalysts, and therefore only subtasks associated with this goal were carried forward. Furthermore, since the noble metal subtask, although showing higher powers in fuel cell tests, was showing a high amount of poisoning and no real path forward toward improved powers without significant investment on the metal catalyst discovery path, this subtask was also discontinued at the end of the third year, with the exception of the alloys identified in year 3, and discussed in Section 8.3. Thus, the only tasks carried forward into year 4 were the enzyme engineering task, the electrochemistry task (primarily for mediator development), and the testing subtask of the architecture task.

Although significant advances in genetically engineered enzymes were made in year 4, and several good mediators were developed, none of these enzymatic systems demonstrated better power than the noble metals in fuel cell tests. Several reasons for these limitations were identified, and serve as the basis for a set of follow on tasks from this grand challenge. They are elucidated below, roughly in the form of most important (from a standpoint of high powers and longer lasting systems) to least important. It should be noted, however, that ALL of these new tasks represent investments into catalysis, due to the low powers currently available from the fuel cell. This is not to diminish the additional work that must be undertaken by the other tasks before a functional fuel cell that can be run on carbohydrates can be fielded for a long duration.

8.1 Immobilized Mediators

Perhaps the most limiting effect within enzyme fuel cells is the need to shuttle electrons from the redox enzyme to the electrode. Although some advances into phenazine based mediators were developed during this project, none of them showed mediation at a voltage that would be deemed compatible with an enzymatic cell.

Regardless of the catalyst being used, the transfer of electrons between the electrode and either the fuel (anode reaction) or oxidant (cathode reaction) is a key element underlying fuel cell operation in the production of electrical energy. However, when enzymes are used to catalyze these fundamental oxidation and reduction reactions, this electron transfer process can be problematic. One of the primary reasons for this behavior lies in the fact that the active site of the enzyme where the redox (oxidation or reduction) reaction occurs lies deeply buried inside the enzyme, at a distance sufficiently

far removed from the electrode surface that a direct electron transfer between the active site and the electrode cannot occur. This is the case for glucose oxidase, which is a glycoprotein that catalyzes the oxidation of glucose (the fuel) to gluconate.

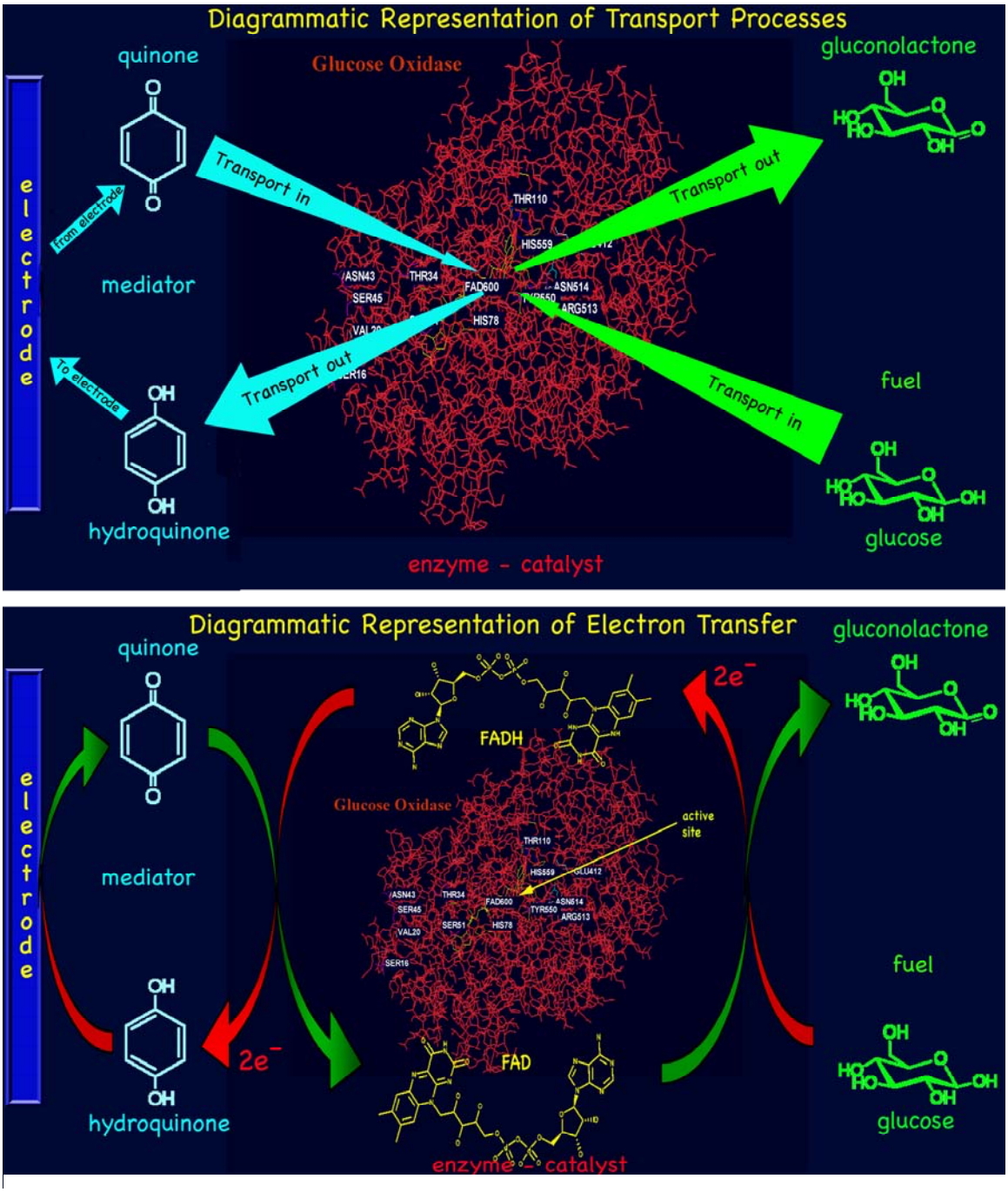

Figure 8.1: Diagrammatic representation of the transport (upper diagram) and electron transfer (lower diagram) processes occurring when oxidizing glucose in a fuel cell using the enzyme glucose oxidase as the catalyst with the concomitant production of electrical energy. The red arrows in the diagram illustrate the flow of electrons from glucose to the electrode. All of the electron transfer reactions occur at the active site of the enzyme that is deeply buried in the enzyme, with the exception of the final electron transfer process between the mediator and the electrode where the electrons are finally transferred to the site connected to the device being powered, that is the portable electronic device. Although the quinone/hydroquinone couple is shown as the mediator in this case, any number of other species can be utilized.

In the case of this enzyme, flavin adenine dinucleotide (FAD) is the electroactive

constituent where the oxidation of glucose occurs, and this compound is permanently anchored and buried deep within the enzyme. In fact, the reaction site is so far removed from the enzyme surface by both the amino acid residues making up the protein structure as well as its overlying sugar coating (since it's a glycoprotein) that a direct electron transfer between it and the electrode cannot occur. One solution to this situation and the one that occurs in naturally occurring systems is to use of another compound, a mediator, to serve as an electron shuttle. In this case, the mediator moves between the active site of the protein and the electrode surface, transferring electrons in the process. The overall process then consists of a series of diffusion and electron transfer steps: 1) glucose moves into the active site of the enzyme, transferring its electrons to FAD in the process and leading to formation of gluconolactone and FADH; 2) gluconolactone moves out of the enzyme, and the mediator moves in; 3) electron transfer from FADH to the mediator occurs, reforming FAD and the reduced mediator; 4) the reduced mediator moves out of the enzyme where it can then interact with other species, including an electrode surface. A diagrammatic representation of this process is is shown in the figure below. (Protons are also involved in this process but are ignored in this discussion.)

Each of these transport processes and redox reactions occur at some fundamental rate and thermodynamic equilibrium value, and these factors (i.e. the kinetics and thermodynamics of the processes) ultimately dictate the power that can be generated. (Recall that power is defined as the product of voltage and current, and these can be equated with the thermodynamics and kinetics of the reactions/processes, respectively.) Consequently, the desire for unlimited power sets a minimum set of constraints on the properties of the mediator. Namely, that: 1) the transport of the oxidized mediator to the active site to the electrode be fast; 2) the electron transfer reaction with the enzyme be fast (kinetics); 3) the free energy of the reaction (thermodynamics) between the mediator and the FADH in the enzymatic active site are well matched; 4) the transport of the reduced mediator to the electrode be fast; 5) the electron transfer reaction with the electrode be fast (kinetics); 6) the free energy of the reaction (thermodynamics) between the reduced mediator and the electrode are well matched.

In addition to these considerations related to power, the mediator and enzyme must also exhibit a number of other characteristics that relate to other power supply

performance attributes. For example, the period of performance of the electronic device (hours, days, weeks, months, years) will dictate the long-term stability requirements for the mediator and enzyme. Also, consideration of the final system design and use conditions must also be taken into account in the design of the electrocatalyst/mediator system. For example, in the event that glucose solutions are pumped through the system, the mediator and electrocatalyst must be sufficiently anchored to prevent their loss. Finally, these general concepts and considerations are applicable to many different enzymes for a number of applications other than just fuel cells, including sensor and biomedical diagnostics. In fact, the work done in the biomedical area for the electrochemical detection and quantitation of glucose for diabetics gave rise, at least to some extent, to the concept of enzymatic catalysis of glucose for the generation of power, i.e. fuel cell applications.

Early attempts to synthesize mediators that run at potentials appropriate to the FAD coenzyme, yet can be covalently linked to the electrode were based on phenazine class molecules. A phenazine functional group was attached to one end of an alkyl chain, and the binding end of the alkyl chain was functionalized with a amine group to allow for covalent bonding to the electrode surface. Once this molecule was synthesized, however, the electrochemistry of the redox potential became quite complicated (see Figure 8.2), and did not function as a mediator

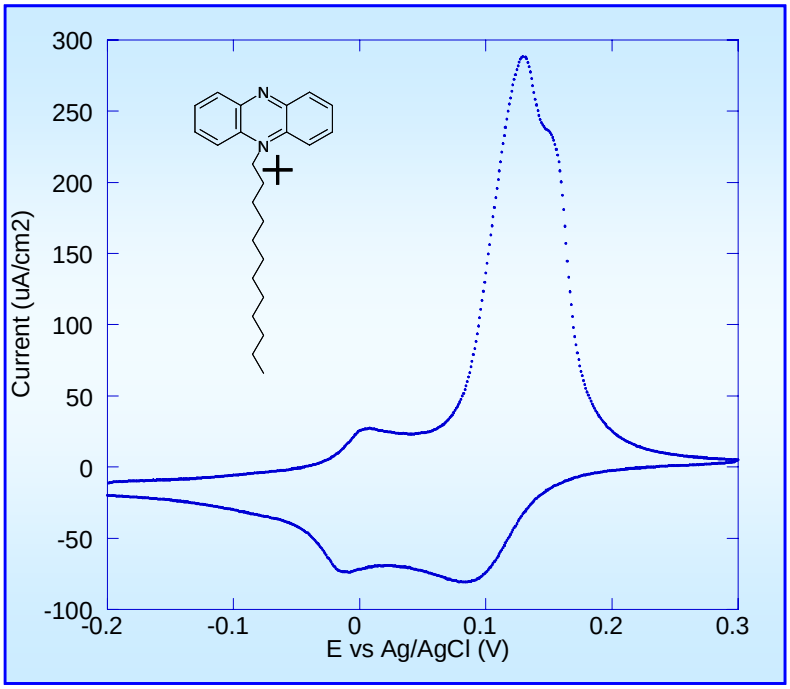

Figure 8.2: CV of the modified phenazine with alkyl chain. Redox potential of unmodified phenazine is -80mV. This synthesized molecule did not exhibit mediation behavior to FAD. Voltammetry Conditions: 25 mV/sec sweep rate, Phosphate Buffer (0.1 M, pH 5)

for this system. Thus, one of the most important steps towards the realization of an enzyme electrode continues to be the fabrication of a redox molecule that has a sufficiently negative redox potential to allow for high cell potentials. This redox molecule must also have some functionalization to allow it to be covalently bound to an electrode surface.

8.2 Improvement of the Genetic Engineering Yield

Throughout the process of protein modification, expression of the modified protein in the *A. Niger* vector, purification of the supernatent to retrieve only the modified enzyme, and final assay of the enzyme to determine the effect of the genetic modification, several losses in the amount of material recovered were suffered. Commercial systems have a much higher capability to successfully express, purify, and assay a given mutant than was demonstrated at Sandia, and this was largely due to inefficiencies in the protocols used for each of these steps. Improvements to the protocol process at each step will allow for a significant increase in the amount of modified protein produced. Since milligram quantities are desired for use in fuel cell assembly and operation, the ability to more successfully produce a high quantity and quality of protein requires further investigation, prior to the development of mutated enzyme electrodes for fuel cell applications.

8.3 Noble Metal combinatorial discovery and powder synthesis

A number of promising noble metal alloys were discovered during the third year of the project, but of these, only one was synthesized into a powder that could be fabricated into a fuel cell. This was Pt-Sn, and synthesis of the electrode required stabilization of the Sn against dissolution during the oxidative cycles of the cell. Thus, the actual powder was a Pt-SnO alloy mix. Performance on these cells did not significantly vary from the performance of the Pt-Ru cells, and showed no great increase in tolerance to poisoning as was hoped. Still, the discovery of the Pt-Ru-Pb ternary shows significant resistance to poisoning by carbohydrates, and was never synthesized into a powder form.

To more fully explore this area will require a large scale effort. The discovery of the Pt-Ru alloy for poisoning resistance for methanol fuel cells was the subject of a decade of concentrated effort by several established research centers. As these alloys are discovered, however, its is imperative that a means be found to synthesize promising alloys into a powder form so that electrodes can be fabricated and in cell testing can be

accomplished, as it has been shown many times that catalyst performance in the discovery phase can often vary widely from the performance of the catalyst in a functioning fuel cell.

8.4 Other subtasks and summary

At the end of the project, a number of large improvements in various areas within Sandia were realized. Low power upconversion of voltage, microneedle harvesting, high temperature and low crossover membranes, and cell architecture all were developed to a significant degree. Additional work, however, must be done before all of these subtasks, together with an improved anode catalyst, can be made into a carbohydrate fuel cell. Thus, additional (outside) funding will need to be sought in order to close these gaps to a functional product. This section provides some insight into the type and nature of external funding that was investigated by the management task during the course of this project.

Although the concept of a biologically fueled power source remains an attractive target for a number of applications, the inaccessibility of the goal in the short term dictates that some effort needs to be put towards developing a follow on funding strategy for the subcomponents of the fuel cell system, rather than for the system as a whole. In particular, the microneedle harvester, the membrane development, the miniature fuel cell architecture, the genetic engineering, and the power manager were identified as subtasks that may have significant technical appeal outside of the power generation field and would therefore represent good prospects, in and of themselves, for a continued funding effort from an interested outside source of funding.

To identify strategic partners for the development of some of these subcomponents, a matrix of technologies that achieved at least a technology readiness level of three from the project was cross referenced against a list of likely partner candidates that would have an interest in those technologies was prepared. Of particular interest was the development of a DARPA program proposal on sustainable micropower systems that has yet, as of this report, to be developed into a call for proposals. However, the interest within the defense and intelligence community for technologies that can be derived from technologies developed from this program is evident.

In summary, the fuel cell grand challenge developed a system that could produce a few milliwatts of power from 1 molar concentrations of glucose in water. This was done using traditional noble metal catalysts. Powers of a few hundred microwatts were demonstrated using an enzymatic catalyst anode, with only 50mM concentrations. Both of these systems, however, were extremely time limited, and performance dropped off after only a few hundred hours of operation (in the case of the noble metal system). Significant advancements in genetic engineering of enzymes at Sandia, membrane development for traditional fuel cells, microneedle harvesting, power management with low overhead power consumption, and catalysis have been demonstrated during the course of the program.

9. Appendix A: Control Code for Power Manager

```
MPASM 03.90 Released                              PWRMNGR_V5.ASM   3-28-
2005  9:28:26         PAGE  1


LOC  OBJECT CODE     LINE SOURCE TEXT
  VALUE

                     00001
;*****************************************
                     00002 ;
                     00003 ;Power Manager 3000+
                     00004 ;Sandia National Laboratories
                     00005 ;19August2004
                     00006 ;Developed by STNG Jason Podgorski, Dept
1738-1
                     00007 ;
                     00008
;*****************************************
                     00009 ;Changes
                     00010 ;       11/04/04        Updated both
disable and short tables to reflec new states for one cell short fo
                           r 30 sec
                     00011 ;                               and 2-3
cells under no load simultaneously
                     00012 ;
                     00013
;*****************************************
                     00014
                     00015
                     00016
                     00017
                     00018         list p=16f737
                     00019         include "p16f737.inc"
                     00001         LIST
                     00002 ; P16F737.INC  Standard Header File,
Version 1.00    Microchip Technology, Inc.
                     00504         LIST
                     00020         radix   hex
                     00021
                     00022
                     00023
                     00024 ;**************Config
words*******************
2007   3FB8          00025                   __CONFIG        _CONFIG1,
_CP_OFF & _CCP2_RC1 & _DEBUG_OFF & _VBOR_2_0 & _BOREN_0 & _MCL
                           R_ON & _PWRTE_OFF & _WDT_OFF & _INTRC_IO
                     00026
2008   3FBC          00027                   __CONFIG        _CONFIG2,
_BORSEN_0 & _IESO_OFF & _FCMEN_OFF
                     00028
;*****************************************
                     00029
                     00030 ;**********Bit
VARIABLES****************************
```

```
                     00031
  00000000           00032 W               equ            0
  00000001           00033 F               equ            1
                     00034
  00000000           00035 EN_GFC0 equ           0
;When high, connects fuel cell to parallel stack
  00000001           00036 EN_GFC1 equ           1
  00000002           00037 EN_GFC2 equ           2
  00000003           00038 EN_GFC3 equ           3
  00000004           00039 EN_GFC4 equ           4
  00000005           00040 EN_GFC5 equ           5
                     00041
  00000000           00042 DIO_A0  equ           0
;Capacitor Addressing
  00000001           00043 DIO_A1  equ           1
  00000002           00044 DIO_A2  equ           2
  00000003           00045 DIO_A3  equ           3
                     00046
  00000004           00047 EN_SERIES       equ     4
;Groups cells in series
  00000005           00048 DIO_REVPOL      equ     5
;Applies reverse polarity across cells
```

```
LOC  OBJECT CODE     LINE SOURCE TEXT
  VALUE

                     00049
  00000000           00050 SH_GFC0 equ             0
;Short out cells
  00000001           00051 SH_GFC1 equ             1
  00000002           00052 SH_GFC2 equ             2
  00000003           00053 SH_GFC3 equ             3
  00000004           00054 SH_GFC4 equ             4
  00000005           00055 SH_GFC5 equ             5
                     00056
                     00057 ;******Timer
Presets**************************
                     00058
  00000080           00059 HI_BYTE         equ             0x80
;HI_BYTE & LO_BYTE presets for Timer1
  00000000           00060 LO_BYTE         equ             0x00
  000000A0           00061 Set_0           equ             0xa0
;Set_0 preset for Timer0
  000000C0           00062 Cap_SW          equ             0xc0
  00000002           00063 SYS_CLK         equ             0x02;10
  000000F8           00064 Wait            equ             0xf8
;Preloads timer for a 30 sec wait?
                     00065 ;R_secs         equ             0x1e
                     00066 ;O_secs         equ             0xf8
                     00067 ;******Interrupt
Masks************************
                     00068
  000000C0           00069 T0_OFF_MSK      equ             0xc0
;Enable interrupts, disable TMR0 interrupt
  000000E0           00070 T0_ON_MSK       equ             0xe0
;Enables TMR0 interrupt
  00000001           00071 PIE1_MSK        equ             0x01
;Enables TMR1 overflow
  00000000           00072 PIE2_MSK        equ             0x00;40
;Disables PIR2 interrupts
  00000041           00073 ADCVRT_MSK      equ             0x41
;Enables AD interrupt
  00000000           00074 CH0_MSK         equ             0x00
;Selects AD Channel 0
  00000008           00075 CH1_MSK         equ             0x08
;Selects AD Channel 1
                     00076
                     00077 ;********STATUS
LEDs*************************
                     00078
                     00079 ;LED0 thru LED5 indicate which cell is
shorted
                     00080 ;LED6 indicates push button activation
                     00081
  00000006           00082 LED7    equ             6
;PortB, LED7 indicates Series Mode
```

```
  00000007            00083 LED8    equ             7
;PortB, LED8 indicates Parallel Mode
                      00084
                      00085 ;*******Variable
Registers***********************
                      00086
  00000023            00087 Wait_TMR                equ
0x23
  00000024            00088 Wait_CNT                equ
0x24
  00000025            00089 W_temp                  equ
0x25            ;Stores W register at time of interrupt
  00000026            00090 S_temp                  equ
0x26            ;Stores Status register at time of interrupt
  00000027            00091 countus_temp    equ             0x27
                      00092
  00000028            00093 AD_REF                  equ
0x28            ;AD Reference, used to compare against Vout
  00000029            00094 AD_INP                  equ
0x29            ;AD Input, if above reference operate in paralle
                           l mode
                      00095
  0000002A            00096 STATE_CNT               equ
0x2a
                      00097
;******VECTORS*********************************
                      00098
0000                  00099         org             0x00
0000   2805           00100         goto    Config
```

```
LOC  OBJECT CODE     LINE SOURCE TEXT
  VALUE

                     00101
0004                 00102         org             0x04
;Interrupt service request
0004   2851          00103         goto    ISR
                     00104
                     00105
;********MAIN************************************
                     00106
                     00107
0005                 00108 Config
0005   0064          00109         CLRWDT
0006   0185          00110         clrf    PORTA
0007   0186          00111         clrf    PORTB
0008   0187          00112         clrf    PORTC
0009   0181          00113         clrf    TMR0
000A   018F          00114         clrf    TMR1H
000B   018E          00115         clrf    TMR1L
000C   0183          00116         clrf    STATUS
                     00117
000D   1683 1303      00118         banksel TRISA           ;Switch to
Bank 1 for setup
                     00119
000F   30C0          00120         movlw   0xc0
Message[302]: Register in operand not in bank 0.  Ensure that bank bits
are correct.
0010   0081          00121         movwf   OPTION_REG      ;Configures
option register
Message[302]: Register in operand not in bank 0.  Ensure that bank bits
are correct.
0011   0087          00122         movwf   TRISC           ;Configures
Port C bits 5:0 as digital output
                     00123
;Configures bits 6 & 7 for serial communication
                     00124
0012   3002          00125         movlw   SYS_CLK
Message[302]: Register in operand not in bank 0.  Ensure that bank bits
are correct.
0013   008F          00126         movwf   OSCCON          ;Configure
osc for 8Mhz and low power operation
                     00127
0014   3000          00128         movlw   0x00
Message[302]: Register in operand not in bank 0.  Ensure that bank bits
are correct.
0015   0086          00129         movwf   TRISB           ;Configures
Port B as digital output
                     00130
0016   300D          00131         movlw   0x0d            ;Configures
AD analog channels
Message[302]: Register in operand not in bank 0.  Ensure that bank bits
are correct.
```

```
0017   009F           00132         movwf   ADCON1
                      00133
0018   3000           00134         movlw   0x00            ;Configures
port A bits 7:2 as digital out
Message[302]: Register in operand not in bank 0.  Ensure that bank bits
are correct.
0019   0085           00135         movwf   TRISA           ;Configures
bits 0 & 1 as analog in
                      00136
001A   3001           00137         movlw   PIE1_MSK
Message[302]: Register in operand not in bank 0.  Ensure that bank bits
are correct.
001B   008C           00138         movwf   PIE1
                      00139
001C   3000           00140         movlw   PIE2_MSK
Message[302]: Register in operand not in bank 0.  Ensure that bank bits
are correct.
001D   008D           00141         movwf   PIE2
                      00142
001E   1283 1303      00143         banksel PORTA           ;Switch to
bank 0 for normal operation
                      00144
0020   0185           00145         clrf    PORTA
```

```
LOC  OBJECT CODE     LINE SOURCE TEXT
  VALUE

                     00146
0021   30F8          00147         movlw   Wait
0022   00A3          00148         movwf   Wait_TMR
                     00149
0023   30C0          00150         movlw   0xc0
0024   0087          00151         movwf   PORTC
                     00152
0025   30C0          00153         movlw   T0_OFF_MSK      ;Disable
TMR0 interrupt
0026   008B          00154         movwf   INTCON
                     00155
0027   1607          00156         bsf             PORTC, EN_SERIES
                     00157
0028   3080          00158         movlw   HI_BYTE
0029   008F          00159         movwf   TMR1H
                     00160
002A   3000          00161         movlw   LO_BYTE
002B   008E          00162         movwf   TMR1L
                     00163
                     00164
002C   1410          00165         bsf             T1CON, TMR1ON
002D   01AA          00166         clrf    STATE_CNT
002E   3008          00167         movlw   0x08
002F   00A4          00168         movwf   Wait_CNT
0030   0AAA          00169         incf    STATE_CNT, F
0031   0AAA          00170         incf    STATE_CNT, F
0032   304E          00171         movlw   0x4e
;Value of state 0, first address of disable table
0033   0086          00172         movwf   PORTB
0034   3004          00173         movlw   04
0035   0085          00174         movwf   PORTA
                     00175
0036                 00176 MAIN
0036   301B          00177         movlw   0x1b
0037   0207          00178         subwf   PORTC, W
0038   1903          00179         btfsc   STATUS, Z
0039   283C          00180         goto    Clr_C
003A   0A87          00181         incf    PORTC, F
003B   2836          00182         goto    MAIN
                     00183
003C                 00184 Clr_C
003C   30F0          00185         movlw   0xf0
003D   0587          00186         andwf   PORTC, F
003E   2836          00187         goto    MAIN
                     00188
                     00189
003F                 00190 Disable
003F   0782          00191         addwf   PCL, F
0040   34C7          00192         retlw   0xc7
0041   344E          00193         retlw   0x4e
```

```
0042   345C          00194         retlw   0x5c
0043   3478          00195         retlw   0x78
0044   34F8          00196         retlw   0xf8
0045   3471          00197         retlw   0x71
0046   3463          00198         retlw   0x63
```

```
LOC  OBJECT CODE     LINE SOURCE TEXT
  VALUE

0047   3447           00199         retlw   0x47
                      00200
0048                  00201 Short
0048   0782           00202         addwf   PCL, F
0049   3400           00203         retlw   0x00
004A   3404           00204         retlw   0x04
004B   3408           00205         retlw   0x08
004C   3410           00206         retlw   0x10
004D   3400           00207         retlw   0x00
004E   3420           00208         retlw   0x20
004F   3480           00209         retlw   0x80
0050   3440           00210         retlw   0x40
                      00211
0051                  00212 ISR
0051   00A5           00213         movwf   W_temp
0052   0E03           00214         swapf   STATUS, W
0053   00A6           00215         movwf   S_temp
                      00216
0054   100C           00217         bcf             PIR1, TMR1IF
                      00218
0055   3080           00219         movlw   HI_BYTE
0056   008F           00220         movwf   TMR1H
                      00221
0057   3000           00222         movlw   LO_BYTE
0058   008E           00223         movwf   TMR1L
                      00224
0059   3000           00225         movlw   0x00
005A   022A           00226         subwf   STATE_CNT, W
005B   1903           00227         btfsc   STATUS, Z
005C   287A           00228         goto    STATE_0
                      00229
005D   3001           00230         movlw   0x01
005E   022A           00231         subwf   STATE_CNT, W
005F   1903           00232         btfsc   STATUS, Z
0060   2889           00233         goto    STATE_1
                      00234
0061   3002           00235         movlw   0x02
0062   022A           00236         subwf   STATE_CNT, W
0063   1903           00237         btfsc   STATUS, Z
0064   28A2           00238         goto    STATE_2
                      00239
0065   3003           00240         movlw   0x03
0066   022A           00241         subwf   STATE_CNT, W
0067   1903           00242         btfsc   STATUS, Z
0068   28B4           00243         goto    STATE_3
                      00244
0069   3004           00245         movlw   0x04
006A   022A           00246         subwf   STATE_CNT, W
006B   1903           00247         btfsc   STATUS, Z
006C   28C6           00248         goto    STATE_4
```

```
                        00249
006D   3005             00250         movlw   0x05
006E   022A             00251         subwf   STATE_CNT, W
```

```
LOC  OBJECT CODE     LINE SOURCE TEXT
  VALUE

006F   1903           00252         btfsc   STATUS, Z
0070   28D5           00253         goto    STATE_5
                      00254
0071   3006           00255         movlw   0x06
0072   022A           00256         subwf   STATE_CNT, W
0073   1903           00257         btfsc   STATUS, Z
0074   28EE           00258         goto    STATE_6
                      00259
0075   3007           00260         movlw   0x07
0076   022A           00261         subwf   STATE_CNT, W
0077   1903           00262         btfsc   STATUS, Z
0078   2900           00263         goto    STATE_7
                      00264
0079   2912           00265         goto    END_ISR
                      00266
007A                  00267 STATE_0
007A   0AA3           00268         incf    Wait_TMR, F
007B   3000           00269         movlw   0x00
007C   0223           00270         subwf   Wait_TMR, W
007D   1D03           00271         btfss   STATUS, Z
007E   2912           00272         goto    END_ISR
                      00273
                      00274
                      00275 ;       movlw   Wait
                      00276 ;       movwf   Wait_TMR
                      00277 ;       incf    Wait_CNT, F
                      00278 ;       movlw   0x09
                      00279 ;       subwf   Wait_CNT, W
                      00280 ;       btfss   STATUS, Z
                      00281 ;       goto    END_ISR
                      00282
007F   0185           00283         clrf    PORTA
                      00284
0080   082A           00285         movf    STATE_CNT, W
0081   203F           00286         call    Disable
0082   0086           00287         movwf   PORTB
                      00288
0083   30F8           00289         movlw   Wait
0084   00A3           00290         movwf   Wait_TMR
0085   0AA3           00291         incf    Wait_TMR, F
0086   0AAA           00292         incf    STATE_CNT, F
0087   01A4           00293         clrf    Wait_CNT
0088   2912           00294         goto    END_ISR
                      00295
0089                  00296 STATE_1
0089   0AA3           00297         incf    Wait_TMR, F
008A   3000           00298         movlw   0x00
008B   0223           00299         subwf   Wait_TMR, W
008C   1D03           00300         btfss   STATUS, Z
008D   2912           00301         goto    END_ISR
```

```
                        00302
008E   30F8             00303          movlw   Wait
008F   00A3             00304          movwf   Wait_TMR
```

```
LOC  OBJECT CODE     LINE SOURCE TEXT
  VALUE

0090   0AA4           00305         incf    Wait_CNT, F
0091   3009           00306         movlw   0x09
0092   0224           00307         subwf   Wait_CNT, W
0093   1D03           00308         btfss   STATUS, Z
0094   2912           00309         goto    END_ISR
                      00310
0095   0185           00311         clrf    PORTA
0096   082A           00312         movf    STATE_CNT, W
0097   203F           00313         call    Disable
0098   0086           00314         movwf   PORTB
                      00315
0099   082A           00316         movf    STATE_CNT, W
009A   2048           00317         call    Short
009B   0085           00318         movwf   PORTA
                      00319
009C   30F8           00320         movlw   Wait
009D   00A3           00321         movwf   Wait_TMR
;Set timer to 'wait' seconds
009E   0AA3           00322         incf    Wait_TMR, F
009F   0AAA           00323         incf    STATE_CNT, F
;Inc to State 2
00A0   01A4           00324         clrf    Wait_CNT
00A1   2912           00325         goto    END_ISR
                      00326
00A2                  00327 STATE_2
00A2   0AA3           00328         incf    Wait_TMR, F
00A3   3000           00329         movlw   0x00
00A4   0223           00330         subwf   Wait_TMR, W
00A5   1D03           00331         btfss   STATUS, Z
00A6   2912           00332         goto    END_ISR
                      00333
                      00334 ;       clrf    PORTA
                      00335 ;       movf    STATE_CNT, W
                      00336 ;       call    Disable
                      00337 ;       movwf   PORTB
                      00338
00A7   0185           00339         clrf    PORTA
00A8   082A           00340         movf    STATE_CNT, W
00A9   203F           00341         call    Disable
00AA   0086           00342         movwf   PORTB
                      00343
00AB   082A           00344         movf    STATE_CNT, W
00AC   2048           00345         call    Short
00AD   0085           00346         movwf   PORTA
                      00347
                      00348
00AE   30F8           00349         movlw   Wait
00AF   00A3           00350         movwf   Wait_TMR
00B0   0AA3           00351         incf    Wait_TMR, F
00B1   0AAA           00352         incf    STATE_CNT, F
```

```
00B2   01A4           00353          clrf    Wait_CNT
00B3   2912           00354          goto    END_ISR
                      00355
00B4                  00356 STATE_3
00B4   0AA3           00357          incf    Wait_TMR, F
```

```
LOC  OBJECT CODE     LINE SOURCE TEXT
  VALUE

00B5   3000           00358         movlw   0x00
00B6   0223           00359         subwf   Wait_TMR, W
00B7   1D03           00360         btfss   STATUS, Z
00B8   2912           00361         goto    END_ISR
                      00362
                      00363 ;       movlw   Wait
                      00364 ;       movwf   Wait_TMR
                      00365 ;       incf    Wait_CNT, F
                      00366 ;       movlw   0x09
                      00367 ;       subwf   Wait_CNT, W
                      00368 ;       btfss   STATUS, Z
                      00369 ;       goto    END_ISR
                      00370
00B9   0185           00371         clrf    PORTA
00BA   082A           00372         movf    STATE_CNT, W
00BB   203F           00373         call    Disable
00BC   0086           00374         movwf   PORTB
                      00375
00BD   082A           00376         movf    STATE_CNT, W
00BE   2048           00377         call    Short
00BF   0085           00378         movwf   PORTA
                      00379
00C0   30F8           00380         movlw   Wait
00C1   00A3           00381         movwf   Wait_TMR
00C2   0AA3           00382         incf    Wait_TMR, F
00C3   0AAA           00383         incf    STATE_CNT, F
00C4   01A4           00384         clrf    Wait_CNT
00C5   2912           00385         goto    END_ISR
                      00386
00C6                  00387 STATE_4
00C6   0AA3           00388         incf    Wait_TMR, F
00C7   3000           00389         movlw   0x00
00C8   0223           00390         subwf   Wait_TMR, W
00C9   1D03           00391         btfss   STATUS, Z
00CA   2912           00392         goto    END_ISR
                      00393
00CB   0185           00394         clrf    PORTA
                      00395
00CC   082A           00396         movf    STATE_CNT, W
00CD   203F           00397         call    Disable
00CE   0086           00398         movwf   PORTB
                      00399
00CF   30F8           00400         movlw   Wait
00D0   00A3           00401         movwf   Wait_TMR
00D1   0AA3           00402         incf    Wait_TMR, F
00D2   0AAA           00403         incf    STATE_CNT, F
00D3   01A4           00404         clrf    Wait_CNT
00D4   2912           00405         goto    END_ISR
                      00406
00D5                  00407 STATE_5
```

```
00D5   0AA3          00408         incf    Wait_TMR, F
00D6   3000          00409         movlw   0x00
00D7   0223          00410         subwf   Wait_TMR, W
```

```
LOC  OBJECT CODE     LINE SOURCE TEXT
  VALUE

00D8   1D03           00411         btfss   STATUS, Z
00D9   2912           00412         goto    END_ISR
                      00413
00DA   30F8           00414         movlw   Wait
00DB   00A3           00415         movwf   Wait_TMR
00DC   0AA4           00416         incf    Wait_CNT, F
00DD   3009           00417         movlw   0x09
00DE   0224           00418         subwf   Wait_CNT, W
00DF   1D03           00419         btfss   STATUS, Z
00E0   2912           00420         goto    END_ISR
                      00421
00E1   0185           00422         clrf    PORTA
00E2   082A           00423         movf    STATE_CNT, W
00E3   203F           00424         call    Disable
00E4   0086           00425         movwf   PORTB
                      00426
00E5   082A           00427         movf    STATE_CNT, W
00E6   2048           00428         call    Short
00E7   0085           00429         movwf   PORTA
                      00430
00E8   30F8           00431         movlw   Wait
00E9   00A3           00432         movwf   Wait_TMR
00EA   0AA3           00433         incf    Wait_TMR, F
00EB   0AAA           00434         incf    STATE_CNT, F
00EC   01A4           00435         clrf    Wait_CNT
00ED   2912           00436         goto    END_ISR
                      00437
00EE                  00438 STATE_6
00EE   0AA3           00439         incf    Wait_TMR, F
00EF   3000           00440         movlw   0x00
00F0   0223           00441         subwf   Wait_TMR, W
00F1   1D03           00442         btfss   STATUS, Z
00F2   2912           00443         goto    END_ISR
                      00444
                      00445 ;       movlw   Wait
                      00446 ;       movwf   Wait_TMR
                      00447 ;       incf    Wait_CNT, F
                      00448 ;       movlw   0x09
                      00449 ;       subwf   Wait_CNT, W
                      00450 ;       btfss   STATUS, Z
                      00451 ;       goto    END_ISR
                      00452
00F3   0185           00453         clrf    PORTA
00F4   082A           00454         movf    STATE_CNT, W
00F5   203F           00455         call    Disable
00F6   0086           00456         movwf   PORTB
                      00457
00F7   082A           00458         movf    STATE_CNT, W
00F8   2048           00459         call    Short
00F9   0085           00460         movwf   PORTA
```

```
                        00461
00FA   30F8             00462          movlw   Wait
00FB   00A3             00463          movwf   Wait_TMR
```

```
LOC  OBJECT CODE     LINE SOURCE TEXT
  VALUE

00FC   0AA3           00464         incf    Wait_TMR, F
00FD   0AAA           00465         incf    STATE_CNT, F
00FE   01A4           00466         clrf    Wait_CNT
00FF   2912           00467         goto    END_ISR
                      00468
0100                  00469 STATE_7
0100   0AA3           00470         incf    Wait_TMR, F
0101   3000           00471         movlw   0x00
0102   0223           00472         subwf   Wait_TMR, W
0103   1D03           00473         btfss   STATUS, Z
0104   2912           00474         goto    END_ISR
                      00475
                      00476 ;       movlw   Wait
                      00477 ;       movwf   Wait_TMR
                      00478 ;       incf    Wait_CNT, F
                      00479 ;       movlw   0x09
                      00480 ;       subwf   Wait_CNT, W
                      00481 ;       btfss   STATUS, Z
                      00482 ;       goto    END_ISR
                      00483
0105   0185           00484         clrf    PORTA
0106   082A           00485         movf    STATE_CNT, W
0107   203F           00486         call    Disable
0108   0086           00487         movwf   PORTB
                      00488
0109   082A           00489         movf    STATE_CNT, W
010A   2048           00490         call    Short
010B   0085           00491         movwf   PORTA
                      00492
010C   30F8           00493         movlw   Wait
010D   00A3           00494         movwf   Wait_TMR
010E   0AA3           00495         incf    Wait_TMR, F
010F   01AA           00496         clrf    STATE_CNT
0110   01A4           00497         clrf    Wait_CNT
0111   2912           00498         goto    END_ISR
                      00499
0112                  00500 END_ISR
                      00501
0112   0E26           00502         swapf   S_temp, W
0113   0083           00503         movwf   STATUS
0114   0EA5           00504         swapf   W_temp, F
0115   0E25           00505         swapf   W_temp, W
0116   0009           00506         retfie
                      00507         end
```

SYMBOL TABLE

LABEL	VALUE
ACKDT	00000005
ACKEN	00000004
ACKSTAT	00000006
ACQT0	00000003
ACQT1	00000004
ACQT2	00000005
ADCON0	0000001F
ADCON1	0000009F
ADCON2	0000009B
ADCS0	00000006
ADCS1	00000007
ADCS2	00000006
ADCVRT_MSK	00000041
ADDEN	00000003
ADFM	00000007
ADIE	00000006
ADIF	00000006
ADON	00000000
ADRESH	0000001E
ADRESL	0000009E
AD_INP	00000029
AD_REF	00000028
BCLIE	00000003
BCLIF	00000003
BF	00000000
BRGH	00000002
C	00000000
C1INV	00000004
C1OUT	00000006
C2INV	00000005
C2OUT	00000007
CCP1CON	00000017
CCP1IE	00000002
CCP1IF	00000002
CCP1M0	00000000
CCP1M1	00000001
CCP1M2	00000002
CCP1M3	00000003
CCP1X	00000005
CCP1Y	00000004
CCP2CON	0000001D
CCP2IE	00000000
CCP2IF	00000000
CCP2M0	00000000
CCP2M1	00000001
CCP2M2	00000002
CCP2M3	00000003
CCP2X	00000005
CCP2Y	00000004
CCP3CON	00000097

```
CCP3IE                          00000001
CCP3IF                          00000001
CCP3M0                          00000000
```

SYMBOL TABLE

LABEL	VALUE
CCP3M1	00000001
CCP3M2	00000002
CCP3M3	00000003
CCP3X	00000005
CCP3Y	00000004
CCPR1H	00000016
CCPR1L	00000015
CCPR2H	0000001C
CCPR2L	0000001B
CCPR3H	00000096
CCPR3L	00000095
CH0_MSK	00000000
CH1_MSK	00000008
CHS0	00000003
CHS1	00000004
CHS2	00000005
CHS3	00000001
CIS	00000003
CKE	00000006
CKP	00000004
CM0	00000000
CM1	00000001
CM2	00000002
CMCON	0000009C
CMIE	00000006
CMIF	00000006
CREN	00000004
CSRC	00000007
CVR0	00000000
CVR1	00000001
CVR2	00000002
CVR3	00000003
CVRCON	0000009D
CVREN	00000007
CVROE	00000006
CVRR	00000005
Cap_SW	000000C0
Clr_C	0000003C
Config	00000005
D	00000005
DATA_ADDRESS	00000005
DC	00000001
DIO_A0	00000000
DIO_A1	00000001
DIO_A2	00000002
DIO_A3	00000003
DIO_REVPOL	00000005
D_A	00000005
Disable	0000003F
END_ISR	00000112

```
EN_GFC0                         00000000
EN_GFC1                         00000001
EN_GFC2                         00000002
```

SYMBOL TABLE

LABEL	VALUE
EN_GFC3	00000003
EN_GFC4	00000004
EN_GFC5	00000005
EN_SERIES	00000004
F	00000001
FERR	00000002
FSR	00000004
GCEN	00000007
GIE	00000007
GO	00000002
GO_DONE	00000002
HI_BYTE	00000080
I2C_DATA	00000005
I2C_READ	00000002
I2C_START	00000003
I2C_STOP	00000004
IBF	00000007
IBOV	00000005
INDF	00000000
INT0IE	00000004
INT0IF	00000001
INTCON	0000000B
INTE	00000004
INTEDG	00000006
INTF	00000001
IOFS	00000002
IRCF0	00000004
IRCF1	00000005
IRCF2	00000006
IRP	00000007
IRVST	00000005
ISR	00000051
LED7	00000006
LED8	00000007
LO_BYTE	00000000
LVDCON	00000109
LVDEN	00000004
LVDIE	00000005
LVDIF	00000005
LVDL0	00000000
LVDL1	00000001
LVDL2	00000002
LVDL3	00000003
MAIN	00000036
NOT_A	00000005
NOT_ADDRESS	00000005
NOT_BO	00000000
NOT_BOR	00000000
NOT_DONE	00000002
NOT_PD	00000003

```
NOT_POR                         00000001
NOT_RBPU                        00000007
NOT_RC8                         00000006
```

SYMBOL TABLE

LABEL	VALUE
NOT_T1SYNC	00000002
NOT_TO	00000004
NOT_TX8	00000006
NOT_W	00000002
NOT_WRITE	00000002
OBF	00000006
OERR	00000001
OPTION_REG	00000081
OSCCON	0000008F
OSCTUNE	00000090
OSFIE	00000007
OSFIF	00000007
OSTS	00000003
P	00000004
PCFG0	00000000
PCFG1	00000001
PCFG2	00000002
PCFG3	00000003
PCL	00000002
PCLATH	0000000A
PCON	0000008E
PEIE	00000006
PEN	00000002
PIE1	0000008C
PIE1_MSK	00000001
PIE2	0000008D
PIE2_MSK	00000000
PIR1	0000000C
PIR2	0000000D
PMADR	0000010D
PMADRH	0000010F
PMCON1	0000018C
PMDATA	0000010C
PMDATH	0000010E
PORTA	00000005
PORTB	00000006
PORTC	00000007
PORTD	00000008
PORTE	00000009
PR2	00000092
PS0	00000000
PS1	00000001
PS2	00000002
PSA	00000003
PSPIE	00000007
PSPIF	00000007
PSPMODE	00000004
R	00000002
RBIE	00000003
RBIF	00000000

```
RC8_9                                   00000006
RC9                                     00000006
RCD8                                    00000000
```

SYMBOL TABLE

LABEL	VALUE
RCEN	00000003
RCIE	00000005
RCIF	00000005
RCREG	0000001A
RCSTA	00000018
RD	00000000
READ_WRITE	00000002
RP0	00000005
RP1	00000006
RSEN	00000001
RX9	00000006
RX9D	00000000
R_W	00000002
S	00000003
SBOREN	00000002
SCS0	00000000
SCS1	00000001
SEN	00000000
SH_GFC0	00000000
SH_GFC1	00000001
SH_GFC2	00000002
SH_GFC3	00000003
SH_GFC4	00000004
SH_GFC5	00000005
SMP	00000007
SPBRG	00000099
SPEN	00000007
SREN	00000005
SSPADD	00000093
SSPBUF	00000013
SSPCON	00000014
SSPCON2	00000091
SSPEN	00000005
SSPIE	00000003
SSPIF	00000003
SSPM0	00000000
SSPM1	00000001
SSPM2	00000002
SSPM3	00000003
SSPOV	00000006
SSPSTAT	00000094
STATE_0	0000007A
STATE_1	00000089
STATE_2	000000A2
STATE_3	000000B4
STATE_4	000000C6
STATE_5	000000D5
STATE_6	000000EE
STATE_7	00000100
STATE_CNT	0000002A

```
STATUS                          00000003
SWDTE                           00000000
SWDTEN                          00000000
```

SYMBOL TABLE

LABEL	VALUE
SYNC	00000004
SYS_CLK	00000002
S_temp	00000026
Set_0	000000A0
Short	00000048
T0CS	00000005
T0IE	00000005
T0IF	00000002
T0SE	00000004
T0_OFF_MSK	000000C0
T0_ON_MSK	000000E0
T1CKPS0	00000004
T1CKPS1	00000005
T1CON	00000010
T1INSYNC	00000002
T1OSCEN	00000003
T1RUN	00000006
T1SYNC	00000002
T2CKPS0	00000000
T2CKPS1	00000001
T2CON	00000012
TMR0	00000001
TMR0IE	00000005
TMR0IF	00000002
TMR1CS	00000001
TMR1H	0000000F
TMR1IE	00000000
TMR1IF	00000000
TMR1L	0000000E
TMR1ON	00000000
TMR2	00000011
TMR2IE	00000001
TMR2IF	00000001
TMR2ON	00000002
TOUTPS0	00000003
TOUTPS1	00000004
TOUTPS2	00000005
TOUTPS3	00000006
TRISA	00000085
TRISB	00000086
TRISC	00000087
TRISD	00000088
TRISE	00000089
TRISE0	00000000
TRISE1	00000001
TRISE2	00000002
TRISE3	00000003
TRMT	00000001
TUN0	00000000
TUN1	00000001

```
TUN2                                    00000002
TUN3                                    00000003
TUN4                                    00000004
```

SYMBOL TABLE

LABEL	VALUE
TUN5	00000005
TX8_9	00000006
TX9	00000006
TX9D	00000000
TXD8	00000000
TXEN	00000005
TXIE	00000004
TXIF	00000004
TXREG	00000019
TXSTA	00000098
UA	00000001
VCFG0	00000004
VCFG1	00000005
W	00000000
WCOL	00000007
WDTCON	00000105
WDTPS0	00000001
WDTPS1	00000002
WDTPS2	00000003
WDTPS3	00000004
W_temp	00000025
Wait	000000F8
Wait_CNT	00000024
Wait_TMR	00000023
Z	00000002
_BOREN_0	00003FBF
_BOREN_1	00003FFF
_BORSEN_0	00003FBF
_BORSEN_1	00003FFF
_CCP2_RB3	00002FFF
_CCP2_RC1	00003FFF
_CONFIG1	00002007
_CONFIG2	00002008
_CP_ALL	00001FFF
_CP_OFF	00003FFF
_DEBUG_OFF	00003FFF
_DEBUG_ON	000037FF
_EXTCLK	00003FEF
_EXTRC_CLKOUT	00003FFF
_EXTRC_IO	00003FFE
_FCMEN_OFF	00003FFE
_FCMEN_ON	00003FFF
_HS_OSC	00003FEE
_IESO_OFF	00003FFD
_IESO_ON	00003FFF
_INTRC_CLKOUT	00003FFD
_INTRC_IO	00003FFC
_LP_OSC	00003FEC
_MCLR_OFF	00003FDF
_MCLR_ON	00003FFF

```
_PWRTE_OFF                      00003FFF
_PWRTE_ON                       00003FF7
_VBOR_2_0                       00003FFF
```

```
SYMBOL TABLE
  LABEL                             VALUE

_VBOR_2_7                         00003F7F
_VBOR_4_2                         00003EFF
_VBOR_4_5                         00003E7F
_WDT_OFF                          00003FFB
_WDT_ON                           00003FFF
_XT_OSC                           00003FED
__16F737                          00000001
countus_temp                      00000027


MEMORY USAGE MAP ('X' = Used,  '-' = Unused)

0000 : X---XXXXXXXXXXXX XXXXXXXXXXXXXXXX XXXXXXXXXXXXXXXX
XXXXXXXXXXXXXXXX
0040 : XXXXXXXXXXXXXXXX XXXXXXXXXXXXXXXX XXXXXXXXXXXXXXXX
XXXXXXXXXXXXXXXX
0080 : XXXXXXXXXXXXXXXX XXXXXXXXXXXXXXXX XXXXXXXXXXXXXXXX
XXXXXXXXXXXXXXXX
00C0 : XXXXXXXXXXXXXXXX XXXXXXXXXXXXXXXX XXXXXXXXXXXXXXXX
XXXXXXXXXXXXXXXX
0100 : XXXXXXXXXXXXXXXX XXXXXXX--------- ---------------- -------------
---
2000 : -------XX------- ---------------- ---------------- -------------
---

All other memory blocks unused.

Program Memory Words Used:   276
Program Memory Words Free:  3820


Errors   :     0
Warnings :     0 reported,     0 suppressed
Messages :     8 reported,     0 suppressed
```

10. References

[1] Laramie, J.; Dicks, A. *Fuel Cell Systems Explained*, John Wiley and Sons, LTD, Baffins Lane, Chichester, West Sussex, England, **2000**

[2] Thomas, S.; Zalbowitz, M. *"Fuel Cells, Green Power"* (web page, August 11, 1999). http://education.lanl.gov/resources/fuelcells/.

[3] Stone, C.; Morrison, A.E. *Solid State Ionics* **2002**, *152-153*, 1.

[4] Huff, J.R. Progress in Batteries and Solar Cells **1989**, 8, 302.

[5] Costamagna, P.; Srinivasan, S. *J. Power Sources* **2001**, *102(1-2)*, 242.

[6] *"Fuel Cells"* http://www.yournextcar.org/fuelcells.html

[7] Largeaud, F., Kokoh, K., Beden, B., Lamy, C., *J. Electroanalytical Chem.* **397** (1995), 261.

[8] Krebs, H., *Perspect. Biol. Med.*, **14***:* 154-170 (1970).

[9] Muzykantov, V., Atochina, E., Ischiropoulos, H., Danilov, S., Fisher, A., Proc., *Natl. Acad. Sci. USA*, **93**, 5213-5218 (1996).

[10] Appleby, A. J., Ng, D. Y., Weinstein, H. *J. App. Electrochem*. **1** (1971), 79-90.

[11] Griss, P., Stemme, G., Proc. *IEEE MEMS. 15th IEEE Intl. Conf MEMS*, Las Vegas, NV (2002), 467-470.

[12] Bostaph, J., Koripella, R., Fisher, A., Zirdel, D., Hallmark, J., Neutzler, J., Bai, L., *Proc. Electrochem. Soc*, **2001-4**, 274-281.

[13] Mench, M., Wang, Z., Bhatia, K., Wang, C., *Proc. ASME IMEC* Vol. 369-4, **2001**, 317-324.

[14] Muller, M., Muller, C., Gromball, F., Wolfle, M, Menz, W., *Microsystem Tech*. **9** (2003) 169-162.

[15] Bostaph, J., Koripella, R., Fisher, A., Zirdel, D., Hallmark, *J. Proc. ECS* **2001-4** (2001) 274-281.

[16] Schmidt, T., Gasteiger, H., Stab, G., Urban, P., Kolb, D., Behm, R., *J Electrochem. Soc*. **145** *7* (1998), 2354-2358.

[17] Mench, M., Wang, C., *J. Electrochem. Soc*., **150** 1 (2003) A79-A85.

[18] Beden, B., Largeaud, F., Kokoh, K., Lamy, C., *Electrochimica Acta* **41** 5 (1996) 701-709.

[19] Kokoh, K., Leger, J.-M., Beden, B., Lamy, C., *Electrochimica Ac*ta **37** 8 (1992) 1333-1342.

[20] Roziere, J.; Jones, D. J. *Annu. Rev. Mater. Res*. **2003**, *33*, 503-555.

[21] Savadogo, O., J. New Mater. Electrochem. Syst., **1998**, 1, 47-66.

[22] Carretta, N.; Tricoli, V.; Picchioni, F. *J. Membr. Sci.* **2000**, *166*, 189-197.

[23] Ding, J.; Chuy, C.; Holdcroft, S. *Chem. Mater*. **2001**, *13*, 2231-2233

[24] Zaidi, S. M. J.; Mikhailenko, S. D.; Robertson, G. P.; Guiver, M. D.; Kaliaguine, S. *J. Membr. Sci*. **2000**, *173*, 17-34.

[25] Jones, D. J.; Roziere, J. *Journal of Membr. Sci*., **2001**, 185, 41-58.

[26] Nolte, R.; Ledjeff, K.; Bauer, M.; Mulhaupt, R. *J. Membr. Sci*. **1993**, *83*, 211-220

[27] Wang, F.; Hickner, M.; Kim, Y. S.; Zawodzinski, T. A.; McGrath, J. E. *J. Membr. Sci.* **2002**, *197*, 231-242.

[28] Kreuer, K. D. *J. Membr. Sci.* **2001**, *185*, 29-39.

[29] Hubner, G; Roduner, E. *J. Mater. Chem*., **1999**, *9*, 409-418.

[30] Kobayashi, T.; Rikukawa, M.; Sanui, Kohei; Ogata, N. *Solid State Ionics*, **1998**, *106*, 219-225.

[31] Hagberg, E. C.; Olson, D. A.; Sheares, V. V. *Macromol*., **2004**, *37*, 7448-4754.

[32] Stille, J. K.; Harris, F. W.; Rakutis, R. O.; Mukamal, H. *J. Polym. Sci., Part B.* **1966**, *4*, 791-793.

[33] Martin, S. J.; Godschalx, J. P.; Mills, M. E.; Shaffer II, E. O.; Townsend, P. H. *Adv. Mater*., **2000**, *12*, 1769-1777.

[34] Olgliaruso, M. A.; Becker, E. I. *J. Org. Chem*., **1965**, *30*, 3354.

[35] Neenan, T. X.; Kumar, U. *Macromol*., **1995**, *28*, 124-130.

[36] Shifrina, Z. B.; Averina, M. S.; Rusanov, A. L.; Wagner, M.; Mullen, K. *Macromol*. **2000**, *33*, 3525-3529.

[37] Noren, G. K.; Stille, J. K. *Macromol. Rev*., **1971**, *5*, 385-429.

[38] Novak, B. M.; Wallow, T. I. *J. Am. Chem. Soc*., **1991**, *91*, 1513

[39] Miyatake, K.; Hay, A. S. *J. Polym. Sci. Part A. Poly. Chem.* **2001**, *39*, 3211-3217

[40] Seung Kim, Y.; Dong, L.; Hickner, M. A.; Glass, T. E.; Webb, V.; McGrath, J. E. . *Macromol.*, **2003**, *36*, 6281-6285.

[41] Kim, Y. S.; Wang, F.; Hickner, M.; McCartney, S.; Hong, Y. T.; Harrion, W.; Zawodzinski, T. A.; McGrath, J. E. *J. Polym. Sci. Part B: Polymer Physics*, **2003**, *41*, 2816-2828.

[42] Wang, Feng; Hickner, Michael; Ji, Qing; Harrison, William; Mecham, Jeffrey; Zawodzinski, Thomas A.; McGrath, James E. *Macromol. Symp*., **2001**, *175*, 387-395.

[43] Einsla, Brian R.; Hong, Young-Taik; Kim, Yu Seung; Wang, Feng; Gunduz, Nazan; McGrath, James E. *J. Polym. Sci. Part A: Polymer Chemistry*, **2004**, *42*, 862-874.

[44] Hickner, M. A., Ph.D. Dissertation, Virginia Polytechnic Institute and State University, **2003**.

[45] Miyatake, K.; Chikashige, Y.; Watanabe, M. *Macromol*., **2003**, 36, 9691-9693.

[46] Chen, T., Barton, S., Binyamin, G., Gao, Z., Zhang, Y., Kim, H-H., Heller, A., *J. Am. Chem. Soc*. **2001**, *123*, 8630-8631.

[47] Kim, H-H., Mano, N., Zhang, Y., Heller, A., *J. Electrochem Soc*., **150** (2) A209-A213 (2003).

[48] Heller, A., *Phys. Chem. Chem. Phys* **2004**, 6, 209-216.

[49] Willner., I., Katz, E., Patolsky, F., Buckmann, A., *J. Chem. Soc., Perkin Trans. 2*, (**1998**) 1817-1822.

[50] Katz, E., Willner, I., Kotlyar, A., *J. Electroanalytical Chem*. **479** (1999) 64-68.

[51] Arico, A. S., Antonucci, V., Giordano, N., Shukla, A. K., Ravikumar, M. K., Roy, A., Barman, S., Sarma, D. D., J. Power Sources; **50**(3), (1994) 295-309

[52] Dosanjh, Nirpjit S.; Kaur, Jagdeep. "Immobilization, stability and esterification studies of a lipase from a Bacillus sp." *Biotechnology and Applied Biochemistry* (2002), 36(1), 7-12.

[53] Shukla, A. K.; Suresh, P.; Berchmans, S.; Rajendran, A. "Biological fuel cells and their applications." *Current Science* (2004), 87(4), 455-468.

[54] Lutz, Stefan; Patrick, Wayne M. "Novel methods for directed evolution of enzymes: quality, not quantity." *Current Opinion in Biotechnology* (2004), 15(4), 291-297; Bornscheuer, Uwe T. "Directed evolution of enzymes." *Angewandte Chemie, International Edition* (1998), 37(22), 3105-3108.

[55] Van der Heide, M.; Hollenberg, C. P.; Van der Klei, I. J.; Veenhuis, M. "Overproduction of BiP negatively affects the secretion of *Aspergillus niger* glucose oxidase by the yeast *Hansenula polymorpha*." *Applied Microbiology and Biotechnology* (2002), 58(4), 487-494.

[56] Kapat, A.; Jung, J.-K.; Park, Y.-H. "Enhancement of glucose oxidase production in batch cultivation of recombinant Saccharomyces cerevisiae: optimization of oxygen transfer condition." *Journal of Applied Microbiology* (2001), 90(2), 216-222.

[57] Wohlfahrt, Gerd; Witt, Susanne; Hendle, Jorg; Schomburg, Dietmar; Kalisz, Henryk M.; Hecht, Hans-Jurgen. "1.8 and 1.9 .ANG. resolution structures of the Penicillium amagasakiense and Aspergillus niger glucose oxidases as a basis for modelling substrate complexes." *Acta Crystallographica, Section D: Biological Crystallography* (1999), D55(5), 969-977.

[58] Bloom, Jesse D.; Wilke, Claus O.; Arnold, Frances H.; Adami, Christoph. "Stability and the evolvability of function in a model protein." *Biophysical Journal* (2004), 86(5), 2758-2764.

[59] Hall, S.B., Khudaish, E.A., and Hart, A.L. Electrochemical oxidation of hydrogen peroxide at platinum electrodes. Part IV: Phosphate buffer dependence. Electrochimica Acta, 1999. **44**(25): p. 4573-4582.

[60] Yang, L., Janle, E., Huang, T.H., Gitzen, J., Kissinger, P.T., Vreeke, M., and Heller, A. Applications of wired peroxidase electrodes for peroxide determination in liquid-chromatography coupled to oxidase immobilized enzyme reactors. Analytical Chemistry, 1995. **67**(8): p. 1326-1331.

[61] Witt, Susanne; Singh, Mahavir; Kalisz, Henryk M. "Structural and kinetic properties of nonglycosylated recombinant Penicillium amagasakiense glucose oxidase expressed in Escherichia coli." *Applied and Environmental Microbiology* (1998), 64(4), 1405-1411.

DISTRIBUTION:

# of copies	MS	Name
2	0603	Christopher Apblett, 1723
1	0603	W. Kent Schubert, 1723
1	1077	Tom E. Zipperian, 1740
1	1078	Steven Martin, 1720
1	0734	Bruce Kelley, 6245
1	1425	Steve Casalnuovo, 1721
1	0612	Daniel Doughty, 2521
1	0613	David Ingersoll, 2521
1	0892	Susan Brozik, 1721
1	1210	Jim Novak, 5935
1	1073	Jason Podgorski, 1712-1
1	9292	Blake Simmons, 8764
1	0734	Chris Cornelius, 6245
1	0123	LDRD Office, 1030
1	9018	Central Technical Files, 8945-1
2	0899	Technical Library, 9616
2	0612	Review and Approval Desk, 9612
		For DOE/OSTI